

University of Kentucky

UKnowledge

---

Theses and Dissertations--Plant Pathology

Plant Pathology

---


2024

## ROLE OF AUTOPHAGY-RELATED GENES IN LIPID TRANSPORT FOR EFFICIENT REPLICATION OF TOMBUSVIRUSES

Yuanrong Kang

*University of Kentucky*, [skyrulerong@gmail.com](mailto:skyrulerong@gmail.com)

Author ORCID Identifier:

 <https://orcid.org/0009-0005-9631-2432>

Digital Object Identifier: <https://doi.org/10.13023/etd.2024.60>

[Right click to open a feedback form in a new tab to let us know how this document benefits you.](#)

### Recommended Citation

Kang, Yuanrong, "ROLE OF AUTOPHAGY-RELATED GENES IN LIPID TRANSPORT FOR EFFICIENT REPLICATION OF TOMBUSVIRUSES" (2024). *Theses and Dissertations--Plant Pathology*. 45.  
[https://uknowledge.uky.edu/plantpath\\_etds/45](https://uknowledge.uky.edu/plantpath_etds/45)

This Doctoral Dissertation is brought to you for free and open access by the Plant Pathology at UKnowledge. It has been accepted for inclusion in Theses and Dissertations--Plant Pathology by an authorized administrator of UKnowledge. For more information, please contact [UKnowledge@lsv.uky.edu](mailto:UKnowledge@lsv.uky.edu).

## **STUDENT AGREEMENT:**

I represent that my thesis or dissertation and abstract are my original work. Proper attribution has been given to all outside sources. I understand that I am solely responsible for obtaining any needed copyright permissions. I have obtained needed written permission statement(s) from the owner(s) of each third-party copyrighted matter to be included in my work, allowing electronic distribution (if such use is not permitted by the fair use doctrine) which will be submitted to UKnowledge as Additional File.

I hereby grant to The University of Kentucky and its agents the irrevocable, non-exclusive, and royalty-free license to archive and make accessible my work in whole or in part in all forms of media, now or hereafter known. I agree that the document mentioned above may be made available immediately for worldwide access unless an embargo applies.

I retain all other ownership rights to the copyright of my work. I also retain the right to use in future works (such as articles or books) all or part of my work. I understand that I am free to register the copyright to my work.

## **REVIEW, APPROVAL AND ACCEPTANCE**

The document mentioned above has been reviewed and accepted by the student's advisor, on behalf of the advisory committee, and by the Director of Graduate Studies (DGS), on behalf of the program; we verify that this is the final, approved version of the student's thesis including all changes required by the advisory committee. The undersigned agree to abide by the statements above.

Yuanrong Kang, Student

Dr. Peter D. Nagy, Major Professor

Nicole Gauthier, Director of Graduate Studies

ROLE OF AUTOPHAGY-RELATED GENES IN LIPID TRANSPORT FOR  
EFFICIENT REPLICATION OF TOMBUSVIRUSES

---

DISSERTATION

---

A dissertation submitted in partial fulfillment of the  
requirements for the degree of Doctor of Philosophy in the  
College of Agriculture, Food and Environment  
at the University of Kentucky

By  
Yuanrong Kang  
Lexington, Kentucky  
Director: Dr. Peter D. Nagy, Professor of Plant Pathology  
Lexington, Kentucky  
2024

Copyright © Yuanrong Kang 2024  
<https://orcid.org/0009-0005-9631-243>

## ABSTRACT OF DISSERTATION

### ROLE OF AUTOPHAGY-RELATED GENES IN LIPID TRANSPORT FOR EFFICIENT REPLICATION OF TOMBUSVIRUSES

Tombusviruses are positive-strand RNA viruses, which utilize numerous co-opted host factors and massive *de-novo* synthesized membrane resources to modify host membranes and form large viral replication organelles (VROs). Among plenty of host cellular processes, autophagy emerges as a potential membrane resource for VROs formation due to its ability to *de-novo* generate the double membrane structures, known as autophagosomes. Besides, as an important host defense pathway, autophagy is also a target for tombusviruses to prevent its antiviral activities. In this study, I identify the role of key autophagy related genes, Atg11, Atg8, and Atg2, which are involved in autophagosome formation, and the selective autophagy receptor NBR1, in tombusviruses replication.

Based on genomics studies, I found that deletion of Autophagy-related 11 (ATG11/FIP200), a component of the Atg1/13 complex involved in selective autophagy, inhibited TBSV and the closely related carnation Italian ringspot virus (CIRV) replication in yeast and similarly in plants. I demonstrated that Atg11 directly interacts with the TBSV p33 replication protein *in vivo* and *in vitro*, facilitating its recruitment into VROs. Interestingly, I observed that the subverted Atg11 affects the recruitment of additional membrane contact site (MCS) proteins, such as Sac1, Scs2 VAP, and Osh6 OSBP1-like proteins, to support the formation of the virus-induced MCS (vMCS), which is important to sterol transfer to VROs. These results indicate a novel function of Atg11 in TBSV replication.

Additionally, I show that the highly conserved Atg8 autophagy regulator proteins are co-opted by both TBSV and CIRV via direct interactions with their viral replication proteins. Knockdown of Atg8f in *Nicotiana benthamiana* plants resulted in reduced tombusvirus replication, thus indicating a pro-viral function for Atg8f. Using RavZ, a *Legionella* effector that inhibits host autophagy through irreversible Atg8 deconjugation, I demonstrated that Atg8-PE is essential for TBSV replication. Monitoring autophagy flux activity via the ratio of GFP/GFP-Atg8 and Atg8-PE/Atg8 revealed that TBSV replication inhibits host autophagy progress. One possible mechanism is non-PE conjugated Atg8 forming bio-condensates with NBR1 selective autophagy receptor, resulting in their

sequestration in condensates near and in VROs. Furthermore, NBR1 also appears to facilitate the accumulation of phospholipids in VROs, indicating a complex and finely regulated mechanism of exploitation of host autophagy by tombusviruses.

Also, Atg2 was identified as a pro-viral host factor, with its function and protein structure closely related to its role as a lipid transfer protein (LTP), where its N-terminal hydrophobic channel can nonspecifically bind and transfer various phospholipids crucial for VRO formation. Subsequent experiments confirmed that silencing Atg2 in plants or its deletion in yeast significantly reduces the enrichment of key phospholipids in VROs as well as inhibits tombusviruses replication.

Overall, through the study of three specific autophagy-related genes, I have identified three independent lipid transport pathways potentially exploited by the tombusviruses. These pathways provide the virus with lipid sources, enabling the rapid establishment of VROs and facilitating viral replication. Ultimately, these advancements open up a new chapter in tombusvirus-host interactions.

**KEYWORDS:** Positive strand RNA virus, autophagy, membrane contact site, phospholipids transfer, lipid transfer proteins

---

Yuanrong Kang

---

Feb 6, 2024

Date

ROLE OF AUTOPHAGY-RELATED GENES IN LIPID TRANSPORT FOR  
EFFICIENT REPLICATION OF TOMBUSVIRUSES

By

Yuanrong Kang

Peter D. Nagy, Ph.D.

---

Director of Dissertation

Nicole Gauthier, Ph.D.

---

Director of Graduate Studies

Feb 6, 2024

---

Date

*To my beloved family, always keep a light in that good night.*

## ACKNOWLEDGMENTS

I would like to express my deepest gratitude to my advisor Dr. Peter D. Nagy, for his invaluable guidance, support, and encouragement throughout my project. His insights and expertise have been truly inspiring, guiding me continuously in the study of biological science. Since 2018, a time when I felt lost and uncertain about my future academic path, his mentorship has guided me through moments of doubt and helped me to restart my journey in science with confidence.

I extend my sincere gratitude to my committee members, Dr. Christopher Schardl, Dr. Lisa Vaillancourt, and Dr. Becky Dutch, for their support and flexibility in scheduling, which greatly facilitated the completion of my doctoral program. Their professional insights on my project have been incredibly valuable, and I am deeply appreciative of their contributions to help me overcome the difficulties as an international student. My thanks also go to my outside examiner, Dr. Van Sanford, for his assistance throughout the completion of my project.

I am grateful to Dr. Judit Pogany and Dr. Shifeng Zhu for their kindly care and concern, which extended beyond professional support to include personal and emotional well-being. This has been extraordinarily meaningful to me. I would like to express my appreciation to my most important colleagues, Dr. Wenwu Lin and Yuyan Liu. I am fortunate to have met you during this journey abroad. Your support in both work and life, your friendship has been invaluable. I also thank to Melissa Molho and Paulina Alatraste, with whom I shared and overcame the challenging times of the pandemic through support and assistance. Additionally, I thank the past and current members of the Nagy lab for all your help and the enjoyable times we spent working together. My gratitude extends to Dr.



Rick Bennet, Dr. Nicole Gauthier, Amy Crume, and the Department of Plant Pathology Office Staff for their support during my Ph.D. program.

I am also thankful for the support of my badminton partners, especially the members of the "Dare to Play in JC " and the "Smash and Swing 17." The moments spent sweating on the court with you all rejuvenated my spirit and restored my confidence to tackle new challenges.

I appreciate Dr. Fan Xia and Dr. Xinyu Yuan for their past care and companionship, offering me significant support in both personal and professional aspects. Thanks to Xianmin, Mengfan, Ning and Mingwei for being part of my life.

A special thank you to Huimin Liang for your support and care. I am deeply grateful for your companionship and thank you being here all the time.

Finally, to my beloved family, my mother, father, and sister, whose unconditional love and support empower me to continue exploring in this vast yet solitary world.

## TABLE OF CONTENTS

ACKNOWLEDGMENTS .....	iii
LIST OF TABLES .....	vi
LIST OF FIGURES .....	vii
CHAPTER 1. INTRODUCTION .....	1
1.1    Tombusviruses .....	1
1.2    Diverse lipids functions in the replication of positive-strand RNA viruses .....	3
1.3    Lipids transport in positive-strand RNA virus replication.....	5
1.4    Autophagy: Mechanisms and TBSV Interactions.....	8
CHAPTER 2. KEY TETHERING FUNCTION OF ATG11 AUTOPHAGY SCAFFOLD PROTEIN IN FORMATION OF VIRUS-INDUCED MEMBRANE CONTACT SITES DURING TOMBUSVIRUS REPLICATION.....	11
2.1    Introduction.....	11
2.2    Results.....	14
2.3    Discussion.....	26
2.4    Materials and methods .....	29
CHAPTER 3. SUBVERSION OF SELECTIVE AUTOPHAGY FOR THE BIOGENESIS OF TOMBUSVIRUS REPLICATION ORGANELLES INHIBITS AUTOPHAGY 78	
3.1    Introduction.....	78
3.2    Results.....	81
3.3    Discussion.....	96
3.4    Materials and methods .....	101
CHAPTER 4. FUNCTIONAL ROLE OF ATG2 AS A LIPID TRANSPORT PROTEIN IN TOMBUSVIRUS REPLICATION .....	164
4.1    Introduction.....	164
4.2    Results.....	168
4.3    Discussion.....	177
4.4    Materials and methods .....	181
CHAPTER 5. CONCLUSIONS AND PERSPECTIVES.....	206
5.1    Conclusions.....	206
5.2    Perspectives.....	212
REFERENCES .....	219
VITA.....	235

## LIST OF TABLES

Table 2.1: Plasmids constructed in chapter 2.....	38
Table 2.2: Plasmids described in previous studies of chapter 2. ....	40
Table 2.3: Reference of table 2.2.....	41
Table 2.4: Primers used in chapter 2.....	41
Table 3.1: Plasmids constructed in chapter 3.....	110
Table 3.2: Plasmids described in previous studies of chapter 3. ....	112
Table 3.3: Reference for table 3.2.....	113
Table 3.4: Primers used in chapter 3.....	113
Table 4.1: Plasmids constructed in chapter 4.....	187
Table 4.2: Plasmids described in previous studies of chapter 4. ....	188
Table 4.3: Reference for table 4.2.....	188
Table 4.4: Primers used in chapter 4.....	189

## LIST OF FIGURES

<i>Figure 2.1. Atg11 autophagy scaffold protein is an essential host factor for tombusvirus replication in yeast.</i> .....	45
<i>Figure 2.2. The effect of Atg11 on tombusvirus replication in N. benthamiana plants.</i> ...	47
<i>Figure 2.3.</i> .....	49
<i>Figure 2.4. Interaction between tombusvirus replication proteins and Atg11.</i> .....	51
<i>Figure 2.5. BiFC studies of the interaction between Atg11 and replication proteins within VROs in N. benthamiana.</i> .....	53
<i>Figure 2.6. Atg11 facilitates the recruitment of the cellular ER-resident VAP protein, Sac1 and Osh6 proteins into tombusvirus replication compartment.</i> .....	55
<i>Figure 2.7. Interaction between Atg11 and Sac1 PI4P phosphatase protein within VROs in N. benthamiana.</i> .....	57
<i>Figure 2.8. Protein proximity-labeling of vMCS proteins with biotin in yeast and plants.</i> .....	59
<i>Figure 2.9. Atg11 affects sterol re-localization to internal sites in yeast replicating TBSV RNA.</i> .....	61
<i>Figure 2.10. Double-deletion of ATG11 and FIS1 further decreases tombusvirus RNA accumulation in yeast.</i> .....	63
<i>Figure 2.11. Deletion of ATG11 sensitizes tombusvirus RNA to RNAi-based degradation in yeast.</i> .....	65
<i>Figure 2.12. A model on the functional role of the Atg11 autophagy scaffold protein in the formation of virus-induced vMCS.</i> .....	67
<i>Figure S2.1. Sequence alignment of the Arabidopsis Atg11 (AT4G30790) and the N. benthamiana Atg11 (Niben101Scf09742g00014.1 and Niben101Scf02359g00022.1) amino acid sequences. The ATG17-like APG17 and Atg11-like domains are indicated.</i> ..	71
<i>Figure S2.2. Sequence alignment of the R2 and R3 regions of NbATG11 genes used for the VIGS experiments.</i> .....	73
<i>Figure S2.3. Supplement to Figure 2.4.</i> .....	75
<i>Figure S2.4. Supplement to Figure 2.8.</i> .....	77
<i>Figure 3.1. Recruitment of ATG8 by the TBSV p33 and the CIRV p36 replication proteins into VROs in N. benthamiana.</i> .....	117
<i>Figure 3.2. Interaction between ATG8 and tombusvirus replication proteins within VROs in N. benthamiana.</i> .....	119
<i>Figure 3.3. The effect of ATG8 on tombusvirus replication in N. benthamiana plants.</i> ..	121
<i>Figure 3.4. Recruitment of NBR1 selective autophagy receptor by the TBSV p33 and the CIRV p36 replication proteins into VROs in N. benthamiana.</i> .....	123
<i>Figure 3.5. Interaction between the co-opted ATG8f and NBR1 proteins within VROs in N. benthamiana.</i> .....	125
<i>Figure 3.6. Separate subversion of ATG8f or NBR1 by TBSV p33 replication protein into VROs.</i> .....	127
<i>Figure 3.7. The effect of NBR1 on tombusvirus replication in N. benthamiana plants.</i> ..	129

<i>Figure 3.8. Contributions of ATG8f and NBR1 to PE enrichment in the viral replication compartment in N. benthamiana protoplasts.</i>	131
<i>Figure 3.9. ATG8 and NBR1 contribute to PI(3)P enrichment within the viral replication compartment in N. benthamiana plants and protoplasts.</i>	133
<i>Figure 3.10. ATG8f promotes the enrichment of VPS34 PI3 kinase within VROs in N. benthamiana plants and yeast.</i>	135
<i>Figure 3.11. TBSV replication protein inhibits autophagic flux in N. benthamiana.</i>	137
<i>Figure 3.12. NBR1 affects inhibition of autophagic flux by TBSV in N. benthamiana.</i>	139
<i>Figure 3.13. ATG8f and NBR1 are present in condensates associated with the TBSV VROs.</i>	141
<i>Figure 3.14. A model on subversion of selective autophagy for tombusvirus replication and inhibition of antiviral autophagy via sequestration of NBR1 and ATG8f in VRO...</i>	143
<i>Figure S3.1. Role of ATG8a and ATG8i in tombusvirus replication in N. benthamiana.</i>	145
<i>Figure S3.2. Co-localization of the minus-strand of replicon RNA with ATG8a in VROs in N. benthamiana leaves infected with CNV.</i>	147
<i>Figure S3.3. Recruitment of core ATG proteins by the TBSV p33 replication protein into VROs in N. benthamiana.</i>	149
<i>Figure S3.4. Additional experiments to confirm interactions between tombusvirus replication proteins and ATG8.</i>	151
<i>Figure S3.5. Interactions between TBSV p33 replication protein and core ATG proteins in N. benthamiana.</i>	153
<i>Figure S3.6. SH3P2 interacts with TBSV p33 replication protein and ATG8f within VROs in N. benthamiana.</i>	155
<i>Figure S3.7. Semi-quantitative RT-PCR analysis of mRNA levels of ATG8 family members in ATG8f silenced plants.</i>	157
<i>Figure S3.8. Nonlipidated ATG8f is recruited by TBSV p33 replication protein into VROs.</i>	159
<i>Figure S3.9. FRAP analysis of ATG8f and NBR1 shows their presence in condensates associated with the TBSV VROs.</i>	161
<i>Figure S3.10. FRAP analysis of core ATG8 proteins in the TBSV VROs.</i>	163
<i>Figure 4.1.</i>	191
<i>Figure 4.2. The effect of Atg2 on tombusvirus replication in N. benthamiana plants.</i>	193
<i>Figure 4.3. Recruitment of Atg2 by the TBSV p33 and the CIRV p36 replication proteins into VROs in N. benthamiana.</i>	195
<i>Figure 4.4. Interaction between Atg2 and tombusvirus replication proteins in N. benthamiana.</i>	197
<i>Figure 4.5. Contributions of Atg2 to PE enrichment in the viral replication compartment in N. benthamiana protoplasts and yeast spheroplasts.</i>	199
<i>Figure 4.6. Atg2 promotes PI(3)P enrichment within the viral replication compartment in N. benthamiana plants and yeasts.</i>	201
<i>Figure 4.7. Atg2 contributes to PS enrichment within the viral replication compartment in N. benthamiana plants and yeast.</i>	203

*Figure 4.8. Atg2's pro-viral role in N. benthamiana plants is autophagy-independent and unrelated to Atg11-mediated pathway. .... 205*

*Figure 5.1. TBSV employed different lipid resources for VROs establishment. .... 218*

## CHAPTER 1.

### INTRODUCTION

#### 1.1 Tombusviruses

Tombusviruses, belonging to the positive-strand RNA virus family, are extensively studied plant viruses with messenger sense RNA genomes (1). The prototypical species, *Tomato bushy stunt virus* (TBSV), serves as a model for understanding various aspects of (+)RNA virus replication, such as replicase assembly and large viral replication organelle (VRO) formation (2-4).

The single-stranded positive-sense RNA genome of TBSV, approximately 4.8 kb nucleotides long, is highly structured with unique features of a 5' non-capped end and a 3' non-polyadenylated end (1). TBSV encodes five viral proteins: the 5' proximally encoded replication proteins p33 and p92 (5), and the 3' proximally encoded capsid protein p42, movement protein p22, and suppressor of gene silencing p19 (6). The replication proteins, p33 and p92, are integral for viral replication, with p33 serving as a replication cofactor involved in template RNA recruitment (7), functioning as the RNA chaperone for RNA synthesis initiation (8), and host factor recruitment for VRO establishment (9, 10). p92, a p33 UAG stop codon read-through product, possesses RNA-dependent RNA polymerase (RdRp) activity and maintains the protein level at approximately a 1:20 ratio with p33 (5). Both proteins have transmembrane domains, and the p33:p92 interaction contributes to the assembly of the viral replicase and its association with subcellular membranes (11).

Tombusviruses, particularly TBSV, have become valuable model viruses for studying (+)RNA virus replication in both yeast and plants. The yeast system relies on the replication proteins p33 and p92, along with the trans-replication of defective interfering (DI) RNAs (12). The prototypical DI-72 RNA, comprising four noncontiguous regions of the viral RNA genome, is crucial for its ability to utilize the parental TBSV replication machinery for self-replication, thus becoming an efficient replicon for TBSV replication in yeast (13). The exploration of fundamental aspects of (+)RNA virus replication and recombination has been significantly advanced by employing yeast as a surrogate host for tombusviruses. In this model, essential replicase proteins, including p33, p92, and DI-72, which serves as a viral replicon RNA (repRNA), are expressed to initiate viral replication. Through genome and proteome-wide screens in yeast, numerous host genes influencing TBSV replication and viral RNA recombination have been identified, providing valuable insights into the intricate mechanisms governing viral replication (14). Additionally, the utilization of cell-free extract methods enables a more precise control of factors involved in virus replication, thereby facilitating a deeper understanding of the viral replication process (15). The plant system primarily utilizes the agrobacterium mediated *Nicotiana benthamiana* transient expression system for TBSV genomic RNA replication as well as sap inoculation (16).

Carnation Italian ringspot virus (CIRV), a tombusvirus closely related to TBSV, exhibits similarities in sequence and replication mechanisms, p36 and RdRP p95, but assembles its replicase complex on the outer membrane of mitochondria (17, 18). Examining CIRV highlights the broad applicability of viral replication mechanisms in different subcellular environments.



In summary, tombusviruses, particularly TBSV, offer a unique platform for investigating various aspects of plant virus replication, host-pathogen interactions, and the manipulation of host cell machinery during infection. The integration of yeast as a model system further enhances our understanding of fundamental aspects of (+)RNA virus biology.

## 1.2 Diverse lipids functions in the replication of positive-strand RNA viruses

Positive-strand RNA viruses induce membrane proliferation and the formation of viral replication organelles in different subcellular locations (19-21). Notably, the phospholipids predominantly constitute the primary membrane components of these *de novo* formed viral replication factories. In eukaryotic cells, phosphatidylcholine (PC) emerges as the predominant glycerophospholipid with a shape conducive to stable planar bilayer organization, while also being recognized as a source signaling molecules (22). The study of *Brome mosaic virus* (BMV) has uncovered the *de novo* synthesis of PC in the perinuclear ER membrane, the site of BMV replication. This process involves the recruitment of Cho2p (choline requiring 2), a host enzyme responsible for PC synthesis, facilitated by the interaction with BMV replication protein 1a (23). In contrast, phosphatidylethanolamine (PE), the second most abundant phospholipid, possesses a small polar head group diameter relative to its fatty-acid chains, resulting in a conical structure. This characteristic introduces negative curvature that promotes membrane fusion (24). TBSV relies on PE not only for the assembly of VROs but also benefits from the enrichment of PE within these VROs, which facilitates virus replication (25). In the *in vitro* study of the TBSV RdRp p92<sup>pol</sup>, although phospholipids alone did not change the RdRp

activity of p92<sup>pol</sup>, the combination of PE and PC with Ssa1p Hsp70 resulted in a 2.5-fold increase in RdRp activity of p92<sup>pol</sup>. This enhancement was achieved by increasing the binding of viral RNA to p92<sup>pol</sup>, whereas phosphatidylglycerol (PG) and cardiolipin (CA or CL) inhibited RdRp activity by inhibiting the viral RNA's ability to bind to p92<sup>pol</sup>. These findings suggest that the TBSV RdRp can sense the cellular lipid environment to determine the conditions favorable for VRO assembly and initiation of virus replication (26). Other negatively charged phospholipids, such as phosphatidylserine (PS), PG, phosphatidylinositol (PI), and phosphatidylinositol phosphates (PIPs), impart negative charge to their enriched locations, potentially attracting specific or non-specific protein effectors involved in various cellular pathways. Among them, PI is characterized by a hydrophilic myo-inositol headgroup linking to the hydrophobic diacylglycerol (DAG) backbone through a phosphodiester bond. The inositol headgroup can undergo reversible phosphorylation at positions 3, 4, or 5 by PI-kinases and dephosphorylation by PI-phosphatases, generating seven distinct PIPs—namely, PI(3)P, PI(4)P, PI(5)P, PI(3,4)P2, PI(3,5)P2, PI(4,5)P2, and PI(3,4,5)P3—which are involved in multiple cellular membrane trafficking events like secretion, vacuolar protein sorting (27, 28). The *in vitro* assay in VeroE6 cells has shown that POPG, PI but not POPC can significantly inhibit SARS-CoV-2 infection, while additional research suggests that POPG and PI can exert antiviral effects by directly binding to negative-strand RNA viruses (RSV and influenza A viruses (IAVs)) and preventing their attachment to host cells both *in vivo* and *in vitro* (29). However, investigations into hepatitis C virus (HCV) and Aichi virus (AiV), both positive-strand RNA viruses, have indicated the significance of phosphatidylinositol 4-kinase III alpha and beta for their individual replication processes, leading to the accumulation of PI4P at

the replication sites (30, 31). The study of tombusviruses reveals the hijacking of Vps34 phosphatidylinositol 3-kinase (PI3K) into the viral replication organelles (VRO) during TBSV and CIRV replication. This leads to the *in situ* biosynthesis of PI3P, subsequently recruiting Rab5-positive early endosomes and PE-rich membranes, thereby facilitating viral replication (32). PI(4,5)P<sub>2</sub> specifically bind to the N-terminal amphipathic helix of HCV nonstructural protein 5A (NS5A). This binding induces a conformational change in the AH domain of NS5A, prolonging and stabilizing the interaction between NS5A and TBC1D20, a Rab GTPase-activating protein (GAP) involved in ER-to-Golgi trafficking. This interaction is crucial for HCV genome replication (33).

The involvement of different phospholipids in regulating distinct cellular processes suggests their potential role in modulating positive-strand RNA virus replication through interactions with viral replication proteins.

### 1.3 Lipids transport in positive-strand RNA virus replication

For the formation of viral replication organelles, pre-existing membrane organelles within the cell serve as the primary membrane sources. Some viruses induce the negative curvature to the donor membranes to form invagination-type viral replication complexes (VRCs), as observed in TBSV on peroxisomes (21), CIRV on the outer membrane of mitochondria (18), and Dengue virus and BMV on ER (20, 34). On the other hand, other viruses use the subverted membranes to form protrusion-type VRCs by introducing positive curvature, as seen with SARS-CoV-2 and HCV, which result in the formation of single membrane, double membrane and multilamellar structures (19, 35). However, these initial membrane components are not optimal for viral replication. Therefore, viruses

modulate membrane lipid composition through various mechanisms to optimize the membrane environment for efficient replication.

The first approach involves the direct recruitment of lipid synthases or enzymes related to lipid metabolism into the viral replication organelle. In addition to Cho2p, phosphatidylinositol 4-kinase III alpha and beta, and VPS34 PI3K, as highlighted in Section 1.2, producing PC, PI4P, and PI3P, respectively, positive-strand RNA viruses also recruit other enzymes. These include fatty acid synthase (FASN), which is recruited by DENV for synthesizing fatty acid chains, the main components of phospholipids (36), and Psd2 phosphatidylserine decarboxylase facilitating the conversion of PS to PE, which has been reported to be recruited by TBSV in the viral replication organelle (9). This process enables the virus to obtain locally synthesized substantial quantity of lipids essential for its replication and plays a pivotal role in reshaping the membrane composition to support viral replication.

The second approach, which has gained significant attention in recent years, involves non-vesicular lipid transport facilitated by the formation of viral-induced membrane contact sites (vMCS). As the primary source of lipid synthesis (37), the ER plays a crucial role as the main donor in non-vesicular lipid transport through vMCS. What is particularly remarkable is that within the MCS, the lipid transfer proteins (LTPs) and close physical proximity between the VROs and ER facilitate precise and rapid lipid exchange, contributing to the robust replication of positive-strand RNA viruses.

Human rhinoviruses (HRVs), members of the Enterovirus genus within the Picornaviridae family, are positive-strand RNA viruses responsible for causing the common cold. To form their replication organelles on Golgi, HRVs utilize a PI4P-

cholesterol counter-currents system at vMCS between the ER and VROs. This intricate interplay involves the coordinated actions of ER-associated PI4P phosphatase Sac1, phosphatidylinositol (PI) transfer protein beta (PITPb), oxysterol-binding protein (OSBP)-like proteins, and phosphatidylinositol 4-kinase class 3beta (PI4K3b). Crucially, OSBP1 plays a pivotal role in transporting PI4P from the virus hijacked membrane to the ER membrane, facilitating the exchange for cholesterol. Simultaneously, Sac1 on the ER membrane converts PI4P to PI, while PITPb transports PI to the virus hijacked membrane. Finally, PI4K3b on the viral subverted membrane enzymatically converts PI to PI4P, completing the cycle for OSBP1-mediated transport (38).

TBSV employs a similar strategy to acquire phytosterols from plants and ergosterols from yeasts for its replication, both of which are sourced from the ER membrane through vMCS. This system involves lipid transfer proteins oxysterol binding proteins (ORPs), VAP (VAMP-associated protein) proteins, and PI4P phosphatase Sac1 (39, 40). Additionally, the retromer complex, consisting of Vps26, Vps29, and Vps35, is hijacked by the p33 protein into VROs to deliver the cargoes, including PI4K $\alpha$ , which facilitates the PI4P synthesis in VROs (9). In Chapter 2, we will introduce a scaffold protein, Atg11, originally known for its role in host-selective autophagy initiation. Atg11 now reveals a novel function as a vital component of TBSV-induced vMCS. In this context, it stabilizes the vMCS structure by anchoring its components together, promoting efficient sterol enrichment in the VRO, and thereby enhancing the robust replication of TBSV.

## 1.4 Autophagy: Mechanisms and TBSV Interactions

Autophagy, also known as “self-eating”, is a fundamental cellular metabolic process highly conserved in eukaryotes (41). Under normal conditions, cells maintain a basal level of autophagy to support cellular homeostasis by recycling misfolded proteins or damaged organelles (42). Additionally, autophagy can be activated in response to various environmental stresses, including nutrient deficiency, drought, oxidative stress, salt, and pathogen infections, highlighting its adaptive function in confronting diverse challenges (43-45). There are two main types of autophagy: selective autophagy and bulk autophagy, both involving the formation of double-membrane vesicles known as autophagosomes (46, 47). These newly formed autophagosomes encapsulate cargos such as protein aggregates, dysfunctional cellular organelles, and pathogens. Subsequently, they fuse with vacuoles or lysosomes for degradation or recycling (48).

Autophagosome formation is initiated at the phagophore assembly site (PAS) through the assembly of the pentameric Atg1 kinase complex (49). Subsequently, multiple functional units are recruited, including the Class III PI3-kinase complex I, which comprises VPS34 PI kinase responsible for converting PI into PI3P, scaffold protein VPS15, activator Atg38, and regulatory subunits Atg6 and Atg14 (50, 51). The Atg2-Atg18-Atg9 complex contributes to autophagosome nucleation and membrane expansion (52-54). Additionally, two ubiquitin-like complexes play a pivotal role in decorating the phagophore membranes with PE, facilitating phagophore expansion and closure (55). The collective action of these units orchestrates the maturation of the isolation membrane into a closed double-membrane autophagosome.

Notably, a key step in these ubiquitin-like systems is the PE conjugation of Atg8. In this process, inactive Atg8 undergoes processing by the Atg4 protease, revealing its C-terminal glycine (56). Subsequently, the activated Atg8 conjugates with the E2-like protein Atg3 and then to the lipid PE through a hexameric ligase complex comprising Atg5, Atg16, and Atg12 (57-59). This generation of Atg8-PE forms a coating on the phagophore membrane, playing a fundamental role in autophagosome formation (60). After the autophagosome membrane fuses with the lysosome/vacuole membrane and the inner membrane degrades with cargo, the outer membrane Atg8 can be processed by Atg4 again, released from PE, and recycled from the autophagosome membrane (61).

In Chapter 3, we will explore the role of Atg8 in TBSV replication. Our investigation has two focal points. Firstly, as a marker for autophagic activity, we aim to unravel the changes in host autophagic processes, as indicated by Atg8, during TBSV replication. Secondly, given Atg8's ability to conjugate with PE, we will examine whether Atg8 along with the core machinery of autophagy can be employed by the virus in establishing its VROs. While exploring the functions of Atg8 and its partner NBR1, we stumbled upon an interesting observation. NBR1, with its distinct condensate physical state (62), appears to act as a pool capable of storing Atg8 to some extent. This peculiar trait seems to be exploited by TBSV during infection, helping the virus trap Atg8 deconjugated from PE in the pool. This, in turn, restricts the subsequent initiation of autophagy, thus inhibiting the antiviral function of autophagy.

Taking a broader perspective, autophagic activity necessitates substantial lipid synthesis, transport, and finally the formation of double membrane vesicles. In Chapter 4, we discuss the potential role of the lipid transfer protein Atg2 in TBSV replication.

Additionally, we explore the potential involvement of other autophagy-related proteins in TBSV replication. Above all, we gain an insight into how TBSV strategically employs autophagy-related proteins in different respects. This intricate utilization plays a pivotal role in providing diverse and multifaceted support for TBSV replication.



## CHAPTER 2.

### KEY TETHERING FUNCTION OF ATG11 AUTOPHAGY SCAFFOLD PROTEIN IN FORMATION OF VIRUS-INDUCED MEMBRANE CONTACT SITES DURING TOMBUSVIRUS REPLICATION

(This chapter was published in *Virology*, July 2022, vol. 572, Pages 1-16. Copyright © 2024 Elsevier B.V.)

#### 2.1 Introduction

Positive-strand (+)RNA viruses of eukaryotic organisms have small genomes and they have to co-opt numerous host factors to support their replication inside the infected cells. Virus replication depends on the biogenesis of viral replication organelles (VROs), which cluster many membrane-bound viral replicase complexes (VRCs) (63-70). VRO biogenesis requires membrane deformation, new lipid biosynthesis, phospholipid and sterol transfer and co-opting vesicular trafficking (4, 69, 71-73). The membranous VROs sequester the viral (+)RNA and viral and co-opted host proteins for efficient replication. In addition, VROs also protect the viral (+)RNA and the dsRNA replication intermediate from recognition and elimination by the host innate immune system (74-76). The VROs coordinate the viral replication process spatiotemporally (69, 71, 77, 78).

Tomato bushy stunt virus (TBSV), which is a small (+)RNA virus of plants, is studied intensively to unravel the basic mechanism of viral RNA replication (79-82). TBSV codes for two essential replication proteins, the p92 RdRp and the p33 replication protein, which is the master regulator of VRO assembly and viral (+)RNA recruitment into VRCs

(7, 83). TBSV replicon (rep)RNA replicates in the surrogate host yeast (*Saccharomyces cerevisiae*) to a high level (80, 84, 85). Yeast-based genome-wide and proteome-wide studies with TBSV led to the identification of numerous host factors co-opted for viral RNA replication and recombination (64, 80, 86-88). Overall, TBSV depends on global phospholipid and sterol biosynthesis (89-91). Formation of VRCs and activation of the viral-coded p92 RdRp requires phosphatidylethanolamine (PE), phosphoinositide and sterols (25, 26, 32, 40, 83, 92-94).

TBSV induces subcellular membrane proliferation and peroxisome aggregation in both yeast and plant cells. One of the characteristic features of TBSV infection is the formation of virus-induced membrane contact sites (vMCSs) (39, 80, 95, 96). vMCS forms between the hijacked subdomain in the ER and the peroxisome with the help of p33 replication protein and co-opted host proteins. For example, a group of oxysterol-binding proteins (OSBP in mammals, Osh proteins in yeast, and ORP proteins in plants) and ER-resident VAP (VAMP-associated protein, Scs2 in yeast, VAP27-1, VAP27-2 and PVA12 proteins in plants) are critical for vMCS formation/function, which are essential for the enrichment of sterols and phosphoinositides within VROs (39). In the absence of sterol or phosphoinositide enrichment within VROs, tombusvirus p33 replication protein becomes sensitive to proteasomal degradation (32, 83). The cytosolic Osh/ORP proteins and the ER-resident VAP proteins must be recruited to vMCSs via protein-protein interactions with p33 replication protein (39). A subdomain of ER, called ERAS (ER arrival site for COPI vesicles), is important for vMCS formation. The main co-opted component of ERAS is the SNARE complex, including the syntaxin18-like Ufe1 and Use1 proteins (97, 98). Another critical host protein in vMCS formation/function is the ER-resident Sac1 PI4P phosphatase,

which is needed for the directional transfer of sterols from the ER to the acceptor membranes through converting PI(4)P phosphoinositide to PI phosphatidylinositol (40). PI(4)P is used by oxysterol binding proteins to exchange for sterol/oxysterols/ergosterols to allow transfer of these lipids at the MCS (99-103). The acceptor membranes (i.e., peroxisomal membrane for TBSV and mitochondrial membrane for CIRV) are recruited into vMCS by TBSV p33/CIRV p36 replication proteins and co-opted Fis1 mitochondrial fission protein (104). In spite of its significance in VRO biogenesis, the complete protein composition of vMCS is not yet known.

Role of the Atg11 adapter and scaffolding protein in selective autophagy, such as pexophagy and mitophagy, is to direct the cargo proteins and autophagy receptors to the phagophore assembly site (PAS), recruit selected group of proteins to PAS in yeast and to tether Atg9 vesicles (105-109). Atg11 is an important hub that coordinates cargo selection, membrane trafficking, membrane tethering, stabilize membrane curvature, and required for membrane expansion of the autophagosome (110, 111). Moreover, Atg11 is a large conserved protein (protein with comparable functions is called FIP200, also called RBCC1 in mammals) with an ortholog in *Arabidopsis thaliana* and other plants, and it is expressed during normal (stationary) conditions (108, 112-114).

We decided to characterize the molecular function of Atg11 during TBSV replication. We based our initial model of Atg11 putative function in TBSV replication on the known features of Atg11, including interaction with Fis1 mitochondrial fission protein, which has been shown as a co-opted tethering protein during vMCS formation (104, 115). Atg11 also interacts with other characterized pro-viral host proteins, such as Vps34 PI3P kinase, and Ypt1 (Rab1), Vps21 (Rab5) and Ypt7 (Rab7) small GTPases, all of which are

recruited by TBSV for functions within the VROs (32, 80, 92, 116, 117). These features place Atg11 as a likely candidate to tether these host factors and membranes and act as an assembly platform in VROs. Indeed, we find that Atg11 is co-opted by the TBSV p33 replication protein into VROs formed from clustered peroxisomes. Atg11 also binds to the p36 replication protein of the closely-related carnation Italian ringspot virus (CIRV) in VROs formed from clustered mitochondria. Instead of the canonical function as a selective autophagy scaffold protein, Atg11 is found to play a pro-viral role in facilitating the formation of vMCS. This function of Atg11 is likely performed in collaboration with the p33/p36 replication protein and co-opted cellular vMCS proteins, such as the ER-resident Scs2/VAP27 VAP tethering proteins, the oxysterol-binding proteins (Osh6 and ORP3), Sac1 PI4P phosphatase and Fis1 mitochondrial fission protein within VROs. We propose that Atg11 serves as a co-opted tethering protein to facilitate the stable formation of vMCSs involving peroxisomes and the ER membrane for TBSV and mitochondria and the ER membrane in case of CIRV. Thus, tombusviruses usurp a key selective autophagy protein for pro-viral functions. Altogether, co-opting Atg11 is critical for tombusvirus VRO biogenesis in yeast and plant cells.

## 2.2 Results

### **Atg11 autophagy scaffold protein is required for tombusvirus replication.**

Based on known interaction of Atg11 with Fis1 mitochondrial fission protein and Vps34 PI3K, which are key co-opted pro-TBSV host factors (32, 104), and other co-opted host proteins (79, 85), Atg11 has emerged as a highly connected putative candidate for TBSV replication. To test the effect of Atg11 on TBSV replication, we expressed tombusvirus

p33 and p92<sup>pol</sup> replication proteins and the replicon (rep)RNA in haploid yeast with *ATG11* deletion. Northern blot analysis of repRNA level revealed ~4-fold reduced accumulation of TBSV and the closely-related cucumber necrosis virus (CNV) in *atg11Δ* yeast in comparison with the WT yeast (Fig. 2.1A-B). Similar to TBSV and CNV, both of which replicate using the peroxisomal membrane surfaces, the mitochondria-associated CIRV, a closely-related tombusvirus, replication was also greatly reduced in *atg11Δ* yeast (Fig. 2.1C). Plasmid-based expression of wt Atg11 partially complemented CNV and CIRV replication in yeast (Fig. 2.1C-D). Remarkably, the expression level of TBSV and CNV p33 and the CIRV p36 replication proteins was also reduced in *atg11Δ* yeast (Fig. 2.1). In addition, over-expression of Atg11 enhanced CIRV replication and the accumulation of p36 replication protein in WT yeast (Fig. 2.1C, lanes 4-6 versus 1-3). These data suggest that Atg11 is critical for tombusvirus replication in different subcellular niches. Because of the observed major effect of Atg11 on the replication of tombusviruses in yeast, Atg11 emerges as a new pro-viral host factor whose function is characterized in more details below.

**Atg11 autophagy-related protein has pro-viral functions in plants.** Atg11 is a large protein in *Arabidopsis* with two predicted domains (supplementary Fig. S2.1), whose function is not yet characterized in detail in plants (112, 113). The two Atg11 proteins are highly similar in *Nicotiana benthamiana* plants (supplementary Fig. S2.1). To study if tombusviruses depend on Atg11 functions in plants, first we tested if Atg11 expression is affected during TBSV infection in *Nicotiana benthamiana* plants. Semi-quantitative RT-PCR and RT-qPCR analyses of Atg11 mRNA levels in TBSV-infected versus mock-

treated *N. benthamiana* leaves revealed up-regulation of Atg11 mRNA level in the TBSV inoculated leaves 2 days after inoculation (dpi), whereas no differences were seen after 1 dpi (Fig. 2.2A, lanes 7-9 versus 10-12 and the RT-qPCR graph, bottom panel). Interestingly, Atg11 mRNA level also increased in the systemically-infected leaves at 4 and 5 dpi (Fig. 2.2A, lanes 13-15 versus 16-18 and the RT-qPCR graph, bottom panel), suggesting that TBSV replication induces high level of Atg11 expression in *N. benthamiana* plants.

Second, we silenced Atg11 expression based on virus-induced gene-silencing (VIGS) in *N. benthamiana* plants. We selected two regions in *NbATG11*, which are almost identical in both *NbATG11* genes (supplementary Fig. S2.2). VIGS-based knockdown of Atg11 in *N. benthamiana* led to ~2-to-3-fold reduction of CNV<sup>20KStop</sup> (not expressing the gene silencing suppressor protein), TBSV and CIRV RNAs, respectively, in the inoculated leaves (Fig. 2.2B-D). Knockdown of Atg11 level did not cause obvious phenotype in *N. benthamiana*. Third, expression of the NbAtg11 in *N. benthamiana* plants increased CNV<sup>20KStop</sup> and CIRV RNA accumulation (Fig. 2.2E-F). Altogether, these data confirmed the pro-viral role of Atg11 in supporting tombusvirus replication in yeast and plants.

**Recruitment of Atg11 into VROs in plants.** To analyze if Atg11 is co-opted by TBSV into large VROs, we co-expressed RFP-tagged Atg11 with BFP-tagged TBSV p33 replication protein and GFP-SKL peroxisomal marker protein in *N. benthamiana* cells infected with TBSV, followed by confocal imaging. We found a high level of co-localization of TBSV p33 replication protein and Atg11 within VROs consisting of aggregated peroxisomes (Fig. 2.3A, top two panels). We noted that Atg11 was present in

a portion of the VROs based on comparison of distribution of p33 and Atg11 punctate structures (Fig. 2.3A). Interestingly, the expression of p33 replication protein without TBSV infection led to the recruitment of Atg11 into VRO-like structures to comparable extent as the actively replicating TBSV did (Fig. 2.3A). Note that the expression of TBSV p33 alone results in VRO-like structures with numerous aggregated peroxisomes, similar to VROs during TBSV infection (118). In the absence of viral components, Atg11 did not localize to peroxisomes in plants (Fig. 2.3A, bottom panel). Expression of only the yeast Atg11-like domain of the NbAtg11 (termed R2) also resulted in co-localization with p33-BFP within VROs in *N. benthamiana* (Fig. 2.3B).

Similar confocal microscopy-based experiments with the closely-related CIRV, which builds VROs using clustered mitochondria, revealed the high extent of co-localization of RFP-Atg11 with the CIRV p36-BFP replication protein and GFP-Tim21 mitochondrial membrane protein (Fig. 2.3C, top panel). The localization pattern of Atg11 within the VROs during CIRV infection was similar to the pattern observed with TBSV infection (compare Fig. 2.3A and 2.3C). In the absence of CIRV replication, Atg11 did not colocalize with mitochondrial marker in *N. benthamiana* (Fig. 2.3C). These data suggest that Atg11 is recruited into the large CIRV VROs with the help of the viral p36 replication protein in plant cells. Based on these experiments, we conclude that Atg11 autophagy-related protein is efficiently recruited by the TBSV p33 and the CIRV p36 replication proteins to VROs in *N. benthamiana*.

**Tombusvirus replication proteins interact with Atg11 *in vitro* and in yeast and plants.** To test if Atg11 interacts with the tombusvirus replication proteins, we Flag-

affinity purified the TBSV replication proteins from yeast expressing His<sub>6</sub>-tagged Atg11. The yeast membranous fraction containing the TBSV replicase was detergent-solubilized, followed by Flag-purification of the tombusvirus replicase. These experiments confirmed the presence of Atg11 in the purified replicase preparations, which are active *in vitro* (Fig. 2.4A see also Fig. S2.3A).

To confirm direct interactions between TBSV p33 and Atg11 protein, we used a pull-down assay with MBP-tagged p33 and GST-His<sub>6</sub>-tagged Atg11 proteins affinity-purified from *E. coli* (Fig. 2.4B). Similar interaction studies were performed with the CIRV p36 replication protein using the pull-down assay (Fig. 2.4B). For the pull-down assay, we used truncated TBSV p33 and CIRV p36 replication proteins missing the N-terminal and the membrane-binding regions to aid their solubility in *E. coli* (Fig. 2.4B). Altogether, the pull-down data show that the TBSV and CIRV replication proteins bind to Atg11 host protein *in vitro*, and the C-terminal domains of the replication proteins facing the cytosolic compartment is involved in binding to Atg11 (Fig. 2.4B).

To provide additional evidence for the interaction between the TBSV p33 replication protein and Atg11 *in vivo*, we used protein proximity-labeling approach based on *E. coli*-derived BirA biotin-ligase and AviTag, which serves as a biotin acceptor peptide (119, 120). First, BirA was fused to p33 for targeting to the replication site, whereas AviTag was fused to Atg11 to monitor proximity to p33 in yeast cells. We co-expressed BirA-p33 and Avi-Atg11 in yeast under low biotin condition, followed by a brief biotin pulse (Fig. 2.4C). This led to biotinylation of Avi-Atg11 in yeast (Fig. 2.4C, lanes 1-2), indicating the close proximity of p33 replication protein and Atg11 in yeast cells. In addition, streptavidin-based capturing of biotinylated proteins also resulted in the recovery



of the biotinylated Avi-Atg11 from yeast expressing BirA-p33 (Fig. 2.4C, second panel). Avi-Atg11 was not biotinylated when His<sub>6</sub>-p33 was expressed as a control, suggesting that yeast does not have nonspecific biotin-ligase activity on Avi-Atg11 (Fig. 2.4C, lanes 3-4). Second, we expressed BirA-tagged p33 replication protein in *N. benthamiana*, which led to biotinylation of Avi-tagged NbAtg11 (Fig. 2.4D, lanes 1-2). The Avi-tagging of Atg11 was necessary to detect the biotinylated Atg11 in the presence of p33-His<sub>6</sub>-BirA in *N. benthamiana* (Fig. 2.4D, lanes 3-4, see also Fig. S2.3B). Third, in a reciprocal setting, co-expression of BirA-tagged NbAtg11 resulted in the biotinylation of Avi-tagged p33 in *N. benthamiana* (Fig. 2.4E, lanes 1-2). In the absence of the BirA fusion, expression of Atg11 did not lead to biotinylation of Avi-tagged p33 in *N. benthamiana* (Fig. 2.4E, lane 3). Altogether, the above data confirm the close proximity of Atg11 host protein and the tombusvirus p33 replication protein in yeast and plant cells.

To provide additional evidence that the plant Atg11 is recruited into VROs through the interactions with the TBSV p33 or CIRV p36 replication proteins, we have conducted bimolecular fluorescence complementation (BiFC) experiments in *N. benthamiana* leaves. The BiFC signals revealed specific interactions between Atg11 and the TBSV p33 and p92<sup>pol</sup> replication proteins within the VROs (Fig. 2.5A, also, see the bottom panel for the negative control experiment). Furthermore, we tested the interaction between the C-terminal Atg11-like and the N-proximal Atg17-like domains (see Fig. 2.3B) of the full-length NbAtg11 and the replication proteins via BiFC. Both domains were involved in the interaction and recruitment of Atg11 by the TBSV replication proteins into VROs, albeit the Atg11-like domain interaction with p33 and p92<sup>pol</sup> was more pronounced than Atg17-like domain in these experiments (Fig. 2.5B). Interestingly, the CIRV p36 replication

protein showed similar interaction with Atg11 and its two domains within the VROs (Fig. 2.5C). Thus, most of the interactions between Atg11 and the tombusviral replication proteins take place within the VROs in *N. benthamiana*.

**Co-purification of co-opted vMCS proteins with the TBSV replicase is affected by ATG11 deletion in yeast.** Although the canonical function of Atg11 is based on its scaffold function during the selective autophagy process (110, 111), we hypothesized that tombusviruses might be able to exploit the tethering function of Atg11 during replication. Our model is based on the documented interaction of Atg11 with Fis1 mitochondrial fission protein, which is involved in virus-induced membrane contact site (vMCSs) formation (104). TBSV induces the formation of vMCSs between the ER membrane and the peroxisomal membrane to facilitate transfer of lipids, sterols and PI(4)P phosphoinositide within VROs (39, 40, 95, 97).

To test the putative role of Atg11 in vMCS formation, first we measured the amount of co-purified VAP (VAMP-associated protein), namely the yeast ER-resident Scs2 VAP protein, which is a tethering protein required for vMCS formation (39). We purified the tombusvirus replicase from membrane fraction derived from *atg11Δ* and WT yeasts, followed by measuring the co-purified His<sub>6</sub>-Scs2 by western blotting. In comparison with the replicase preparations from WT yeast, the replicase preparations from *atg11Δ* yeast contained less Scs2 VAP (Fig. 2.6A, compare lanes 1-2 and 3-4). These observations suggest that recruitment of Scs2 VAP protein to the viral replication compartment, likely to vMCSs, is affected by Atg11.

Another vMCS protein is Osh6 oxysterol-binding protein, which must be recruited from the cytosol to vMCSs via protein-protein interactions (39). In comparison with the replicase preparations from WT yeast, the replicase preparations from *atg11Δ* yeast contained ~5-times less Osh6 (Fig. 2.6B, compare lanes 1-2 and 3-4). Thus, Atg11 affects the recruitment of Osh6 protein to vMCSs.

The third vMCS host protein tested was Fis1 mitochondria/peroxisome fission protein, which serves as a tether in the acceptor membrane (i.e, peroxisome) during vMCS formation (104). The replicase preparations from *atg11Δ* yeast contained similar amounts of Fis1 protein as in the replicase preparations from WT yeast (Fig. 2.6C, compare lanes 1-2 and 3-4). Thus, Fis1 recruitment by p33 into vMCS does not depend on the co-opted Atg11 protein. This Atg11 independency might be due to binding of p33 to the mitochondrial/peroxisomal Fis1 prior to recruitment of the cytosolic Atg11 into vMCS.

The fourth vMCS protein studied here was the ER-resident Sac1 PI4P phosphatase, which forms a protein interaction hub with the syntaxin18-like Ufe1 SNARE protein in the ER to help formation of vMCS by the p33 replication protein (40, 97). Interestingly, the replicase preparations from *atg11Δ* yeast contained ~6-times less amounts of Sac1 protein than present in the replicase preparations from WT yeast (Fig. 2.6D, compare lanes 1-2 and 3-4). These data suggest that in the absence of Atg11, vMCS formation is likely less efficient. In addition, Atg11 likely participates in the early steps of vMCS formation, which also depends on Sac1 and Fis1 (40, 104).

### **Co-localization and protein proximity-labeling of Atg11 and vMCS proteins.**

First, we performed BiFC experiments with Atg11 and Sac1 vMCS protein in plants. Interestingly, we found that the interaction between Atg11 and Sac1 takes place within a limited portion of the large VROs induced by the TBSV p33 replication protein in *N. benthamiana* (Fig. 2.7A). Similar picture was obtained for the interaction between Atg11 and Sac1 in VROs induced by the CIRV p36 replication protein (Fig. 2.7B). These data strongly indicate that Atg11 interacts with Sac1 vMCS protein within VROs of tombusviruses. We noted that Atg11 also interacts with Sac1 in the absence of tombusvirus infections in plant cells, albeit the interaction does not take place in the peroxisomal membranes (marked by RFP-SKL, Fig. 2.7A).

We also used BirA-Atg11-based expression to show that the vMCS proteins Osh6, Scs2 VAP and Sac1 lipid phosphatase, which were individually Avi-tagged, were biotin-labeled in yeast (Fig. 2.8). The expression of p33 replication protein did not influence the extent of the above proximity-labeling. BirA-p33 expression also showed that the vMCS proteins (Avi-Osh6, Avi-Scs2, Avi-Fis1 and Avi-Sac1) were biotin-labeled in yeast (Fig. 2.8B-C), whereas eEF1A (Avi-Tef1) translation elongation factor, which strongly interacts with the p92 RdRp and the TBSV (+)RNA (121-123), was not biotin-labeled (Fig. S2.4). Expression of Atg11-BirA in *N. benthamiana* infected with CNV or mock-inoculated led to the biotin-labeling of the Avi-tagged PVA12 VAP and ORP3 oxysterol-binding protein (co-opted members of vMCS) (Fig. 2.8D). Based on these data, we suggest that Atg11 is localized in close proximity of the known vMCS proteins in yeast and plants. This supports that Atg11 is part of the tombusvirus-induced vMCS.

**Atg11 contributes to vMCS functions.** First, we tested the major function of the virus-induced vMCSs, which is to facilitate the enrichment of sterols within internal compartments (39), in the absence of *ATG11* in yeast. The re-distribution of ergosterols (the sterol component in yeast) in yeast cells was monitored with filipin dye using fluorescent microscopy (124). As documented previously (39, 40, 104), we found that TBSV replication resulted in redistribution of ergosterol mostly from the plasma membrane to internal locations into punctate structures (Fig. 2.9). However, *ATG11* deletion in yeast greatly reduced the internal ergosterols in the presence of the TBSV components, based on the much smaller-sized and dimmer lipid puncta than those observed in WT yeast (Fig. 2.9). We calculated ~4 times less number of yeast cells containing large internal puncta (filling 20% or more of the cell volume) in case of *atg11* $\Delta$  versus WT yeasts replicating TBSV (Fig. 2.9). Ergosterol redistribution in *atg11* $\Delta$  yeast was comparable to the ergosterol localization in *fis1* $\Delta$  yeast replicating TBSV (Fig. 2.9) as we documented before (104). Fis1 mitochondrial fission protein acts as a co-opted tethering protein during vMCS formation (104). Expression of Atg11 from a plasmid in *atg11* $\Delta$  yeast replicating TBSV led to efficient redistribution of ergosterol to internal locations, comparable to those observed in WT yeast (Fig. 2.9). *ATG11* deletion in yeast caused some changes in ergosterol distribution, resulting in ergosterol accumulation in both the plasma membrane and in small punctate structures in the absence of the viral components (Fig. 2.9). These ergosterol-containing punctate structures were frequently associated with the plasma membrane. Overall, ergosterol distribution in *atg11* $\Delta$  yeast was mostly comparable with that seen in WT yeast in the absence of the viral components (Fig. 2.9). These data suggest

that the co-opted Atg11 is involved in ergosterol enrichment, likely within vMCSs induced by p33 replication protein in yeasts.

The second approach was based on the previous observation (104) that different co-opted tethering proteins within vMCS affect the function of other tethering proteins, thus influencing TBSV replication. For example, over-expression of tethering proteins in yeast can partially complement the inhibitory effect of deletion of a different tethering protein in vMCS on TBSV replication (104). Therefore, we made a double-deletion yeast strain missing *ATG11* and *FIS1*. TBSV replication was decreased to ~half level in *atg11Δ/fis1Δ* yeast strain when compared to the replication level in single deletion *atg11Δ* or *fis1Δ* yeast strains (Fig. 2.10A, lanes 8-10). The accumulation level of p33 was further reduced in the double-deletion yeast strain as well, indicating reduced stability of p33 under these conditions, likely due to reduced sterol enrichment at vMCS in *atg11Δ/fis1Δ* yeast strain (83).

Over-expression of Sac1 PI4P phosphatase, which is a co-opted vMCS protein with tethering function as well (40, 104) in *atg11Δ* yeast led to partial recovery of TBSV repRNA accumulation (Fig. 2.10B, lanes 4-6 versus 1-3). Therefore, we suggest that when Sac1 is abundant in cells, then Sac1 could easily be recruited by the tombusvirus replication proteins even in the absence of Atg11. These data suggest that Sac1 scaffold function partially complements the putative tethering function of Atg11 at vMCS, but only when Sac1 is abundant due to over-expression.

Over-expression of Sac1 in the double-deletion (*atg11Δ/fis1Δ*) yeast strain only resulted in partial complementation of TBSV replication (Fig. 2.10B, lanes 10-12 versus

7-9). TBSV replication was very low under this condition, suggesting that the lack of two tethering proteins (i.e., Atg11 and Fis1) cannot be compensated by over-expression of a single Sac1 scaffold protein to fully support TBSV replication, likely due to incomplete vMCS functions. Nevertheless, the single deletion yeast strains showed that the expression of all these co-opted tethering proteins is needed to support robust TBSV replication, as observed in WT yeast. This is likely due to the limited accessibility of these proteins in yeast, thus “forcing” tombusviruses to compete with normal cellular processes to subvert the host factors for pro-viral functions within vMCS.

**Tombusvirus VROs become RNAi-sensitive in the absence of Atg11 autophagy protein in yeast.** The VROs formed in WT yeast or in plants provide protection against antiviral responses, including RNAi (40, 75, 104, 118). The ability of VROs to protect the viral RNA can be tested using the reconstituted RNAi machinery from *S. castellii* with the two-component *DCR1* and *AGO1* genes (75, 125). This approach allows for the probing of the contribution of individual co-opted host factors to the protection of the viral RNAs (75, 104). We expressed the reconstituted RNAi machinery in *atg11Δ* yeast replicating TBSV repRNA and compared it with the RNA protection provided in *fis1Δ* and WT yeasts. Interestingly, deletion of *ATG11* gene in yeast led to poor protection of the TBSV RNA (Fig. 2.11). The ~50% reduction of repRNA in *atg11Δ* expressing the RNAi components was comparable with that observed in *fis1Δ* yeast strain (104), but less than that found in WT yeast (Fig. 2.11). As previously found, VROs formed in WT yeast protected the viral RNAs against the RNAi machinery (Fig. 2.11) (75, 126). Based on these data, we suggest

that similar to Fis1, Atg11 is also needed for the biogenesis of the protective VROs against the antiviral RNAi machinery.

### 2.3 Discussion

**A surprising novel role of Atg11 autophagy-related protein in the formation of vMCS to support tombusvirus VRO biogenesis.** A major emerging theme in tombusvirus-host interactions is the complexity of the VRO biogenesis, which is central in virus replication (4, 10, 80, 96, 127). The viral replication proteins act coordinately together with many co-opted host proteins and subcellular membranes to provide the building blocks, tethers, scaffolds for assembly platforms and enzymatic activities to create VROs (32, 39, 40, 92, 128). Tombusviruses only provide the viral RNA, the p33 master regulator and the p92 RdRp to support successful VRO assembly in yeast and plants (32, 39, 40, 92). However, the list of the co-opted host components and the full arsenal of subverted functions they provide for VRO biogenesis is growing, but it is still incomplete. In this paper, we show evidence for a new co-opted host factor, the Atg11 autophagy protein that contributes to VRO biogenesis.

We find that Atg11 interacts with the viral replication proteins *in vitro*, in yeast and plant, which leads to extensive recruitment of Atg11 into VROs in cells. Protein proximity-labeling, BiFC, pull-down assay, and the presence of co-purified Atg11 in the tombusvirus replicase preparations, all suggest direct interaction between Atg11 and the viral replication proteins. Deletion of Atg11 in yeast and Atg11 knockdown in plants has inhibitory effect on the peroxisome-associated TBSV or the mitochondria-associated CIRV replication.



Therefore, this study establishes a novel, pro-viral function for the Atg11 autophagy scaffold protein.

The current work shows evidence that Atg11 is involved in the formation of vMCS and the biogenesis of VROs. Accordingly, Atg11 is shown via BiFC to interact with the co-opted Sac1 PI4P phosphatase within VROs in plant cells. In addition, protein proximity-labeling shows the presence of Atg11 in the vicinity of Sac1, Fis1 mitochondrial fission protein, oxysterol transfer protein (Osh6 in yeast) and Scs2 VAP, which are the core proteins involved in vMCS formation within VROs (40, 104, 118). Based on TBSV replicase purification experiments, Atg11 affected the recruitment of the core vMCSs-localized proteins, such as the ER-resident VAP protein and Sac1 and the cytosolic Osh6 protein into VROs. On the other hand, we did not find a role for Atg11 in recruitment of the peroxisomal/mitochondrial Fis1 into the tombusvirus replicase. Interestingly, the extent of Atg11 contribution to tombusvirus replication seems to be similar to that observed with Fis1, Sac1, Osh proteins or VAP proteins (39, 40, 104). Via inducing vMCS formation, these co-opted host proteins are needed to provide optimal lipid/membrane microenvironment for TBSV replication within VROs. Similar to Atg11, the core vMCS proteins also contribute to p33 stabilization and protection of the viral RNA from degradation by RNAi and other nucleases (39, 40, 95). The p33 replication protein binds to sterols in the membranes via its CRAC and CARC-like sequences, which are needed to stabilize p33 in yeast or plants (83). Therefore, the reduced sterol enrichment in VROs in the absence of one or more of the co-opted vMCS proteins results in reduction in p33 levels. This low level of p33 was also observed in the absence of Atg11 as well (Fig. 2.1).

Overall, the data obtained with Atg11 support the model that Atg11 contributes to vMCSs formation (Fig. 2.12). For example, biotin-labeling showed close proximity of p33 and Atg11 to the hijacked core vMCS proteins during tombusvirus replication. Deletion of Atg11 resulted in reduced recruitment of core vMCS proteins by p33. In addition, deletion/depletion of Atg11 has similar inhibitory effects on TBSV replication and protection of the viral RNA from RNAi as depletion of the above vMCSs proteins in yeast and plants. The vMCS structure is unusually stable and abundant (39, 96) in comparison with regular, more dynamic MCS structures in healthy cells. These stable vMCS structures are essential for the robust tombusvirus-induced subcellular changes required for rapid and efficient VRO formation, including lipid/sterol enrichment. We propose that the co-opted Atg11, based on its tethering and scaffolding function in selective autophagy (110, 111), also provides comparable tethering and scaffolding function by stabilizing vMCSs within VROs (Fig. 2.12). Similar picture might be valid for other unrelated human viruses, such as enteroviruses, which also induce and stabilize vMCSs in order to manipulate the lipid composition of the membranes within the viral replication compartment (95, 129, 130). The possible autophagic role of Atg11 in tombusvirus replication will be addressed in subsequent works.

In summary, the roles of increasing number of co-opted host proteins with tethering and scaffolding functions during VRO biogenesis suggest that the tombusviral VRO is an elaborate and complex organelle-like structure. Based on complementation experiments, it seems that the recruitment of the co-opted host tethering proteins, such as Atg11, Fis1, the VAP proteins, Sac1 and Osh6 or ORP3 for viral replication is a rate-limiting step. Nevertheless, tombusviruses need to efficiently recruit the core vMCS proteins to build

VRO structures with optimal lipid composition. Moreover, by efficiently recruiting these tethering proteins away from their canonical cellular functions, tombusviruses might affect many cellular processes, which might lead to disease states in infected plants. It will be interesting to learn if other (+)RNA viruses also exploit vMCS and tethering proteins for their replication.

In conclusion, the co-opted Atg11 scaffold protein is required for the formation of membrane contact sites within VROs. This helps tombusviruses to enrich lipids and extend membrane surfaces within VROs, which become ribonuclease-insensitive. The emerging picture is that formation of tombusvirus VROs requires several co-opted tethering and scaffold proteins. Targeting these pro-viral membrane-tethering proteins by inhibitors could open up new antiviral strategies.

## 2.4 Materials and methods

**Yeast strains and plasmid construction.** Plasmids pJW1506 and pJW1234 were obtained from Addgene (120). Yeast strain *fis1* $\Delta$  was kindly provided by Dr. Agnes Delahodde (University of Paris-Sud). To create *atg11* $\Delta$  and *fis1* $\Delta$ /*atg11* $\Delta$  yeast strains, the hygromycin resistance gene *hphNTI* was PCR-amplified from vector pFA6a-*hphNTI* (Euroscarf) (131) with primers #7890 and primers #7891 and the PCR product was transformed into BY4741 and *fis1* $\Delta$  respectively. Plasmids constructed and primers used in this study are listed in supplementary Table 2.1-2.4.

**Virus RNA replication in yeast.** To test repRNA replication, BY4741 (wild type) and *atg11* $\Delta$ , *fis1* $\Delta$  and *atg11* $\Delta$ /*fis1* $\Delta$  yeast strains were transformed with plasmids HpGBK-CUP1-Flagp33/Gal10-DI72, LpGAD-CUP1-Flagp92 and UpYES2-NT. To test if plasmid-

borne Atg11 expression can rescue virus replication, *atg11Δ* yeast strain was transformed with HpGBK-CUP1-Flagp33/Gal10-DI72, LpGAD-CUP1-Flagp92 and UpYES2-HisATG11. To test if over-expression of membrane contact sites-associated Sac1 protein can complement tombusvirus replication in *atg11Δ* yeast strain, wild type BY4741 and *atg11Δ* yeasts were transformed with HpGBK-CUP1-Flagp33/Gal10-DI72, LpGAD-CUP1-Flagp92 and UpYC-ScSac1. For CIRV replication assay, BY4741 and *atg11Δ* yeast were co-transformed with plasmids HpESC-CUP1-Flagp36/Gal10-DI72 and LpESC-CUP1-Flagp95 with either UpYES2-NT or UpYES2-HisATG11.

The transformed yeasts were pre-grown in SC-ULH<sup>-</sup> (synthetic complete medium without urea, leucine, and histidine) media supplemented with 2% galactose media and 100 μM BCS at 23 °C for 16 h. Then, the yeast cells were cultured in SC-ULH<sup>-</sup> media supplemented with 2% galactose and 50 μM CuSO<sub>4</sub> at 23 °C for 24 h.

For TBSV replication, yeast strain BY4741 and *atg11Δ* were transformed with pGBK-Gal-HisT33/Gal-DI72, pGAD-Gal-HisT92 and pYES2-NT. TBSV replication was induced by growing cells at 23°C in SC-ULH<sup>-</sup> medium supplemented with 2% galactose for 24 h at 23°C.

To test the effect of RNAi on TBSV repRNA accumulation in yeast, we expressed DCR1 and AGO1 proteins (75). BY4741 and *atg11Δ* yeast strains were transformed with plasmids HpGBK-CUP1-Hisp33/Gal-DI-72 and LpGAD-CUP1-His92, UpESC-Ura (as a control) or UpESC-Ura-Gal1-HisAgo1-Gal10-HisDcr1. Transformed yeast cells were pre-grown in SC-ULH<sup>-</sup> media supplemented with 2% glucose and 100 μM BCS at 29 °C for 16 h. Then, yeasts were cultured in SC-ULH<sup>-</sup> media supplemented with 2% galactose and 100 μM BCS at 23 °C for 24 h. Then, the yeast cells were cultured in SC-ULH<sup>-</sup> media

supplemented with 2% galactose and 50  $\mu$ M CuSO<sub>4</sub> at 23 °C for 16 h. Total RNA and protein extraction and northern-blot and western-blot analyses were done as described (12, 132).

To test the combined functions of Atg11 and other vMCS proteins, we transformed *atg11* $\Delta$  and *atg11* $\Delta$ /*fis1* $\Delta$  yeast strains with HpGBK-CUP1-Flagp33/Gal10-DI72, LpGAD-CUP1-Flagp92 and pYES2-NT or pYES2-Sac1 (40). Yeast culturing, total RNA extraction and northern-blot analyses were done as described above.

**Virus replication in plants.** To identify *ATG11* gene sequence in *N. benthamiana*, we used the sequence of *Arabidopsis thaliana ATG11* (AT4G30790) and performed a BLAST search in the QUT Sol101\_N. *benthamiana\_predicted\_transcriptome\_v101* transcripts database. We find two hits, namely Niben101Scf09742g00014.1 and Niben101Scf02359g00022.1, the coding region of which shares 96.4% identity in amino acid sequence (supplementary Fig. S2.1). A chimeric fragment composed of R2 and R3, selected based on highly conserved region within two NbATG11 transcripts, was inserted into TRV2 vector (133) to generate pTRV2-NbATG11-R2+R3 (supplementary Fig. S2.2). *Agrobacterium* C58C1 competent cells were transformed with pTRV2-NbATG11-R2+R3. *N. benthamiana* plants of 4-leaves stage were agroinfiltrated with pTRV1 and pTRV2-NbATG11-R2+R3 or pTRV2-cGFP as a control (OD<sub>600</sub> 0.5). On the 10<sup>th</sup> day post agroinfiltration (dpi), upper leaves were agroinfiltrated to express CNV<sup>20kstop</sup> or inoculated with TBSV or CIRV saps (16). To determine RNA accumulation of TBSV, CNV, and CIRV, the inoculated leaves were collected at 2, 2.5 and 3 dpi, respectively. Total RNA extraction and northern blot analyses were performed as described previously (16). The accumulation of *NbATG11* mRNA and internal reference control *tubulin* mRNA

was determined by semi-quantitative RT-PCR with primers oligo-d(T) (for RT), #7938 and #7939 for *NbATG11* and #2859 and #2860 for tubulin mRNA (16).

To further test the pro-viral role of Atg11, transient over-expression of Atg11 in *N. benthamiana* leaves was performed by co-agroinfiltration with pGD-ATG11-Myc (OD<sub>600</sub> 0.6) and pGD-P19 (OD<sub>600</sub> 0.1). Then the leaves were inoculated with either TBSV or CIRV sap at 16 h post agroinfiltration and the inoculated leaves were collected at 2 and 3 dpi, respectively. For CNV, *N. benthamiana* leaves were co-agroinfiltrated with CNV<sup>20Kstop</sup> (OD<sub>600</sub> 0.4) and pGD-ATG11-Myc (OD<sub>600</sub> 0.6) and pGD-P19 (OD<sub>600</sub> 0.1), samples were collected at 2.5 dpai. NbATG11 protein level was determined by western blot assay using anti-myc antibody. Total RNA extraction and northern blot analyses were described above.

**Confocal laser microscope studies in plants.** To analyze the subcellular localization of NbATG11 in the presence or absence of viral components in *N. benthamiana* leaves, pGD-35S-BFP-p33, pGD-35S-BFP-C36, pGD-35S-RFP-NbATG11, pGD-35S-RFP-NbATG11-S1, pGD-35S-RFP-NbATG11-R2, pGD-35S-GFP-SKL (as a peroxisome marker) and pGD-35S-GFP-AtTim21 (as a mitochondrial marker) (92) were transformed into agrobacterium strain C58C1. Then, agrobacterium suspensions with different combinations were infiltrated into *N. benthamiana* leaves, followed by virus inoculation with sap at 16 h post agroinfiltration. At 2.5 dpai, the agroinfiltrated leaves were subjected to confocal laser microscopy (Olympus FV1200 and FV3000).

To detect interaction of NbATG11 with TBSV p33 or CIRV p36 replication proteins using bimolecular fluorescence complementation assay (BiFC), pGD-35S-T33-cYFP, pGD-35S-C36-cYFP, pGD-35S-C-cYFP (as a negative control), pGD-35S-nYFP-NbATG11, pGD-35S-nYFP-NbATG11-R2, pGD-35S-nYFP-MBP (as a negative control),

pGD-35S-RFP-SKL (as a peroxisome marker) and pGD-35S-RFP-AtTim21 (as a mitochondrial marker) were transformed into agrobacterium strain C58C1. The Agrobacterium transformants with different combinations were used to infiltrate *N. benthamiana* leaves, followed by virus inoculation with sap at 16 h post agroinfiltration. At 2.5 dpai, the agroinfiltrated leaves were subjected to confocal laser microscopy.

To test if NbATG11 interacts with AtSac1 in the presence or absence of virus infection, *N. benthamiana* leaves were co-agroinfiltrated with pGD-35S-nYFP-NbATG11, pGD-35S-AtSac1-cYFP and either a combination of pGD-35S-BFP-p33 and pGD-35S-RFP-SKL or pGD-35S-BFP-C36 and pGD-35S-RFP-AtTim21. The agro-infiltrated *N. benthamiana* leaves at 16 hpai were inoculated with TBSV and CIRV sap, respectively, and then were subjected to confocal laser microscopy at 2.5 dpai.

**Protein co-purification assays.** The FLAG-tag based replicase purification from detergent-solubilized membrane fraction of yeast was performed as described (123). In brief, plasmids HpGBK-CUP1-Hisp33/Gal-DI-72 and LpGAD-CUP1-His92 (as a control) or HpGBK-CUP1-Flagp33/Gal-DI-72 and LpGAD-CUP1-Flag92 were co-transformed with UpYES2-HisATG11 into BY4741. To determine recruitment efficiency of MCS-associated proteins by TBSV p33 into VROs in the presence or absence of Atg11, HpGBK-CUP1-Flagp33/Gal-DI-72 and LpGAD-CUP1-Flag92 were co-transformed with UpYC-Osh6, UpYC-Scs2, UpYC-Fis1 and UpYC-Sac1 respectively into BY4741 and *atg11Δ* yeasts. All transformed yeast cells were pre-grown in SC-ULH<sup>-</sup> media supplemented with 2% glucose and 100 μM BCS at 29°C for 16 h. Then yeast cultures were re-suspended in SC-ULH<sup>-</sup> medium supplemented with 2% galactose and 100 μM BCS and grown at 23°C for 24 h, followed by culturing yeast cells in SC-ULH<sup>-</sup> medium supplemented with 2%

galactose and 50  $\mu$ M CuSO<sub>4</sub> at 23°C for 6 h. The cultures were resuspended and incubated in 35 ml phosphate-buffered saline (PBS) buffer containing 1% formaldehyde for 1 h on ice to cross-link proteins. Then, glycine (to 0.1M) was added to quench the formaldehyde and the yeasts were incubated on ice for 5 min. Finally, yeast pellets were harvested after washing twice with PBS buffer and proteins were FLAG affinity-purified as described previously (123).

For the pull down assay (134), 100  $\mu$ l crude lysate containing MBP, MBP-p33C (of TBSV) or MBP-p36C (of CIRV) were incubated with 20  $\mu$ l amylose resin at 4 °C for 1 hour. Then, the columns were washed with 800  $\mu$ l washing buffer twice and then further incubated with the same amount of affinity-purified GST-His<sub>6</sub>-ATG11 at 4 °C for 1 hour. After incubation, the bound proteins from the columns were eluted with 30  $\mu$ l SDS-loading buffer, followed by boiling the samples for 10 min prior to loading to PAGE.

**Protein proximity-labeling assay in yeasts.** To detect close proximity of p33 replication protein and Atg11 in yeasts, we transformed plasmids LpGAD-Gal-p92, UpYC-Avi-ATG11 (Avi-tag: GLNDIFEAQKIEWHW; a biotin acceptor) (120) and LpESC-His-Gal-BirA-p33-Gal10-DI72 (or pESC-His-Gal-p33-Gal10-DI72 as control) into BY4741 yeast strain. Transformed yeasts were pre-grown in 20 ml SC-ULH<sup>-</sup> media supplemented with 2% glucose at 29 °C for 20 h, followed by culturing yeast cells in 30 ml SC-ULH<sup>-</sup> media supplemented with 2% galactose at 23 °C for 24 h. Subsequently, 500 nM Biotin were added to the yeast cultures, followed by shaking at 29 °C for 2 h. The yeast cultures were centrifuged and washed with 1 $\times$ phosphate buffer saline (PBS). Then, the yeast cells were harvested and broken by glass beads and the membrane-fraction was solubilized by treatment with Triton X-100 as described (123). The solubilized membrane



fractions were added to the column filled with anti-strep-Tactin agarose to capture biotinylated proteins (Strep-tactin resin, cat# No.2-1201-002 from IBA) according to manufacturer's recommendations. The captured proteins were eluted in SDS-loading dye, followed by treatment in a heat block at 100 °C for 5 min. The purified Avi-Atg11 was detected by western-blotting with AP-conjugated anti-strep antibody.

To detect close proximity of p33 replication protein to the vMCS-associated proteins Osh6, Sac1, Scs2 and Fis1 in yeasts, we transformed plasmids LpGAD-Gal-p92 and LpESC-His-Gal-BirA-p33-Gal10-DI72 with one of the following plasmids: UpYC-Osh6-Avi, UpYC-Avi-Sac1, UpYC-Avi-Fis1 and UpYC-Avi-Scs2 into BY4741 yeast strain. Transformed yeast cells were grown in 2 ml SC-ULH<sup>-</sup> media supplemented with 2% galactose at 29 °C for 24 hours. Then 250 nM Biotin were added to cultures, followed by growing the yeast cultures at 29 °C for 30 min. Biotinylated proteins were detected by western-blotting using AP-conjugated anti-strep antibody.

To determine if overexpression of Atg11 enhances the proximity of p33 replication protein to these vMCS-associated proteins, plasmids HpESC-His-Gal-BirA-p33-Gal10-DI72 and LpESC-Cup-ScATG11 (LpESC-Cup-EV as control) were co-transformed with either UpYC-Osh6-Avi or UpYC-Avi-Scs2 into yeast strain BY4741-p92 (expressing p92<sup>pol</sup> from a chromosomal location (135)). Transformed yeast cells were grown in 2 ml SC-ULH<sup>-</sup> media supplemented with 2% galactose and 50 μM CuSO<sub>4</sub> at 29 °C for 24 h. Then 250 nM Biotin were added to cultures, followed by growing the yeast culture at 29 °C for 30 min. Biotinylated vMCS proteins were detected by western-blotting using anti-strep antibody.

To detect close proximity of Atg11 to the vMCS-associated proteins Osh6, Sac1, Scs2 and Fis1 in yeast in the presence or absence of viral replication proteins, plasmids LpESC-Gal-BirA-ATG11 and HpGBK-CUP1-Hisp33/Gal10-DI72, (or HpESC-Gal-EV as control) were co-transformed with one of the following plasmids: UpYC-Osh6-Avi, UpYC-Avi-Sac1, UpYC-Avi-Fis1 and UpYC-Avi-Scs2 into yeast strain BY4741-p92. Transformed yeast cells were grown in 2 ml SC-ULH<sup>-</sup> media supplemented with 2% galactose and 50  $\mu$ M CuSO<sub>4</sub> at 29 °C for 24 h. Then, 250 nM Biotin were added to cultures, followed by growing the yeast culture at 29 °C for 30 min. Biotinylated vMCS proteins were detected by western-blotting using anti-strep antibody.

For time course assay, we transformed plasmids LpGAD-Gal-p92, UpYC-Osh6-Avi and HpESC-His-Gal-BirA-p33-Gal10-DI72 into BY4741 and *atg11* $\Delta$  yeast strains, respectively. Transformed yeast cells were pre-grown in 2 ml SC-ULH<sup>-</sup> media supplemented with 2% glucose at 29 °C for 16 h and then cultured yeast cells were washed and resuspended in 2 ml SC-ULH<sup>-</sup> media supplemented with 2% galactose with 250 nM Biotin. The yeast cultures were grown at 29 °C for 6 h, 12 h, and 24 h, followed by detecting the biotinylated Osh6 protein via western-blotting using anti-strep antibody.

**Protein proximity-labeling assay in plants.** To detect the close proximity of p33 replication protein and Atg11 in plants, *N. benthamiana* leaves were agroinfiltrated with pGD-p33-His-BirA (OD<sub>600</sub> 0.4), pGD-NbATG11-HA-Avi (OD<sub>600</sub> 0.4) and pGD-P19 (OD<sub>600</sub> 0.2). Agroinfiltration with pGD-NbATG11-Myc (OD<sub>600</sub> 0.4) and pGD-p33-His (OD<sub>60</sub> 0.4) was used as a control. The infiltrated leaves at 3 dpai were further infiltrated with 200  $\mu$ M Biotin. Then the infiltrated leaves after 40 min of biotin treatment were harvested and subjected to protein extraction. Biotinylated Atg11-HA-Avi protein was

detected by western blotting using anti-strep antibody. Reciprocal experiments were done via agroinfiltration of *N. benthamiana* leaves with pGD-NbATG11-His-BirA (OD<sub>600</sub> 0.4), pGD-p33-HA-Avi (OD<sub>600</sub> 0.4) and pGD-P19 (OD<sub>600</sub> 0.2). Agroinfiltration with pGD-ATG11-Myc (OD<sub>600</sub> 0.4) was used as a control. Biotinylated p33-HA-Avi protein was detected by western blotting using AP-conjugated anti-strep antibody.

To test if virus infection might affect close proximity of vMCS proteins and Atg11 in plants, we agroinfiltrated *N. benthamiana* leaves with pGD-P19 (OD<sub>600</sub> 0.1), pGD-NbATG11-His-BirA (OD<sub>600</sub> 0.3) and either pGD-Avi-His-AtORP3 (OD<sub>600</sub> 0.3) or pGD-Avi-His-AtPVA12 (OD<sub>600</sub> 0.3) with or without pGD-CNV<sup>20KSTOP</sup> (OD<sub>600</sub> 0.3). We tested three different time points, namely 31 h, 48 h, and 56 h via infiltration with 200 µM Biotin at each time point. Then the infiltrated leaves after 40 minutes of biotin treatment were harvested and subjected to protein extraction. The biotinylated vMCS proteins were detected by western blotting using AP-conjugated anti-strep antibody.

**Detection of Ergosterol distribution in yeasts.** BY4741 and atg11Δ yeast strains were transformed with plasmids HpESC-Gal-Hisp33/Gal10-DI72, LpGAD-Gal-Hisp92 and UpYES2-ATG11 (or UpYES2-NT as a control). Filipin dye-staining was used to visualize ergosterol in yeast cells as described (39). Fixed yeast cells (2 µl resuspend cultures) were spotted onto a poly-Lysine coated slide and examined in the ZEISS UV light microscope with the DAPI filter set.

Table 2.1: Plasmids constructed in chapter 2.

Plasmid name	insert source	insert digestion sites	primers for insert amplification	vector source	vector digestion sites
UpYES-NT-ATG11	Yeast genome DNA	BamHI and Sall	#5629 and #5630	UpYES-NT	BamHI and XhoI
HpESC-Gal-BirA-Hisp33/Gal-DI72	PJW1234	BamHI	#8339 and #8340	HpESC-Gal-Hisp33/Gal-DI72	BamHI
UpYC2-Avi-His-SCS2	UpYC-Scs2	BglII and XhoI	#8369 and #2991 / #8370 and #2991	UpYC2-CT-Vector	BamHI and XhoI
UpYC2-NT-Fis1	yeast genomic DNA	BamHI and XhoI	#7206 and #6775	UpYC2-CT-Vector	BamHI and XhoI
UpYC2-NT-Sac1	yeast genomic DNA	BglII and Sall	#7831 and #7832	UpYC2-CT-Vector	BamHI and XhoI
UpYC2-Avi-His-Sac1	yeast genomic DNA	BglII and Sall	#7831 and #7832	UpYC2-Avi-His-SCS2	BamHI and XhoI
LpESC-His-BirA-ScATG11	HpESC-Gal-BirA-Hisp33/Gal-DI72	BglII	#5680 and #8416	LpESC-ScATG11	BamHI
UpYC2-Avi-His-ScATG11	yeast genomic DNA	BamHI and Sall	#5629 and #5630	UpYC2-Avi-His-SCS2	BamHI and XhoI
LpESC-Cup-Flag-ScATG11	yeast genomic DNA	BamHI and Sall	#5629 and #5630	LpESC-Cup-Flag	BamHI and Sall
pGD-nYFP-NbATG11-S1(ATG17 LIKE)	<i>N.benthamiana</i> cDNA	BamHI and XhoI	#7939 and #7940	pGD-nYFP-MBP	BamHI and Sall
pGD-nYFP-NbATG11-S2(ATG11 LIKE)	<i>N.benthamiana</i> cDNA	BamHI and XhoI	#7941 and #7942	pGD-nYFP-MBP	BamHI and Sall

Table 2.1 (continued)

pGD-nYFP-NbATG11 (FULL LENGTH)	<i>N.benthamiana</i> a cDNA	BamHI and XhoI	#7937 and #7938	pGD-nYFP-MBP	BamHI and Sall
pGD-RFP-NbATG11 (FULL LENGTH)	<i>N.benthamiana</i> a cDNA	BamHI and XhoI	#7937 and #7938	pGD-N-RFP	BamHI and Sal
pGD-RFP-NbATG11-S2	<i>N.benthamiana</i> a cDNA	BamHI and XhoI	#7941 and #7942	pGD-N-RFP	BamHI and Sal
pGEX-ScATG11	pYES-NT-ATG11	BamHI and Sall	#5629 and #5630	pGEX-His-RE	BamHI and XhoI
TRV2-NbATG11 S2+S3	<i>N.benthamiana</i> a cDNA	BamHI and XhoI	#7941 and #8109; #7977 and #8110	TRV2-empty	BamHI and XhoI
pGD-NbATG11-C-myc	<i>N.benthamiana</i> a cDNA	BamHI and XhoI	#7937 and #8365	pGD-35S-L-p33	BamHI and XhoI
pGD-NbATG11-His-BirA	HpESC-Gal-BirA-Hisp33/Gal-DI72	XhoI and Sall	#8420 and #8421	pGD-NbATG11nonstop	XhoI
pGD-Avi-his-AtPVA12	<i>A. thaliana</i> cDNA	BamHI and XhoI	#4252 and #4253	pGD-Avi-His-ScSCS2	BamHI and XhoI
pGD-Avi-his-AtORP3A	<i>A. thaliana</i> cDNA	BamHI and XhoI	#5477 and #5478	pGD-Avi-His-ScSCS2	BamHI and XhoI
pGD-Avi-his-AtVAP27-1	<i>A. thaliana</i> cDNA	BamHI and XhoI	#3458 and #3459	pGD-Avi-His-ScSCS2	BamHI and XhoI
pGD-Avi-His-ScSCS2	UpYC-Scs2	BglII and XhoI	#8369 and #2991 / #8370 and #2991	pGD-35S-L-p33	BamHI and XhoI
pGD-P33nonstop	HpESC-Gal-Hisp33/Gal-DI72	BamHI and XhoI	#4326 and #6793	pGD-35S-L-p33	BamHI and XhoI
pGD-P33-HA-Avi	PJW1506	XhoI and Sall	#8422 and #8423	pGD-P33nonstop	XhoI and Sall

Table 2.1 (continued)

pGD-P33-His-BirA	HpESC-Gal-BirA-Hisp33/Gal-DI72	XhoI and Sall	#8420 and #8421	pGD-P33nonstop	XhoI and Sall
pGD-NbATG11-HA-Avi	<i>N.benthamiana</i> cDNA	BamHI and XhoI	#7937 and #8366	pGD-P33-HA-Avi	BamHI and XhoI
pGD-cYFP-CT-AtSacI	<i>A. thaliana</i> cDNA	BamHI and PstI	#7644 and #7645	pGD-cYFP-NT	BamHI and PstI

Table 2.2: Plasmids described in previous studies of chapter 2.

Plasmid name	Source
HpGBK-Gal-HisT33/Gal-DI-72	Dr. Kai Xu (University of Kentucky)
LpGAD-Gal-HisT92	Dr. Kai Xu (University of Kentucky)
HpGBK-CUP1-Hisp33/Gal-DI-72	[1] Barajas et al., 2009
LpGAD-CUP1-Hisp92	[1] Barajas et al., 2009
HpESC-CUP1-Hisp36/Gal-DI-72	Dr. J. Pogany (University of Kentucky)
LpESC-CUP1-Hisp95	Dr. J. Pogany (University of Kentucky)
UpYC-ScOsh6	[2] Barajas et al., 2014
UpYC-ScScs2	[2] Barajas et al., 2014
pESC-Ura-Gal10-HisDcr1	[3] Kovalev et al., 2017
pESC-Ura-Gal1-HisAgo1-Gal10-HisDcr1	[3] Kovalev et al., 2017
HpGBK-CUP1-Flagp33/Gal-DI-72	[1] Barajas et al., 2009
LpGAD-CUP1-Flag92	[1] Barajas et al., 2009
pGD-35S-p19	[4] Xu and Nagy, 2016
pMALc-2X-T33C	[4] Xu and Nagy, 2016
pMALc-2X-C36C	[4] Xu and Nagy, 2016
pGD-35S-T33-BFP	[4] Xu and Nagy, 2016
pGD-35S-C36-BFP	[4] Xu and Nagy, 2016
pGD-35S-GFP-SKL	[4] Xu and Nagy, 2016
pGD-35S-GFP-AtTim21	[4] Xu and Nagy, 2016
pGD-35S-T33-cYFP	[4] Xu and Nagy, 2016
pGD-35S-C36-cYFP	[4] Xu and Nagy, 2016
pGD-35S-C-cYFP	[4] Xu and Nagy, 2016
pGD-35S-nYFP-MBP	[4] Xu and Nagy, 2016
pGD-35S-RFP-SKL	[4] Xu and Nagy, 2016

Table 2.2 (continued)

pGD-35S-RFP-AtTim21	[4] Xu and Nagy, 2016
PJW1234	[5] Jan et al., 2014
PJW1506	[5] Jan et al., 2014
pYC-Osh6-TEV-AVI	Dr. Nick. Kovalev
HpESC-Gal-Hisp33/Gal-DI72	Dr. Tadas. Panavas
LpGAD-Gal-His92	Dr. Daniel. Barajas
pGD-P33-Myc	Dr. Zhike. Feng
pGBK-ADH-DI72	Dr. Tadas. Panavas

Table 2.3: Reference of table 2.2.

[1]	Barajas, D., Li, Z., and Nagy, P.D. (2009b). The Nedd4-type Rsp5p ubiquitin ligase inhibits tombusvirus replication by regulating degradation of the p92 replication protein and decreasing the activity of the tombusvirus replicase. <i>J Virol</i> <b>83</b> , 11751–11764
[2]	Barajas, D., Xu, K., de Castro Marti ´n, I.F., Sasvari, Z., Brandizzi, F., Risco, C., and Nagy, P.D. (2014b). Co-opted oxysterol-binding ORP and VAP proteins channel sterols to RNA virus replication sites via membrane contact sites. <i>PLoS Pathog</i> <b>10</b> , e1004388.
[3]	Kovalev, N., Inaba, J.I., Li, Z. and Nagy, P.D. (2017) .The role of co-opted ESCRT proteins and lipid factors in protection of tombusviral double-stranded RNA replication intermediate against reconstituted RNAi in yeast. <i>PLoS Pathog</i> <b>13</b> , e1006520.
[4]	Xu, K., and Nagy, P.D. (2016). Enrichment of phosphatidylethanolamine in viral replication compartments via co-opting the endosomal Rab5 small GTPase by a positive-strand RNA virus. <i>PLoS Biol</i> <b>14</b> , e2000128.
[5]	Jan CH, Williams CC, Weissman JS. (2014). Principles of ER cotranslational translocation revealed by proximity-specific ribosome profiling. <i>Science</i> <b>346(6210)</b> :1257521.

Table 2.4: Primers used in chapter 2.

Name	Sequence(5' to 3')
#5629/ATG11/BamHI/F	CGCGGATCCATGGCAGACGCTGATGA ATATAGC
#5630/ATG11/SalI/R	ACGCGTCGACTCAAACCTCCCTGGTAT GAAACCAC
#8339/BirA/BamHI/F	CGGGATCCATGAAGGATAACACCGTG CC

Table 2.4 (continued)

#8340/BirA/BamHI/3XGSS/nonstop/R	CGGGATCCTCCACCGGACCCTCCTGA GCCACCAGATTTTTCTGCACTACGCAG G
#8369/Avi/TEV/His/F	ATTGAATGGCATGAGTCAGAAAATTT GTATTTTCAAGGAGGGGGTTCTCATC ATC
#2991/SCS2/NheI/STOP/XhoI/R	CGGCTCGAGTTAGCTAGCTCTGTAGA ACCATCCTAAAAC
#8370/BglII/Avi/F	GAAGATCTATGGGTTTGAATGATATTT TTGAAGCTCAAAAAATTGAATGGCAT GAGTCA
#7206/Fis1-S/BamHI/F	CGCGGATCCATGACCAAAGTAGATTT TTGGCC
#6775/Fis1/XhoI/R	CCGCTCGAGTTACCTTCTTGTTTCT TAAGA
#7831/ScSac1/BglII/F	CTGAAGATCTATGACAGGTCCAATAG TGTACGTTC
#7832/ScSac1/SalI/R	ACGCGTCTGACTTAATCTCTTTTTAAAG GATCCGGC
#5680/BglII/YFP/F	GAGAGATCTATGGGAGGTTCTCATCA TCA
#8416/BirA/nonstop/BglII/3XSGG/R	GAAGATCTTCCACCGGACCCTCCTGA GCCACCAGATTTTTCTGCACTACGCAG G
#5629/ATG11/BamHI/F	CGCGGATCCATGGCAGACGCTGATGA ATATAGC
#5630/ATG11/SalI/R	ACGCGTCTGACTCAAACCTCCCTGGTAT GAAACCAC
#8421/His-BirA/3XGGS/XhoI/F	ACCGCTCGAGGGTGGCTCTGGAGGGT CAGGTGGTTCCATGGGAGGTTCTCAT CATCA
#8420/BirA/SalI/R	ACGCGTCTGACTTATTTTTCTGCACTAC GCAGG
#4326/p92/AUG/Bam/Nco/KozakF	GGAGGGATCCACCATGGATACCATCA AGAGGATGCTG
#6793/CNV/p33nostop/XhoI/R	GCCGCTCGAGTTTACACCAAGGGAC TCA
#7939/NbATG11/VIGS/S1/BamHI/F	ACGCGGATCCATGCCGATGTATGAAT GCCATGAG
#7940/NbATG11/VIGS/S1/stop/XhoI/R	ACCGCTCGAGTCACAGTCCCATGGAA GCCAAAATATC
#7941/NbATG11/VIGS/S2/BamHI/F	ACGCGGATCCATGGCTGCAAATAAAC AGCTAACG



Table 2.4 (continued)

#7942/NbATG11/VIGS/S2/stop/XhoI/R	ACCGCTCGAGTCATAACATGGCTACT GTCACTACGAAG
#7937/NbATG11/BamHI/F	ACGCGGATCCATGAGTTCATCAAATG CTTCATCAGG
#7938/NbATG11/stop/XhoI/R	ACCGCTCGAGTCAGGAAGTAGGTGAT GAATGAATGG
#5629/ATG11/BamHI/F	CGCGGATCCATGGCAGACGCTGATGA ATATAGC
#5630/ATG11/SalI/R	ACGCGTCGACTCAAACCTCCCTGGTAT GAAACCAC
#8109/NbATG11/combS2+S3/F	CTTCGTAGTGACAGTAGCCATGTTAC AGCAATATCGTAGCCATTC
#7977/NbATG11/VIGS/S3/stop/XhoI/R	ACCGCTCGAGATGGTCTCTGATAGCT AGTTCCAC
#8110/NbATG11/combS2+S3/R	TAACATGGCTACTGTCACTACGAAG
#8365/NbATG11/nonstop/XhoI/myc	ACCGCTCGAGCTACAGATCCTCTTCTG AGATGAGTTTTTTGTTCCCCGGAAGTA GGTGATGAATGAATGG
#4253/At2g45140-VAP/stp/XhoI/R	CGGCTCGAGTCATGTCCTCTTCATAAT G
#4252/At2g45140-VAP/BamHI/F	GCCGGATCCATGAGTAACGAGCTTCT CAC
#5478/ATORP3A/SPE/STP/XHO/R	GCCGCTCGAGTTAACTAGTAGCAGAG AGATCTTGGAATTG
#5477/ATORP3A/BAM/XMA/F	CGGCGGATCCCCCGGGATGGCTTCTA ACGATCCAAAAAAC
#3458/VAP27-1/BamHI/F	GCCGGATCCATGAGTAACATCGATCT GATTGGG
#3459/VAP27-1/NheI/STOP/XhoI	CGGCTCGAGTTAGCTAGCTGTCCTCTT CATAATGTATCC
#8422/HA/Avi/SalI/R	ACGCGTCGACTTACTCATGCCATTCAA T
#8423/HA/Avi/XhoI/F	ACCGCTCGAGGGAGGTTTCATACCCAT ACGACGTCCCA
#8366/ NbATG11/nonstop/XhoI/R	ACCGCTCGAGGGAAGTAGGTGATGAA TGAATGG

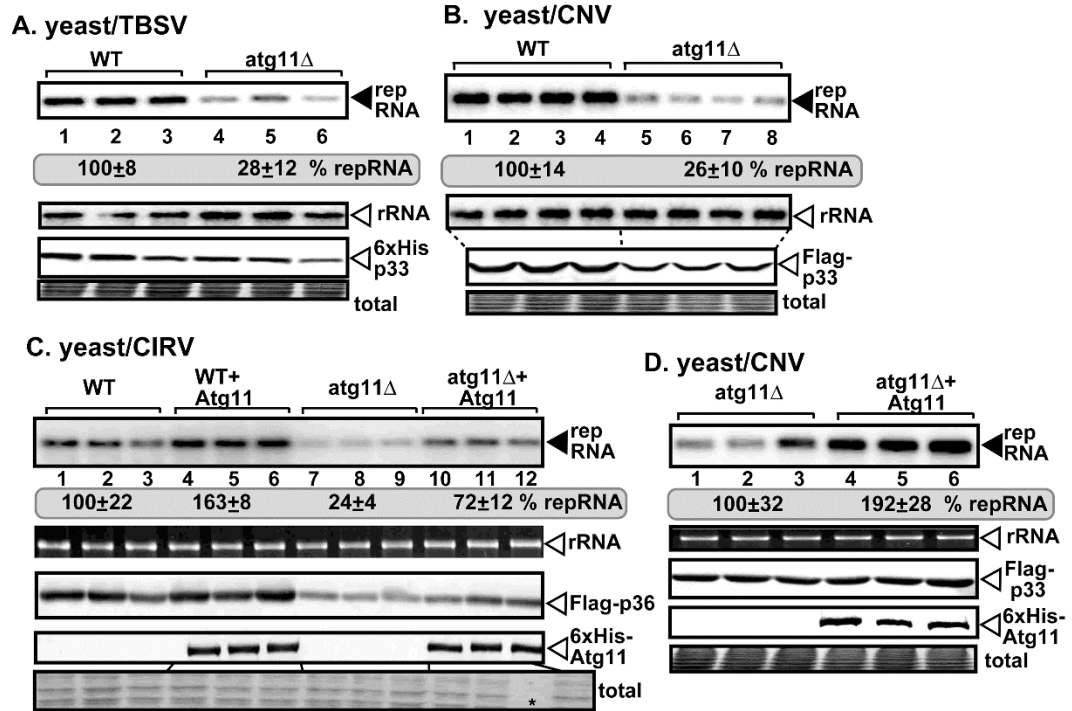
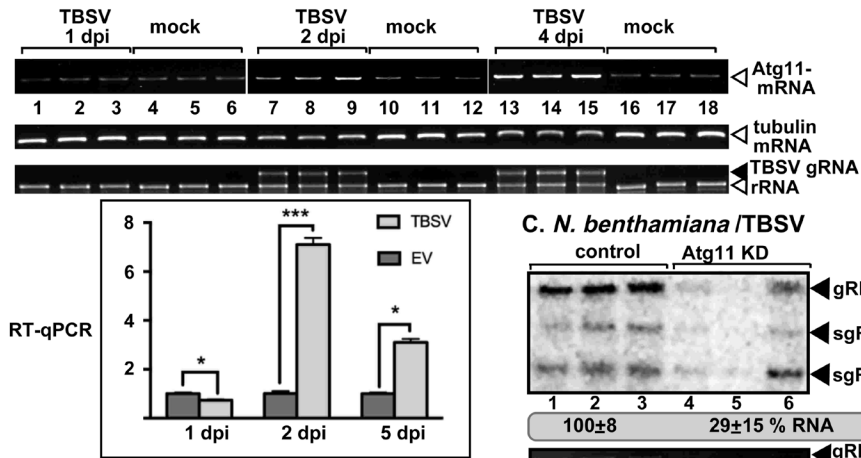


Figure 2.1

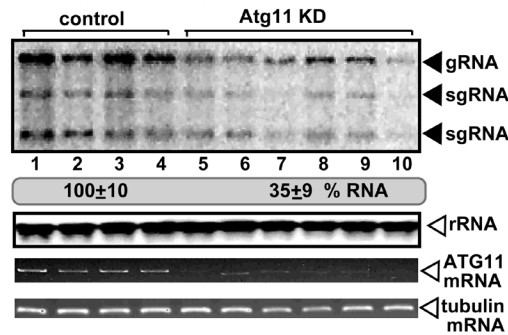
*Figure 2.1. Atg11 autophagy scaffold protein is an essential host factor for tombusvirus replication in yeast.*

(A-B) Deletion of *ATG11* inhibits TBSV, and CNV RNA replication in yeast. Top panels: northern blot analyses of repRNA using a 3' end specific probe demonstrate reduced accumulation of repRNA in *atg11Δ* yeast strain in comparison with the WT (BY4741) yeast strain. The replication proteins His<sub>6</sub>-p33 and His<sub>6</sub>-p92<sup>pol</sup> of TBSV were expressed from plasmids from the galactose-inducible *GALI* promoter, whereas the Flag-p33 and Flag-p92 of CNV were expressed from plasmids from the copper-inducible *CUPI* promoter. The DI-72(+) replicon (rep)RNA was expressed from the *GALI0* promoter. His<sub>6</sub>-Atg11 was expressed from the *GALI* promoter from a plasmid. Second panel: northern blot with 18S ribosomal RNA specific probe was used as a loading control. Bottom images: western blot analysis of the level of His<sub>6</sub>-tagged proteins and Flag-tagged proteins with anti-His or anti-Flag-antibodies, respectively. Coomassie blue-stained SDS-PAGE was used as protein loading control. (C) Deletion of *ATG11* inhibits CIRV replication in yeast. Top panel: northern blot analyses of repRNA. The CIRV Flag-p36 and Flag-p95<sup>pol</sup> were expressed from plasmids from the *CUPI* promoter. His<sub>6</sub>-Atg11 was expressed from the *GALI* promoter from a plasmid. See further details in panel A-B. (D) Complementation of *atg11Δ* yeast strain with plasmid-borne Atg11 enhances CNV replication. His<sub>6</sub>-Atg11 was expressed from the *GALI* promoter from a plasmid. See further details in panel A-B. Each experiment was repeated three times.

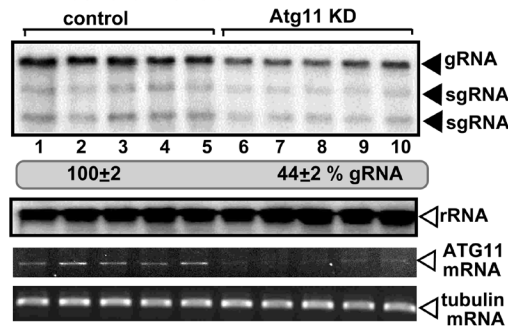
**A. Atg11 mRNA induction / *N. benthamiana***



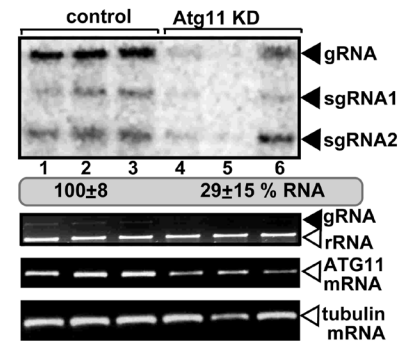
**B. *N. benthamiana* / CNV**



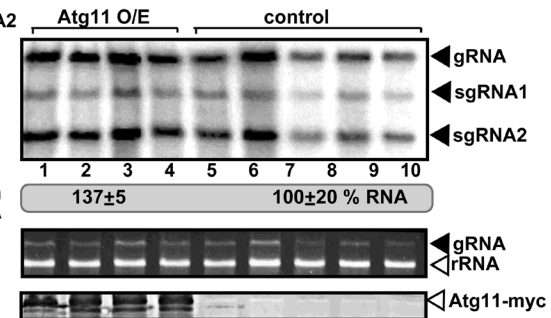
**D. *N. benthamiana* / CIRV**



**C. *N. benthamiana* / TBSV**



**E. *N. benthamiana* / CNV**



**F. *N. benthamiana* / CIRV**

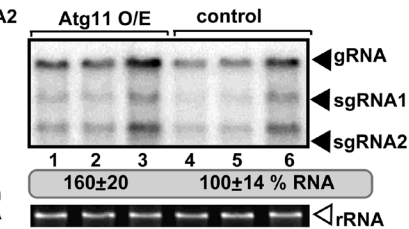


Figure 2.2

Figure 2.2. The effect of *Atg11* on tombusvirus replication in *N. benthamiana* plants.

(A) Top panel: Induction of *Atg11* mRNA expression in the inoculated leaves (1 and 2 dpi, respectively) or systemically-infected leaves (4 dpi) of *N. benthamiana* plants infected with TBSV was detected by semi-quantitative RT-PCR. Middle panel: Semi-quantitative RT-PCR of tubulin mRNA was used as a control. Middle panel: Ribosomal RNA is shown as a loading control in an ethidium-bromide stained agarose gel. Note that the TBSV gRNA is also visible in this gel. Bottom panel: Graph: Real time RT-qPCR analysis of *Atg11* mRNA levels in the agroinfiltrated leaves (1 and 2 dpi, respectively) or systemically-infected leaves (5 dpi) of *N. benthamiana* plants agroinfiltrated with pCAM-TBSV or pGD empty vectors as control. (B-D) Top panel: The accumulation of the CNV, TBSV and CIRV genomic (g)RNA in *Atg11*-silenced (*Atg11* KD) *N. benthamiana* plants 2.5, 2 and 3 dpi, respectively, in the inoculated leaves was measured by northern blot analysis. Agroinfiltration of pGD-CNV<sup>20Kstop</sup> or sap inoculation with TBSV and CIRV was done 10 days after silencing of *Atg11* expression. Agroinfiltration of tobacco rattle virus (TRV) vector carrying Nb*Atg11*-R2+R3 or 3'-terminal GFP (as a control) sequences was used to induce VIGS. Second panel: Ribosomal RNA is shown as a loading control in a northern blot or in an ethidium-bromide stained agarose gel. Third panel: Semi-quantitative RT-PCR analysis of Nb*Atg11* mRNA level in the silenced and control plants. Fourth panel: Semi-quantitative RT-PCR analysis of tubulin mRNA level in the silenced and control plants. Each experiment was repeated three times. (E-F) Overexpression of *Atg11* stimulates CNV and CIRV gRNA accumulation in *N. benthamiana* plants.

(Note: Experiments in Figure 2.2 A were in collaboration with Dr. Wenwu Lin)

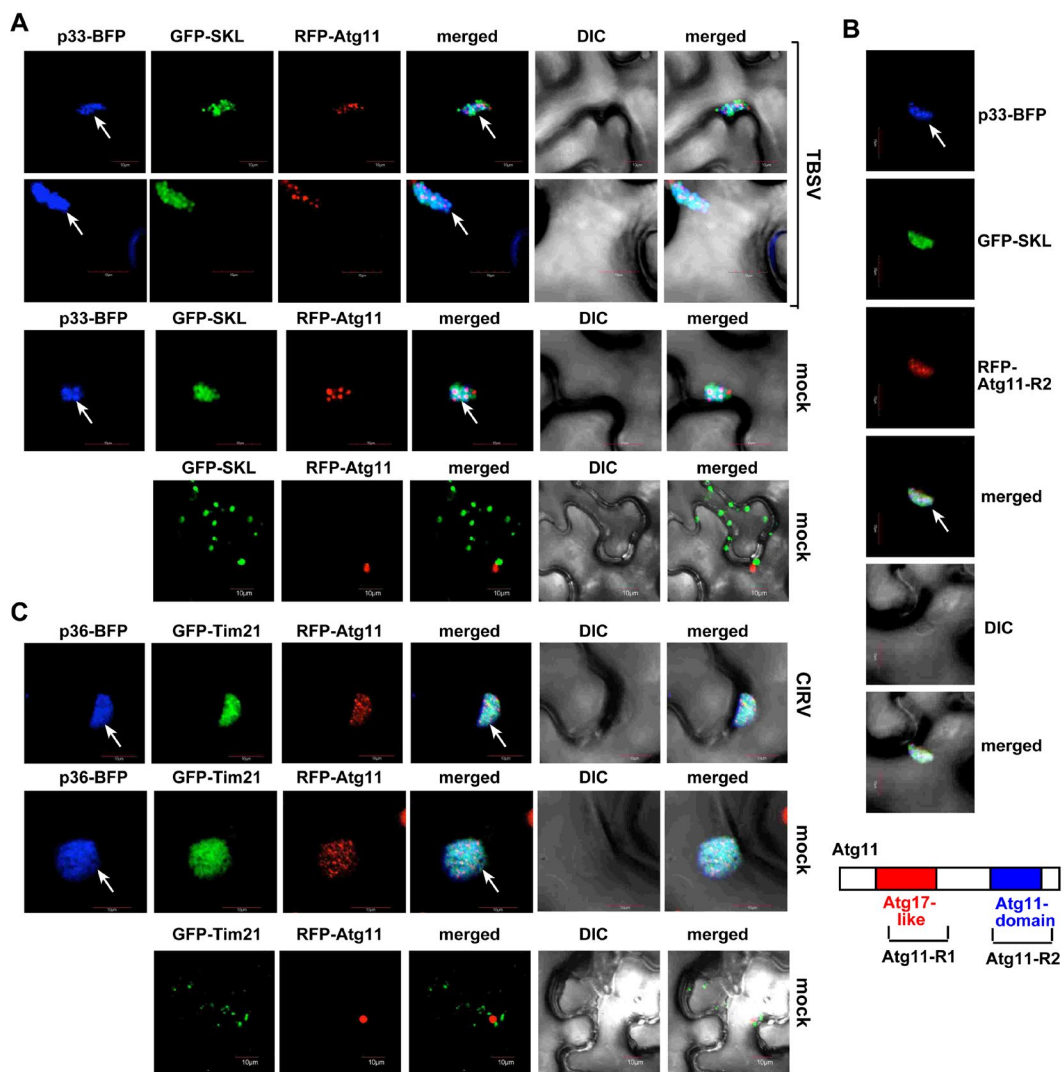


Figure 2.3

*Figure 2.3. Recruitment of Atg11 by the TBSV p33 and the CIRV p36 replication proteins into VROs in N. benthamiana.*

(A) Confocal microscopy images show efficient co-localization of TBSV p33-BFP replication protein and the RFP-Atg11 within VROs consisting of clustered peroxisomes, marked by GFP-SKL peroxisomal matrix marker in *N. benthamiana* leaves. Expression of these proteins from the 35S promoter was done after co-agroinfiltration into *N. benthamiana* leaves. The plant leaves were either TBSV-infected or mock-inoculated as shown. Scale bars represent 10  $\mu\text{m}$ . (B) Co-localization of the R2 domain of Atg11 with TBSV p33 in plant cells. See further details in panel A. (C) Confocal microscopy images show efficient co-localization of CIRV p36-BFP replication protein and the RFP-Atg11 within VROs consisting of clustered mitochondria, marked by GFP-AtTim21 mitochondrial marker in *N. benthamiana* leaves. See further details in panel A. Scale bars represent 10  $\mu\text{m}$ . Each experiment was repeated.

(Note: Experiments in Figure 2.3 were in collaboration with Dr. Wenwu Lin)

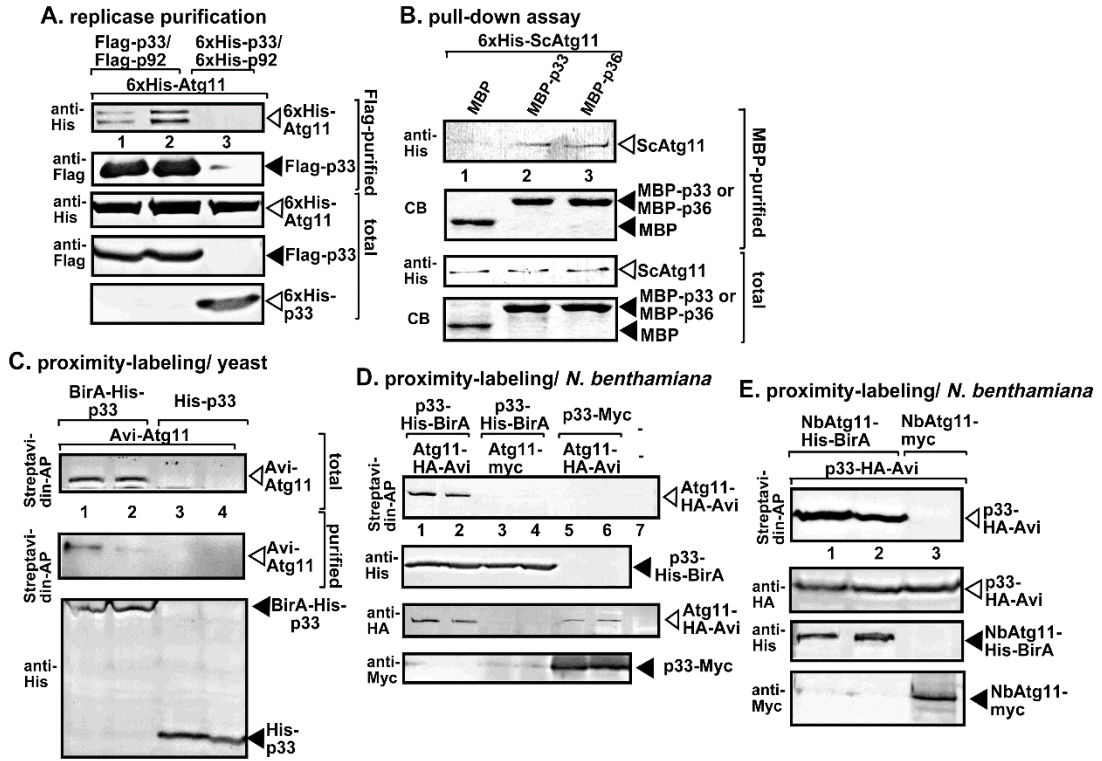


Figure 2.4



Figure 2.4. Interaction between tombusvirus replication proteins and Atg11.

(A) Co-purification of the yeast His<sub>6</sub>-Atg11 with TBSV Flag-p33 and Flag-p92<sup>pol</sup> replication proteins from detergent-solubilized subcellular membranes. Top two panels: western blot analysis of co-purified His<sub>6</sub>-Atg11 (lanes 1-2) with Flag-affinity purified Flag-p33 and Flag-p92<sup>pol</sup>. His<sub>6</sub>-tagged proteins were detected with anti-His antibody, while Flag-p33 was detected with anti-Flag antibody. The negative control was from yeast expressing His<sub>6</sub>-p33 and His<sub>6</sub>-p92<sup>pol</sup> purified in a Flag-affinity column (lane 3). Samples were cross-linked with formaldehyde. Bottom two panels: western blot of total His<sub>6</sub>-Atg11 and Flag-p33 in the total yeast extracts. (B) Pull-down assay including the yeast GST-His<sub>6</sub>-Atg11 and either the MBP-tagged TBSV p33 or CIRV p36 replication proteins. Note that we used the soluble C-terminal region of TBSV p33 or CIRV p36 replication proteins, which lacked the N-terminal trans-membrane domain. Top panel: western blot analysis of the captured yeast GST-His<sub>6</sub>-Atg11 with the MBP-affinity purified p33/p36 was performed with anti-His antibody. The negative control was the MBP (lane 1). Middle panel: Coomassie-blue stained SDS-PAGE of the captured MBP-p33, MBP-p36 and MBP. Bottom panels: western blot analysis of GST-His<sub>6</sub>-Atg11 in total extracts. Coomassie-blue stained SDS-PAGE of the MBP-p33, MBP-p36 and MBP in total extracts. Each experiment was repeated three times. (C) Protein proximity-labeling with biotin in yeast. P33 replication protein was fused to BirA biotin ligase, whereas Atg11 was fused to Avi-tag. Biotin treatment lasted for 2h. Top image shows the western blot analysis of the biotinylated Avi-Atg11 in total protein extract, whereas the second image shows the streptavidin-based purified biotinylated Avi-Atg11. Biotinylated Avi-Atg11 was detected with streptavidin-conjugated AP. Bottom image shows western blot analysis of BirA-His<sub>6</sub>-p33 in total protein extracts. Yeast expressing His<sub>6</sub>-p33 and Avi-Atg11 was used as a negative control. (D) Protein proximity-labeling with biotin in *N. benthamiana*. Agroinfiltration was used to express p33 replication protein, which was fused to BirA biotin ligase, and Atg11-Avi-tag. Biotin treatment lasted for 40 min. Top image shows the western blot analysis of the biotinylated Atg11-Avi detected with streptavidin-conjugated AP in total protein extracts. See further details in panel C. (E) Reciprocal protein proximity-labeling with biotin in *N. benthamiana*. Agroinfiltration was used to express Atg11-His<sub>6</sub>-BirA, and p33-HA-Avi-tag replication protein. See further details in panel D.

(Note: Experiments in Figure 2.4 A and B were in collaboration with Dr. Wenwu Lin)

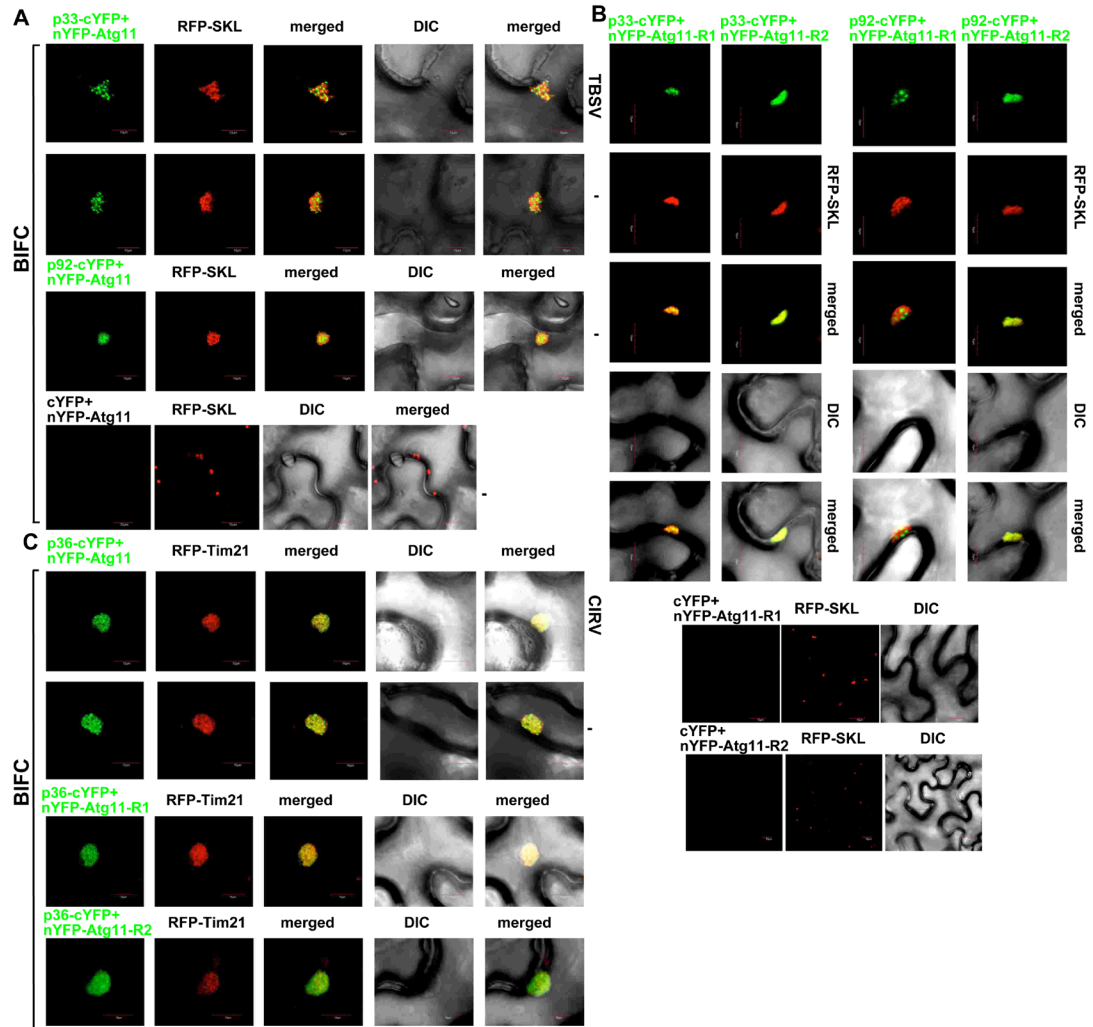


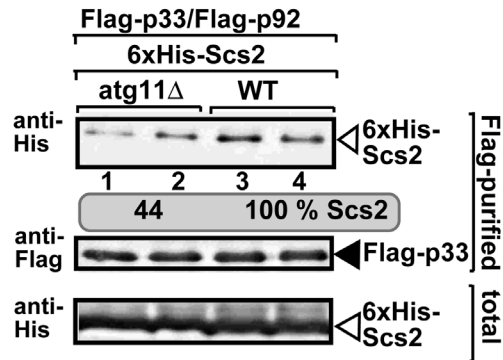
Figure 2.5

*Figure 2.5. BiFC studies of the interaction between Atg11 and replication proteins within VROs in N. benthamiana.*

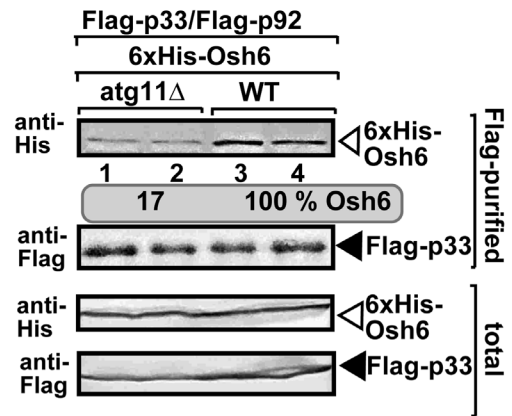
(A) Top two panels: Interaction between TBSV p33-cYFP replication protein and the nYFP-Atg11 protein was detected by BiFC. The merged images show the efficient co-localization of RFP-SKL with the BiFC signal, indicating that the interaction between p33 replication protein and Atg11 occurs in VROs in clustered peroxisomal membranes. Third panel: Interaction between TBSV p92-cYFP replication protein and the nYFP-Atg11 protein was detected by BiFC. Bottom panel: negative BiFC control. (B) Interaction between TBSV p33-cYFP or p92-cYFP replication proteins and the R1 (Atg17-like) or R2 (Atg11-like) domains of Atg11 proteins were detected by BiFC. See further details in panel A. (C) Interactions between CIRV p36-cYFP replication protein and the nYFP-Atg11 protein or the R1 or R2 domains of Atg11 were detected by BiFC. The merged images show the efficient co-localization of RFP-AtTim21 with the BiFC signal, indicating that the interaction between p36 replication protein and Atg11 occurs in VROs consisting of aggregated mitochondria. See further details in panel A. Scale bars represent 10  $\mu$ m. Each experiment was repeated three times.

(Note: Experiments in Figure 2.5 were in collaboration with Dr. Wenwu Lin)

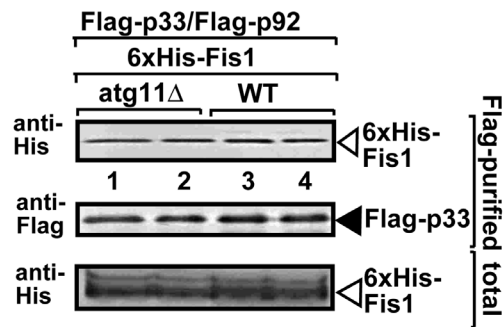
**A. replicase purification**



**B. replicase purification**



**C. replicase purification**



**D. replicase purification**

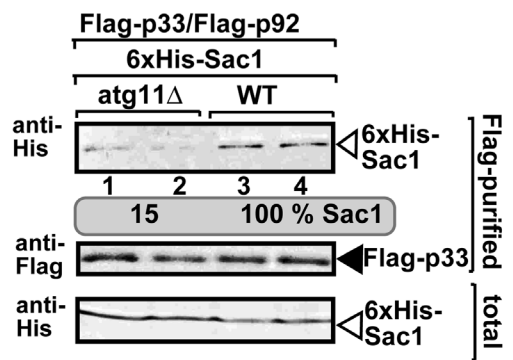


Figure 2.6

*Figure 2.6. Atg11 facilitates the recruitment of the cellular ER-resident VAP protein, Sac1 and Osh6 proteins into tombusvirus replication compartment.*

(A) Co-purification of the yeast His<sub>6</sub>-Scs2 VAP protein with TBSV Flag-p33 and Flag-p92<sup>pol</sup> replication proteins from subcellular membranes of WT or atg11Δ yeast strains. Top two panels: western blot analysis of co-purified His<sub>6</sub>-Scs2 detected with anti-His antibody, whereas Flag-p33 was detected with anti-Flag antibody. Samples were cross-linked with formaldehyde. Bottom panel: western blot of total His<sub>6</sub>-Scs2 in the total yeast extracts. (B) Co-purification of the yeast His<sub>6</sub>-Osh6 with TBSV Flag-p33 and Flag-p92<sup>pol</sup> replication proteins from subcellular membranes of WT or atg11Δ yeast strains. See further details in panel A. (C) Co-purification of the yeast His<sub>6</sub>-Fis1 with TBSV Flag-p33 and Flag-p92<sup>pol</sup> replication proteins from subcellular membranes of WT or atg11Δ yeast strains. See further details in panel A. (D) Co-purification of the yeast His<sub>6</sub>-Sac1 with TBSV Flag-p33 and Flag-p92<sup>pol</sup> replication proteins from subcellular membranes of WT or atg11Δ yeast strains. See further details in panel A. Each experiment was repeated.

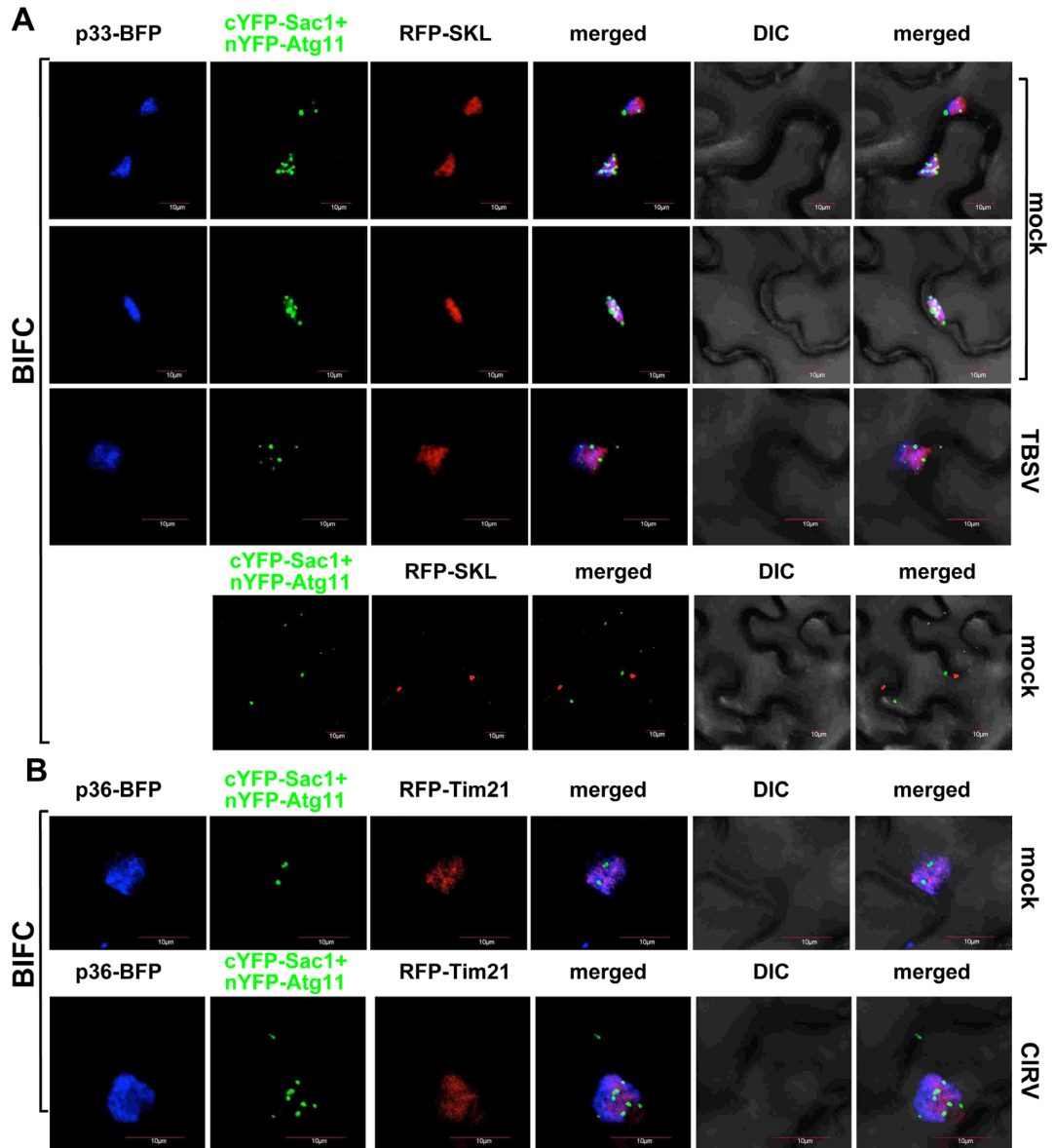


Figure 2.7

*Figure 2.7. Interaction between Atg11 and Sac1 PI4P phosphatase protein within VROs in N. benthamiana.*

(A) BiFC approach was used to demonstrate interaction between nYFP-Atg11 and cYFP-Sac1 proteins within the TBSV p33-BFP-positive VROs (B) or CIRV p36-BFP-positive VROs. Expression of the above proteins from 35S promoter was done after co-agroinfiltration into *N. benthamiana* leaves infected with either TBSV or CIRV or mock-inoculated. Scale bars represent 10  $\mu$ m. Each experiment was repeated.

(Note: Experiments in Figure 2.7 were in collaboration with Dr. Wenwu Lin)

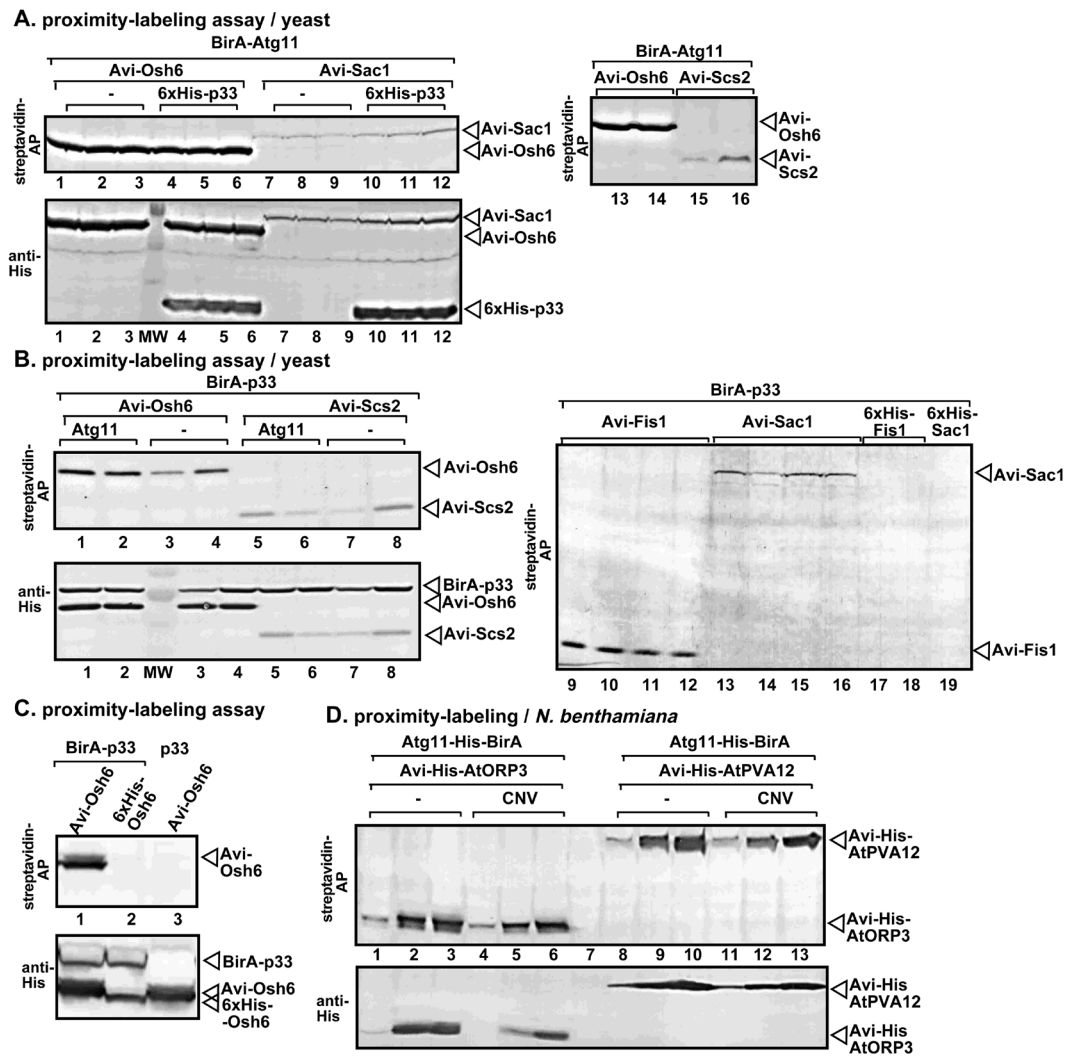


Figure 2.8



*Figure 2.8. Protein proximity-labeling of vMCS proteins with biotin in yeast and plants.*

(A) Proximity labeling with BirA-Atg11 of the Avi-tagged Osh6, Sac1 and Scs2 vMCS proteins. His<sub>6</sub>-p33 was co-expressed in the marked samples. Biotin treatment lasted for 30 min. Top image shows the western blot analysis of the biotinylated Avi-tagged proteins detected with streptavidin-conjugated AP in total protein extracts. Bottom image shows western blot analysis of vMCS proteins via anti-His antibody in total protein extracts. (B) Proximity labeling with BirA-p33 of Avi-tagged Osh6, Scs2 Fis1 and Sac1 vMCS proteins. Atg11 was co-expressed in the marked samples. Biotin treatment lasted for 30 min. Top image shows the western blot analysis of the biotinylated Avi-tagged proteins detected with streptavidin-conjugated AP in total protein extracts. Bottom image shows western blot analysis of vMCS proteins via anti-His antibody in total protein extracts. (C) Control experiment for proximity labeling with BirA-p33 of Avi-Osh6. See panel B for further details. (D) Proximity labeling with Atg11-BirA of the Avi-tagged ORP3 oxysterol-binding protein and PVA12 VAP protein, which are core vMCS proteins. The time points were 31 h (lanes 1, 4, 8 and 11); 48 h (lanes 2, 5, 9 and 12); and 56 h (lanes 3, 6, 10 and 13) after agroinfiltration. Biotin treatment lasted for 60 min. Plants were infected with CNV or not-infected as shown. Top image shows the western blot analysis of the biotinylated Avi-tagged proteins detected with streptavidin-conjugated AP in total protein extracts. Bottom image shows western blot analysis of vMCS proteins via anti-His antibody in total protein extracts.

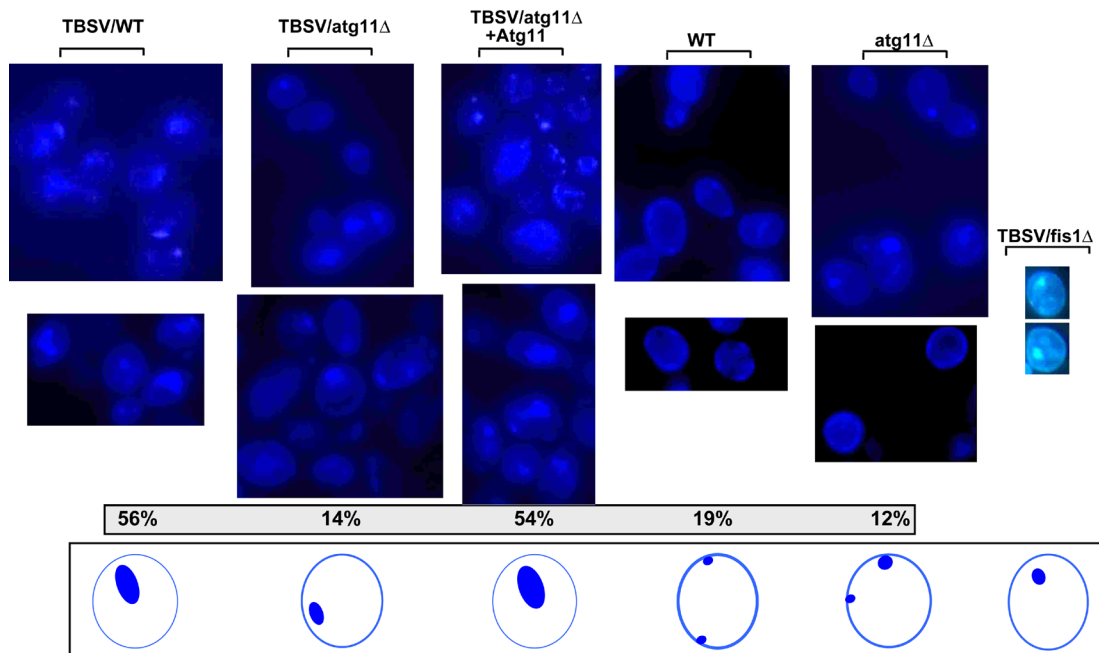
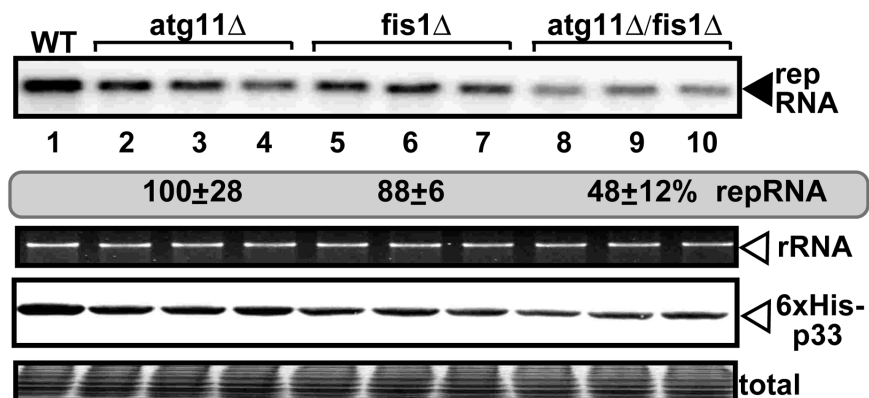


Figure 2.9

*Figure 2.9. Atg11 affects sterol re-localization to internal sites in yeast replicating TBSV RNA.*

Fluorescent microscopic images of yeast cells stained with the filipin dye. Decreased level of re-localization of ergosterols to internal punctate structures in *atg11* $\Delta$  yeast replicating TBSV (second row from left) in comparison with WT yeast (first row from left) or *atg11* $\Delta$  yeast expressing *Atg11* from a plasmid (third row from left). Yeasts expressed the p33 and p92 replication proteins and the TBSV repRNA. We also show the previously characterized effect of *Fis1* deletion on sterol distribution in *fis1* $\Delta$  yeast replicating TBSV, which results in reduced ergosterol re-distribution from the plasma membrane to internal punctate structures, similar to that observed in *atg11* $\Delta$  yeast. The control fluorescent microscopic images of yeast cells lacking viral components are shown in the panels on the right. Note that filipin stains ergosterols present mostly in the plasma membrane in virus-free WT or *atg11* $\Delta$  yeast cells. We calculated the percentage of yeast cells, which represented ergosterol-rich membranes filling 20% or more of the intracellular space in yeast versus minimal or no intracellular puncta. We have based our calculations on total of ~100 or more yeast cells for each experiment. The bottom panel illustrates the representative size and distribution of sterol-rich punctate structures and the plasma membrane. Each experiment was repeated.

**A. yeast**



**B. yeast**

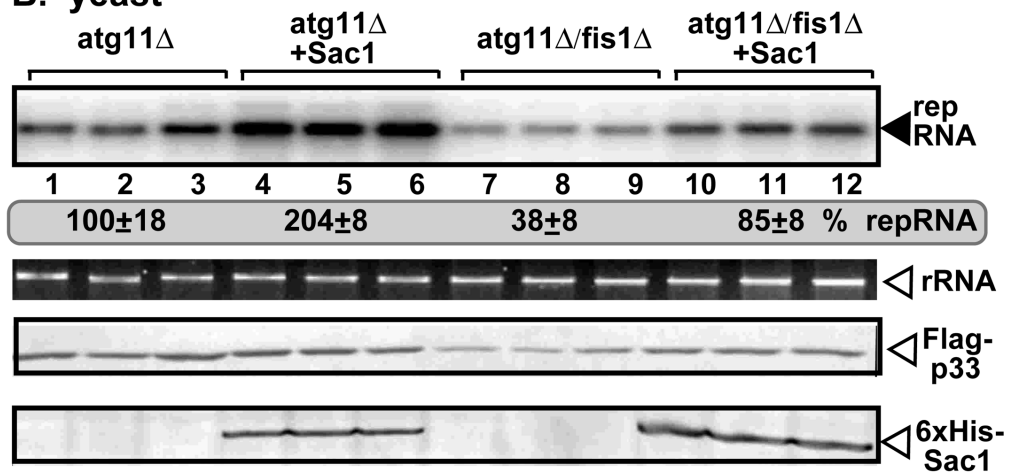


Figure 2.10

*Figure 2.10. Double-deletion of ATG11 and FIS1 further decreases tombusvirus RNA accumulation in yeast.*

(A) Replication of the TBSV repRNA was measured by northern blotting 24 h after initiation of TBSV replication in the shown yeast strains. The accumulation level of repRNA was normalized based on the ribosomal (r)RNA. TBSV RNA accumulation in *atg11Δ* yeast strain was taken as 100% in each experiment. The third panel shows the accumulation of His<sub>6</sub>-p33 based on western blotting with anti-His antibody. (B) Complementation of *ATG11* and *FIS1* deletion or double-deletion by over-expression of SacI vMCS protein yeast. Northern and western blots with anti-His antibody were done as described in panel A. Each experiment was repeated.

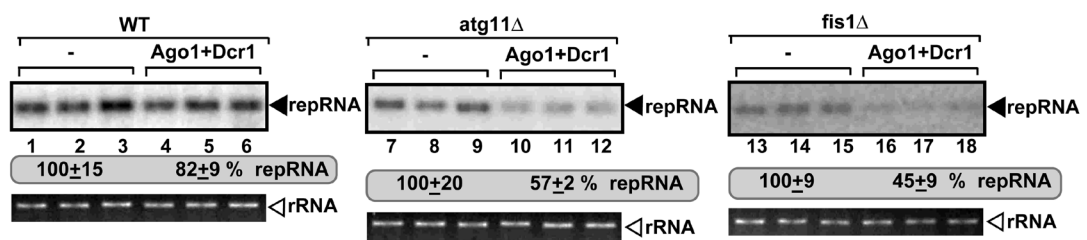


Figure 2.11

*Figure 2.11. Deletion of ATG11 sensitizes tombusvirus RNA to RNAi-based degradation in yeast.*

Co-expression of *S. castellii* AGO1 and DCR1 in *atg11Δ* and *fis1Δ* yeasts reduces TBSV repRNA accumulation to a larger extent than in WT yeast (BY4741). Top panel: Replication of the TBSV repRNA was measured by northern blotting 24 h after initiation of TBSV replication. The accumulation level of repRNA was normalized based on the ribosomal (r)RNA. Note that the TBSV repRNA, p33 and p92 replication proteins were expressed from plasmids. Each sample is obtained from different yeast colonies. Yeast strain not expressing RNAi components is taken as 100% in each experiment. Average value and standard deviation is calculated from all the biological repeats. Ribosomal RNA is shown as a loading control. Each experiment was repeated three times.

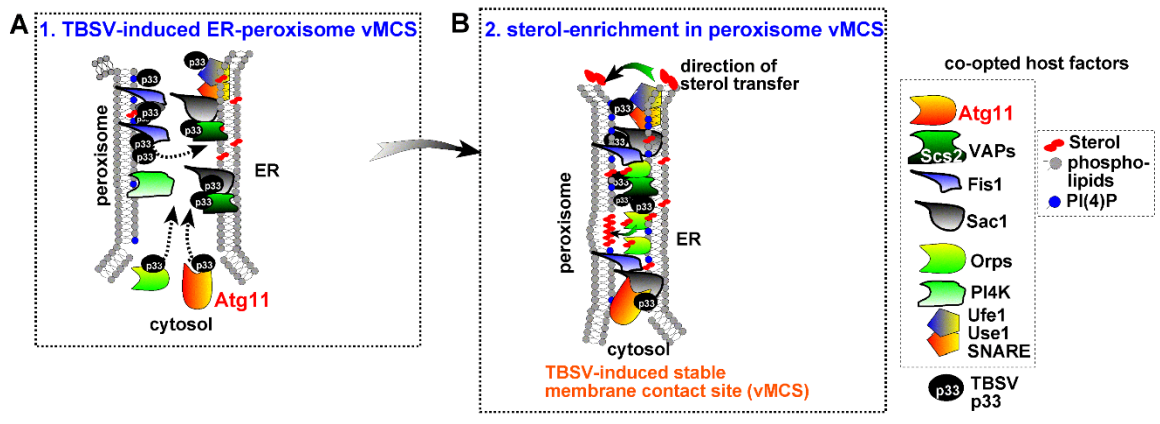


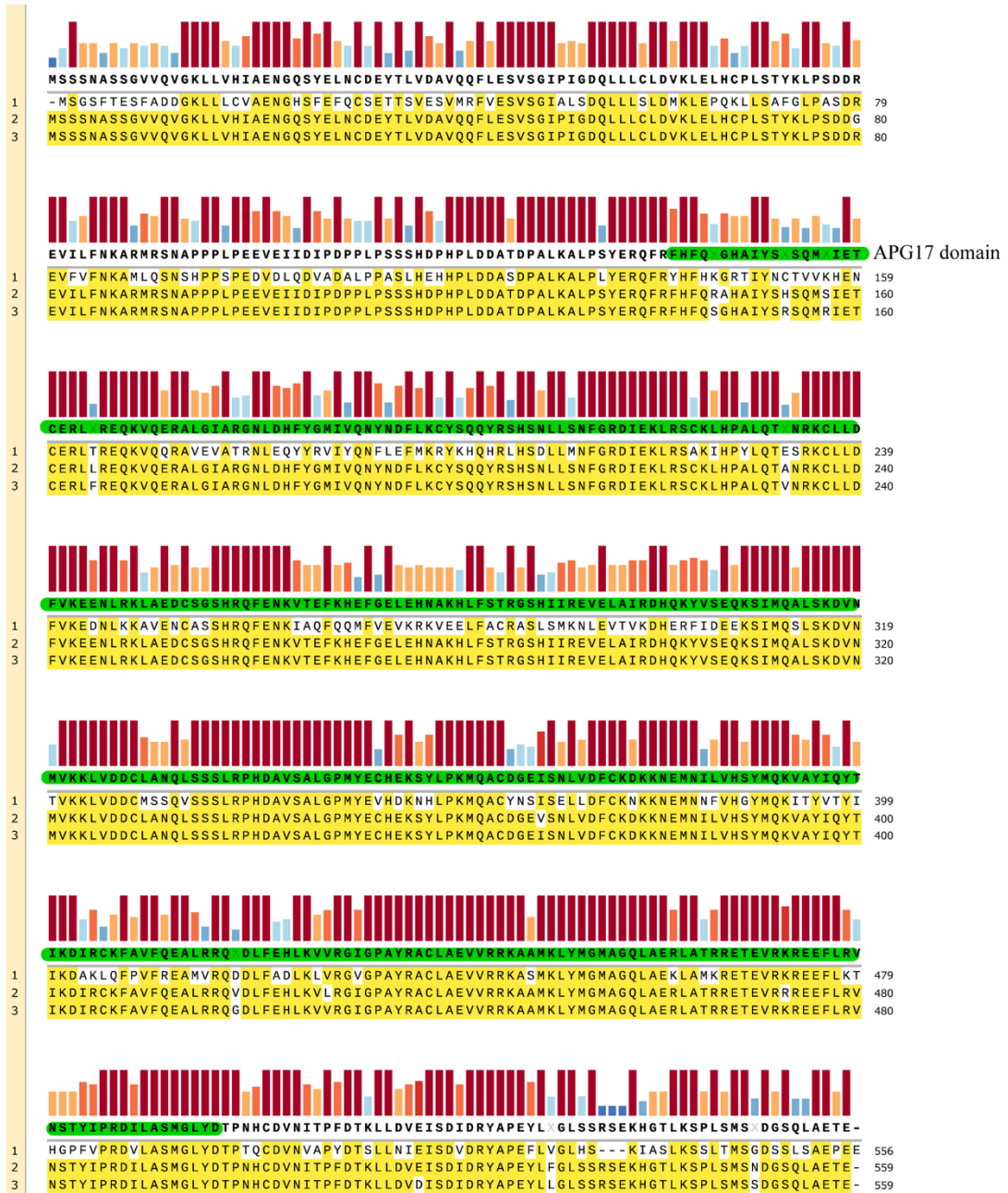
Figure 2.12

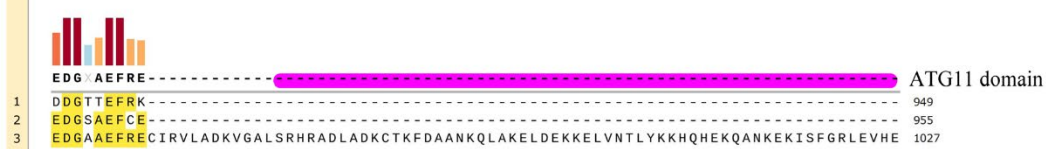


*Figure 2.12. A model on the functional role of the Atg11 autophagy scaffold protein in the formation of virus-induced vMCS.*

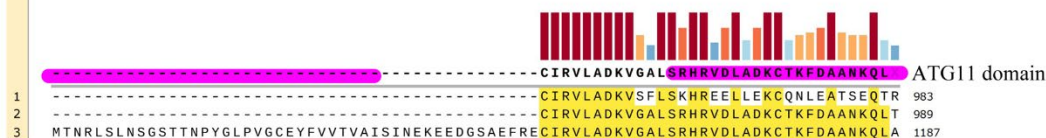
(A) Expression of the abundant p33 replication protein of TBSV leads to p33 molecules-driven efficient recruitment of Atg11 to vMCS. P33 and Atg11 bind to other vMCS proteins, including the ER-resident VAP tethering protein and Sac1 PI4P phosphatase, the peroxisomal Fis1 mitochondria fission protein and the cytosolic oxysterol-binding proteins (ORP). The cellular PI4K kinase and Ufe1 and Use1 SNARE complex are also recruited into vMCS. We propose that all these interactions lead to the tethering of the peroxisomal membranes to the subdomains of the ER membrane, resulting in the formation and stabilization of vMCSs. (B) The interplay between the co-opted ORP proteins, PI(4)P phosphoinositide and Sac1 facilitates the enrichment of sterols and other lipids within the peroxisomal membranes. These processes render the peroxisomal membranes highly suitable for the formation of VROs needed for virus replication. Please note the related CIRV co-opts similar set of host proteins and builds similar virus-induced vMCS structures utilizing mitochondrial membranes, instead of peroxisomes, and the ER membranes.

1. AT4G30790
2. Niben101Scf09742g00014.1
3. Niben101Scf02359g00022.1





ATG11 domain starts with SKHRE...



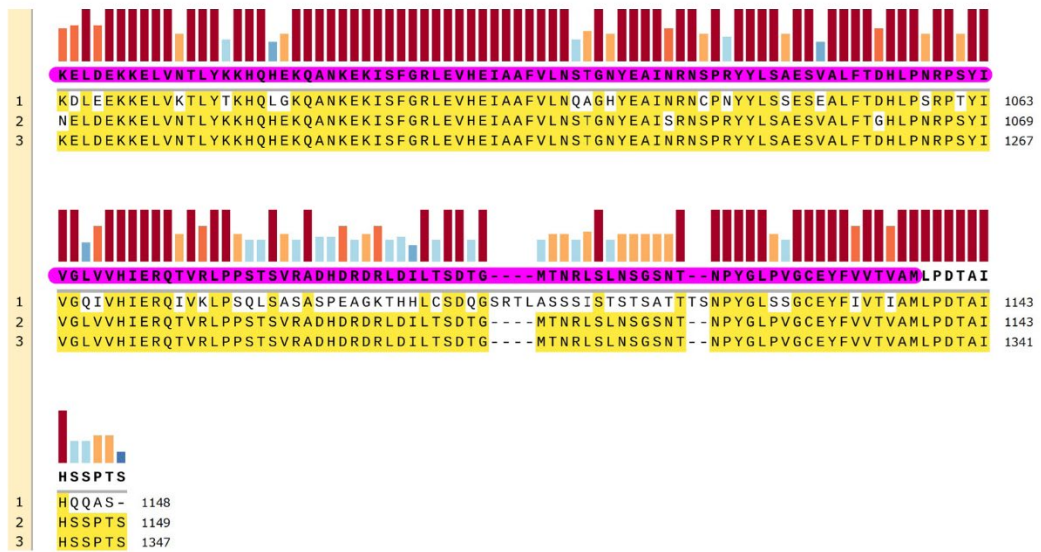


Figure S2.1

*Figure S2.1. Sequence alignment of the Arabidopsis Atg11 (AT4G30790) and the N. benthamiana Atg11 (Niben101Scf09742g00014.1 and Niben101Scf02359g00022.1) amino acid sequences. The ATG17-like APG17 and Atg11-like domains are indicated.*

(Note: Experiments in Figure S2.1 were in collaboration with Dr. Wenwu Lin)

## Figure S2: Sequence alignment for NbATG11-silencing

### R2:

CLUSTAL O(1.2.4) multiple sequence alignment

```

Niben101Scf02359g00022.1-S2      GCTGCAATAAACAGCTAGCGAAGGAGTTGGACGAAAAGAAGAATTGGTTAACACCCCTC   60
Niben101Scf09742g00014.1-S2      GCTGCAATAAACAGCTAACGAATGAGTTGGACGAAAAGAAGAATTGGTTAACACCCCTC   60
*****

Niben101Scf02359g00022.1-S2      TATAAAAAGCATCAACATGAGAAGCAGGCAAAACAAGAGAAGATATCATTGGGCGTTTA   120
Niben101Scf09742g00014.1-S2      TATAAAAAGCATCAACACGAGAAGCAGGCAAAACAAGAGAAGATATCATTGGGCGTTTA   120
*****

Niben101Scf02359g00022.1-S2      GAAGTCCATGAAATTGCAGCATTGTACTCACTCTACTGGAAATTATGAGGCTATCAAT   180
Niben101Scf09742g00014.1-S2      GAAGTTCATGAAATTGCAGCATTGTCTTAECTACTGGAAATTATGAGGCTATCAGT     180
*****

Niben101Scf02359g00022.1-S2      CGAAACAGTCCACGTTACTATCTGTCTGCAGAATCTGTGGCATTGTTTACTGACCATCTT   240
Niben101Scf09742g00014.1-S2      CGAAACAGTCTCTGTTACTACCTCTCTGCAGAGCTGTGGCATTGTTTACTGACCATCTT   240
*****

Niben101Scf02359g00022.1-S2      CCAAATCGTCCAAGCTATATCGTAGGGCTGGTGTGCATATTGAACGACAGACTGTGAGG   300
Niben101Scf09742g00014.1-S2      CCAAATCGTCCAAGCTACATTGTAGGGCTGGTGTGCATATTGAACGACAGACTGTGAGG   300
*****

Niben101Scf02359g00022.1-S2      CTGCCACCCTCAACATCAGTTGCGAGCTGACCATGATAGAGACCGTTTAGATATACTGACT   360
Niben101Scf09742g00014.1-S2      CTGCCACCCTCAACATCAGTTGCGAGCTGACCATGATAGAGACCGTTTAGATATACTGACT   360
*****

Niben101Scf02359g00022.1-S2      TCTGACACAGGAATGACCAATCGTTTGCCTTGAATTCAGGATCAAATACGAACCCGTAT   420
Niben101Scf09742g00014.1-S2      TCTGACACAGGAATGACCAATCGTTTGCCTTGAATTCAGGATCAAATACGAACCCGTAT   420
*****

Niben101Scf02359g00022.1-S2      GGTCTCCCTGTGGCTGTGAATACTTCGTAGTG                               453
Niben101Scf09742g00014.1-S2      GGTCTCCCTGTGGCTGTGAATACTTCGTAGTG                               453
*****

```

### R3:

```

Niben101Scf02359g00022.1-S3      CAGCAATATCGTAGCCATTCTAATTTGCTATCTAATTTTGAAGGGATATAGAGAAGTTG   60
Niben101Scf09742g00014.1-S3      CAGCAATATCGTAGCCATTCTAATTTGCTATCTAATTTTGAAGGGATATAGAGAAGTTG   60
*****

Niben101Scf02359g00022.1-S3      AGGCTTGGCAAACCTTCATCCTGCTTTGCAAACCTGTTAACCGCAAGTGCTTGCTGGATTC   120
Niben101Scf09742g00014.1-S3      AGATCTTGCAAACCTTCATCCTGCTTTGCAAACCTGTTAACCGCAAGTGCTTGCTGGATTC   120
**

Niben101Scf02359g00022.1-S3      GTGAAAGAAGAGAACCTTGCAGGAAAGTTGGCAGAGGATTGTAGTGGTTTCGATAGGCAGTTT   180
Niben101Scf09742g00014.1-S3      GTGAAAGAAGAGAACCTTGCAGGAAAGTTGGCAGAGGATTGTAGTGGTTTCGATAGGCAGTTT   180
*****

Niben101Scf02359g00022.1-S3      GAGAATAAAGTACCAGAAATTAAGCACGAGTTTGGAGAGCTAGAGCACAAATGCTAAGCAT   240
Niben101Scf09742g00014.1-S3      GAGAATAAAGTACCAGAAATTAAGCACGAGTTTGGAGAGCTAGAGCACAAATGCTAAGCAT   240
*****

Niben101Scf02359g00022.1-S3      TTATTTTCTACCAGAGTTTACATATTATTAGGGAAGTGGAACTAGCTATCAGAGACCAT   300
Niben101Scf09742g00014.1-S3      TTATTTTCTACCAGAGTTTACATATTATTAGGGAAGTGGAACTAGCTATCAGAGACCAT   300
*****

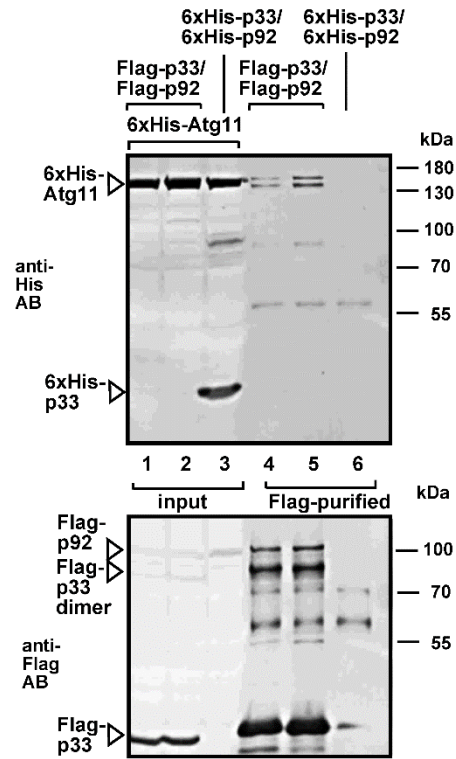
```

Figure S2.2

*Figure S2.2. Sequence alignment of the R2 and R3 regions of NbATG11 genes used for the VIGS experiments.*

## FIGURE S3

### A. supplement to replicase purification



### B. supplement to proximity-labeling/ *N. benthamiana*

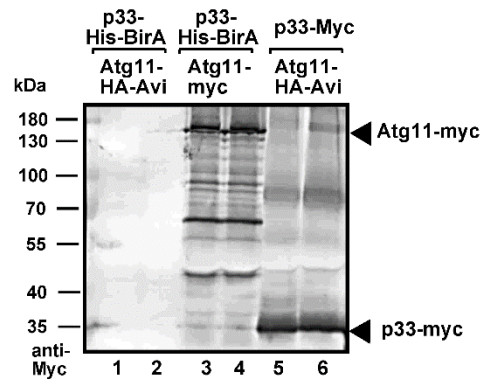


Figure S2.3



*Figure S2.3. Supplement to Figure 2.4.*

(A) Western blot analysis of co-purified yeast His<sub>6</sub>-Atg11 with TBSV Flag-p33 and Flag-p92<sup>pol</sup> replication proteins from detergent-solubilized subcellular membranes. See further details in Figure 2.4A. (B) Western blot analysis of accumulation of Atg11-myc and p33-myc in *N. benthamiana*. See further details in Figure. 2.4D.

# FIGURE S4

proximity-labeling assay / yeast

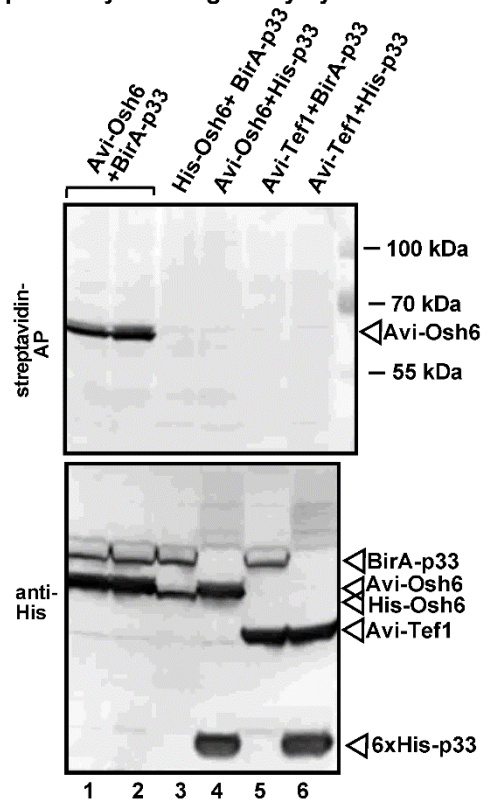


Figure S2.4

*Figure S2.4. Supplement to Figure 2.8.*

Lack of proximity labeling with BirA-p33 of Avi-tagged Tef1 protein in yeast. Avi-Tef1 was co-expressed in the marked samples. Avi-Osh6 co-expression with BirA-p33 served as a positive control. Biotin treatment lasted for 30 min. Western blot analysis show the detection of the biotinylated Avi-tagged proteins with streptavidin-conjugated AP in total protein extracts. See further details in Figure 2.8B.

## CHAPTER 3.

### SUBVERSION OF SELECTIVE AUTOPHAGY FOR THE BIOGENESIS OF TOMBUSVIRUS REPLICATION ORGANELLES INHIBITS AUTOPHAGY

(This chapter was published in Plos Pathogens, March 14, 2024. 20(3): e1012085.  
Copyright © 2024 Kang et al.)

#### 3.1 Introduction

Positive-strand (+)RNA viruses infect and cause many diseases in eukaryotic organisms. (+)RNA viruses have small genomes and they have to co-opt numerous host factors to support their replication inside the infected cells. Virus replication depends on the biogenesis of viral replication organelles (VROs), which cluster many membrane-bound viral replicase complexes (VRCs) (63-70). VRO biogenesis requires usurping various intracellular organelles, membrane deformation, new lipid biosynthesis, phospholipid and sterol transfer and co-opting vesicular trafficking (4, 69, 71-73). The membranous VROs sequester the viral (+)RNA and viral and co-opted host proteins for efficient replication. In addition, VROs also protect the viral (+)RNA and the dsRNA replication intermediate from recognition and elimination by the host innate immune system (74-76, 136-140). Altogether, the VROs coordinate the viral replication process spatiotemporally (64, 69, 71, 77, 78).

Tomato bushy stunt virus (TBSV), which is a small (+)RNA virus of plants, is studied intensively to unravel the basic mechanism of viral RNA replication (79-82). TBSV codes for two essential replication proteins, the p92 RdRp and the p33 replication protein, which is the master regulator of VRO assembly and viral (+)RNA recruitment into VRCs

(7, 83). TBSV replicon (rep)RNA replicates in the surrogate host yeast (*Saccharomyces cerevisiae*) to a high level (80, 84, 85). Yeast-based genome-wide and proteome-wide studies with TBSV led to the identification of numerous host factors co-opted for viral RNA replication and recombination (64, 80, 86-88, 141). Overall, TBSV depends on global phospholipid and sterol biosynthesis (89-91). Formation of viral replicase complexes (VRCs) and activation of the viral-coded p92 RdRp requires phosphatidylethanolamine (PE), phosphoinositides and sterols (25, 26, 32, 40, 83, 90, 92-94).

TBSV induces subcellular membrane proliferation and peroxisome aggregation in both yeast and plant cells. One of the characteristic features of TBSV infection is the formation of virus-induced membrane contact sites (vMCSs) (39, 80, 95, 96). vMCS forms between the hijacked subdomain in the ER and the peroxisome with the help of p33 replication protein and co-opted host proteins, such as oxysterol-binding proteins, ER-resident Sac1 PI4P phosphatase and VAP proteins and Fis1 mitochondrial fission protein (39, 40, 104). vMCS function is essential for the enrichment of sterols and phosphoinositides within VROs (39) to protect TBSV replication protein from proteasomal degradation (32, 83). In addition to subversion of peroxisomes by TBSV and mitochondria by the closely related carnation Italian ringspot virus (CIRV), these viruses also co-opt a subdomain of ER containing a SNARE complex, including the syntaxin18-like protein (97, 98). Moreover, tombusviruses hijack Rab5-positive endosomes, Rab1-positive COP II vesicles and the retromer tubular transport carriers. These co-opted vesicles provide membranes, lipids, and lipid synthesis and modification enzymes for VRO biogenesis (9, 92, 117, 128).

Autophagy plays an important role in maintaining cellular homeostasis and also in defense against invading pathogens in plants and animals. Autophagy is initiated by autophagy-related proteins (ATGs) at the phagophore assembly site (PAS) by recruitment of cargo proteins or damaged organelles, followed by maturation into autophagosome (105-109). The autophagosomes are double-membrane organelles, which deliver the cargoes into vacuoles for degradation and recycling. Recent studies revealed an important antiviral role of autophagy that leads to degradation of viral proteins or virions. However, several viruses block autophagy or utilize autophagy to degrade host defense factors, whereas other viruses exploit autophagy to support virus replication (110, 111, 142-148). Autophagy also targets plant viruses and it is a major player in antiviral innate immunity (149-155). Several plant viruses manipulate the autophagy machinery to inhibit antiviral defenses in plants (156-160). However, plant viruses also exploit autophagy for pro-viral functions (145, 161, 162).

ATG8 is a ubiquitin-like protein that is essential for autophagy (163, 164). ATG8 is activated through sequential steps by several ATG proteins, ultimately leading to lipidation of ATG8. ATG8 conjugated to phosphatidylethanolamine (PE) is bound to the phagophore membrane and it interacts with several ATG proteins and also with cargo receptor proteins, such as NBR1 (149, 165, 166). Together with the cargoes, a fraction of ATG8-PE is delivered to the vacuole by the matured autophagosome for degradation.

We have previously found that ATG11 selective autophagy scaffold protein is recruited by the TBSV p33 replication protein into VROs (167). The co-opted ATG11 facilitates the formation of vMCS, thus playing a pro-viral role. The findings that

tombusviruses usurp a key selective autophagy protein for pro-viral functions open the question: Do tombusviruses usurp additional autophagy proteins or membranes?

In this work, we demonstrate that the key autophagy protein, ATG8, is recruited into TBSV VROs via interaction with the p33 replication protein. Moreover, NBR1 selective autophagy protein is also subverted by p33. Knockdown of ATG8f or NBR1 in *Nicotiana benthamiana* led to decreased TBSV and CIRV replication, suggesting pro-viral function of selective autophagy in tombusvirus replication. Co-opting the above autophagy proteins into the VROs resulted in reduced autophagic flux, suggesting that tombusviruses regulate the autophagy pathway in plants. We observed that a fraction of the usurped ATG8f or NBR1 formed biomolecular condensates associated with VROs, likely trapping those proteins away from the general autophagy pathway. Overall, tombusviruses hijack selective autophagy to provide phospholipid-rich membranes for replication and to regulate the antiviral autophagic flux.

### 3.2 Results

**Recruitment of ATG8 into tombusvirus VROs in plants.** To learn if additional autophagy component(s) is usurped by TBSV into VROs, we selected small ubiquitin-like ATG8 key autophagy protein, based on the ability of ATG8 to bind most cargo receptors and core autophagy proteins (163). Confocal imaging showed that co-expression of GFP-tagged ATG8f2 (called ATG8f hereafter) with BFP-tagged TBSV p33 replication protein and RFP-SKL peroxisomal marker protein in *N. benthamiana* cells infected with TBSV led to the accumulation of GFP-ATG8f in TBSV VROs. Higher magnification of the images showed that GFP-ATG8f partially co-localized with the TBSV p33 replication

protein in the VRO representing clustered peroxisomes (Fig 3.1A, top panels). GFP-ATG8f also formed small punctate structures within the VROs. Induction of autophagy via darkness treatment of *N. benthamiana* plants (168) did not interfere with the recruitment of GFP-ATG8f into VRO (Fig 3.1A, middle panels). However, we noted ~4-fold increased number of small punctate structures containing GFP-ATG8f within the VROs after darkness treatment. GFP-ATG8f was localized in the cytosol of *N. benthamiana* cells in the absence of TBSV infection (Fig 3.1A).

Confocal microscopy-based experiments showed that the closely-related CIRV, which usurps clustered mitochondria for replication, co-opted GFP-ATG8f into VROs marked with the CIRV p36-BFP replication protein and RFP-Tim21 mitochondrial membrane protein (Fig 3.1B, top panels). After darkness treatment of *N. benthamiana*, the localization pattern of GFP-ATG8f within the CIRV VROs was similar to the pattern observed with TBSV VROs (compare Fig 3.1A and 3.1B). Also, we counted ~4-fold increased number of small punctate structures containing GFP-ATG8f within the CIRV VROs after darkness treatment.

To test if additional members of the ATG8 protein family were also co-opted by TBSV, we selected ATG8a and ATG8i. Interestingly, both GFP-ATG8a and GFP-ATG8i were usurped into TBSV and CIRV VROs, forming small number of punctate structures (Fig 3.1C and S3.1A-C Fig). We also found that the minus stranded replicon RNA, which is the replication intermediate and marks the site of virus replication (104, 169) was co-localized with p33 replication protein and ATG8a in the replication compartment in *N. benthamiana* replicating the closely-related cucumber necrosis (CNV) helper virus, which supplied the RdRp (S3.2 Fig). Therefore, we suggest that ATG8a is recruited to VROs that



are active in viral RNA synthesis. Based on these experiments, we conclude that ATG8 autophagy-related proteins are efficiently recruited by tombusviruses to VROs in *N. benthamiana*.

To test if additional core autophagy proteins were recruited into tombusvirus VROs, we performed confocal microscopy experiments, which revealed that GFP-ATG4, GFP-ATG1a, GFP-ATG101, and GFP-ATG5 core autophagy proteins were co-localized with TBSV p33 replication proteins within VROs marked by RFP-SKL peroxisomal marker (S3.3 Fig). We also tested the plant specific autophagy adaptor protein SH3P2, a BAR domain protein, which participates in membrane deformation of phagophore assembly site (170, 171). Moreover, SH3P2 is targeted by the *Xanthomonas* effector protein, XopL, for degradation to suppress autophagy (172). Interestingly, GFP-SH3P2 is re-localized to the VROs in the presence of p33 replication protein (S3.3 Fig). Taken together, several autophagy proteins are re-localized to TBSV VROs, suggesting that TBSV hijacks the autophagy machinery in plant cells.

**Tombusvirus replication proteins interact with ATG8 in plants.** To test if the TBSV p33 replication protein interacts with ATG8f, bimolecular fluorescence complementation (BiFC) experiments were conducted in *N. benthamiana* leaves. The BiFC signals revealed specific interaction between TBSV p33 replication protein and ATG8f and the interaction occurred in the VROs marked with RFP-SKL peroxisomal marker (Fig 3.2A, and the bottom panel for the negative control experiment). BiFC assays showed that the CIRV p36 replication protein interacted with ATG8f within the VROs (Fig 3.2B). Similar experiments also showed interactions between the TBSV p33 or CIRV p36

replication proteins and ATG8a (Fig 3.2C), and TBSV p33 or CIRV p36 and ATG8i (S3.1D Fig) in VROs. Thus, bulk of the interactions between the tombusviral replication proteins and ATG8 takes place within the VROs in *N. benthamiana*.

To confirm interactions between the TBSV p33 replication protein and ATG8f, we performed protein proximity-labeling approach. This was based on *E. coli*-derived BirA biotin-ligase and Avi tag, which serves as a biotin acceptor peptide (119, 120). The BirA was fused to p33, which targets the fusion protein to VROs (167). The Avi tag was fused to ATG8f to monitor proximity to p33-BirA in plant cells. Co-expression of p33-BirA and Avi-ATG8f in *N. benthamiana* led to biotinylation of Avi-ATG8f (Fig 3.2D, lanes 1-2). Co-expression of Myc-tagged p33 (absence of the BirA fusion), and Avi-ATG8f did not lead to its biotinylation in *N. benthamiana*, thus excluding endogenous biotin ligase activity in plant (Fig 3.2D, lanes 3-4). GFP-BirA was expressed in *N. benthamiana* to measure basal level of biotinylation of Avi-ATG8f (Fig. 3.2D. lanes 8-10). Altogether, the above data confirm the close proximity of ATG8f autophagy protein to the tombusvirus p33 replication protein in plant cells.

To further confirm interactions between the TBSV p33 replication protein and ATG8, we performed three additional assays. The first one was based on affinity-purification of Flag-p33 from detergent-solubilized membrane fraction of plants expressing YFP-ATG8f (Fig 3.2E) or His<sub>6</sub>-ATG8a (S3.4A Fig) (104). The negative control was plants expressing His<sub>6</sub>-p33 and YFP-ATG8f or His<sub>6</sub>-ATG8a. The second interaction assay was a pull-down assay with MBP-tagged p33 or MBP-p36 and GST-6xHis-tagged ATG8a purified from *E. coli* (Fig 3.2F). For the pulldown assay, we used N-terminally truncated TBSV p33 and CIRV p36 replication proteins lacking their membrane-binding

regions to aid their solubility in *E. coli*. Altogether, the pulldown data suggest that the replication proteins of TBSV and CIRV use their C-terminal domains facing the cytosolic compartment to directly interact with ATG8a protein *in vitro*. Additional pulldown experiments also showed that the very N-terminal region of TBSV p33 (1-82 aa, lacking the membrane-binding regions) bound with ATG8f (S3.4B Fig). Mutagenesis of the predicted ATG8-binding motif (AIM1) within the N-terminal region did not completely eliminate binding to ATG8f, whereas deletion of the N-terminal 36 aa eliminated binding to ATG8f (S3.4B Fig). These data suggest that p33 sequences outside of AIM1 contribute to binding to ATG8f. The third interaction assay was based on the split-ubiquitin-based membrane yeast two-hybrid assay (MYTH) (173). We found that both ATG8a protein and the yeast ScATG8 protein interacted with the full-length TBSV p33 replication protein in yeast (S3.4C Fig).

Protein proximity-labeling also showed close proximity of ATG4, ATG101 and ATG5 autophagy proteins to the tombusvirus p33 replication protein in plant cells (S3.5A Fig). We confirmed the interactions of ATG4, ATG5 and ATG101 with the TBSV p33 replication protein using affinity-purification of Flag-p33 from detergent-solubilized membrane fraction of plants (S3.5B Fig). BiFC studies demonstrated interactions between TBSV p33 and SH3P2 autophagy adaptor protein and ATG8f and SH3P2 in the VROs (S3.6A-B Fig). These data suggest that the TBSV p33 replication protein actively recruits several autophagy proteins via protein-protein interactions into VROs.

**ATG8 autophagy protein facilitates tombusvirus replication in plants.** The robust recruitment of ATG8 autophagy protein into VROs might have an effect on

tombusvirus replication. To test this possibility, we silenced ATG8f expression using virus-induced gene-silencing (VIGS) in *N. benthamiana* plants. The region selected in NbATG8f was specific to the highly similar f1 and f2 members of the ATG8 gene family. Knockdown of ATG8f in *N. benthamiana* led to ~3-fold reduction of TBSV and the closely related cucumber necrosis virus (CNV<sup>20KStop</sup>, which does not express the gene silencing suppressor protein) replication, and ~6-fold reduction of CIRV RNA accumulation in the inoculated leaves (Fig 3.3A-C). Knockdown of ATG8f level did not cause obvious phenotype in *N. benthamiana*. Silencing of ATG8f expression did not affect the expression of ATG8a or ATG8i (S3.7 Fig). Knockdown of ATG8a in *N. benthamiana* plants also reduced TBSV RNA accumulation by >2-fold (Fig 3.3D), whereas knockdown of ATG8i did not have much effect on TBSV replication (S3.1E Fig). Based on the most pronounced effect of ATG8f knockdown on tombusvirus replication, we focused on ATG8f in subsequent studies.

To test if ATG8f expression is affected during TBSV infection in *N. benthamiana* plants, RT-qPCR analysis was performed. Comparison of ATG8f mRNA levels in TBSV-infected versus mock-treated *N. benthamiana* leaves revealed 2-fold up-regulation of ATG8f mRNA level in the TBSV inoculated leaves 2 days after inoculation (dpi) (Fig 3.3E). Interestingly, ATG8f mRNA level was ~20-fold higher in systemically-infected leaves in comparison with similar leaves in the control uninfected plants (Fig 3.3E). These data indicate that TBSV replication induces high level expression of ATG8f in *N. benthamiana* plants.

During autophagy process, ATG8 becomes lipidated by the ATG12-ATG5-ATG16 complex, making ATG8-PE (phosphatidylethanolamine), which is membrane bound and

shows enhanced activities (163). To test if ATG8 lipidation is important during TBSV infections, we knocked down ATG5 via VIGS in *N. benthamiana*. TBSV RNA accumulation was reduced by ~4-fold in ATG5 knockdown plants (Fig 3.3F), suggesting a role of ATG8 lipidation in TBSV replication. To test the combined role of the ATG8 family members and ATG8 lipidation in TBSV replication, we expressed RavZ protease, which is an effector protein from *Legionella* bacterium (174, 175). RavZ has been shown to cleave lipidated LC3 (an ATG8 ortholog) of the mammalian host, effectively destroying LC3/ATG8 function in autophagy (174, 175). We confirmed that expression of RavZ protease inhibited general autophagy in *N. benthamiana* based on ‘free’ GFP analysis using GFP-ATG8f (Fig 3.3G, lane 2 versus 4). This assay is based on that autophagy pathway sends GFP-ATG8f into the vacuole for degradation. However, the GFP portion of the fusion protein is relatively stable in the vacuole and the protease-driven degradation process results in the release of ‘free’ GFP from the fusion protein, which can be detected via western blotting (176). In addition, expression of RavZ eliminated the ATG8f-PE form in plant cells (Fig 3.3H, lanes 1-2 versus 3-4). We found that expression of RavZ inhibited TBSV replication by >2-fold in *N. benthamiana* (Fig 3.3I). Altogether, the above data confirmed that ATG8 members, especially ATG8f, play pro-viral roles in tombusvirus replication in plants. Moreover, the inhibitory effect of RavZ effector expression on TBSV replication also supported the role of lipidated ATG8.

**NBR1 selective autophagy receptor is recruited into TBSV VROs.** Because ATG8 participates in both bulk and selective autophagy pathways (163), we tested if TBSV usurps NBR1 selective autophagy receptor (149, 166, 177) into VROs. Confocal imaging

showed that co-expression of eGFP-NBR1 with BFP-tagged TBSV p33 replication protein and RFP-SKL peroxisomal marker protein in *N. benthamiana* cells infected with TBSV led to the accumulation of eGFP-NBR1 in TBSV VROs (Fig 3.4A). Interestingly, eGFP-NBR1 formed different patterns within the VROs. These included small punctate structures within the TBSV and CIRV VROs (Fig 3.4A-B), similar to those seen with ATG8f (Fig 3.1A). Several puncta showed the co-localization of eGFP-NBR1 with the replication proteins (see enlarged panel Fig 3.4A-B), whereas other puncta were enriched with mostly eGFP-NBR1. eGFP-NBR1 also formed larger puncta, which did not co-localize with p33 replication protein, but were associated with the VROs (Fig 3.4A, central panel). BiFC experiments showed interaction between TBSV p33 and NBR1 within the VROs (Fig 3.4C). Two types of patterns were present in BiFC images, one forming mostly circles around the peroxisomes (top image, Fig 3.4C) and the other type showing small puncta (bottom image, Fig 3.4C). To confirm interactions between the TBSV p33 replication protein and NBR1, we performed protein proximity-labeling approach with p33-BirA and Avi-NBR1. Co-expression of p33-BirA and Avi-NBR1 in *N. benthamiana* led to biotinylation of Avi-NBR1 (S3.5 Fig, lanes 13-14). Co-expression of Myc-tagged p33 (absence of the BirA fusion), and Avi-NBR1 did not lead to its biotinylation in *N. benthamiana* (S3.5 Fig, lanes 15-16). Altogether, the above data confirm the close proximity of NBR1 selective autophagy receptor to the tombusvirus p33 replication protein in plant cells. Interaction between CIRV p36 replication protein and NBR1 was also observed by BiFC (Fig 3.4D). These data support the model that TBSV and CIRV hijack NBR1, and the selective autophagy.

NBR1 is known to interact with ATG8f in plant cells (149, 177). Indeed, we observed that eGFP-NBR1 co-localized with RFP-ATG8f and p33-BFP replication protein in small puncta within the VROs (Fig 3.5A). Using BiFC by co-expressing nYFP-NBR1 and cYFP-ATG8f in *N. benthamiana* infected with TBSV, we found that the co-opted NBR1 and ATG8f interacted within the VROs marked with TBSV p33-BFP (Fig 3.5B). Interestingly, the interacting eGFP-NBR1 and RFP-ATG8f were mostly present in punctate structures associated with the VROs. Moreover, when eGFP-NBR1 and RFP-ATG8f together formed larger puncta, then p33 replication protein and the co-opted peroxisomes seemed to be excluded from the puncta. However, the puncta and the co-opted peroxisomes were always located in close vicinity within the VROs (Fig 3.5B). This suggests maturation of eGFP-NBR1 and RFP-ATG8f puncta into “bodies” sequestering eGFP-NBR1 and RFP-ATG8f within VROs.

To test if ATG8f affects the recruitment of NBR1 into the VROs, we knocked down ATG8f levels via VIGS in *N. benthamiana* infected with TBSV. Confocal microscopy analysis showed that eGFP-NBR1 was efficiently recruited into the VROs marked either by p33-BFP or RFP-SKL in ATG8f knockdown cells (Fig 3.6A). Expression of RavZ protease, which eliminates ATG8-PE (Fig 3.3H), did not interfere with the subversion of NBR1 to the TBSV VROs (Fig 3.6B). Knocking down NBR1 levels via VIGS in *N. benthamiana* infected with TBSV did not seem to inhibit the recruitment of GFP-ATG8f into VROs (Fig 3.6C). Expression of RavZ protease did not interfere with the subversion of ATG8f to the TBSV VROs (S3.8 Fig), suggesting that TBSV p33 could recruit the nonlipidated ATG8f to the VROs. Thus, NBR1 and ATG8f are co-opted by p33 replication

protein seemingly separately into VROs. However, we cannot exclude that the co-opted NBR1 and ATG8f is recruited as a complex by p33 into VROs in WT plants.

**The co-opted NBR1 autophagy receptor promotes tombusvirus replication in plants.** Knockdown of NBR1 in *N. benthamiana* via VIGS resulted in ~2-fold decrease in TBSV replication and >3-fold reduction of CIRV RNA accumulation in the inoculated leaves (Fig 3.7A-B). Knockdown of NBR1 mRNA level did not cause phenotype in *N. benthamiana*. These experiments suggest that subversion of NBR1 by p33 has a pro-viral role in tombusvirus replication in plants.

To test if TBSV infection affects NBR1 expression in *N. benthamiana* plants, we used RT-qPCR analysis, which showed increased production of NBR1 mRNA at 48 h post inoculation in comparison with mock-treated *N. benthamiana* leaves (Fig 3.7C). These data suggest that TBSV replication induces NBR1 expression in *N. benthamiana* plants.

**Enrichment of PE in TBSV VRO membrane is affected by ATG8 and NBR1.** We have previously shown that TBSV induces the remarkable enrichment of PE within membranes of VROs (25). To determine if ATG8 and the selective autophagy pathway plays a role in PE enrichment within VROs, we tested PE distribution in ATG8f and NBR1 knockdown *N. benthamiana* protoplasts (single cells without the cell wall) infected with TBSV. Confocal microscopy was used to detect the subcellular distribution of PE by applying biotinylated duramycin peptide and streptavidin conjugated with Alexa Fluor 405 (25, 92). Interestingly, PE enrichment was low within TBSV VROs in ATG8f knockdown protoplasts (Fig 3.8A), whereas PE was highly enriched within VROs in control protoplasts



(Fig 3.8A). To confirm the role of ATG8 in PE-enrichment in TBSV VROs, we expressed RavZ protease in *N. benthamiana* infected with TBSV. Confocal microscopic analysis of protoplasts expressing RavZ protease showed reduced enrichment of PE within the TBSV VROs (Fig 8A). NBR1 knockdown also reduced PE enrichment within TBSV VROs in protoplasts (Fig 3.8B). Altogether, these data support the role of ATG8f and NBR1 and the selective autophagy pathway in PE enrichment within TBSV VRO membranes in *N. benthamiana*. Thus, TBSV utilizes the selective autophagy pathway to contribute PE and membranes to the biogenesis of VROs in plants.

**Enrichment of PI(3)P within the TBSV replication compartment is affected by ATG8 and NBR1.** Previously, we have shown that TBSV infection induces the production and enrichment of PI(3)P within VRO membranes, which facilitates viral replication (9, 32, 117). The autophagic membranes are enriched in PI(3)P (163, 178). Therefore, we tested if recruitment of ATG8 or NBR1 by the TBSV p33 replication protein could affect enrichment of VRO membranes with PI(3)P. ATG8f level was knocked down via VIGS and the accumulation of PI(3)P was determined in *N. benthamiana* protoplasts infected with TBSV. In comparison with the control protoplasts, PI(3)P accumulation within the TBSV VROs was poor (barely detectable) in ATG8f silenced protoplasts (Fig 3.9A). We also expressed RavZ protease to destroy ATG8 activities in *N. benthamiana* infected with TBSV, followed by detecting PI(3)P accumulation using RFP-2xFYVE biosensor in VROs. RFP-2xFYVE selectively binds to PI(3)P in cells, including plant cells (9, 179). RavZ expression inhibited the accumulation of PI(3)P in TBSV VROs, confirming the role

of ATG8 in facilitating PI(3)P production in TBSV VROs (Fig 3.9B). NBR1 knockdown also reduced PI(3)P accumulation within TBSV VROs in protoplasts (Fig 3.9C).

**ATG8f promotes the recruitment of VPS34 PI3 kinase into VROs.** VPS34 PI(3) kinase is recruited to autophagic membranes to produce PI(3)P from PI phospholipid (163). TBSV has been shown to hijack VPS34 into VROs to produce PI(3)P (9, 32). Usurping ATG8 and the selective autophagy pathway might be one of the ways for TBSV to efficiently co-opt the cytosolic VPS34. This idea was tested by co-expressing GFP-VPS34 and p33-BFP in ATG8f knockdown *N. benthamiana* infected with TBSV. Quantification of fluorescent signals in VROs by confocal microscopic analysis revealed reduction in VPS34 amount in ATG8f knockdown *N. benthamiana* in comparison with the control plants (Fig 3.10A-B). We also conducted BiFC experiments between nYFP-VPS34 and p33-cYFP in ATG8f knockdown plants. Interestingly we observed ~40% decrease in the BiFC signals in ATG8f knockdown versus control plants (Fig 3.10C-D). These findings support the role of ATG8f and the autophagy pathway in subversion of VPS34 PI3K by TBSV in *N. benthamiana*. Yeast has only one ATG8 gene and we used the null mutant (*atg8Δ*) to purify Flag-p33 from the detergent-solubilized membrane fraction. Interestingly, the co-purified HA-tagged VPS34 was ~4-fold less from *atg8Δ* yeast than from the WT yeast (Fig 3.10E, lanes 2-3 versus 1). This finding further supports the role of autophagy pathway in subversion of VPS34 PI3K by TBSV.

**Tombusvirus replication protein inhibits autophagic flux in *N. benthamiana*.**

Hijacking of ATG11 (167), NBR1, ATG8 and VPS34 and several other key autophagy

components by tombusviruses into VROs might affect the autophagy pathway in infected cells. On the other hand, viral proteins are known to induce autophagy, leading to their degradation (180). To test these possibilities, we expressed p33-GFP and followed its degradation in *N. benthamiana*. However, we did not detect the released ‘free’ GFP derived from p33-GFP in *N. benthamiana* (Fig 3.11A, lane 2). This suggests that p33 does not induce the complete autophagy pathway and p33 is not a substrate of autophagy under the conditions used. Accordingly, inhibition of autophagic degradation via ConA or E64d treatments did not alter p33 levels in *N. benthamiana* (Fig 3.11B). To test if induced bulk autophagy pathway could target p33 replication protein, we applied darkness treatment of plants (168) expressing p33-GFP. Interestingly, p33 was a poor autophagy substrate even under induced conditions in *N. benthamiana* (Fig 3.11A, lanes 3-4). In contrast, the control eGFP-ATG8f was a good autophagy substrate after darkness treatment of *N. benthamiana* expressing eGFP-ATG8f (Fig 3.11A, lane 1). To further test the effect of tombusviruses on the autophagy pathway, we infected *N. benthamiana* expressing eGFP-ATG8f with TBSV or the closely-related CNV. Interestingly, autophagic degradation of eGFP-ATG8f was not observed (Fig 3.11C, lanes 1 versus 4; Fig 3.11D, lanes 1 versus 5) suggesting that TBSV and CNV infections poorly induced the complete autophagy pathway in *N. benthamiana*. The basal level of autophagic flux was low in *N. benthamiana* without darkness treatment (Fig 3.11C, lanes 1 versus 2 and 3; Fig 3.11D, lanes 1 versus 2-4). To test the possible effect of tombusviruses on the autophagy pathway, we induced autophagy via darkness or AZD8055-treatment (181) of *N. benthamiana* expressing eGFP-ATG8f and infected with either TBSV or CNV. Interestingly, reduced autophagic degradation of eGFP-ATG8f was observed in CNV or TBSV-infected versus non-infected plants (Fig

3.11C-D). To identify which TBSV proteins inhibit the autophagic degradation of eGFP-ATG8f, we expressed p33 and p92 replication proteins together with DI-72 replicon RNA, and separately, the coat protein and the movement protein of TBSV in *N. benthamiana* followed by darkness treatment. These experiments revealed that only the replication system inhibited the autophagic degradation of eGFP-ATG8f (Fig 3.11E).

We also performed another assay, which is based on lipidation of ATG8. Conjugation of ATG8 with PE is needed for the autophagy pathway (163). The ATG8f lipidation assay revealed that expression of p33 replication protein or TBSV infection of *N. benthamiana* reduced ATG8f-PE conjugation by ~2-fold (Fig 3.11F), suggesting that TBSV infection interferes with the activation of autophagy to some extent.

We also observed that autophagy-driven degradation of eGFP-NBR1 was inhibited in TBSV-infected *N. benthamiana* (Fig 3.12A). Autophagic flux was also inhibited by TBSV in NBR1 knockdown plants (Fig 3.12B). However, the inhibition of autophagic flux by TBSV was less pronounced than in the control plants, suggesting that inhibition of autophagic flux by TBSV requires NBR1. Similarly, ATG8f lipidation assay revealed that TBSV infection of NBR1 silenced *N. benthamiana* reduced ATG8f-PE conjugation to lesser extent than in control plants (Fig 3.12C). Altogether, these data suggest that hijacking of NBR1 by TBSV facilitates the inhibition of autophagy. It is likely that hijacking NBR1 (single gene) is more robust than the efficient hijacking of the ATG8 family (multiple genes) by the TBSV p33, which might explain why TBSV targets NBR1 selective autophagy receptor to inhibit selective autophagy.

**The co-opted ATG8f and NBR1 are present in biomolecular condensates associated with TBSV VROs.** We frequently observed round shaped puncta formed by ATG8f and NBR1 associated with TBSV or CIRV VROs in confocal images of plant cells (Fig 3.1 and 3.5A). Frequent round shaped puncta were also found using BiFC based on ATG8f and NBR1 (Fig 3.5B) in TBSV-infected cells. It is known that LC3/ATG8 and p62/NBR1 form condensates under some conditions (182). Therefore, we performed FRAP experiments on plant cells infected with TBSV. *N. benthamiana* also co-expressed eGFP-NBR1 and RFP-ATG8f and TBSV p33-BFP to mark the VROs. After photobleaching a portion of the VROs, we followed the recovery of fluorescent signals within the bleached area. As expected, the fluorescent signal for the membrane-bound p33-BFP did not recover (Fig 3.13A). This is likely due to limited movement of p33 anchored to the VRO membrane. On the other hand, the fluorescent signals for both eGFP-NBR1 and RFP-ATG8f in VROs were partially recovered after 180 sec (Fig 3.13A). The fluorescent signals for both eGFP-NBR1 and RFP-ATG8f, when they formed larger puncta associated with VROs, were also partially recovered after 180 sec (S3.9A Fig). The fluorescent signals were also partially recovered after 180 sec when RFP-ATG8f and eGFP-NBR1 were expressed separately in *N. benthamiana*, which also expressed p33-BFP (S3.9B-C Fig). These findings could be explained that a significant fraction of eGFP-NBR1 and RFP-ATG8f molecules are present in condensates within the VROs, which allow some internal molecular movement. Interestingly, fluorescent signals for other co-opted core autophagy proteins, such as ATG4, ATG5 and ATG101, were also partially recovered in 60-180 sec after photobleaching of portions of VROs (S3.10 Fig). The only exception was ATG1a, whose fluorescent signal was not recovered in VROs (S3.10 Fig). Thus, co-opted core

autophagy proteins seem to be present and sequestered in condensate-like substructures in VROs.

We also performed FRAP experiments in combination with BiFC between nYFP-NBR1 and cYFP-ATG8f in plant cells infected with TBSV. The VROs were marked with p33-BFP. Interestingly, the BiFC signals within the VROs were partially recovered after 180 sec (Fig 3.13B). This suggests that NBR1 and ATG8f are present in the same condensates within the VROs. Treatment of condensates with 1,6-hexanediol disrupts weak hydrophobic interactions, which could dissolve condensates (183, 184). We found that treatment of plant cells infected with TBSV by 1,6-hexanediol partially dissolved the punctate structures containing NBR1 and ATG8f within the VROs (Fig 3.13C). On the contrary, 1,6-hexanediol treatment did not significantly affect the distribution of membrane-bound p33 within the VROs (Fig 3.13C). In the negative control experiments, treatment of plants cells with digitonin did not affect the punctate structures containing NBR1 and ATG8f within the VROs (Fig 3.13C). Overall, these results may suggest that a significant portion of NBR1 and ATG8f is sequestered within condensate-like substructures within the TBSV VROs.

### 3.3 Discussion

**A complex interplay between selective autophagy and the tombusvirus replication protein supports VRO biogenesis.** VRO biogenesis, which is the central step in tombusvirus replication, is a complex process depending on multiple interactions between tombusvirus and its host (80, 96, 127). The master regulator and major driver of VRO biogenesis is the TBSV p33 replication protein, which subverts many co-opted host

proteins and subcellular membranes (32, 39, 40, 92, 128). The list of subverted proviral host factors now includes several autophagy proteins. VIGS-based knockdown of ATG8f and ATG5 core autophagy proteins and NBR1 selective autophagy receptor demonstrated the dependency of TBSV and the closely related CIRV replication on autophagy. We showed that the efficient recruitment of ATG8f and NBR1 by p33 replication protein into VROs contributed/enriched important lipids, such as PE and PI(3)P and VPS34 PI3K, to the VRO membranes. We have shown previously that these lipids are critical for spherules formation, the sites of viral replication, in host cells (9, 25, 32, 92, 185). The autophagy membranes are enriched in PE and PI(3)P (178). Interestingly, TBSV also hijacks Rab5-positive endosomes and retromer tubular vesicles to further increase PE and PI(3)P lipids in VRO membranes (9, 25, 32, 92, 185). Subversion of multiple pathways and vesicles by TBSV to build VRO membranes seems to be necessary for robust and efficient viral replication. In addition, hijacking multiple pathways by TBSV could be advantageous in different hosts and cells, which could differ in various lipid resources.

Although TBSV usurps lipids from the autophagy membranes, we think it is unlikely that TBSV directly utilizes the double-membrane autophagy compartment for virus replication. Numerous previous publications showed that TBSV and other tombusviruses use either the limiting membrane of peroxisomes or the outer mitochondrial membrane for virus replication (39, 75, 96, 186-191). We propose that TBSV hijacks the autophagosome lipids/membranes during the early membrane expansion phase and repurposes the lipids for membrane proliferation in VROs.

**Subversion of ATG8f and NBR1 by p33 replication protein leads to reduced autophagy flux during virus replication.** The emerging picture from this work is that, by usurping ATG8f and NBR1 and other autophagy components, such as ATG1a, ATG4, ATG5, ATG101 and SH3P2, TBSV inhibits the autophagic flux in plants. Accordingly, we found that p33 replication protein was not prone to degradation by autophagy. Moreover, p33 expression or TBSV infection inhibited the autophagic degradation of ATG8f and NBR1 under induced conditions (darkness or AZD8055 treatments of plants). In addition, TBSV moderately inhibited the lipidation of ATG8f, which is needed for the autophagy pathway (163). Yet, we found that TBSV replication depended on the lipidation of ATG8f, based on (i) expression of RavZ protease that eliminated the lipidated form of ATG8 and inhibited TBSV replication; (ii) knockdown of ATG5, which is part of the ATG12-ATG5-ATG16 complex that lipidates ATG8s, also resulted in inhibition of TBSV replication. Thus, it seems that TBSV regulates the activity of the autophagy pathway to provide lipid/membrane resources for VRO biogenesis without turning on the antiviral activity of autophagy (Fig 3.14).

**ATG8f and NBR1 are sequestered by p33 replication protein into condensates associated with VROs during virus replication.** How can TBSV inhibit the activation of the antiviral selective autophagy? We observed that a large fraction of ATG8f and NBR1 autophagy receptor was sequestered into small punctate structures within the VROs. FRAP analysis showed the partial fluorescent signal recovery for ATG8f and NBR1, but not for the membrane-anchored p33 replication protein, within the VROs. The fluorescent signal recovery for ATG8f also suggests that ATG8f is not lipidated within the puncta since



membrane association would significantly limit the movement of ATG8f-PE within the VROs. We also found that the co-opted ATG8f and NBR1 interacted with each other within the puncta in VROs. Therefore, the emerging picture is that TBSV sequesters and “traps” the inactive ATG8f and NBR1 and other co-opted core autophagy proteins within condensates associated with VROs to regulate the autophagy pathway in *N. benthamiana* (Fig 3.14). Moreover, it seems that overexpression of NBR1 promoted the ‘trapping’ of ATG8f in large puncta within VROs.

We previously demonstrated that the TBSV p33 and the CIRV p36 replication proteins organize condensate formation by co-opted cytosolic proteins, such as glycolytic and fermentation enzymes and the proteasomal RPN11 protein interaction ‘hub’ within the VROs. The p33 replication protein organized condensate substructure co-exists with the membranous substructure within the VROs. These substructures are likely hold together by the co-opted ER membranes and actin filaments, which form meshwork in the VROs. We propose that the co-opted autophagy proteins are also sequestered into the condensate substructure of the VROs, not inside the spherules (Fig 3.14). Altogether, sequestration of autophagy proteins in condensates associated with VROs might explain the inhibitory effect of TBSV infection on the autophagy pathway.

Interestingly, SARS-CoV-2 also induces condensates containing p62 (similar functions to the plant NBR1) and trapping selective ER-phagy receptors via the viral ORF8 protein (192). The ORF8/p62 condensate formation leads to inhibition of ER-phagy and increased viral replication. In uninfected cells, the p62 condensate (also called p62 body) contains ubiquitinated cargoes and is degraded by autophagy to maintain cellular homeostasis (62, 182, 193, 194). Several negative-strand RNA viruses replicate in

membraneless condensates formed by replication proteins and viral RNA in addition to co-opted host proteins (195-197). Condensates formation is also observed during immune responses against infecting viruses (197-200). Plant RNA virus movement depends on condensate formation (201). Plant potyviruses induce RNA granules to facilitate virus replication (202). Therefore, it seems that several RNA viruses exploit condensates for various viral functions.

Altogether, tombusviruses hijack the selective autophagy pathway in order (i) to enrich PE and PI(3)P lipids and VPS34 PI3K in VROs; (ii) to inhibit the antiviral autophagic flux; and (iii) to sequester and trap ATG8 and NBR1 in condensates associated with VROs. Overall, tombusviruses exploit autophagy for pro-viral functions. Other viruses also exploit autophagy for viral replication. Turnip mosaic virus co-opts NBR1, ATG8f and TIP1, which allows the viral replicase to associate with the tonoplast membrane to promote viral replication (145). Zika virus and Dengue virus were shown to induce lipophagy and suppress ER-phagy by cleaving the ER-phagy receptor (FAM134B) (203, 204). Coronaviruses, enteroviruses and hepatitis C virus induce autophagy to hijack the double-membrane autophagosomes for replication or virion assembly (205). The most frequent cases of viral exploitation of autophagy are based on viral protein-driven degradation of antiviral proteins, such as AGO1, suppressor of gene silencing 3 (SGS3) or SGS3/RDR6 bodies (159, 206-208). The emerging picture is that the interplay between autophagy and viruses is amazingly diverse, indicating forever lasting arms race between viruses and their hosts.

### 3.4 Materials and methods

**Plant materials and plasmids.** Wild type *N. benthamiana* plants were potted in soil and placed in growth room at 25°C under a 16 h light/8 h dark cycle. The nucleotide sequences of *N. benthamiana* genes NbATG5 (KX369397.1), NbATG8a (KX120976), NbATG8f2 (MG733107) and NbNBR1 (MG710800) were downloaded from NCBI GenBank. Total RNA extraction from *N. benthamiana* leaves was used for gene amplification. Reverse transcription was performed with Moloney Murine Leukemia Virus Reverse Transcriptase (M-MLV RT) (Promega) with Oligo(dT). Plasmids constructed (Table 3.1) plasmids from previous works (Table 3.2) and primers used in this study are listed in (Table 3.3).

**Virus replication in plants.** Virus induced gene silencing (VIGS) in *N. benthamiana* was performed as described in (133). The cDNA of NbATG8f2 5'-terminal fragment of 205 bp in length (#8554: CGGGATCCATGGCTAAGAGCTCATTCAAG and #8576: CCGCTCGAGCTCAATTTGATTCTCTTGCG) was selected to insert into TRV2 vector, to generate pTRV2-NbATG8f, which was used for VIGS in *N. benthamiana*. *Agrobacterium* competent cells C58C1 were transformed with pTRV2-NbATG8f. *N. benthamiana* plants of 4-leaves stage were agroinfiltrated with pTRV1 and pTRV2-NbATG8f or pTRV2-cGFP as a control (OD<sub>600</sub> 0.5). On the 9th day post agroinfiltration (dpi), upper leaves were agroinfiltrated to express CNV<sup>20kstop</sup> or inoculated with TBSV or CIRV saps (16). To determine RNA accumulation of TBSV, CNV, and CIRV, the inoculated leaves were collected at 2, 2.5 and 3 dpi, respectively. Total RNA extraction and northern blot analyses were performed as described previously (16). The

transcriptional accumulation of NbATG8 mRNA and internal reference control tubulin mRNA was determined by semi-quantitative RT-PCR with primers oligo-d(T) (for RT), #8554 and #8555 (for PCR to detect NbATG8f) and #2859 and #2860 (for PCR to detect tubulin mRNA) (16, 167).

To analyze the function of NbATG8a in tombusvirus replication, the 5'-terminal fragments of 224 bp in length (#7877: ACGCGGATCCATGGCCAAAAGCTCCTTCAAATTGG and #8575: CCGCTCGAGTTCTCAGCACTAAGCTTT) was selected to insert into TRV2 vector, to generate pTRV2-NbATG8a, which was used for VIGS in *N. benthamiana*. Agrobacterium competent cells C58C1 were transformed with pTRV2-NbATG8a. *N. benthamiana* plants of 4-leaves stage were agroinfiltrated with pTRV1 and pTRV2-NbATG8a or pTRV2-cGFP as a control (OD<sub>600</sub> 0.5). On the 9th day post agroinfiltration, the upper leaves were infiltrated with agrobacterium harboring virus infectious clone CNV20k<sup>stop</sup> or inoculated with TBSV or CIRV sap. Total RNA extraction and northern blot analyses were described above.

To analyze the function of NbNBR1 in tombusvirus replication, the fragment of 400 bp in length (#8580: CGGGATCCATAGTGGGGAGGAGAAGG and #8581: CCGCTCGAGTGACCCCTTTTATATGGG) was inserted into the TRV2 vector to generate pTRV2-NbNBR1, which was used for VIGS in *N. benthamiana*. Agrobacterium competent cells C58C1 were transformed with pTRV2-NbNBR1. *N. benthamiana* plants of 4-leaves stage were agroinfiltrated with pTRV1 and pTRV2-NbNBR1 or pTRV2-cGFP as a control (OD<sub>600</sub> 0.5). On the 9th day post agroinfiltration, the upper leaves were

inoculated with TBSV or CIRV sap. Total RNA extraction and northern blot analyses were described above.

To analyze the function of NbATG5 in tombusvirus replication the NbATG5 3'-terminal fragment of 384 bp in length (#7749: CCGCTCGAGCTTACATAAACAGACCTG and #7750: CGGGATCCATATGGTGATGGGTTCTTG) to insert into TRV2 vector, to generate pTRV2-ATG5, which was used for VIGS in *N. benthamiana*. *N. benthamiana* plants of 4-leaves stage were agroinfiltrated with pTRV1 and pTRV2-NbATG5 or pTRV2-cGFP as a control (OD<sub>600</sub> 0.5). On the 9th day post agroinfiltration, the upper leaves were infiltrated with agrobacterium harboring virus infectious clone CNV20k<sup>stop</sup> or inoculated with TBSV or CIRV sap. Total RNA extraction and northern blot analyses were described above.

**Confocal laser microscope studies in plants.** To analyze the subcellular localization of NbATG8f, NbATG8a and NbNBR1 in the presence or absence of viral components in *N. benthamiana* leaves, pGD-35S-p33-BFP, pGD-35S-C36-BFP, pGD-35S-GFP-NbATG8f, pGD-35S-GFP-NbATG8a, pGD-35S-GFP-NbNBR1, pGD-35S-RFP-SKL (as a peroxisome marker) and pGD-35S-RFP-AtTim21 (as a mitochondrial marker) (92) were transformed into agrobacterium strain C58C1. Then agrobacterium cultures with different combinations were infiltrated into *N. benthamiana* leaves, followed by virus inoculation with TBSV or CIRV sap at 16 h post agroinfiltration. At 2.5 dpai, the agroinfiltrated leaves were subjected to confocal laser microscopy with Olympus FV3000.

To detect interactions between NbATG8f and NbNBR1 and TBSV p33 or CIRV p36 replication proteins, bimolecular fluorescence complementation (BiFC) assay was

performed. pGD-35S-T33-cYFP, pGD-35S-C36-cYFP, pGD-35S-C-cYFP (as a negative control), pGD-35S-nYFP-NbATG8f, pGD-35S-nYFP-NbNBR1, pGD-35S-nYFP-MBP (as a negative control), pGD-35S-RFP-SKL (as a peroxisome marker) and pGD-35S-RFP-AtTim21 (as a mitochondrial marker) were transformed into agrobacterium strain C58C1. The Agrobacterium transformants with different combinations were used to infiltrate *N. benthamiana* leaves. At 2.5 dpai, the agroinfiltrated leaves were subjected to confocal laser microscopy.

To test if NbATG8f interacts with NbNBR1 in the presence or absence of TBSV p33, *N. benthamiana* leaves were co-agroinfiltrated with pGD-35S-nYFP-NbNBR1, pGD-35S-NbATG8f-cYFP, pGD-35S-BFP-p33 and pGD-35S-RFP-SKL. The agroinfiltrated *N. benthamiana* leaves were subjected to confocal laser microscopy at 2.5 dpai.

To observe the subcellular distribution of PE (phosphatidylethanolamine) in plant mesophyll protoplasts, first we silenced ATG8f and NBR1, respectively, in *N. benthamiana* via VIGS as above for 10 d. Then, the top leaves were agroinfiltrated to express p33-RFP (pGD-p33-RFP), p19 (pGD-p19) with or without RavZ expression (128). Protoplasts were isolated from the agroinfiltrated leaves of *N. benthamiana* 2 d later. The protoplasts were fixed with 3.7% paraformaldehyde and stained with duramycin as described previously (25).

To observe the subcellular distribution of PI(3)P (Phosphatidylinositol 3-phosphate) in plant mesophyll protoplasts, protoplasts were isolated from *N. benthamiana* leaves 2 dpi after the agroinfiltration with pGD-p33-BFP, pGD-p19 with or without RavZ. The protoplasts were fixed with 3.7% paraformaldehyde and incubated with purified anti-PI(3)P mouse antibody (Echelon Biosciences Inc. Cat#Z-P003) as described previously

(9). RFP-2xFYVE was used as a PI(3)P biosensor to visualize PI(3)P distribution upon virus replication in plant leaves (32).

To detect interaction of AtVps34 with TBSV p33 replication protein based on BiFC assay, plasmids pGD-35S-T33-cYFP, pGD-35S-nYFP-AtVps34, pGD-35S-RFP-SKL (as a peroxisome marker) were transformed separately into agrobacterium strain C58C1. Mixed agrobacterium cultures were used to infiltrate ATG8f-silenced and control leaves separately (see above). At 2 dpai, the agroinfiltrated leaves were subjected to confocal laser microscopy using the same laser power.

**Protein proximity-labeling assay in plants.** To detect the close proximity of p33 replication protein and NbATG8f in plants, *N. benthamiana* leaves were agroinfiltrated with pGD-p33-His-BirA (OD<sub>600</sub> 0.4), pGD-His-Avi-NbATG8f (OD<sub>600</sub> 0.4) and pGD-P19 (OD<sub>600</sub> 0.1) (120, 167). Agroinfiltration with pGD-P33-Myc (OD<sub>600</sub> 0.4) was used as a control. The infiltrated leaves at 3 dpai were further infiltrated with 50 μM Biotin. Then the infiltrated leaves, after 40 minutes of biotin treatment, were harvested and subjected to protein extraction. Biotinylated His-Avi-NbATG8f protein was detected by western-blotting using Strep-AP (167).

**Protein purification from yeast.** *S. cerevisiae* strain BY4741 (MATa his3Δ1 leu2Δ0 met15Δ0 ura3Δ0) was purchased from Open Biosystems and stored in a -80°C refrigerator. Yeast strain atg8Δ was generated as described previously from the BY4741 parental strain by replacing ATG8 ORF with a hphNT1 cassette sequentially using homologous recombination (131).

For co-purification of VPS34 protein with the TBSV p33/p92 replication proteins from yeasts, plasmids HpGBK-CUP1-Hisp33/Gal-DI-72 and LpGAD-CUP1-His92 (as a control) or HpGBK-CUP1-Flagp33/Gal-DI-72 and LpGAD-CUP1-Flag92 were co-transformed with UpYES-HA-ScVPS34 into yeast strain BY4741 and *atg8Δ*. All transformed yeasts were pre-grown in SC-ULH<sup>-</sup> media supplemented with 2% glucose and 100 μM BCS at 29°C for 16 h. Then, yeast cultures were resuspended in SC-ULH<sup>-</sup> medium supplemented with 2% galactose and 100 μM BCS and grown at 23°C for 24 h, followed by culturing yeast cells in (N<sup>-</sup>) SC-ULH<sup>-</sup> medium supplemented with 2% galactose and 50 μM CuSO<sub>4</sub> at 23°C for 6 h. Finally, yeast pellets were harvested after washing twice with PBS buffer and proteins were Flag-affinity purified as described previously (123).

**Protein purification from *N. benthamiana*.** Various combinations of expression vectors were co-agroinfiltrated into *N. benthamiana* leaves and samples were harvested at 2.5 days post agroinfiltration and ground in a cooled mortar in GEN buffer (10% [v/v] glycerol, 25 mM Tris-HCl, pH 7.5, 1 mM EDTA, 150 mM NaCl, 10 mM DTT, 0.5% [v/v] Triton X-100 and protease inhibitor cocktail). The supernatants were incubated with anti-Flag M2 affinity agarose (Sigma-Aldrich) in Bio-spin chromatography columns (Bio-rad) for 2 h at 4°C on a rotator, followed by washing with the washing buffer (10% [v/v] glycerol, 25 mM Tris-HCl, pH 7.5, 1 mM EDTA, 150 mM NaCl, 1mM DTT and 0.1% [v/v] Triton X-100). Elution of purified proteins was as described above (123).

**Pull-down assay.** For expression of MBP or MBP-tagged p33C (C-terminal portion of the TBSV p33) and p33C mutant, plasmids pMALc-2X, pMALc-2X-T33C,



pMALc-2X-T33C-F32A/V35A and pMALc-2X-T33C-37-82 were transformed into Epicurion BL21-codon-plus (DE3)-R1L cells, followed by IPTG induction. After sonication, 500  $\mu$ l lysates were incubated with 30  $\mu$ l amylose resin (NEB) in Bio-spin chromatography columns for 2 h at 4°C, followed by five times washing with column buffer (209). The amylose columns containing the MBP or MBP-tagged p33C or p33C mutants were then incubated with 3  $\mu$ g of the purified GST-His<sub>6</sub>-NbATG8f for 2 h at 4°C. Then, the washed beads were incubated in 1 $\times$  SDS loading buffer for 15 min at 85°C. The MBP-tagged proteins were analyzed by SDS-PAGE followed by coomassie staining and GST-His<sub>6</sub>-tagged proteins were separated by SDS-PAGE for protein gel blot analysis with anti-His antibody (209).

**Monitoring autophagic activity in plants.** To measure the autophagic activity in plants during TBSV replication, we employed the free-GFP release assay (176). *N. benthamiana* leaves were agroinfiltrated with pGD-eGFP-ATG8f (OD<sub>600</sub> 0.4) and different agrobacterium combinations. The infiltrated leaves at 1.5 dpai were exposed to darkness for 16 h or infiltrated with 10  $\mu$ M AZD8055 (181). Then leaf samples were harvested and subjected to protein extraction. Free GFP was detected by western blotting using anti-GFP antibody.

NbATG8f-II (PE conjugation) detection assay was performed to detect the autophagic activity (56, 176). *N. benthamiana* leaves were agroinfiltrated with pGD-Flag-ATG8f (OD<sub>600</sub> 0.3) and different agrobacterium combinations. At 2 dpi, leaf samples were harvested and subjected to protein extraction. Total protein was loaded onto 15% polyacrylamide gels containing 6 M urea to separate ATG8f-PE from unconjugated

ATG8f. NbATG8f-I and NbATG8f-II forms were detected by western blotting using anti-Flag antibody.

The effect of autophagic degradation on p33 protein levels was tested by using autophagic inhibitors. After 2 days post-agroinfiltration to express p33-Flag in whole *N. benthamiana* leaves, half-leaf inhibitor treatment was conducted. In brief, either 1  $\mu$ M ConA or 100  $\mu$ M E64d was infiltrated at the left side of each *N. benthamiana* leaf and the right side of leaves was treated with 0.5% DMSO as a control. After treatment for 12 h, leaf samples were harvested for total protein extraction and western blot analysis with anti-Flag antibody was performed as above.

**FRAP assay.** FRAP assays were performed using an Olympus FV3000 confocal microscope (210). *N. benthamiana* leaves were agroinfiltrated with different agrobacterium combinations. After 48 h, target region was bleached for 10 s at intensity of 30% at 405 nm laser. Fluorescence recovery was recorded over 180 s with 60 s interval. Mean fluorescence intensity was quantified by Image J and the values were normalized to background.

We applied 1,6 Hexanediol to characterize the VRO-associated condensates (211, 212). *N. benthamiana* leaves were agroinfiltrated with different agrobacterium combinations. After 48 h, leaves were infiltrated with 10% 1,6 hexanediol (dissolved in 10  $\mu$ g/ml digitonin) or digitonin (10  $\mu$ g/ml) as negative control. Images of VROs were recorded over 30 min with 10 min intervals.

**Quantification and statistical analysis.** Statistical analysis was performed using GraphPad Prism 8 software. Details of the statistical tests and sample sizes are provided in

the figure legends. Results with a p value of less than 0.05 were considered statistically significant, while results with a p value greater than 0.05 were considered statistically non-significant (ns).

Table 3.1: Plasmids constructed in chapter 3.

Plasmid name	insert source	insert digestion sites	primers for insert amplification	vector source	vector digestion sites
pGD-nYFP-NbATG8f2	<i>N. benthamiana</i> cDNA	BamHI and XhoI	#8554 and #8555	pGD-nYFP-MBP	BamHI and Sall
pGD-eGFP-NbATG8f2	<i>N. benthamiana</i> cDNA	BamHI and XhoI	#8554 and #8555	pGD-2X-35s-eGFP	BamHI and Sall
pGD-nYFP-NbNBR1	<i>N. benthamiana</i> cDNA	BclII and Sall	#8558 and #8559	pGD-nYFP-MBP	BamHI and Sall
pGD-eGFP-NbNBR1	<i>N. benthamiana</i> cDNA	BclII and Sall	#8558 and #8559	pGD-2X-35s-eGFP	BamHI and Sall
pTRV2-NbATG8a	<i>N. benthamiana</i> cDNA	BamHI and XhoI	#7877 and #8575	pTRV2-empty vector	BamHI and XhoI
pTRV2-NbATG8f	<i>N. benthamiana</i> cDNA	BamHI and XhoI	#8554 and #8576	pTRV2-empty vector	BamHI and XhoI
pTRV2-NbNBR1	<i>N. benthamiana</i> cDNA	BamHI and XhoI	#8580 and #8581	pTRV2-empty vector	BamHI and XhoI
pTRV2-ATG5	<i>N. benthamiana</i> cDNA	BamHI and XhoI	#7749 and #7750	pTRV2-empty vector	BamHI and XhoI
pGD-cYFP-Flag-NbATG8f2	<i>N. benthamiana</i> cDNA	BamHI and XhoI	#8554 and #8555	pGD-cYFP-Flag-MCS	BamHI and Sall
pGD-3XFlag-ATG8f	<i>N. benthamiana</i> cDNA	BamHI and XhoI	#8554 and #8555	pGD-3XFlag-MCS	BamHI and Sall
pGD-RFP-NbNBR1	<i>N. benthamiana</i> cDNA	BclII and Sall	#8558 and #8559	pGD-2X-35s-RFP	BamHI and Sall
pGD-RFP-ATG8f	<i>N. benthamiana</i> cDNA	BamHI and XhoI	#8554 and #8555	pGD-2X-35s-RFP	BamHI and Sall
pGD-Avi-his-NbATG8f	<i>N. benthamiana</i> cDNA	BamHI and XhoI	#8554 and #8555	pGD-Avi-His-ScSCS2	BamHI and XhoI
pGD-p33-His-BirA	PJW1234	XhoI and Sall	#8420 and #8421	pGD-T33/nonstop	XhoI and SAP

Table 3.1 (continued)

pGD-nYFP-AtSH3P2	<i>A. thaliana</i> cDNA	BamHI and Sall	#8544 and #8545	pGD-nYFP-MBP	BamHI and Sall
pGD-eGFP-AtSH3P2	<i>A. thaliana</i> cDNA	BamHI and Sall	#8544 and #8545	pGD-2X-35s-eGFP	BamHI and Sall
pGD-eGFP-AtATG4	<i>A. thaliana</i> cDNA	BamHI and Sall	#8844 and #8845	pGD-2X-35s-eGFP	BamHI and Sall
pGD-eGFP-NbATG1a	<i>N. benthamiana</i> cDNA	BamHI and Sall	#8827 and #8828	pGD-2X-35s-eGFP	BamHI and Sall
pGD-BFP-NbATG1a	<i>N. benthamiana</i> cDNA	BamHI and Sall	#8827 and #8828	pGD-2X-35s-BFP	BamHI and Sall
pGD-RFP-AtATG4	<i>A. thaliana</i> cDNA	BamHI and Sall	#8844 and #8845	pGD-2X-35s-RFP	BamHI and Sall
pGD-eGFP-NbATG5	<i>N. benthamiana</i> cDNA	BamHI and Sall	#8832 and #8833	pGD-2X-35s-eGFP	BamHI and Sall
pGD-RFP-NbATG5	<i>N. benthamiana</i> cDNA	BamHI and Sall	#8832 and #8833	pGD-2X-35s-RFP	BamHI and Sall
pGD-eGFP-NbATG101	<i>N. benthamiana</i> cDNA	BamHI and Sall	#8836 and #8837	pGD-2X-35s-eGFP	BamHI and Sall
pGD-RFP-NbATG101	<i>N. benthamiana</i> cDNA	BamHI and Sall	#8836 and #8837	pGD-2X-35s-RFP	BamHI and Sall
pGD-Avi-his-AtATG4	<i>A. thaliana</i> cDNA	BamHI and Sall	#8844 and #8845	pGD-Avi-His-ScSCS2	BamHI and XhoI
pGD-Avi-his-NbATG5	<i>N. benthamiana</i> cDNA	BamHI and Sall	#8832 and #8833	pGD-Avi-His-ScSCS2	BamHI and XhoI
pGD-Avi-his-NbATG101	<i>N. benthamiana</i> cDNA	BamHI and Sall	#8836 and #8837	pGD-Avi-His-ScSCS2	BamHI and XhoI
pGD-nYFP-NbATG8i	<i>N. benthamiana</i> cDNA	BamHI and XhoI	#8556 and #8557	pGD-nYFP-MBP	BamHI and Sall
pGD-eGFP-NbATG8i	<i>N. benthamiana</i> cDNA	BamHI and XhoI	#8556 and #8557	pGD-2X-35s-eGFP	BamHI and Sall

Table 3.1 (continued)

pTRV2-NbATG8i	<i>N. benthamiana</i> cDNA	BamHI and XhoI	#8556 and #8577	pTRV2-empty vector	BamHI and XhoI
pMal-T33-N82aa	pGD-35S-T33-BFP	BglII and XhoI	#4000 and #5710	pMal-EV	BamHI and Sall
pMal-T33-N82-F32A/V35A	pGD-nYFP-T33-F32A/V35A	BglII and XhoI	#4000 and #5710	pMal-EV	BamHI and Sall
pMal-T33-N37-82	pGD-nYFP-T33-F32A/V35A	BglII and XhoI	#5707 and #5710	pMal-EV	BamHI and Sall
pGD-YFP-3XHA-ATG8f	<i>N. benthamiana</i> cDNA	BamHI and XhoI	#8554 and #8555	pGD-YFP	BamHI and Sall
pGD-eGFP-His-BirA	pGD-2X-35s-eGFP	XhoI and Sall	#8420 and #8421	HpESC-Gal-BirA-Hisp33/Gal-DI72	XhoI and SAP
pGEX-His-Atg8f	<i>N. benthamiana</i> cDNA	BamHI and XhoI	#8554 and #8555	pGEX	BamHI and Sall

Table 3.2: Plasmids described in previous studies of chapter 3.

Plasmid name	Source
pGD-35S-p19	[1] Xu and Nagy, 2016
pGD-35S-T33-BFP	[1] Xu and Nagy, 2016
pGD-35S-C36-BFP	[1] Xu and Nagy, 2016
pGD-35S-GFP-SKL	[1] Xu and Nagy, 2016
pGD-35S-GFP-AtTim21	[1] Xu and Nagy, 2016
pGD-35S-T33-cYFP	[1] Xu and Nagy, 2016
pGD-35S-C36-cYFP	[1] Xu and Nagy, 2016
pGD-35S-C-cYFP	[1] Xu and Nagy, 2016
pGD-35S-nYFP-MBP	[1] Xu and Nagy, 2016
pGD-35S-RFP-SKL	[1] Xu and Nagy, 2016
pGD-35S-RFP-AtTim21	[1] Xu and Nagy, 2016
PJW1234	[2] Jan et al., 2014
pGD-P33-Myc	Dr. Zhike. Feng
pGD-YFP-RavZ	[3] Inaba et al., 2019

Table 3.2 (continued)

pGD-GFP-AtVps34	[4] Feng et al., 2019
pGD-Avi-His-ScSCS2	[5] Kang et al., 2022
pGD-nYFP-VPS34	[4] Feng et al., 2019
pEsc-Vps34-3xHA	[4] Feng et al., 2019
pGBK-His-p33-DI72	[6] Barajas et al., 2009
pGAD-His-p92	[6] Barajas et al., 2009
pGBK-Flag-p33-DI72	[6] Barajas et al., 2009
pGAD-Flag-p92	[6] Barajas et al., 2009

Table 3.3: Reference for table 3.2.

[1]	Xu, K., and Nagy, P.D. (2016). Enrichment of phosphatidylethanolamine in viral replication compartments via co-opting the endosomal Rab5 small GTPase by a positive-strand RNA virus. <i>PLoS Biol</i> <b>14</b> , e2000128.
[2]	Jan CH, Williams CC, Weissman JS. (2014). Principles of ER cotranslational translocation revealed by proximity-specific ribosome profiling. <i>Science</i> <b>346(6210)</b> :1257521.
[3]	Inaba, J. I., Xu, K., Kovalev, N., Ramanathan, H., Roy, C. R., Lindenbach, B. D., & Nagy, P. D. (2019). Screening Legionella effectors for antiviral effects reveals Rab1 GTPase as a proviral factor coopted for tombusvirus replication. <i>Proceedings of the National Academy of Sciences</i> , <i>116</i> (43), 21739-21747.
[4]	Feng, Z., Xu, K., Kovalev, N., & Nagy, P. D. (2019). Recruitment of Vps34 PI3K and enrichment of PI3P phosphoinositide in the viral replication compartment is crucial for replication of a positive-strand RNA virus. <i>PLOS pathogens</i> , <i>15</i> (1), e1007530.
[5]	Kang, Y., Lin, W., Liu, Y., & Nagy, P. D. (2022). Key tethering function of Atg11 autophagy scaffold protein in formation of virus-induced membrane contact sites during tombusvirus replication. <i>Virology</i> , <i>572</i> , 1-16.
[6]	Barajas, D., Li, Z., & Nagy, P. D. (2009). The Nedd4-type Rsp5p ubiquitin ligase inhibits tombusvirus replication by regulating degradation of the p92 replication protein and decreasing the activity of the tombusvirus replicase. <i>Journal of virology</i> , <i>83</i> (22), 11751-11764.

Table 3.4: Primers used in chapter 3.

Name	Sequence(5' to 3')
#8554/NbATG8f/BamHI/F	CGGGATCCATGGCTAAGAGCTCATTC AAG

Table 3.4 (continued)

#8555/NbATG8f/XhoI/R	ACCGCTCGAGCTACAGCTCGTTCGGG TCCCCGA
#8558/NbNBR1/BclI/F	ACGTGATCAATGGCCATGGAGTCTGC TATTGTCATCAAGGTCAAG
#8559/NbNBR1/SalI/R	ACGCGTCGACCTACTGCTCTCCAGCA ATAAG
#7877/NbATG8a/BamHI/F	ACGCGGATCCATGGCCAAAAGCTCCT TCAAATTGG
#8575/TRV-NbATG8a/XhoI/R	CCGCTCGAGTTCTCAGCACTAAGCTTT
#8576/TRV-NbATG8f1/XhoI/R	CCGCTCGAGCTCAATTTGATTCTCTTG CG
#8580/TRV-NbNBR1/BamH/F	CGGGATCCATAGTGGGGAGGAGAAG G
#8581/TRV-NbNBR1/XhoI/R	CCGCTCGAGTGACCCCTTTTATATGGG
#7749/TRV-NbATG5/BamH/F	CCGCTCGAGCTTACATAAACAGACCT G
#7750/TRV-NbATG5/XhoI/R	CGGGATCCATATGGTGATGGGTTCTT G
#8421/His-BirA/3XGGS/XhoI/F	ACCGCTCGAGGGTGGCTCTGGAGGGT CAGGTGGTTCCATGGGAGGTTCTCAT CATCA
#8420/BirA/SalI/R	ACGCGTCGACTTATTTTTCTGCACTAC GCAGG
#8937/NbATG8f-qPCR/F	GGGCAATTTGTCTATGTCATTTCG
#8938/NbATG8f-qPCR/R	AGGAAACCATCTTCATCCTTCTT
#8994/NbNBR1-qPCR/F	CCCTAGTGGAGCATCTAAT
#8995/NbNBR1-qPCR/R	GGCATCTAACGCATCATC
#8544/SH3P2/BamH/F	CGCGGATCCATGGATGCAATTAGAAA AC
#8545/SH3P2/SalI/R	ACGCGTCGACTCAGAAAACCTTCGGAC AC
#8844/ATG4/F	ACGCGGATCCATGAAGGCTTTATGTG ATAG
#8845/ATG4/R	ACGCGTCGACTCAGAGCATTGCCAG TCATC
#8827/ATG1a/F	ACGCGGATCCATGGCTCAATCGATGA GCAG
#8828/ATG1a/R	ACGCGTCGACTTAAGGAGAGCAGTGT TGATC
#8832/ATG5/F	ACGCGGATCCATGGGAAGTAAAGGGG CAG
#8833/ATG5/R	ACGCGTCGACCTATATGGTGATGGGT TCTTG



Table 3.4 (continued)

#8836/ATG101/F	ACGCGGATCCATGAATTGTGAAGTTT GCCAG
#8837/ATG101/R	ACGCGTCTGACTCAGCTGAGCATAGTT GGATG
#8556/ATG8i/F	CGCGGATCCATGGGGAAGGCTTTCAA AAAAG
#8557/ATG8i/R	ACCGCTCGAGTCAACTATTTGCACGA CCAAAGG
#6532/eGFP/F/BglII	GGAAGATCTATGGTGAGCAAGGGCGA G
#8875/TBSV P33/F32A/V35A/R	TCTCAGAACCACACGACACGCCAATT GAGCGATGTTCAACCGAACTGT
#8874/TBSV P33/F32A/V35A/F	GCTCAATTGGCGTGTTCGTGTGGTTCTG AGA
#810/TBSV P33/XhoI/R	GGAGCTCGAGCTATTTGACACCCAGG GAC
#4000/TBSV P33/BglII/F	CCAGAGATCTATGGAGACCATCAAGA GAATG
#1593/TBSV P33/stop/XhoI/R	CGGCTCGAGCTATTTGACACCCAGGG ACTCCTGT
#5710/TBSV P33/82aa/XhoI/R	CCGCTCGAGTTAATCACCCCTCTGCCG TC
#5707/TBSV P33/37aa/BglII/F	GGAAGATCTCGTGTGGTTCTGAGATA CATGAG

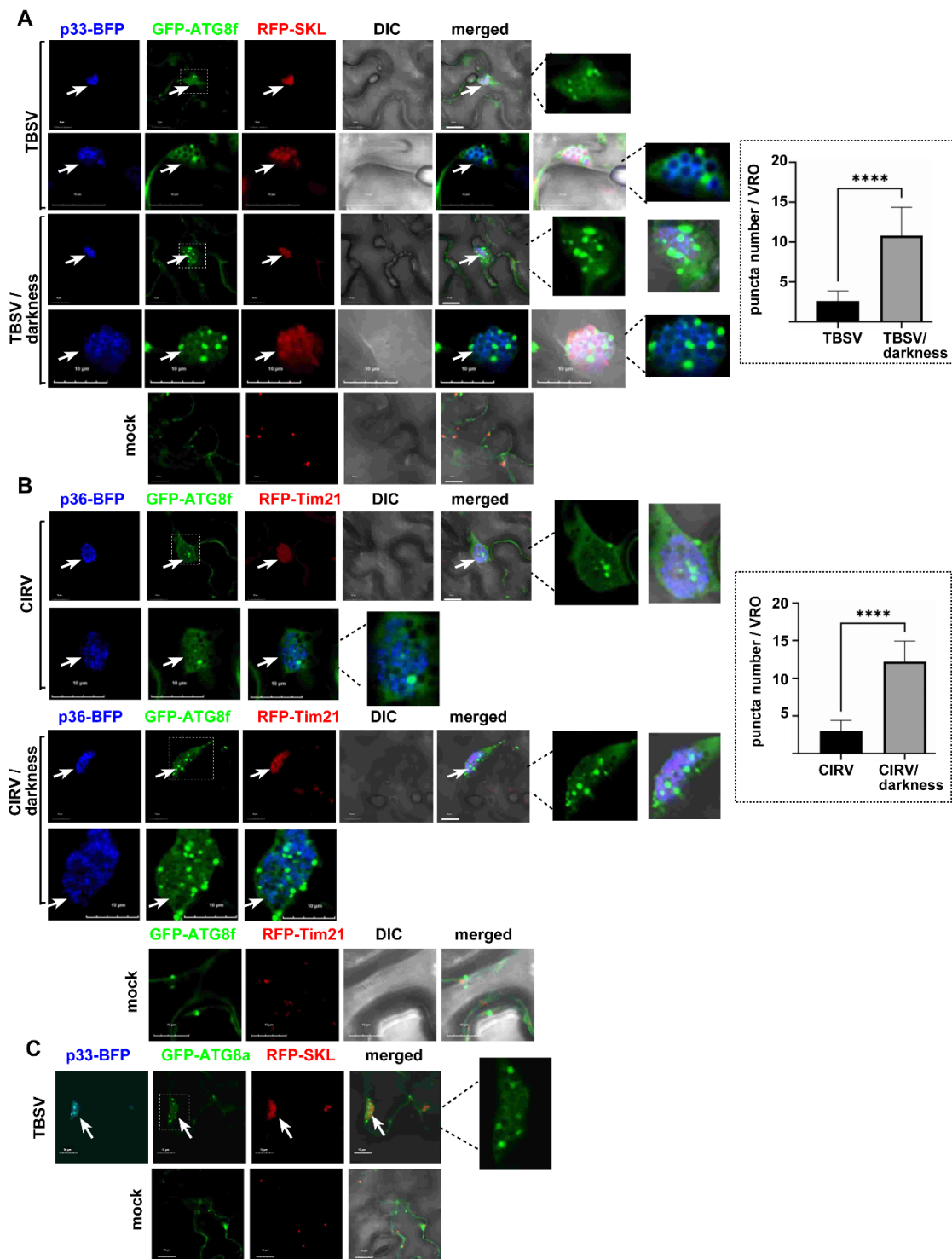


Figure 3.1

*Figure 3.1. Recruitment of ATG8 by the TBSV p33 and the CIRV p36 replication proteins into VROs in N. benthamiana.*

(A) Confocal microscopy images show efficient co-localization of TBSV p33-BFP replication protein and GFP-ATG8f within VROs consisting of clustered peroxisomes, marked by RFP-SKL peroxisomal matrix marker in *N. benthamiana* leaves. The expression of these proteins, driven by the 35S promoter, was achieved through co-agroinfiltration into *N. benthamiana* leaves. The plant leaves were either TBSV-infected and applied darkness treatment (to induce bulk autophagy) or mock-inoculated as shown. The VROs are marked with arrows. The enlarged images of VROs (boxed) are shown on the right. Scale bars represent 10  $\mu\text{m}$ . The graph shows the number of ATG8f puncta / VRO. Error bars represent SD (n = 10). Student t-test was used to statistically analyze the data (\*\*\*P < 0.0001). (B) Confocal microscopy images show efficient co-localization of CIRV p36-BFP replication protein and GFP-ATG8f within VROs consisting of clustered mitochondria, marked by RFP-AtTim21 mitochondrial marker in *N. benthamiana* leaves. See further details in panel A. (C) Confocal microscopy images show co-localization of TBSV p33-BFP replication protein and GFP-ATG8a within VROs in *N. benthamiana* leaves. Note that ATG8a localized in both the cytosol and nucleus in the absence of tombusvirus infection. See further details in panel A. Each experiment was repeated.

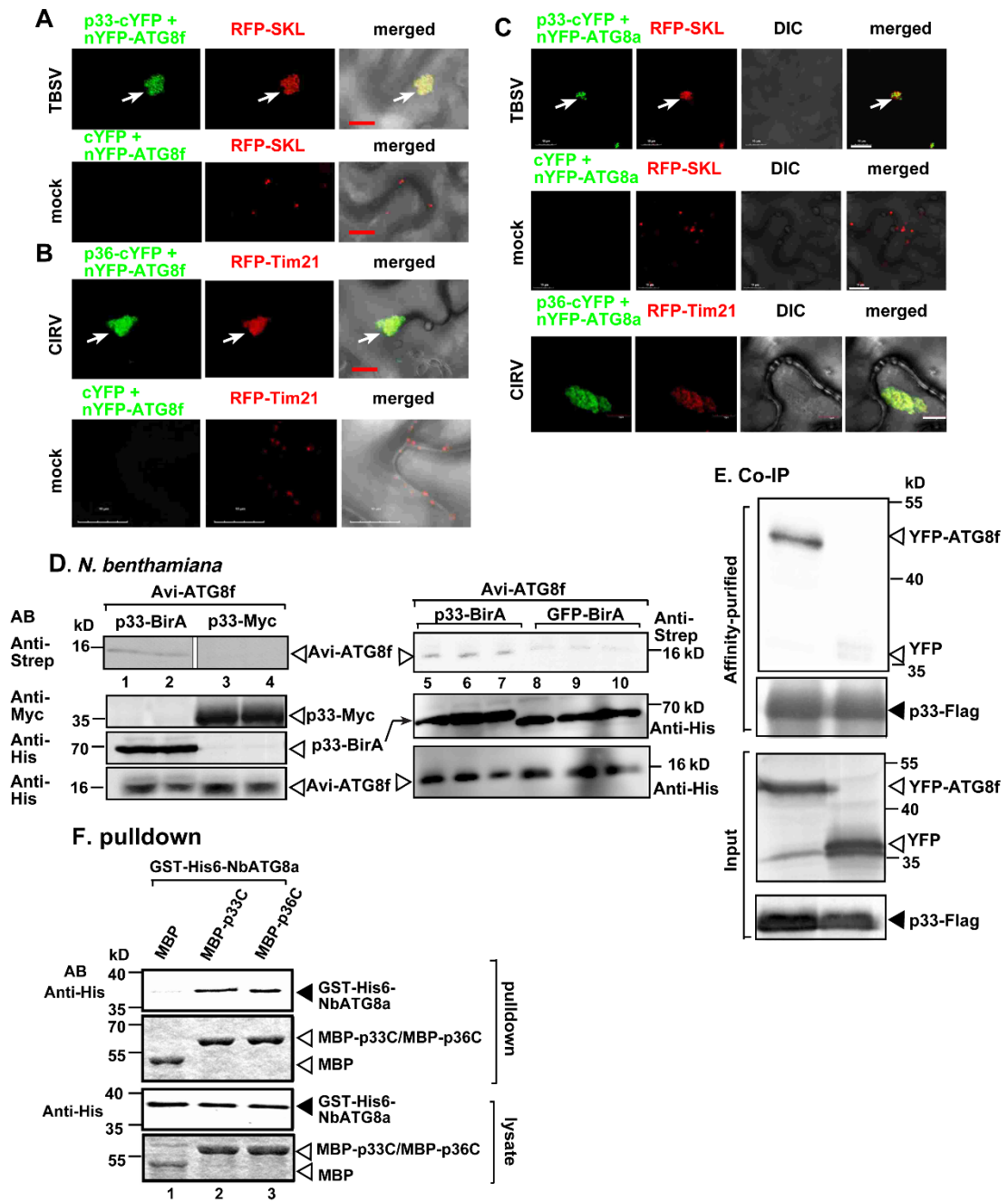


Figure 3.2

Figure 3.2. Interaction between ATG8 and tombusvirus replication proteins within VROs in *N. benthamiana*.

(A) Interaction between TBSV p33-cYFP replication protein and the nYFP-ATG8f protein was detected by BiFC. The merged images show the co-localization of RFP-SKL with the BiFC signal, indicating that the interaction between p33 replication protein and ATG8f occurs in VROs in clustered peroxisomal membranes. The VROs are marked with arrows. Scale bars represent 10  $\mu\text{m}$ . Each experiment was repeated three times. (B) Interaction between CIRV p36-cYFP replication protein and the nYFP-ATG8f protein were detected by BiFC. The merged images show the co-localization of RFP-AtTim21 with the BiFC signal, indicating that the interaction between p36 replication protein and ATG8f occurs in VROs consisting of aggregated mitochondria. See further details in panel A. (C) Interactions between TBSV p33-cYFP or CIRV p36-cYFP replication proteins and the nYFP-ATG8a protein were detected by BiFC. See further details in panel A. (D) Protein proximity-labeling with biotin in *N. benthamiana*. *N. benthamiana* leaves were agroinfiltrated to express p33 replication protein, which was fused to BirA biotin ligase, and Avi-tagged ATG8f. Note that both fusion proteins carry a 6xHis tag. Biotin treatment lasted for 40 min. The image shows the western blot analysis of the biotinylated Avi-ATG8f detected with streptavidin-conjugated AP in total protein extracts. p33-myc was used as a negative control to show plant does not have biotin ligase activity. GFP-BirA was expressed (lanes 8-10) to measure basal level of biotinylation of Avi-ATG8f. The experiments were repeated. (E) Co-purification of YFP-ATG8f with TBSV Flag-p33 replication protein from subcellular membranes. *N. benthamiana* leaves were agroinfiltrated to express YFP-ATG8f with TBSV Flag-p33. Top two panels: western blot analysis of co-purified YFP-ATG8f detected with anti-YFP antibody, while Flag-p33 was detected with anti-Flag antibody. The negative control was from plants expressing YFP purified on a Flag-affinity column. Bottom two panels: western blot of input YFP-ATG8f, YFP and Flag-p33 in the total protein extracts. (F) Pull-down assay including His<sub>6</sub>-NbATG8a and the MBP-tagged TBSV p33 or CIRV p36 replication proteins. Note that we used the soluble C-terminal region of TBSV p33 or CIRV p36 replication proteins, which lacked the N-terminal domain. Top panel: western blot analysis of the captured His<sub>6</sub>-NbATG8a with the MBP-affinity purified p33C/p36C was performed with anti-His antibody. The negative control was the MBP (lanes 1). Middle panel: Coomassie-blue stained SDS-PAGE of the captured MBP-p33C, MBP-p36C and MBP. Bottom panels: western blot analysis of His<sub>6</sub>-NbATG8a in total extracts. Coomassie-blue stained SDS-PAGE of the MBP-p33C, MBP-p36C and MBP in total extracts. Each experiment was repeated three times.

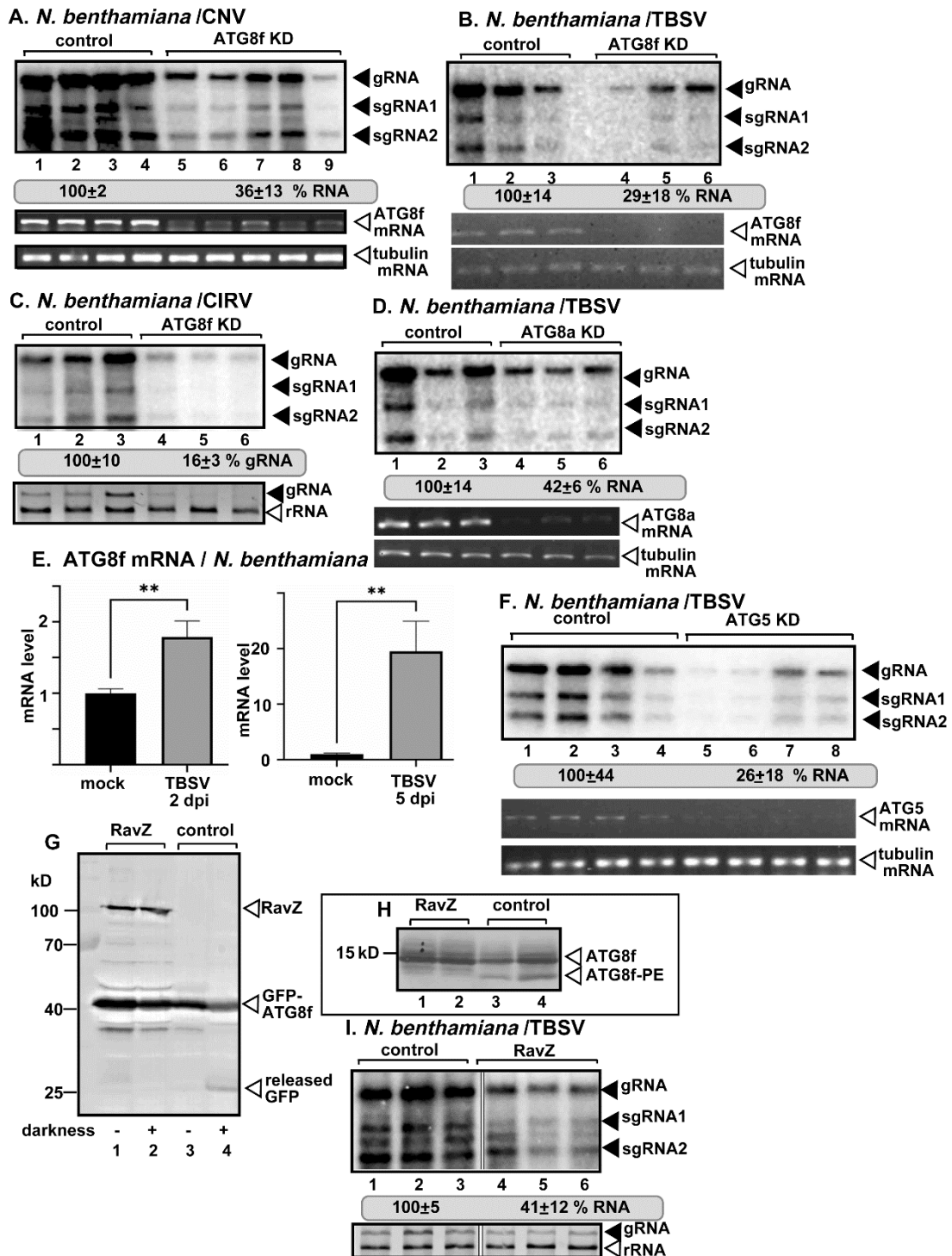


Figure 3.3

Figure 3.3. The effect of ATG8 on tombusvirus replication in *N. benthamiana* plants.

(A-B) Top panel: The accumulation of the CNV and TBSV RNAs in ATG8f-silenced (ATG8f KD) *N. benthamiana* plants 2.5 and 2 dpi, respectively. The genomic (g)RNA levels in the inoculated leaves were measured by northern blot analysis. Agroinfiltration of pGD-CNV<sup>20Kstop</sup> or inoculation with TBSV sap was done 10 days after silencing of ATG8f expression. Agroinfiltration of tobacco rattle virus (TRV) vectors carrying either ATG8f or 3'-terminal GFP (as a control) sequences was used to induce VIGS. Second panel: Semi-quantitative RT-PCR analysis of ATG8f mRNA level in the silenced and control plants. Third panel: Semi-quantitative RT-PCR analysis of tubulin mRNA level in the silenced and control plants. (C) Top panel: The accumulation of the CIRV RNAs in ATG8f-silenced (ATG8f KD) *N. benthamiana* leaves at 3 dpi. See more details in panel A. Bottom panel: Ribosomal (r)RNA is shown as a loading control in an ethidium-bromide-stained agarose gel. (D) The accumulation of the TBSV RNAs in ATG8a-silenced (ATG8a KD) *N. benthamiana* leaves at 2 dpi. See more details in panel A. (E) Real time RT-qPCR analysis of the expression of ATG8f mRNA in the TBSV-inoculated leaves (2 dpi) or systemically infected leaves (5 dpi) of *N. benthamiana* plants. The same amounts of total RNA extracts were used in RT-qPCR analysis. (F) Accumulation of the TBSV RNAs in ATG5-silenced (ATG5 KD) *N. benthamiana* leaves at 2 dpi. See more details in panel A. (G) The effect of *Legionella* RavZ effector on autophagy flux. The plants expressed GFP-ATG8f and either exposed to darkness to induce bulk autophagy or not as shown. The released 'free' GFP band is marked with an arrowhead. The left two lanes include samples from plants co-expressing RavZ and GFP-ATG8f, which show lack of released 'free' GFP band. Total protein extracts were immunoblotted with anti-GFP antibody. The RavZ and GFP-ATG8f proteins were expressed via agroinfiltration. (H) The effect of *Legionella* RavZ effector on ATG8f-PE conjugation. The two lanes on the right display plants expressing Flag-ATG8f, where both Flag-ATG8f and Flag-ATG8f-PE are present as marked by arrowhead. The left two lanes show that RavZ expression eliminated the Flag-ATG8f-PE band, but not the Flag-ATG8f band. Total protein extracts were loaded on 15% polyacrylamide gels containing 6 M urea and immunoblotted with anti-Flag antibody. (I) Top panel: The accumulation of the TBSV RNAs in *N. benthamiana* leaves expressing RavZ at 2 dpi. The RavZ protein was expressed via agroinfiltration. The control leaves were agroinfiltrated with the same amounts of bacteria with 'empty' plasmid. See more details in panel A. Bottom panel: Ribosomal RNA is shown as a loading control in an ethidium-bromide-stained agarose gel. Each experiment was repeated three times.

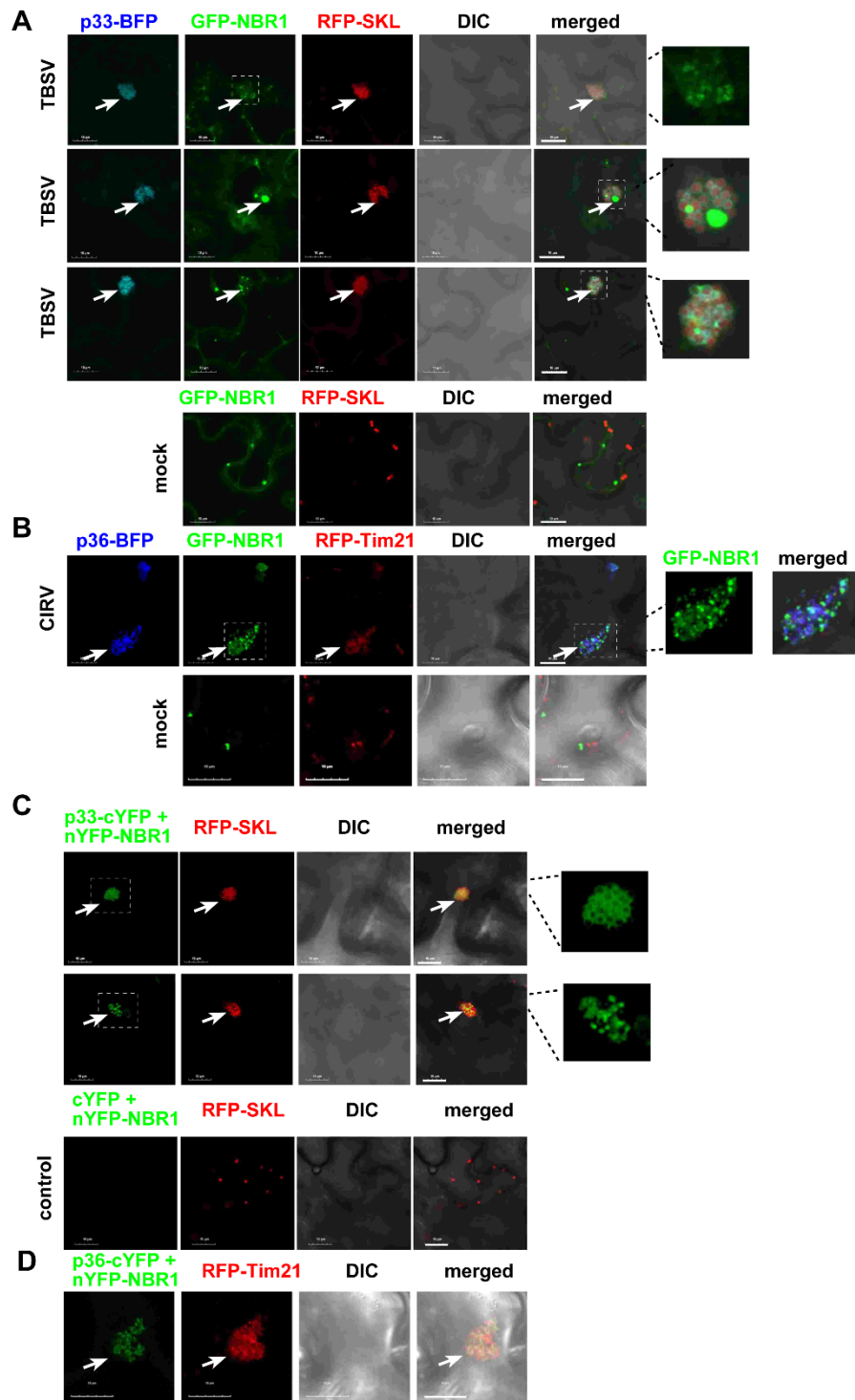


Figure 3.4



*Figure 3.4. Recruitment of NBR1 selective autophagy receptor by the TBSV p33 and the CIRV p36 replication proteins into VROs in N. benthamiana.*

(A) Confocal microscopy images show co-localization of TBSV p33-BFP replication protein and the eGFP-NBR1 within a VRO consisting of clustered peroxisomes, marked by RFP-SKL peroxisomal matrix marker in *N. benthamiana* leaves. The expression of these proteins, driven by the 35S promoter, was achieved through co-agroinfiltration into *N. benthamiana* leaves. The plant leaves were either TBSV-infected, or mock-inoculated as shown. Note that eGFP-NBR1 formed different patterns as visible in the enlarged images on the right. Scale bars represent 10  $\mu\text{m}$ . See further details in Fig 1A. (B) Confocal microscopy images show co-localization of CIRV p36-BFP replication protein and the eGFP-NBR1 within a VRO consisting of clustered mitochondria, marked by RFP-AtTim21 mitochondrial marker in *N. benthamiana* leaves. See further details in panel A. (C) Interaction between TBSV p33-cYFP replication protein and the nYFP-NBR1 protein was detected by BiFC. The merged images show the co-localization of RFP-SKL with the BiFC signals, indicating that the interaction between p33 replication protein and NBR1 occurs in VROs. The interacting proteins formed different patterns as visible in the enlarged images on the right. (D) Interaction between CIRV p36-cYFP replication protein and the nYFP-NBR1 protein was detected by BiFC. See further details in panel C above. Each experiment was repeated.

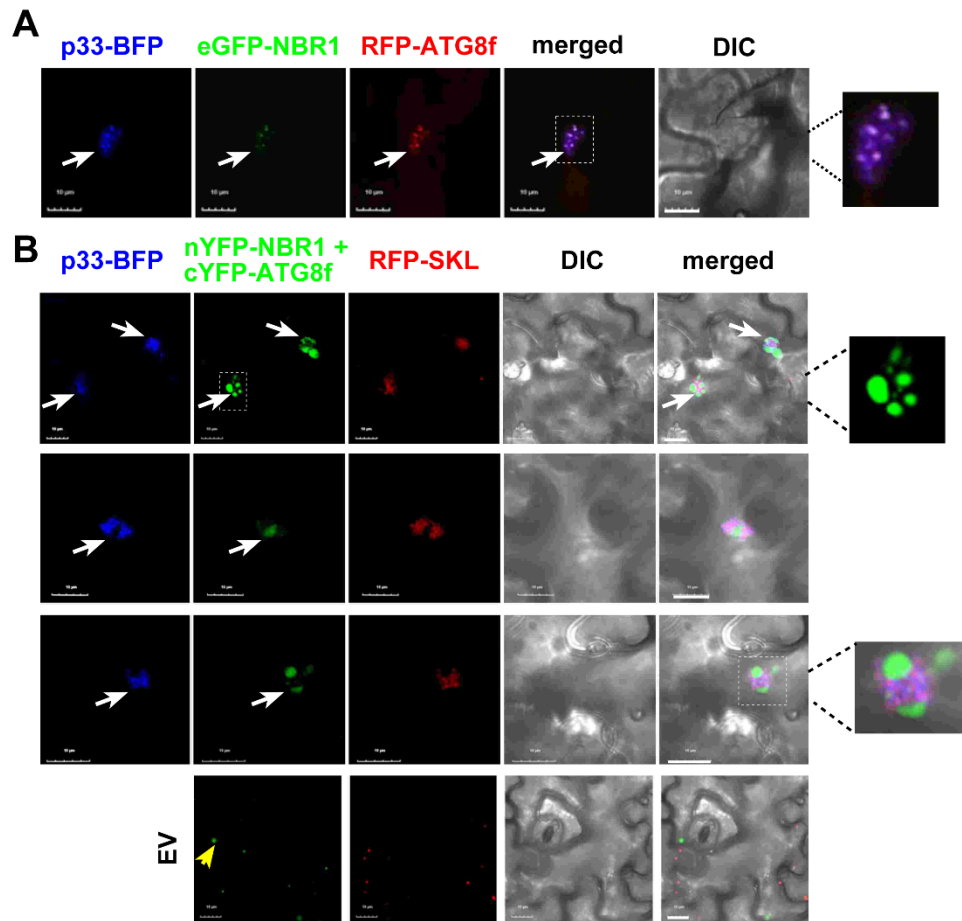


Figure 3.5

*Figure 3.5. Interaction between the co-opted ATG8f and NBR1 proteins within VROs in N. benthamiana.*

(A) Confocal microscopy images show co-localization of TBSV p33-BFP replication protein and the co-opted RFP-ATG8f and eGFP-NBR1 within a VRO consisting of clustered peroxisomes in *N. benthamiana* leaves. The expression of these proteins, driven by the 35S promoter, was achieved through co-agroinfiltration into *N. benthamiana* leaves. The VROs are marked with arrows. Scale bars represent 10  $\mu\text{m}$ . (B) BiFC approach was employed to demonstrate interaction between nYFP-NBR1 and cYFP-ATG8f proteins associated with the TBSV p33-BFP-positive VROs. Co-agroinfiltration into *N. benthamiana* leaves was used for protein expression. 'EV' represents plant cells not expressing p33-BFP. Scale bars represent 10  $\mu\text{m}$ . Each experiment was repeated.

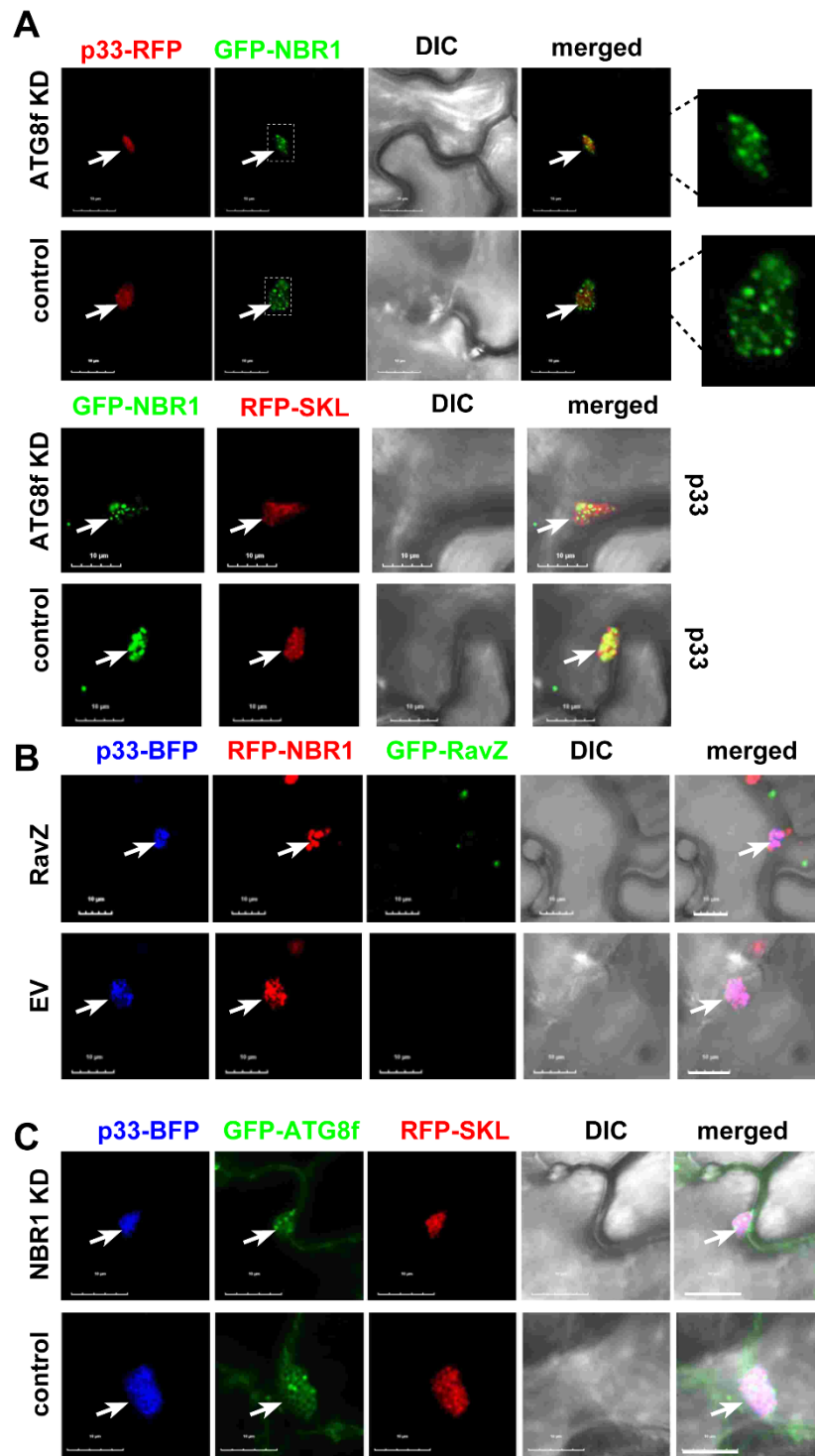


Figure 3.6

*Figure 3.6. Separate subversion of ATG8f or NBR1 by TBSV p33 replication protein into VROs.*

(A) Confocal microscopy images show co-localization of eGFP-NBR1 and p33-RFP (top two panels), or eGFP-NBR1 and RFP-SKL co-expressing cYFP-p33 (bottom panels), within VROs in ATG8f-silenced (ATG8f KD) or control *N. benthamiana* cells. The expression of these proteins, driven by the 35S promoter, was achieved through co-agroinfiltration into *N. benthamiana* leaves. TRV vector carrying MBP sequences was used as a VIGS control. Scale bars represent 10  $\mu\text{m}$ . The VROs are marked with arrows. (B) Confocal microscopy images show co-localization of RFP-NBR1 and p33-BFP in *N. benthamiana* cells. The plants either expressed GFP-RavZ effector (top panel), or pGD vector as control (bottom panel). See further details in panel A. (C) Confocal microscopy images show co-localization of GFP-ATG8f and p33-BFP in NBR1-silenced (NBR1 KD) *N. benthamiana* cells. See more detail in panel A. Scale bars represent 10  $\mu\text{m}$ . Each experiment was repeated.

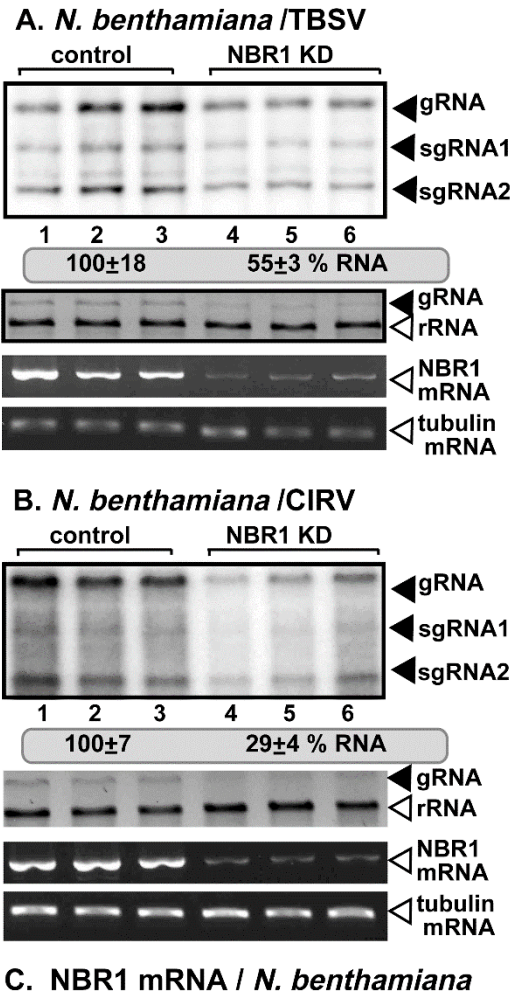


Figure 3.7

*Figure 3.7. The effect of NBR1 on tombusvirus replication in N. benthamiana plants.*

(A) Top panel: The accumulation of TBSV RNAs in NBR1-silenced (NBR1 KD) inoculated leaves of *N. benthamiana* at 2 dpi was measured by northern blot analysis. Sap inoculation with TBSV was done 10 days after silencing of NBR1 expression. Agroinfiltration of TRV vector carrying NBR1 or 3'-terminal GFP (as a control) sequences was used to induce VIGS. Second panel: Ribosomal RNA is shown as a loading control in an ethidium-bromide stained agarose gel. Third panel: Semi-quantitative RT-PCR analysis of NBR1 mRNA level in the silenced and control plants. Fourth panel: Semi-quantitative RT-PCR analysis of tubulin mRNA level in the silenced and control plants. Each experiment was repeated three times. (B) The accumulation of CIRV RNAs in NBR1-silenced (NBR1 KD) inoculated leaves of *N. benthamiana* at 2.5 dpi was measured by northern blot analysis. Sap inoculation with CIRV was done 10 days after silencing of NBR1 expression. See further details in panel A above. (C) Real time RT-qPCR analysis of the induction of NBR1 mRNA expression in the TBSV-inoculated leaves (2 dpi) of *N. benthamiana* plants. The same amounts of total RNA extracts were used in RT-qPCR analysis. Each experiment was repeated three times.

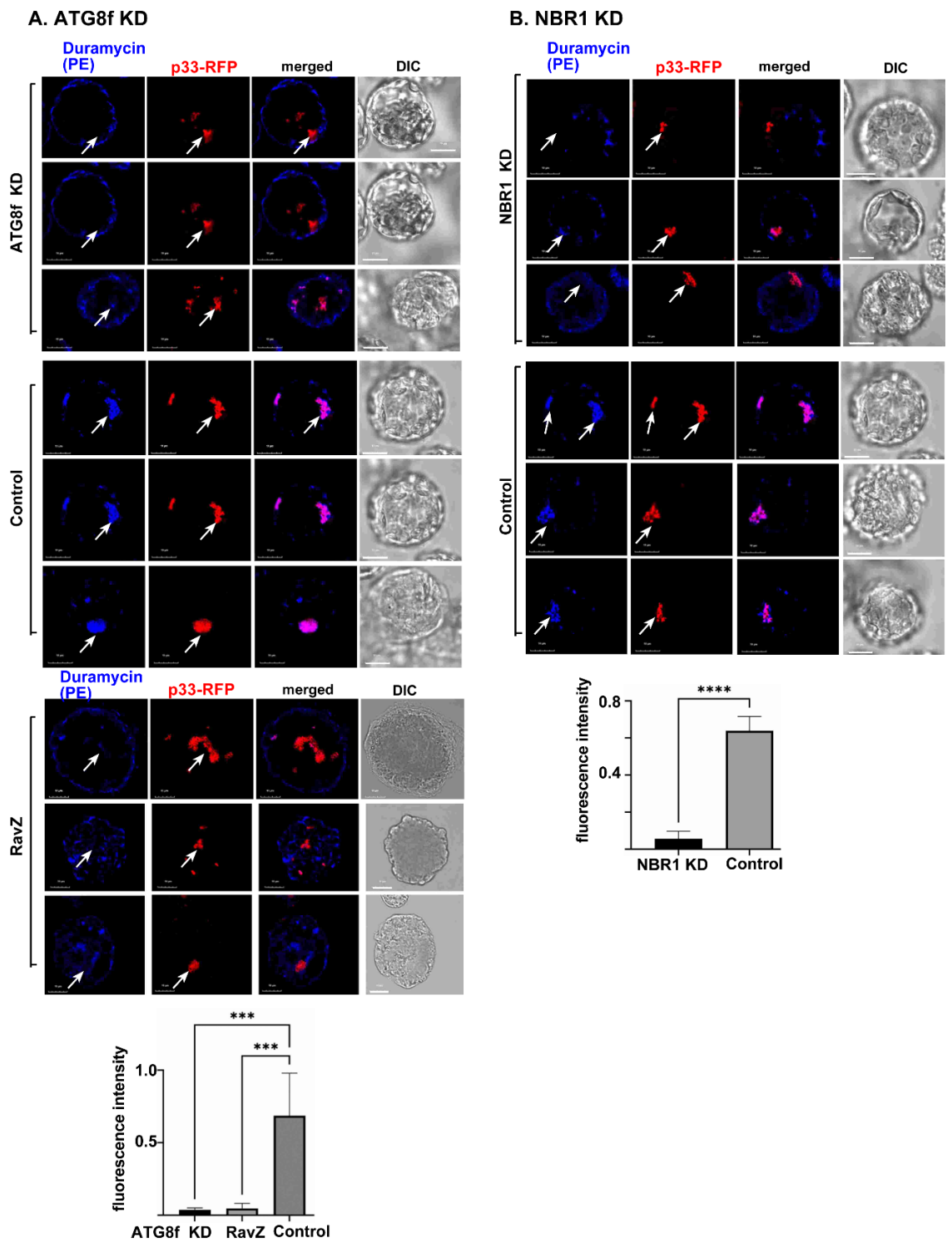


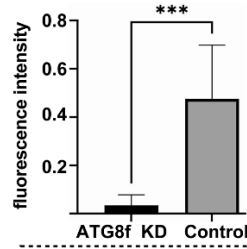
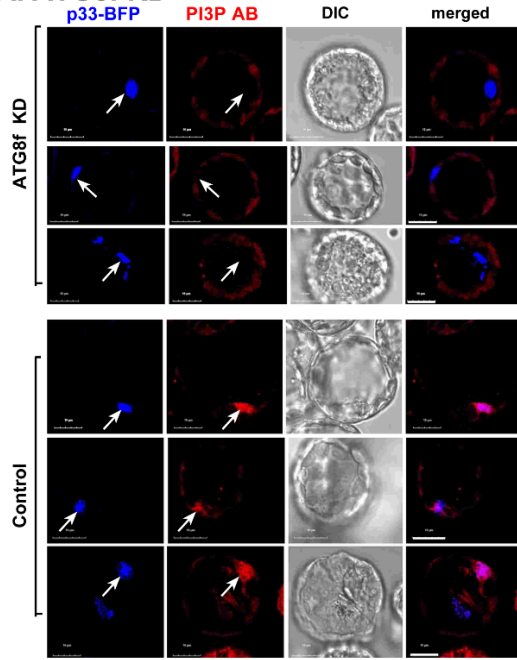
Figure 3.8



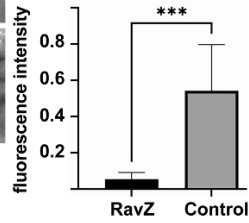
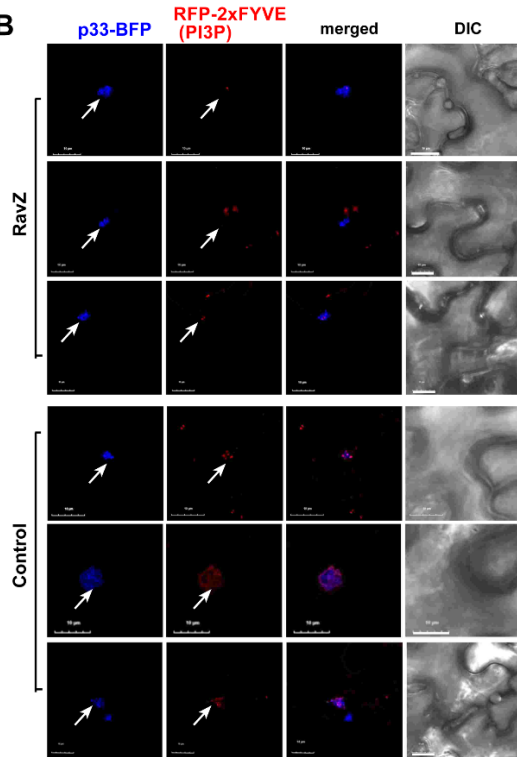
*Figure 3.8. Contributions of ATG8f and NBR1 to PE enrichment in the viral replication compartment in N. benthamiana protoplasts.*

(A) Top panel: Confocal microscopy images reveal poor PE enrichment in VROs marked with p33-RFP in protoplasts prepared from ATG8f-silenced (ATG8f-KD) *N. benthamiana* (top image). Central panel: PE enrichment is visible in VROs in control *N. benthamiana* protoplasts. Differential interference contrast (DIC) images are shown on the right. PE distribution is detected by a staining probe using biotinylated duramycin peptide and streptavidin conjugated with Alexa Fluor 405. Bottom panel: Confocal microscopy images show poor PE re-distribution into VROs in *N. benthamiana* protoplasts co-expressing RFP-p33 and RavZ. Scale bars represent 10  $\mu$ m. The fluorescence intensity of Duramycin was quantified within the VROs marked with arrows using Image J. Error bars represent SD (n = 10). Student t-test was used for statistical analysis (\*\*P < 0.001, \*\*\*\*P < 0.0001). (B) Confocal microscopy images show poor PE re-distribution into VROs marked with p33-RFP in NBR1-silenced (NBR1-KD) *N. benthamiana* protoplasts (top image). TRV vector carrying partial GFP sequences was used as a VIGS control. See more details in panel A above. Each experiment was repeated three times.

**A. ATG8f KD**



**B**



**C. NBR1 KD**

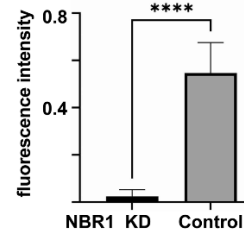
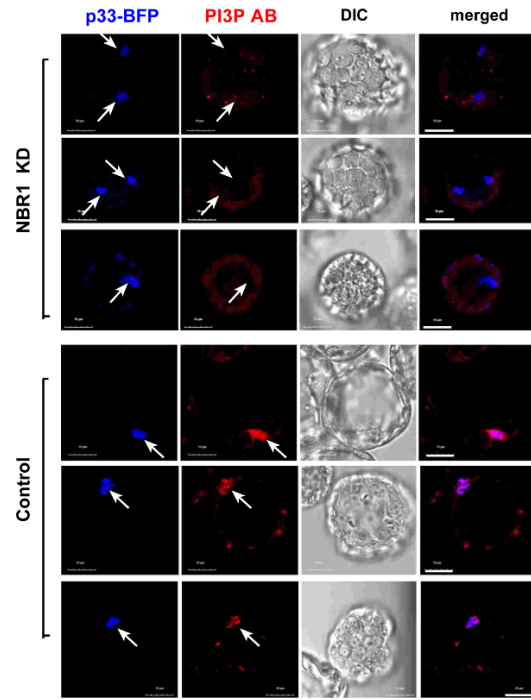


Figure 3.9

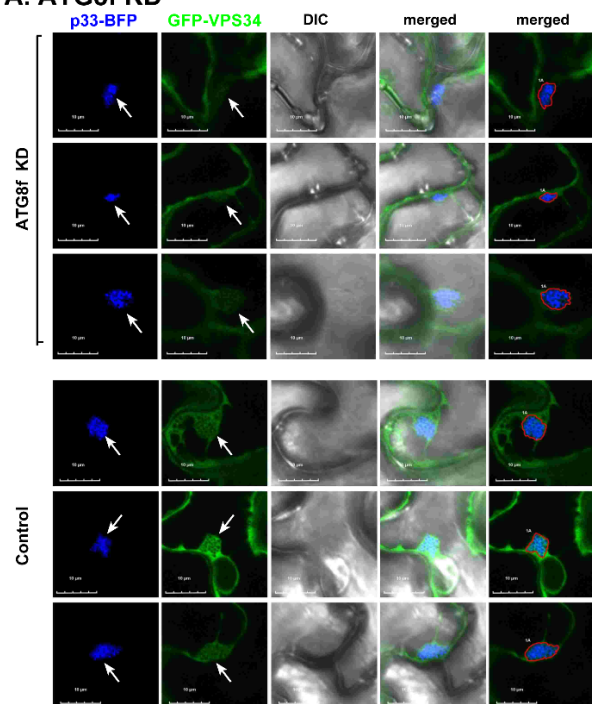
*Figure 3.9. ATG8 and NBR1 contribute to PI(3)P enrichment within the viral replication compartment in N. benthamiana plants and protoplasts.*

(A) Confocal microscopy images reveal poor PI(3)P enrichment in VROs marked with p33-BFP in ATG8f-silenced (ATG8f-KD) *N. benthamiana* protoplasts. PI(3)P enrichment is visible in VROs in control *N. benthamiana* protoplasts. PI(3)P distribution is detected by PI(3)P antibody and then incubated with anti-mouse secondary antibody conjugated with Alexa Fluor 568. Scale bars represent 10  $\mu$ m. The fluorescence intensity for PI(3)P was quantified within the VROs marked with arrows using Image J. Error bars represent SD (n = 10). Student t-test was used for statistical analysis (\*\*P < 0.01, \*\*\*P < 0.001, \*\*\*\*P < 0.0001).

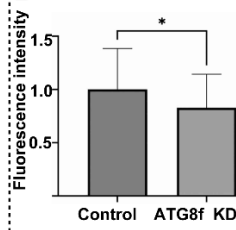
(B) Confocal microscopy images show reduced enrichment of PI(3)P in VROs in *N. benthamiana* leaves co-expressing RFP-2xFYVE protein, p33-BFP and RavZ. Note that RFP-2xFYVE selectively binds to PI(3)P. PI(3)P enrichment is visible in VROs in control *N. benthamiana* cells. Scale bars represent 10  $\mu$ m. See more details in panel A above.

(C) Confocal microscopy images show PI(3)P distribution in NBR1-silenced (NBR1-KD) or TRV2-cGFP control (bottom image) *N. benthamiana* protoplasts expressing p33-BFP. See more details in panel A above.

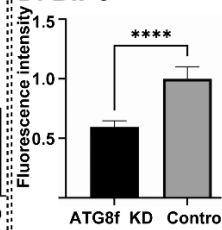
### A. ATG8f KD



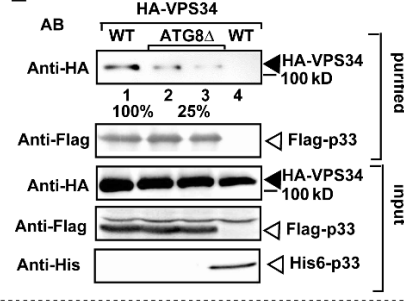
### B



### D. BiFC



### E



### C. BiFC

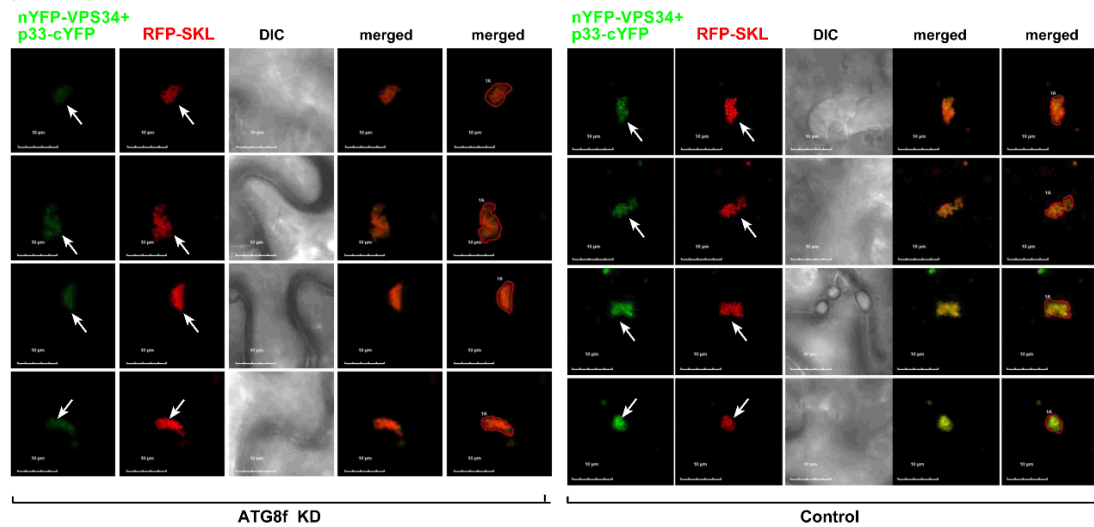


Figure 3.10

Figure 3.10. *ATG8f* promotes the enrichment of VPS34 PI3 kinase within VROs in *N. benthamiana* plants and yeast.

(A) Confocal microscopy images show co-localization of TBSV p33-BFP replication protein and the AtVPS34-GFP, the PI(3) kinase, in ATG8f-silenced (ATG8f-KD) (top image) or TRV2-MBP control (bottom image) *N. benthamiana* cells. (B) Quantitative GFP fluorescence intensity values were measured for ~50 samples to calculate relative AtVPS34-GFP levels in VROs. The statistical analysis was performed using a t-test, and the results showed a significant difference between the two groups ( $p < 0.05$ ). Each experiment was repeated. (C) BiFC-based assay was used to measure the effect of ATG8f knockdown on enrichment of VPS34 in VROs. *N. benthamiana* plants expressed TBSV p33-cYFP and AtVps34-nYFP in ATG8f-silenced (ATG8f-KD) (left panels) or TRV2-MBP control (right panels). (D) YFP fluorescence intensity values were quantified using Image J. YFP fluorescence intensity in control was arbitrarily set as 1. Error bars represent SD ( $n = 60$ ). Student t-test was used for statistical analysis of data (\*\*\*\*P < 0.0001). (E) Co-purification of HA-VPS34 with Flag-p33 from either *atg8Δ* or WT (BY4741) yeasts. The membrane fraction of yeasts was detergent-solubilized and Flag-p33 was purified on the anti-Flag column, followed by elution. Western blotting was used to detect the co-purified HA-VPS34 using anti-HA antibody. Bottom panels: western blot of input HA-VPS34 in the total yeast extracts.

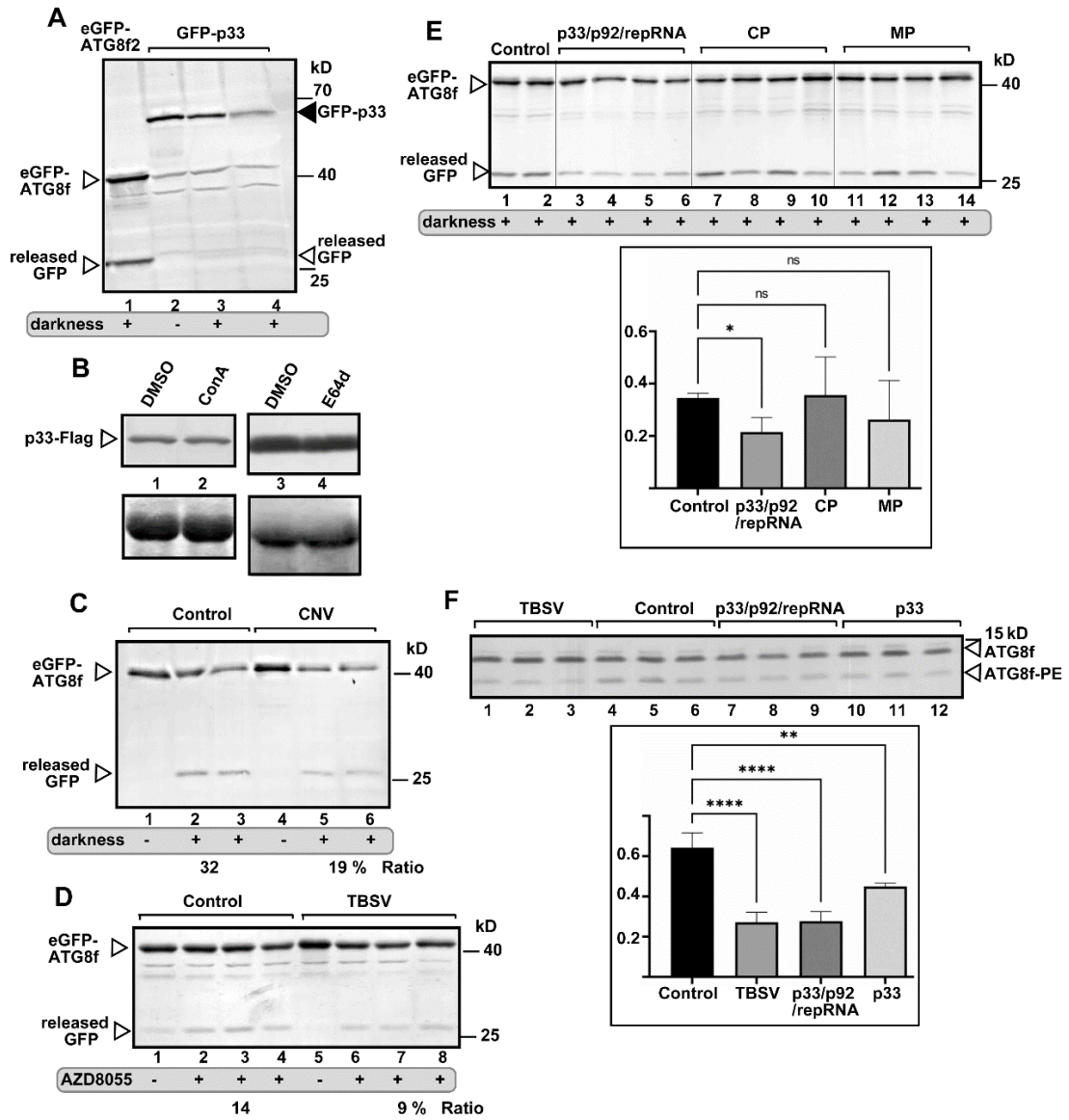


Figure 3.11

Figure 3.11. TBSV replication protein inhibits autophagic flux in *N. benthamiana*.

(A) Agroinfiltrated *N. benthamiana* plants expressing GFP-p33 were exposed to darkness for 16 h to induce bulk autophagy (lanes 3 and 4) or kept under normal condition (lane 2). Total protein extracts were probed using western blot with anti-GFP antibody. *N. benthamiana* plants expressing GFP-ATG8f were used as a control (lane 1). The released 'free' GFP is marked with an arrowhead. (B) TBSV p33-Flag was expressed in *N. benthamiana* plants via agroinfiltration. 2.5 days later, the agroinfiltrated leaves were treated with either 1  $\mu$ M ConA or 100  $\mu$ M E64d to inhibit autophagic degradation and samples were taken after 16 h. Western blotting was done with anti-Flag antibody. (C) Expression of GFP-ATG8f in *N. benthamiana* infected with CNV<sup>20kstop</sup> (lanes 4-6) or pGD vector as the control (lanes 1-3) was done through agroinfiltration. At 1.5 dpi, two plants from each group were exposed to darkness for 16 h. Total protein extracts were probed using western blot with anti-GFP antibody. The released 'free' GFP is marked with an arrowhead. Autophagic flux was measured based on the ratio of GFP/GFP-ATG8f using Image J software. (D) Expression of GFP-ATG8f in *N. benthamiana* infected with TBSV (lanes 5-8) or pGD vector as the control (lanes 1-4) was done through agroinfiltration. The same leaves were infiltrated with 10  $\mu$ M AZD8055 to induce bulk autophagy at 1.5 dpi or with 10  $\mu$ M DMSO. Total protein extracts were obtained 8 h later and probed using western blot with anti-GFP antibody. The released 'free' GFP is marked with an arrowhead. Autophagic flux was measured based on the ratio of GFP/GFP-ATG8f using Image J software. (E) Expression of GFP-ATG8f (i) with the pGD vector as the control (lanes 1-2), (ii) with TBSV p33/p92/repRNA combination (lanes 3-6), (iii) with the TBSV coat protein (CP) (lanes 7-10) or (iv) with the movement protein (MP) (lanes 11-14) in *N. benthamiana* leaves was done through agroinfiltration. At 1.5 dpi all plants underwent 16 h darkness treatment. See more details in panel B above. The statistical analysis was performed using an ANOVA-test, and the results showed a significant difference between the control and 'p33/p92/repRNA combination group' ( $p < 0.05$ ), while no significant difference between the control and CP or MP. (F) Expression of Flag-ATG8f (i) with the pGD vector as the control (lanes 4-6), (ii) with TBSV (lanes 1-3) (iii) with p33/p92/repRNA combination (lanes 7-9), or (iv) with TBSV p33 in *N. benthamiana* leaves was done through agroinfiltration. At 2 dpai, total protein extracts were obtained and probed using western blot with anti-Flag antibody. Autophagic flux was measured based on the ratio of ATG8f-PE/ATG8f using Image J software. The statistical analysis was performed using an ANOVA-test. \*\* ( $p < 0.01$ ), \*\*\*\* ( $p < 0.0001$ ). Each experiment was repeated.

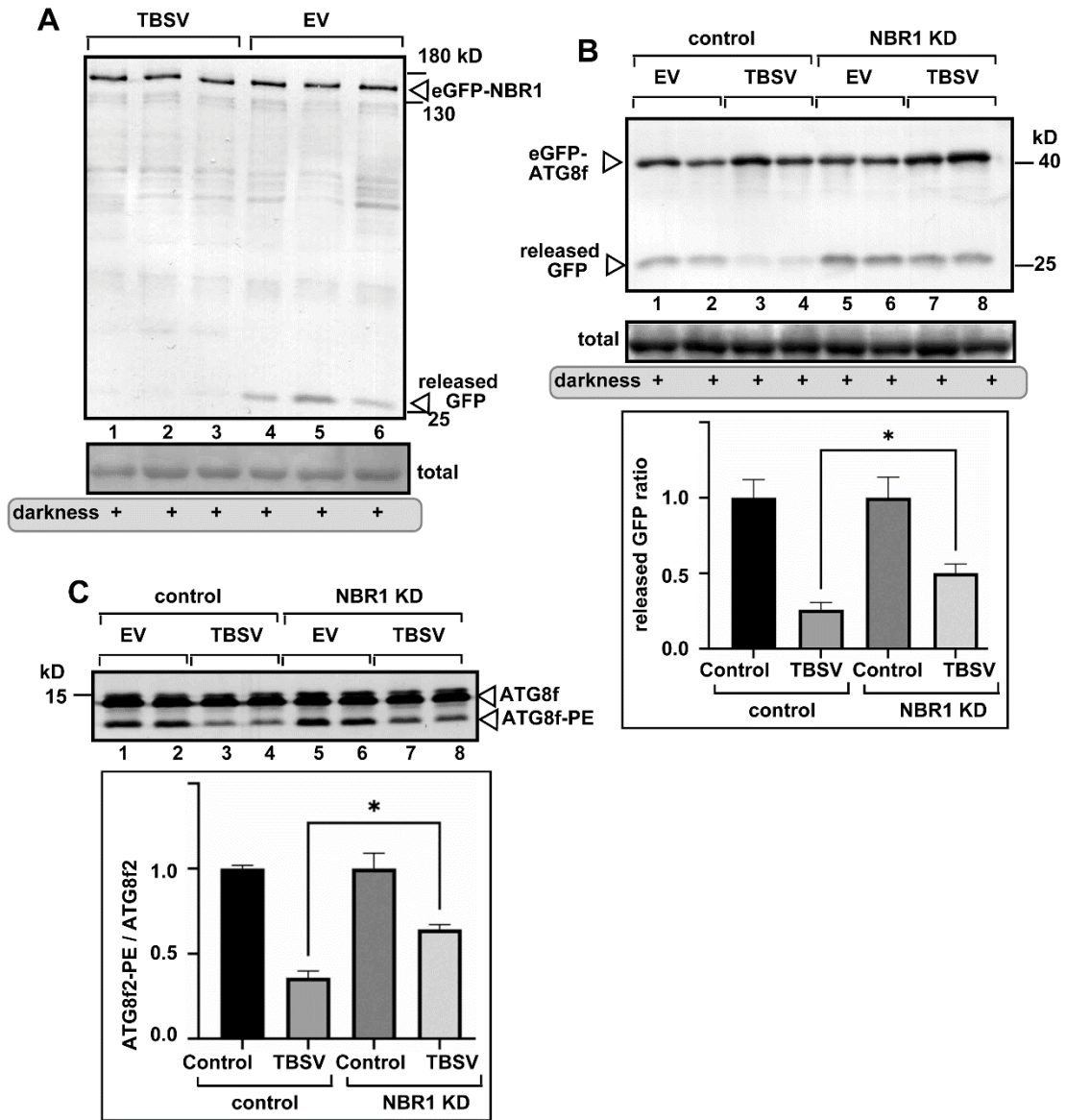


Figure 3.12



Figure 3.12. *NBR1* affects inhibition of autophagic flux by TBSV in *N. benthamiana*.

(A) Agroinfiltrated *N. benthamiana* plants co-expressing eGFP-NBR1 and either TBSV (lanes 1-3) or pGD vector control (lanes 4-6) were exposed to darkness for 16 h to induce bulk autophagy. Total protein extracts were obtained at 2 dpi and probed using western blot with anti-GFP antibody. The released ‘free’ GFP is marked with an arrowhead. (B) VIGS was used to obtain NBR1-silenced (NBR1-KD) or control (TRV2-MBP) *N. benthamiana* plants. Then, 10 days later, agroinfiltration was used to co-express GFP-ATG8f and either TBSV (lanes 3-4 and 7-8) or pGD vector control (lanes 1-2 and 5-6). Plants were exposed to darkness for 16 h to induce bulk autophagy. Total protein extracts were obtained and probed using western blot with anti-GFP antibody. The released ‘free’ GFP is marked with an arrowhead. Autophagic flux was measured based on the ratio of GFP/GFP-ATG8f using Image J software. We used the controls (1.0 value) for normalization of inhibition of autophagy by TBSV for each group. (C) VIGS was used to obtain NBR1-silenced (NBR1-KD) or control (TRV2-MBP) *N. benthamiana* plants. Then, 10 days later, agroinfiltration was used to co-express Flag-ATG8f and either TBSV (lanes 3-4 and 7-8) or pGD vector control (lanes 1-2 and 5-6). At 2 dpi, total protein extracts were obtained and probed using western blot with anti-Flag antibody. Autophagic flux was measured based on the ratio of ATG8f-PE/ATG8f using Image J software. We used the controls (1.0 value) for normalization of inhibition of autophagy by TBSV for each group. Each experiment was repeated. The statistical analysis was performed using an ANOVA-test. \* ( $p < 0.05$ ).

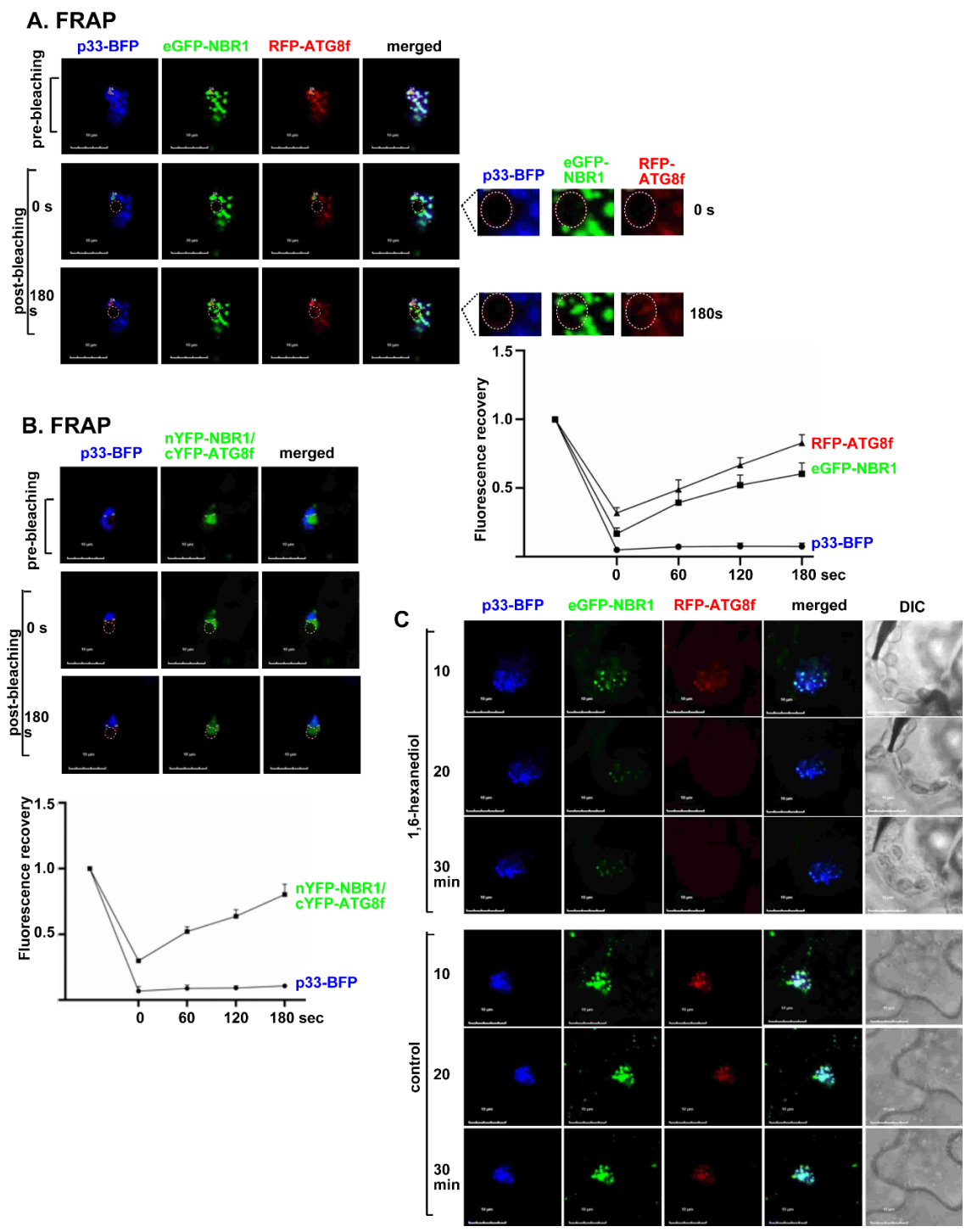


Figure 3.13

*Figure 3.13. ATG8f and NBR1 are present in condensates associated with the TBSV VROs.*

(A) Agroinfiltrated *N. benthamiana* leaves co-expressing p33-BFP, eGFP-NBR1 and RFP-ATG8f were used in fluorescence recovery after photobleaching (FRAP) assay. Confocal images were taken before and after photobleaching for 180 sec. Time '0 s' indicates the time of photobleaching. Scale bars represent 10  $\mu$ m. Right panel: Quantification of FRAP signals of p33-BFP, eGFP-NBR1 and RFP-ATG8f in the photobleached area was done at the indicated time points after photobleaching. (B) FRAP analysis shows the fluorescence recovery of the BiFC signals after photobleaching within a single VRO induced by TBSV p33-BFP in a *N. benthamiana* cell. Agroinfiltrated *N. benthamiana* plants co-expressed nYFP-NBR1 and cYFP-ATG8f and p33-BFP. The graph shows the extent of fluorescence recovery in four individual VROs. (C) Agroinfiltrated *N. benthamiana* leaves co-expressing p33-BFP, eGFP-NBR1 and RFP-ATG8f for 1.5 d were treated with 10% 1,6-hexanediol or digitonin (control) for 30 min with 10 min intervals. Confocal images of four individual VROs were taken every 10 min. Scale bars represent 10  $\mu$ m. Each experiment was repeated three times.

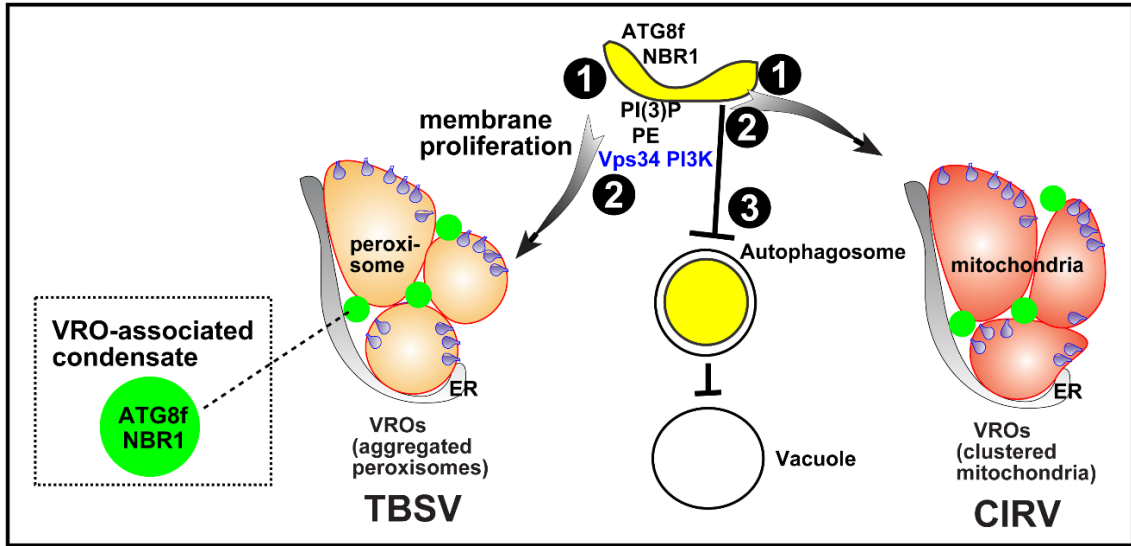


Figure 3.14

*Figure 3.14. A model on subversion of selective autophagy for tombusvirus replication and inhibition of antiviral autophagy via sequestration of NBR1 and ATG8f in VRO-associated condensates.*

(#1) The TBSV p33 replication protein recruits ATG8f and NBR1 and other core autophagy proteins into VROs formed from clustered peroxisomes. The CIRV p36 replication protein performs comparable recruitment into VROs formed from clustered mitochondria. The co-opted ATG8f and NBR1 are sequestered and ‘trapped’ in condensates associated with VROs. (#2) Hijacking the autophagy pathway results in recruitment of VPS34 PI3 kinase and enrichment of phospholipids, such as PE and PI(3)P phosphoinositide needed for VROs biogenesis. (#3) Sequestration of ATG8f and NBR1 in VRO-associated condensate leads to inhibition of antiviral cellular autophagy, thus facilitating tombusvirus replication.

S1 FIG

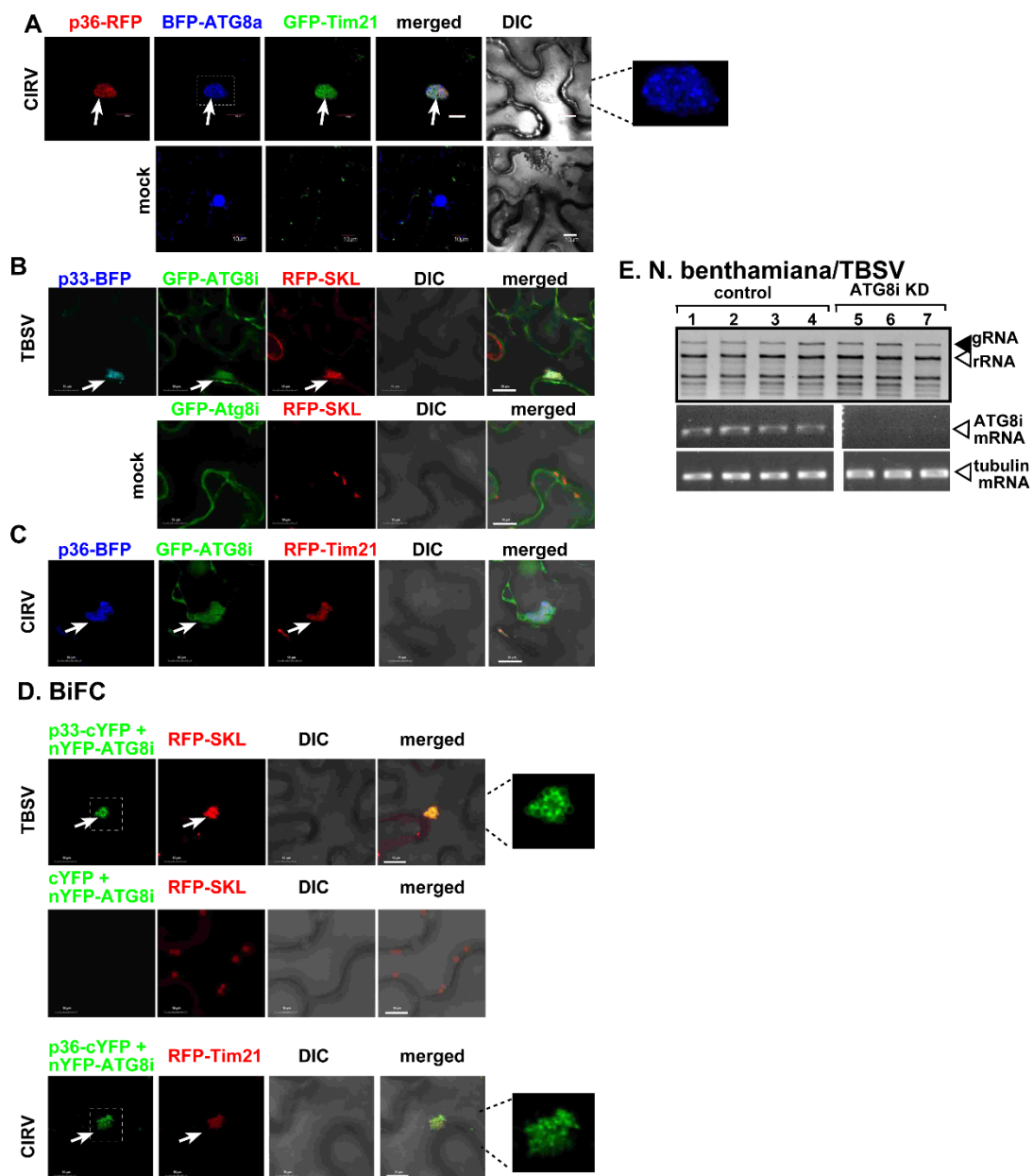
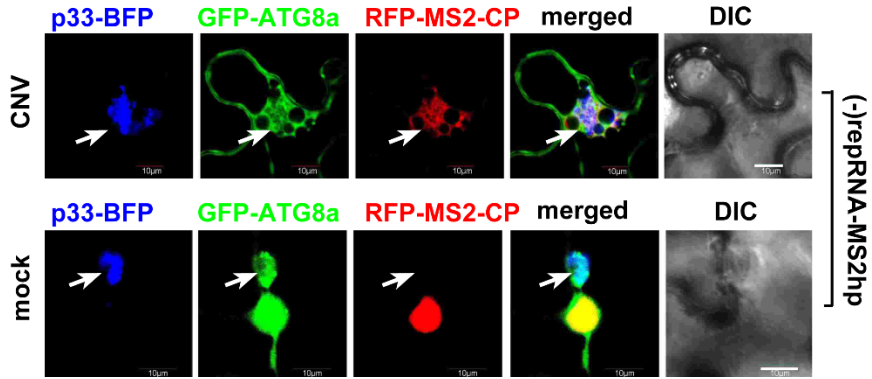


Figure S3.1

*Figure S3.1. Role of ATG8a and ATG8i in tombusvirus replication in N. benthamiana.*

(A) Confocal microscopy images show co-localization of CIRV p36-RFP replication protein and BFP-ATG8a within VROs in *N. benthamiana* leaves. See further details in Fig 1A. (B) Confocal microscopy images show co-localization of TBSV p33-BFP replication protein and GFP-ATG8i within VROs consisting of clustered peroxisomes, marked by RFP-SKL peroxisomal matrix marker in *N. benthamiana* leaves. The expression of these proteins, driven by the 35S promoter, was achieved through co-agroinfiltration into *N. benthamiana* leaves. The plant leaves were TBSV-infected as shown. Scale bars represent 10  $\mu\text{m}$ . (C) Confocal microscopy images show co-localization of CIRV p36-BFP replication protein and the GFP-ATG8i within VROs consisting of clustered mitochondria, marked by RFP-AtTim21 mitochondrial marker in *N. benthamiana* leaves. See further details in panel A. (D) BiFC experiments revealed interaction of nYFP-ATG8i with both TBSV p33-cYFP and CIRV p36-cYFP replication proteins. The merged images show co-localization of RFP-SKL (top panel) or RFP-AtTim21 (bottom panel) with the BiFC signals, indicating that the interactions take place in VROs. Scale bars represent 10  $\mu\text{m}$ . (E) Top panel: The accumulation of the TBSV genomic (g)RNA in ATG8i-silenced (ATG8i KD) *N. benthamiana* plants at 2 dpi is shown in an ethidium-bromide stained gel. Inoculation with TBSV sap was done 10 days after silencing of ATG8i expression. TRV vectors carrying either ATG8i or 3'-terminal GFP (as a control) sequences were used to induce VIGS. Second panel: Semi-quantitative RT-PCR analysis of ATG8i mRNA level in the silenced and control plants. Third panel: Semi-quantitative RT-PCR analysis of tubulin mRNA level in the silenced and control plants. The bottom two panels were from the same gels, respectively. Each experiment was repeated.

**S2 FIG**



*Figure S3.2*



*Figure S3.2. Co-localization of the minus-strand of replicon RNA with ATG8a in VROs in N. benthamiana leaves infected with CNV.*

The (-)replicon RNA [(-)repRNA-MS2hp] is based on DI-72 replicon RNA. However, it also carries 6 copies of the 19 nt long hairpin sequence from the MS2 phage, which is specifically recognized by the RFP-tagged MS2-CP (coat protein). Note that the hairpin structures form only on the minus strand RNAs, which are made during replication. RFP-MS2-CP is localized to the nucleus in the absence of replication of (-)repRNA-MS2hp (no helper CNV infection). Confocal microscopy images show the co-localization of the minus strand (-)repRNA-MS2hp, which is the replication intermediate, with GFP-ATG8a within the VRO. The VRO is marked by TBSV p33-BFP. Expression of the above proteins and the (-)repRNA-MS2hp was from 35S promoter via co-agroinfiltration into *N. benthamiana* leaves also infected with CNV to provide the replication proteins. Scale bars represent 10  $\mu\text{m}$ . The experiment was repeated.

(Note: Experiments in Figure S3.2 were in collaboration with Dr. Wenwu Lin)

S3 FIG

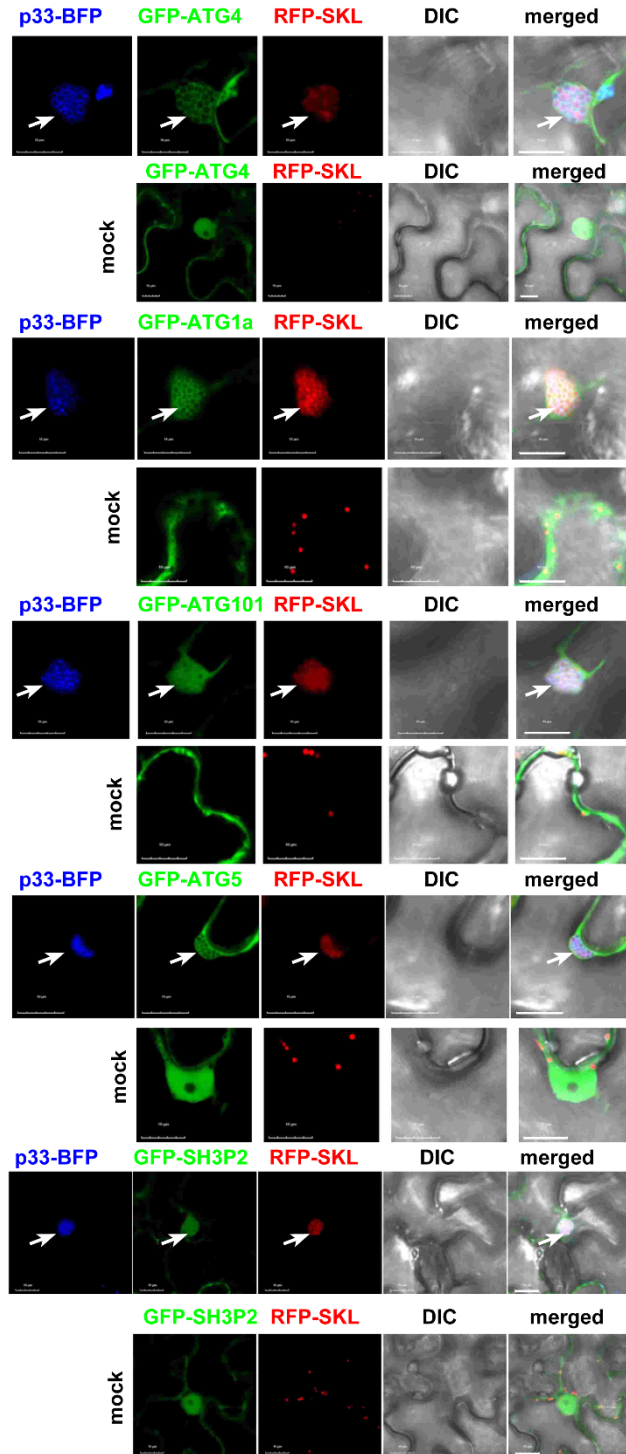


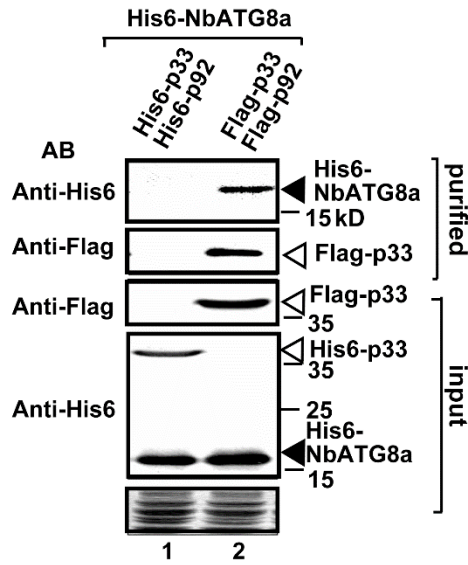
Figure S3.3

*Figure S3.3. Recruitment of core ATG proteins by the TBSV p33 replication protein into VROs in N. benthamiana.*

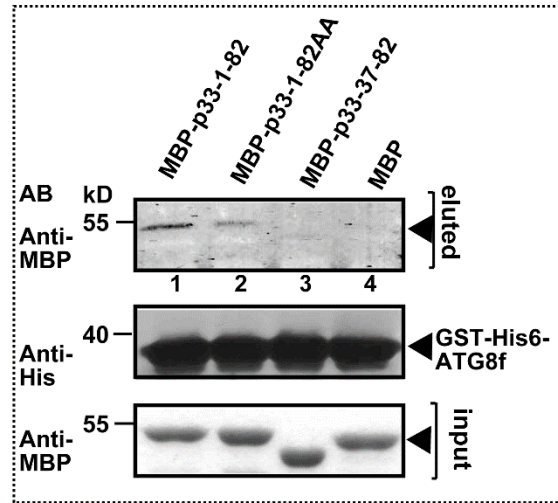
Confocal microscopy images show co-localization of TBSV p33-BFP replication protein and ATG proteins (GFP-AtATG4, GFP-NbATG5, GFP-NbATG1a, GFP-NbATG101, and GFP-AtSH3P2) within VROs consisting of clustered peroxisomes, marked by RFP-SKL peroxisomal matrix marker in *N. benthamiana* leaves. Control experiments included the localization of the above ATG proteins in the absence of TBSV p33-BFP replication protein. The expression of these proteins, driven by the 35S promoter, was achieved through co-agroinfiltration into *N. benthamiana* leaves. Scale bars represent 10  $\mu\text{m}$ . Each experiment was repeated.

## S4 FIG

### A. copurification/yeast



### B. pulldown



### C. MYTH

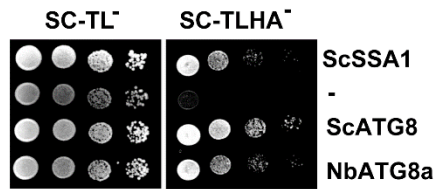


Figure S3.4

*Figure S3.4. Additional experiments to confirm interactions between tombusvirus replication proteins and ATG8.*

(A) Co-purification of His<sub>6</sub>-NbATG8a with TBSV Flag-p33 and Flag-p92<sup>pol</sup> replication proteins from subcellular membranes of yeast. Top two panels: western blot analysis of co-purified His<sub>6</sub>-NbATG8a detected with anti-His antibody, while Flag-p33 was detected with anti-Flag antibody. The negative control was from yeast expressing His<sub>6</sub>-p33 purified on a Flag-affinity column (lane 1). Samples were cross-linked with formaldehyde. Bottom two panels: western blot of input His<sub>6</sub>-NbATG8a and Flag-p33 in the total yeast extracts. (B) Pulldown assay including GST-His<sub>6</sub>-ATG8f and the MBP-tagged TBSV p33 replication protein. Note that we used the soluble N-terminal region (1-82 aa) of TBSV p33, which contains the predicted AIM1 motif (NIFQLV). The F and V amino acids were mutated to As to eliminate the canonical AIM1 in p33-1-82AA (S4B Fig, lane 2). Top panel: western blot analysis of the eluted MBP-p33 protein was performed with anti-MBP antibody. The negative control was the MBP (lane 4). Middle panel: Western blot analysis of the eluted GST-His<sub>6</sub>-ATG8f from the GST column. Bottom panels: Coomassie-blue stained SDS-PAGE of affinity-purified MBP-p33 proteins and MBP from *E. coli*. (C) The split ubiquitin-based MYTH assay was used to test binding between either GST-His<sub>6</sub>-ScATG8 or GST-His<sub>6</sub>-NbATG8a and TBSV p33 protein in yeast. The bait p33 was co-expressed with the shown prey proteins. The bait p33 and the empty prey vector (NubG) were used as negative controls, and the bait p33 and ScSSA1 as a positive control, respectively. The right panel shows the interactions, whereas the left panel demonstrates that comparable amounts of yeasts were used for these experiments.

(Note: Experiments in Figure S3.4 A and C were in collaboration with Dr. Wenwu Lin)

### S5 FIG

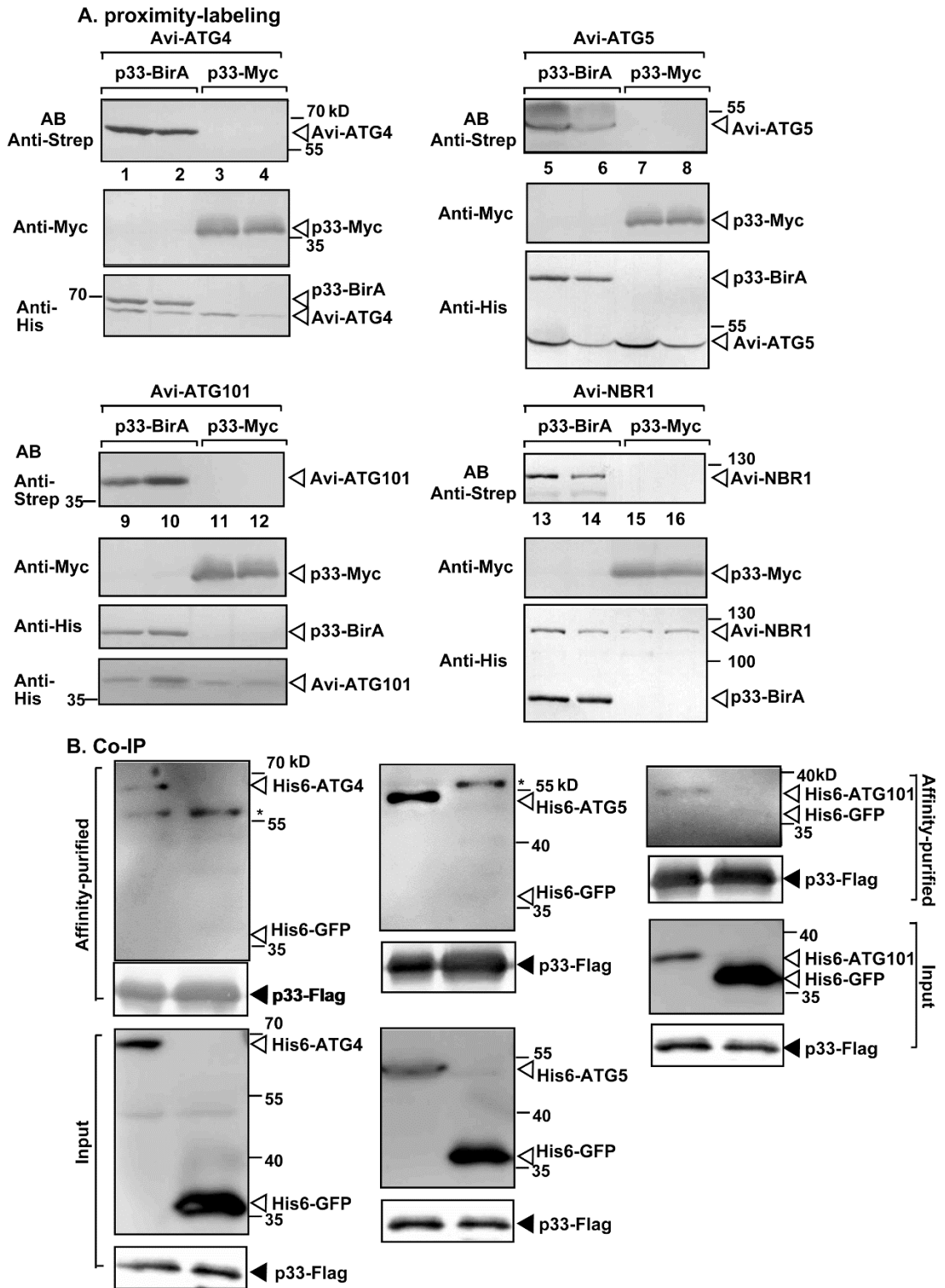
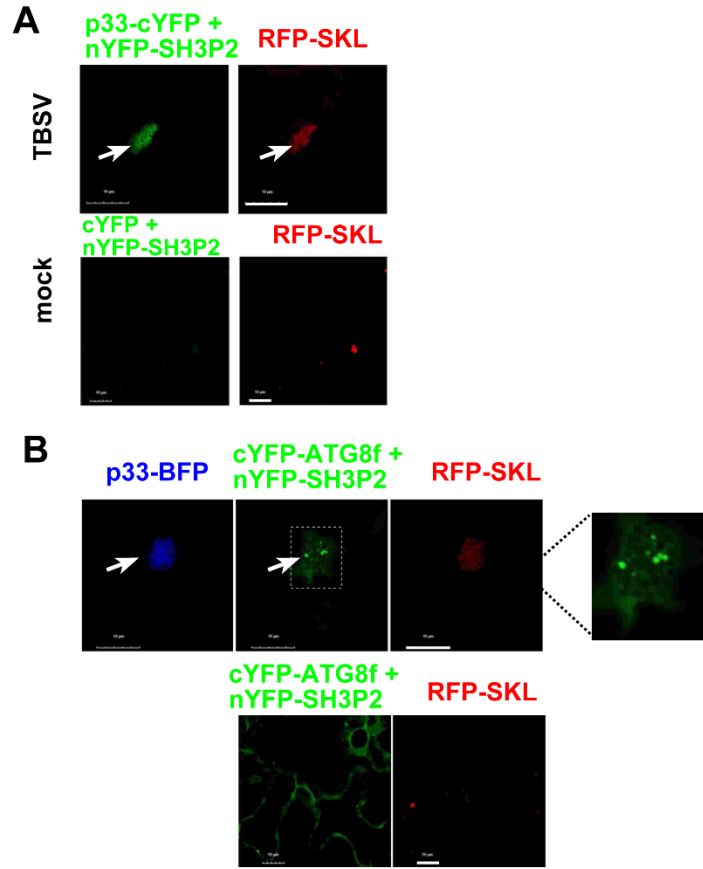


Figure S3.5

*Figure S3.5. Interactions between TBSV p33 replication protein and core ATG proteins in N. benthamiana.*

(A) Protein proximity-labeling was performed with biotin *in planta*. *N. benthamiana* leaves were agroinfiltrated to express p33 replication protein, which was fused to BirA biotin ligase, and Avi-tagged ATG proteins (Avi-ATG4, Avi-ATG5, Avi-ATG101 and Avi-NBR1). Biotin treatment lasted for 40 min. The image shows the western blot analysis of the biotinylated Avi-ATG proteins and Avi-NBR1 detected with streptavidin-conjugated AP in total protein extracts. The experiment was repeated. (B) Co-purification of ATG proteins (His<sub>6</sub>-ATG4, His<sub>6</sub>-ATG5, or His<sub>6</sub>-ATG101) with TBSV Flag-p33 replication protein from *N. benthamiana* plants. Top two panels: western blot analysis of co-purified His<sub>6</sub>-ATG proteins detected with anti-His antibody, whereas Flag-p33 was detected with anti-Flag antibody. Bottom panel: western blot of total His<sub>6</sub>-ATG proteins in the total protein extracts.

**S6 FIG**



*Figure S3.6*



*Figure S3.6. SH3P2 interacts with TBSV p33 replication protein and ATG8f within VROs in N. benthamiana.*

(A) Interaction between TBSV p33-cYFP replication protein and the nYFP-SH3P2 protein was detected by BiFC. The merged images show the co-localization of RFP-SKL with the BiFC signals, indicating that the interaction between p33 replication protein and SH3P2 occurs in VROs in clustered peroxisomal membranes. Scale bars represent 10  $\mu\text{m}$ . (B) BiFC assay was conducted to demonstrate the interaction between nYFP-SH3P2 and cYFP-ATG8f proteins within the p33-BFP-positive VROs. The expression of proteins was achieved via co-agroinfiltration into *N. benthamiana* leaves. Scale bars represent 10  $\mu\text{m}$ . Each experiment was repeated three times.

## S7 FIG

*N. benthamiana*

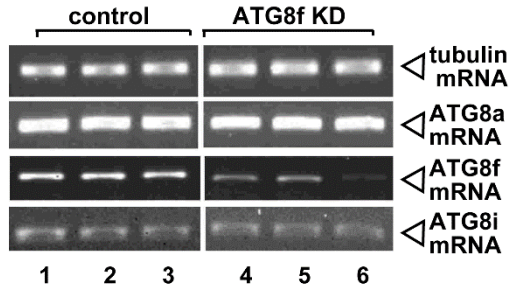


*Figure S3.7*

*Figure S3.7. Semi-quantitative RT-PCR analysis of mRNA levels of ATG8 family members in ATG8f silenced plants.*

The semi-quantitative RT-PCR analysis was conducted on the same set of plant samples to assess the effectiveness of ATG8f silencing. The second panel shows comparable mRNA levels of ATG8a and bottom panel for ATG8i, indicating selective gene silencing of ATG8f. Top panel: Semi-quantitative RT-PCR analysis of tubulin mRNA level in the ATG8f-silenced (lanes 4-6) and control (lanes 1-3) plants. The panels were from the same gels, respectively. The experiment was repeated.

**S8 FIG**

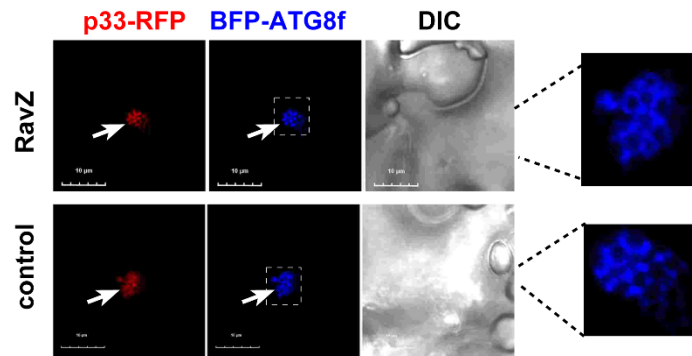


*Figure S3.8*

*Figure S3.8. Nonlipidated ATG8f is recruited by TBSV p33 replication protein into VROs.*

Confocal microscopy images show co-localization of RFP-ATG8f and p33-BFP in *N. benthamiana* cells. The leaves either expressed GFP-RavZ effector (top panel), or pGD vector as control (bottom panel). The VROs are marked with arrows. See further details in Fig 6B. The experiment was repeated.

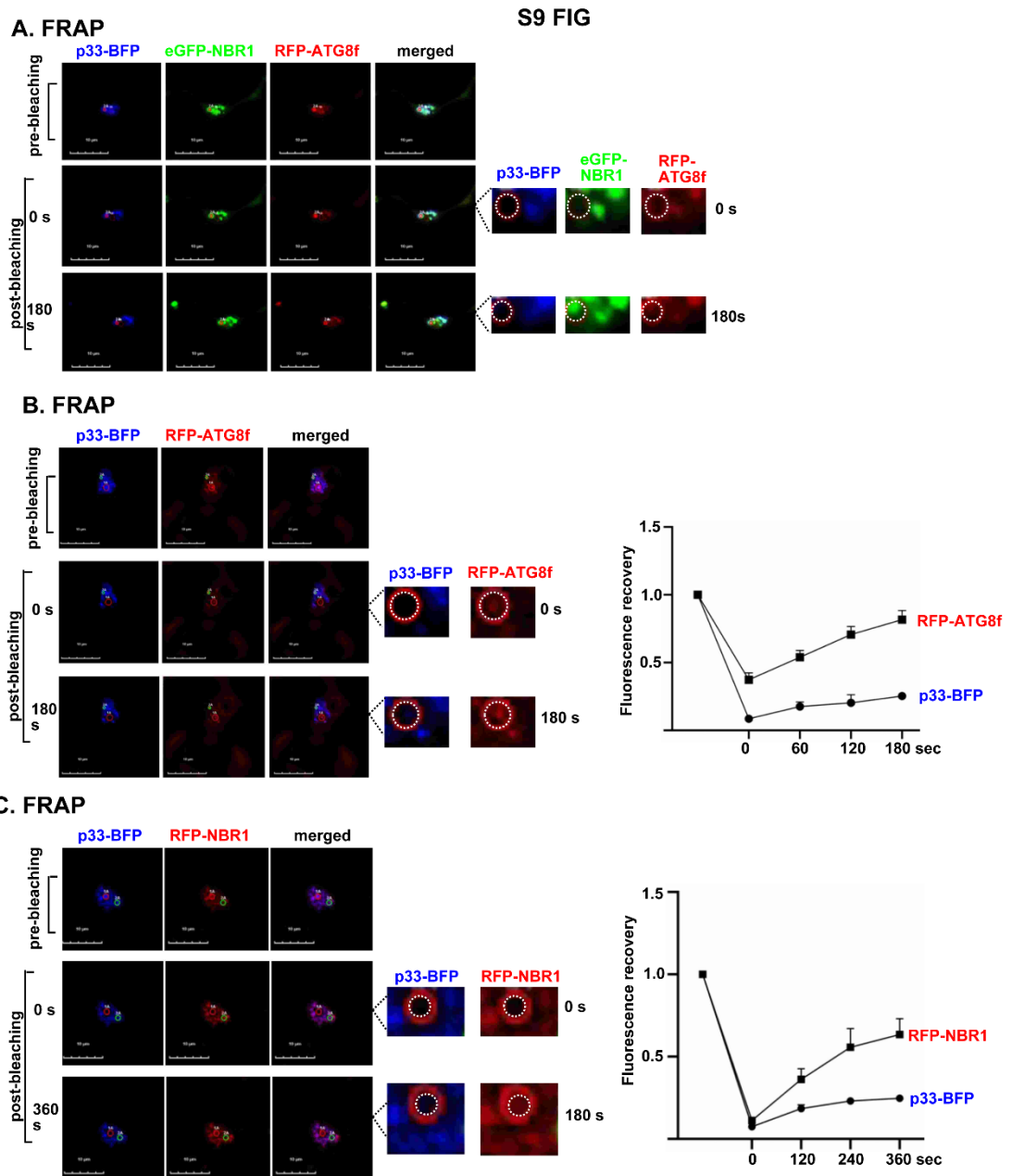


Figure S3.9

*Figure S3.9. FRAP analysis of ATG8f and NBR1 shows their presence in condensates associated with the TBSV VROs.*

(A) Agroinfiltrated *N. benthamiana* leaves co-expressing p33-BFP, eGFP-NBR1 and RFP-ATG8f were used in fluorescence recovery after photobleaching (FRAP) assay. Confocal images were taken before and after photobleaching for 180 sec. Time '0 s' indicates the time of photobleaching. Note that we selected a large punctate structure for photobleaching. Scale bars represent 10  $\mu$ m. (B-C) Agroinfiltrated *N. benthamiana* leaves co-expressing p33-BFP and RFP-ATG8f (B) or p33-BFP and RFP-NBR1 (C) were used in a FRAP assay. Confocal images were taken before and after photobleaching for 180-360 sec. Time '0 s' indicates the time of photobleaching. Scale bars represent 10  $\mu$ m. Quantification of FRAP signals of p33-BFP, RFP-ATG8f and RFP-NBR1 in the photobleached area was done at the indicated time points after photobleaching. Confocal images of four individual VROs were taken. Scale bars represent 10  $\mu$ m. Each experiment was repeated three times.

S10 FIG

A. FRAP

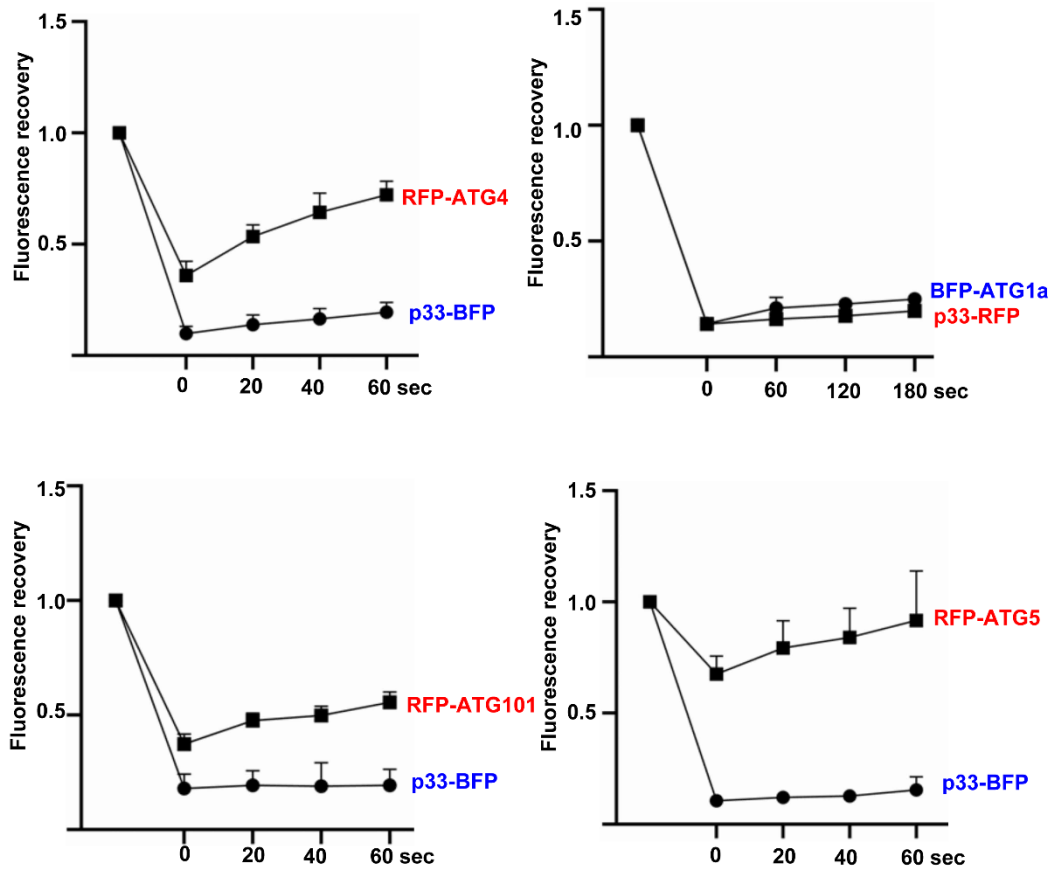


Figure S3.10



*Figure S3.10. FRAP analysis of core ATG8 proteins in the TBSV VROs.*

(A) Agroinfiltrated *N. benthamiana* leaves co-expressing p33-BFP, and one of following: RFP-ATG4, BFP-ATG1a, RFP-ATG101 and RFP-ATG5 were used in FRAP assays. Confocal images were taken before and after photobleaching for 60-180 sec. Time '0 s' indicates the time of photobleaching. Quantification of FRAP signals of p33-BFP, RFP-ATG4, BFP-ATG1a, RFP-ATG101 and RFP-ATG5 in the photobleached area was done at the indicated time points after photobleaching. Confocal images of four individual VROs were taken. Each experiment was repeated three times.

## CHAPTER 4.

### FUNCTIONAL ROLE OF ATG2 AS A LIPID TRANSPORT PROTEIN IN TOMBUSVIRUS REPLICATION

#### 4.1 Introduction

Positive-strand RNA viruses are infectious to eukaryotic organisms, causing a series of diseases (213-215). With relatively small genomes, positive-strand RNA viruses co-opt a variety of host factors to facilitate their replication in host cells (9, 10). One critical step of this replication process is the biogenesis of viral replication organelles (VROs), housing numerous membrane-bound viral replicase complexes (VRCs). For smaller-genome viruses like TBSV, the typical size range of VROs is around 40 nm-70 nm, while larger-genome viruses like coronaviruses may have VROs reaching sizes up to 250 nm. (96, 216). VROs play a pivotal role in sequestering viral (+) RNA as well as co-opted host proteins to support efficient replication through concentrating the key elements of replication in a specific area inside the cells (4). Additionally, the VRCs serve a physical protective function by shielding the viral (+) RNA by re-modeling host cellular membranes to escape from host antiviral immune system, such as RNA interference (RNAi) in plants and mammals (217, 218). Collectively, for positive-strand RNA viruses, the successful establishment of stable and complete VROs is crucial for their replication, subsequent proliferation, and transmission among host cells.

Tomato Bushy Stunt Virus (TBSV), a small positive-strand RNA virus of plants, has emerged as an excellent model organism for unraveling the molecular mechanisms of positive-strand RNA virus replication within the host cells (9, 10, 167, 211, 219). TBSV

encodes five proteins, with two replication proteins, the p92 RNA-dependent RNA polymerase (RdRp) and the p33 replication protein, playing an important role in the establishment of VROs (1, 4). p33 serves as a master regulator in template RNA recruitment (7), RNA synthesis initiation (8), and host factors recruitment (9, 10). The assembly of the viral replicase and its association with subcellular membranes are facilitated by the transmembrane domains of p33 and p92, along with p33:p92 interaction (11). An extensive genome-wide screen and gene function analysis conducted with TBSV in yeast and plants identified numerous pro-viral host factors involved in viral RNA replication and VROs establishment (14, 167, 211). These factors participate in various cellular physiological processes, including the synthesis and metabolism of nucleic acids, proteins, and lipids, as well as intracellular transport, targeted protein degradation, and recycling processes (9, 10, 32, 167, 211, 220).

TBSV primarily establishes its own VROs in plants and yeast by hijacking and aggregating peroxisomes (21). In the process of VROs formation induced by TBSV, a pivotal event is the establishment of virus-induced membrane contact sites (vMCS) (39). The formation of the vMCS is advantageous for the rapid and substantial acquisition of necessary lipid components from the endoplasmic reticulum (ER) to the virus VROs. This enables the modification of peroxisome membrane composition, leading to the formation of specific negative curvature by phosphatidylethanolamine (PE) enrichment and a membrane environment conducive to TBSV replication (25). There are two main types of MCS under discussion currently. The first type involves oxysterol-binding proteins acting as lipid transfer proteins (LTP), binding to phosphatidylinositol 4-phosphate (PI4P) enriched on the virus hijacked acceptor membrane. The assistance of ER-resident VAP

(VAMP-associated protein) and a phosphoinositide (PI) gradient formed by Sac1 PI4P phosphatase facilitates the specific exchange of sterols from the ER membrane to the VRO-associated membrane, contributing to the formation and structural stability of VROs (39, 40). In addition to these three main proteins, previous studies have identified other host proteins, ER-resident soluble NSF attachment protein receptor (SNARE) proteins, Fis1 mitochondrial fission protein and Atg11 autophagy related scaffold protein, participating in vMCS formation (97, 167, 211). Although these proteins are not directly involved in lipid exchange, their significance is in triggering vMCS formation and maintaining its structural stability, facilitating sustained lipid exchange.

In contrast to the MCS type mentioned above, which exchanges sterols with PI4P specificity and modifies membrane component precisely, another MCS type involves the rapid and bulk transport of various phospholipids from the donor membrane to the acceptor membrane through the specific bridge-like LTPs (221). An example is vacuolar protein sorting 13 homologue (Vps13), where its C-terminus selectively binds to the receptor membrane, determining the direction of lipid transport, while its N-terminus forms a nonspecific glycerolipids binding hydrophobic channel, facilitating the rapid and bulk transport of multiple lipids (222, 223). The formation of these two types of MCS overcomes the drawbacks of ATP-consuming and slow lipid vesicular trafficking, enabling efficient exchange of specific lipid types. This assists the virus in rapidly modifying subverted host membranes to establish VROs, promoting extensive proliferation and dissemination.

Autophagy-related protein 2 (Atg2) is a crucial component in the intricate machinery of autophagy, contributing significantly to the autophagosome formation

process (224-226). As a core member of the ATG proteins, one of the distinguishing features of Atg2 is its involvement in lipid transfer protein activities (53, 227). *In vitro* studies have demonstrated that both the full-length Atg2A protein and its N-terminal fragment possess the ability to bind and transport lipids. Furthermore, the analysis of lipids using liquid chromatography/tandem mass spectrometry has demonstrated that Atg2A predominantly associates with glycerophospholipids, such as phosphatidylcholine (PC), PE, phosphatidylinositol (PI), and phosphatidylserine (PS), exhibiting nonspecific binding (227). Despite the apparent absence of well-defined functional domains, Atg2 protein exhibits a conserved structural region in its N-terminus known as the chorein\_N region. This domain is conserved not only in Atg2 but also in Vps13. Crystallographic analysis of SpAtg2<sup>NR</sup> has revealed that this N-terminal sequence forms a hydrophobic cavity, facilitating the binding of acyl chains of phospholipids (53, 227). In its important role in autophagosome formation, Atg2 physically tethers the growing edge of the phagophore to the ER while utilizing its lipid-binding and transport functions to supply essential phospholipids from the ER, promoting the expansion of the isolating membrane (228).

In this study, we demonstrate the recruitment of the key autophagy protein, Atg2, into TBSV VROs through its interaction with the p33 replication protein. Deletion of Atg2 in yeast and knockdown of Atg2 in *Nicotiana benthamiana* resulted in decreased TBSV and CIRV replication, indicating a pro-viral role for Atg2 in tombusvirus replication. Phospholipid analysis of PE, PI3P, and PS—essential for TBSV replication—in *atg2Δ* yeast and Atg2-KD plants, highlights the importance of Atg2 in enriching the necessary phospholipids within VROs (9). This work unveils a critical proviral function for Atg2, acting as a lipid transfer protein, in the establishment of TBSV viral replication organelles.

## 4.2 Results

**Atg2 autophagy related protein exhibits pro-viral function in TBSV replication in yeast.** To investigate the role of autophagy-related proteins in TBSV replication, I conducted targeted yeast mutant screening to identify host proteins involved in this process. Using the yeast replication system, I separately expressed the tombusvirus p92<sup>pol</sup> and p33 replication proteins, along with the replicon (rep)RNA DI72, in both BY4741 yeast wild type strain and the Atg2 knock-out strain (*atg2Δ*). Northern blot analysis of repRNA accumulation indicated a decrease in TBSV replication by approximately 60% in the *atg2Δ* strain compared to the control (Fig 4.1A, lanes 4-6 versus lanes 1-3).

To determine if Atg2 is necessary for tombusvirus replication in different subcellular environments, I analyzed the replication of CIRV, which replicates in the outer membrane of mitochondria, in both the *atg2Δ* yeast mutant strain and the BY4741 wild type strain. Northern blot results showed about a 70% reduction in repRNA levels in the *atg2Δ* mutant strain (Fig 4.1B, lanes 4-6 versus lanes 1-3). However, partial recovery of replication levels was observed in the mutant strain with plasmid-based Atg2 expression (Fig 4.1B, lanes 7-9 versus lanes 4-6). Additionally, in the BY4741 strain, overexpression of plasmid-based Atg2 enhanced CIRV replication when co-expressed with replication proteins p36, p95<sup>pol</sup> (Fig 4.1B, lanes 10-12 versus lanes 1-3).

These combined results indicate that Atg2, an autophagy-related protein, acts as a pro-viral factor in different subcellular environments. This discovery provides new insights

into the intricate dynamics of tombusvirus-host interactions and presents Atg2 as a critical factor in the virus replication process.

**Pro-viral function of Atg2 in TBSV replication in plant host.** To study whether tombusviruses rely on Atg2 functions in plants, I initially employed virus-induced gene silencing (VIGS) to suppress Atg2 expression in *N. benthamiana*. The reduction of Atg2 expression levels did not lead to obvious phenotypic changes in *N. benthamiana*. After silencing the Atg2 gene, I inoculated the plants with TBSV sap by rubbing the leaves and then collected leaf samples at 1.5 days post-inoculation (dpi) for RNA extraction. Northern blot analysis revealed that the TBSV genomic RNA level in the Atg2 knockdown (Atg2-KD) plants was reduced by approximately 65% compared to the control (Fig 4.2A). I also examined CNV<sup>20KStop</sup>, a closely related virus to TBSV lacking a gene-silencing suppressor, and CIRV, which replicates on the outer membrane of mitochondria. The viral genomic RNA levels of both CNV<sup>20KStop</sup> and CIRV showed a significant decrease in the Atg2-KD plants, with about a 60% reduction for CNV<sup>20KStop</sup> (Fig 4.2B) and a 50% reduction for CIRV (Fig 4.2C), relative to the controls. Overall, these results highlight the pro-viral role of Atg2 in facilitating tombusvirus replication in both yeast and plant.

Subsequently, I analyzed the relative mRNA levels of Atg2 in both mock-treated control plants and plants inoculated with TBSV sap at 2 dpi using real-time RT-qPCR. The results showed a significant four-fold increase in Atg2 expression following TBSV inoculation (Fig 4.2D top panel). Similarly, upon CIRV inoculation, Atg2 expression significantly increased by six-fold (Fig 4.2D bottom panel). These findings indicate that tombusviruses infection induces an up-regulation of Atg2 mRNA levels.

### **Subcellular colocalization of Atg2 with tombusvirus-induced VROs in plants.**

To study if Atg2 is co-opted within TBSV-induced VROs during viral replication, I used an Agrobacterium-mediated transient expression system in *N. benthamiana* leaves to co-express GFP-tagged Atg2, BFP-tagged TBSV replication protein p33, and RFP-tagged peroxisome luminal marker SKL. Confocal fluorescence microscopy showed that at 2 dpi tobacco epidermal cells simultaneously expressed all three fluorescently tagged proteins. The locations of VROs were indicated by the aggregation of peroxisomes indicated by RFP-SKL, which was induced by the TBSV replication protein p33. Notably, the GFP-Atg2 signal colocalized with BFP-p33 within the VROs, suggesting that Atg2 is indeed co-opted during TBSV replication (Fig 4.3A). Conversely, in control plants without viral components (mock), GFP-Atg2 did not colocalize with the RFP-SKL peroxisome marker, highlighting the specific subcellular localization of Atg2 within virus-induced VROs during TBSV replication (Fig 4.3A).

I also examined the subcellular localization of Atg2 during CIRV replication. In this experiment, I utilized the same Agrobacterium-mediated co-infiltration to simultaneously express GFP-tagged Atg2, BFP-tagged CIRV replication protein p36, and RFP-tagged mitochondrial membrane marker Tim21 in *N. benthamiana* leaves. Confocal fluorescence microscopy revealed the VROs formed by CIRV, marked by aggregated mitochondria with RFP-Tim21, and the colocalization of GFP-Atg2 with BFP-p36 within these VROs (Fig 4.3B). In control plants lacking viral components, Atg2 did not colocalize with the mitochondrial marker Tim21 (Fig 4.3B). These results suggest that Atg2 is co-opted within VROs during tombusvirus replication.



**Atg2 interacts with tombusvirus replication protein in VROs.** To test whether Atg2 co-opted in VROs during viral replication is due to its interaction with tombusvirus replication proteins, I first conducted a bimolecular fluorescence complementation (BiFC) experiment in *N. benthamiana* leaves. Confocal fluorescence microscopy results revealed an interaction between Atg2 tagged with the nYFP fragment and p33 tagged with cYFP in the epidermal cells. This interaction led to the reconstitution of a fluorescent YFP molecule. The BiFC signal localized with clustered peroxisomes indicated by RFP-SKL, suggesting that Atg2-p33 interaction takes place in VROs (Fig 4.4A). Additionally, employing the same approach, I examined the interaction between Atg2 and the CIRV replication protein p36 in *N. benthamiana*. The BiFC results indicated that these proteins also interacted within plant cells, with this interaction occurring in clusters of mitochondria marked by a mitochondrial marker RFP-Tim21, indicative of CIRV VROs (Fig 4.4B). The above results suggest that Atg2 is recruited to VROs for functional roles through direct interactions with tombusvirus replication proteins p33 and p36.

To further validate the interaction between Atg2 and TBSV p33, I carried out a co-immunoprecipitation (co-IP) experiment in *N. benthamiana*. After purifying Flag-tagged p33 from the plant membrane fraction using a Flag affinity column, western blot analysis showed the presence of HA-tagged Atg2 in the purified fraction alongside Flag-p33 (Fig 4.4C, left lane). In contrast, purification of control Flag-MBP did not lead to co-purification of HA-Atg2, indicating that the co-purification of HA-Atg2 with TBSV replication protein p33 was specific (Fig 4.4C, right lane). This result suggested that Atg2 interacts with p33 in plants, providing further evidence of their association in the viral replication process.

**Atg2 facilitates PE enrichment during TBSV replication.** In our previous research, we demonstrated that PE is a crucial membrane component in the formation of TBSV-induced VROs (25). Considering that Atg2 is an LTP with the ability to bind and transfer PE, I investigated whether Atg2 participates in the transport and enrichment of PE within TBSV-induced VROs. I utilized biotinylated duramycin peptide, a bio-sensor molecule that specifically binds to PE, followed by using streptavidin conjugated with Alexa Fluor 405 to detect PE distribution. Confocal fluorescence microscopy was used to observe the intracellular distribution of PE. In yeast, I observed the formation of large VRO structures in the control BY4741 strain co-expressing GFP-labeled TBSV replication proteins p33, p92<sup>pol</sup>, and DI72. After fixing the yeast cells with 3.7% formaldehyde, I treated the yeast cell walls with Zymolyase-20T (Seikagaku, America) to create spheroplasts. Subsequently detection revealed significant co-localization of the duramycin signal within the GFP-p33 marked VROs, indicating substantial PE accumulation in VROs in WT yeast (Fig 4.5A). However, in the *atg2* $\Delta$  mutant yeast strain, there was an approximately 70% reduction in the duramycin fluorescence signal within the VROs, suggesting that *atg2* deficiency significantly impairs the ability of TBSV to enrich PE in VROs (Fig 4.5B).

To further investigate the impact of Atg2 on the enrichment of PE during TBSV replication in plant cells, I silenced the expression of the Atg2 gene in *N. benthamiana* by VIGS. At 10 dpi, RFP-labeled TBSV replication protein p33 was expressed in the upper leaves of both control and Atg2-KD plants via agrobacterium-mediated transient expression. Two days later, I isolated protoplasts from the agroinfiltrated leaves, fixed them

with 3.7% formaldehyde, and used the duramycin biosensor method to show the subcellular distribution of PE in plant cells. Confocal microscopy revealed the formation of VROs indicated by RFP-p33 in protoplasts of both the control and Atg2-KD plants (Fig 4.5C). However, compared to the control protoplasts, the intensity of the duramycin signal within the VROs was significantly reduced by about 80% in the Atg2-KD protoplasts (Fig 4.5D). This result suggests that the enrichment of PE within VROs is compromised in Atg2-KD plants. In summary, the co-opted Atg2 plays a vital role in the enrichment of PE within VROs during TBSV replication, both in yeast and plants.

**Atg2 promotes PI3P enrichment in TBSV induced VROs.** To investigate the role of Atg2 in the enrichment of PI3P during TBSV-induced VRO formation, I conducted experiments in both yeast and *N. benthamiana*. Previous research has highlighted the critical role of PI3P, despite its minor proportion in membrane composition, in TBSV-induced VRO formation (32, 126). Atg2 is a non-specific phospholipid-binding LTP capable of binding and transferring the PI3P precursor PI (227). Considering that PI in VROs is phosphorylated to PI3P by Vps34p PI3K, which is recruited to VROs by the p33 replication protein (32), I employed the PI3P-specific FYVE peptide biosensor for this study (229). In yeast, I co-expressed RFP-FVYE, along with GFP-tagged TBSV replication proteins p33, p92<sup>pol</sup>, and DI72 in the control group. Confocal microscopy results showed colocalization of RFP-FYVE signal within GFP-p33 indicated VROs, suggesting PI3P enrichment in TBSV formed VROs (Fig 4.6A). However, in the *atg2Δ* strain, the intensity of RFP-FYVE signal colocalized within GFP-p33 indicated VROs was significantly reduced by about 80%, suggesting low PI3P levels in VROs (Fig 4.6B).

Similarly, in *N. benthamiana*, I used the RFP-FYVE biosensor to monitor the subcellular distribution of PI3P. First, I used VIGS to silence *Atg2* expression in *N. benthamiana*. 10 days later, agrobacterium-mediated transient expression was performed to co-express BFP-p33 and RFP-FYVE in the upper leaves of both control and *Atg2*-KD plants. Fluorescence microscopy observations showed an accumulation of punctate RFP-FYVE signals on TBSV-induced VROs marked by BFP-P33 in control plant cells (Fig 4.6C), whereas the intensity of RFP-FYVE signals aggregated in VROs was reduced by about 70% in *Atg2*-KD plant cells (Fig 4.6D). In conclusion, *Atg2* plays an important role in facilitating the enrichment of PI3P within VROs during TBSV replication in both yeast and plants.

#### ***Atg2* contributes to the enrichment of PS in TBSV induced VROs formation.**

In previous studies, it was found that phosphatidylserine (PS) decarboxylases Psd1p and Psd2p, which catalyze the conversion of PS to PE, significantly promoting TBSV replication when no other sources of PE synthesis are available (92). This implies that PS, as a precursor of PE, plays a crucial role in TBSV replication. Additionally, *in vitro* experiments using giant unilamellar vesicles (GUVs) containing a certain proportion of PS also indicated a facilitatory effect on TBSV replication (9). These findings suggest the importance of PS in TBSV replication. To investigate whether *Atg2* is involved in the enrichment of PS in VROs during TBSV replication, I utilized the PS-specific binding Lactadherin C2 (LactC2) peptide as a biosensor to examine PS distribution within cells (230). In yeast, I co-expressed GFP-labeled LactC2 with RFP-labeled TBSV replication proteins p33, p92<sup>pol</sup>, and DI72. Confocal microscopy results showed that in BY4741

control yeast, the GFP-LactC2 signal colocalized with TBSV VROs, as indicated by RFP-p33. This suggests an enrichment of PS in the VROs formed by TBSV, while PS is mostly present in the inner leaflet of the plasma membrane (PM) in the absence of TBSV (Fig 4.7A) (231). However, in the *atg2* $\Delta$  mutant yeast strain, the GFP-LactC2 signal colocalizing with RFP-p33 was significantly reduced by about 60% (Fig 4.7B), indicating that the *atg2* deficiency impairs the ability of TBSV to enrich PS in VROs.

Similarly, in *N. benthamiana*, I used the GFP-LactC2 biosensor to detect PS distribution. After silencing the *Atg2* gene using VIGS, at 10 dpi, I co-expressed GFP-LactC2 and BFP-p33 in the upper leaves of both control and *Atg2*-KD plants. Fluorescence microscopy results revealed strong colocalization of the GFP-LactC2 fluorescence signal with BFP-p33 indicated TBSV VROs in the control plants, along with punctate GFP-LactC2 signals around the VROs (Fig 4.7C). Compared to the control plants, TBSV VROs in *Atg2*-KD plant cells showed a significant reduction of about 30% in GFP-LactC2 fluorescence intensity, with the punctate signals almost completely absent (Fig 4.7D). These results demonstrate that *Atg2* plays a key role in facilitating the enrichment of PS within VROs during TBSV replication.

**Independent role of *Atg2* in TBSV replication beyond *ATG8f* and *Atg11*-mediated lipid and sterol enrichment in VROs.** In our prior research, it was demonstrated that TBSV can suppress host autophagy, a key defense mechanism against microbial invasion that might compromise virus replication within host cells. Notably, TBSV not only inhibits this autophagic response but also manipulates autophagy-related pathways to its advantage as mentioned in chapter 3. This includes exploiting the *Atg8*-PE

pathway to enhance the accumulation of phospholipids within VROs, thereby boosting viral replication. Additionally, the Atg11 scaffold protein exhibits a novel role during TBSV replication by participating in stabilizing vMCS. This stabilization ensures a steady, non-vesicular supply of sterols essential for the maturation of TBSV VROs. Given that Atg2 is an autophagy-related gene and a lipid transfer protein typically functioning at MCS, I explored whether the function of Atg2 in facilitating phospholipid enrichment in TBSV VROs is independent of the previously identified autophagy-related proviral pathways. First, I silenced Atg5 in *N.benthamiana* plants using VIGS. Atg5 is involved in Atg8-PE conjugation, a process previously shown to be crucial for Atg8's proviral function. At 10 dpi, I co-infiltrated CNV<sup>20kstop</sup> along with either Atg2-expressing constructs or empty controls into the Atg5-KD plants. Two days later, leaf samples were collected for CNV<sup>20kstop</sup> replication analysis. Northern blot results showed that compared to the controls, expression of Atg2 in Atg5-KD plants led to a partial recovery of about 30% in CNV<sup>20kstop</sup> genomic RNA levels (Fig 4.8A), suggesting that Atg2's role in promoting TBSV replication is likely independent of the Atg8 pathway.

Subsequently, I silenced Atg11 in *N. benthamiana* using VIGS to determine if the proviral function of Atg2 is independent of the Atg11. At 10 dpi, CNV<sup>20kstop</sup> was co-infiltrated with Atg2-expressing constructs or controls into Atg11-KD plants. Northern blot analysis of total RNA from 2 dpi inoculated leaf samples revealed that compared to the controls, Atg2 expression in Atg11-KD plants led to a partial recovery of about 50% in CNV<sup>20kstop</sup> genomic RNA levels (Fig 4.8B), indicating that the proviral function of Atg2 is also likely independent of the Atg11 function.

In summary, these results indicate that Atg2 facilitates lipid enrichment in TBSV VROs through a mechanism independent of both the Atg8 and Atg11 functions.

### 4.3 Discussion

Positive-strand RNA viruses are known for manipulating host cell machinery to support their replication and survival (19, 33, 232). TBSV, in particular, exemplifies this intricate interplay between viruses and host cellular processes. TBSV utilizes various host cell processes, including autophagy and lipid metabolism, to facilitate its replication (25, 32, 92, 126, 167).

In this study, I employed yeast and plants as model organisms to investigate TBSV replication. Targeted screening among yeast mutants with autophagy-related genes identified Atg2 as a potential proviral host factor contributing to TBSV replication. The observed subcellular co-localization of Atg2 with TBSV replication protein p33 alongside their interaction, indicates that Atg2 is recruited by p33 to function within the virus induced VROs during TBSV replication. Considering the role of Atg2 as a LTP in the ER-autophagosome MCS during autophagosome formation, it is possible that Atg2 similarly operates within vMCS between ER and VROs, thereby playing a critical role in TBSV VROs formation. To validate this hypothesis, I checked the distribution of specific lipids, PE, PI3P, and PS, which are crucial to TBSV replication, in yeast *atg2Δ* strain and Atg2-KD plant cells. The results show that the absence or reduced expression of Atg2 significantly reduces the enrichment of these lipids in TBSV VROs. These results suggest that Atg2 is involved in binding and transferring key phospholipids to TBSV VROs,

thereby facilitating rapid VRO formation, membrane proliferation, and extensive viral replication.

Our previous studies have demonstrated that TBSV can suppress host autophagy—a crucial defense mechanism—potentially to avoid cellular responses that could inhibit its replication. This suppression, however, is coupled with a strategic exploitation of autophagy-related pathways. Our study on Atg2, an autophagy-related gene and LTP, shows its important role in facilitating lipid accumulation within TBSV VROs. This function of Atg2 is particularly noteworthy as it likely operates independently of other autophagy-related pathways involving Atg8-PE and Atg11, suggesting a unique mode of action during viral replication. This sophisticated strategy introduces an additional potential phospholipid resource for TBSV replication, potentially reflecting an evolutionary adaptation that may be applicable to other positive-strand RNA viruses. Investigating whether similar mechanisms exist in other viruses could provide valuable insights into universal strategies employed by viruses and potential pan-viral therapeutic targets.

In addition, the independent role of Atg2 from Atg8 and Atg11 in TBSV replication suggests a complex network of interactions within the host cell exploited by the virus. Viruses, including TBSV, can selectively and strategically hijack host cellular pathways. This strategic hijacking represents a fine-tuned evolutionary adaptation, aiming to optimize replication efficiency while minimizing damage to the host cell, thus ensuring viral survival and transmission. Moreover, understanding the selective hijacking of specific components of host cellular processes can reveal new aspects of autophagy process, potentially leading to broader applications in understanding cellular autophagy process and disease



mechanisms beyond viral infections. Our study paves the way for future research into the molecular mechanisms by which viruses manipulate host autophagy pathways. It would be fascinating to explore how TBSV, and similar viruses balance the suppression of autophagy as a defense mechanism while simultaneously exploiting autophagy-related processes for their benefit.

The ability of TBSV to manipulate host lipid metabolism is further evident in our observations on the enrichment of specific lipids such as PE, PI3P, and PS within VROs (9, 25, 32, 92). These lipids are crucial for the integrity and functionality of VROs, and our data suggest that Atg2 plays a significant role in their accumulation. During the formation of TBSV VROs, the ER serves as a primary lipid source (37). The virus orchestrates the formation of numerous vMCS between the ER and VRO containing membranes, such as those on peroxisome membranes, to enable non-vesicular lipid transport (39, 167, 211). This transport process includes not only specific modification of peroxisome membrane components through sterol exchange from the ER membrane for PI4P enriched on the VROs membrane, a process involving Osh proteins, but also the non-specific binding and transfer of phospholipids by Atg2, an LTP. The Atg2 leads to a rapid and substantial enrichment of phospholipids necessary for VRO formation, thereby facilitating extensive viral replication. Similar to the formation of VROs, the formation of any newly synthesized cellular organelles involves MCS and extensive lipid transfer through these sites. Independent of its role in autophagy, Atg2 has been found to function as an LTP within MCS, facilitating lipid transfer in lysosome repair (233). This raises an intriguing prospect that other LTPs, due to their capacity for rapid and extensive lipid transfer, might also be co-opted by viruses and hijacked into VROs or, more specifically, into vMCS, to fulfill

their roles as LTPs. This aspect of TBSV replication provides a novel perspective on the importance of lipid dynamics within viral life cycles and suggests potential directions for therapeutic intervention. Future research could focus on developing inhibitors that disrupt the interaction between viral proteins and lipid transfer proteins, including but not limited to Atg2. Such strategies could impede the formation of functional VROs, offering new approaches to combat viral infections. This study not only advances our understanding of TBSV replication mechanisms but also opens new insights for studies in the field of cell biology.

In conclusion, our study, based on the investigation of Atg2's impact on TBSV replication mechanisms in both yeast and plant hosts, unveils broader implications of virus-host interactions, particularly in the context of autophagy and lipid metabolism. The intricate interplay between viral replication strategies and host cellular responses highlights the complexity of these interactions and virus fine-tuned exploitation of host cellular processes during evolution. These insights provide fundamental theoretical support for future research into novel antiviral strategies targeting the specific host factors and pathways utilized by viruses like TBSV. Simultaneously, this study also is helpful in enhancing our understanding of cell biology by utilizing TBSV as a tool to manipulate specific cellular processes. Such an approach not only advances our knowledge of viral mechanisms but also enriching our comprehension of the dynamic nature of host-pathogen interactions.

#### 4.4 Materials and methods

**Yeast strain.** *S. cerevisiae* strain BY4741 (MATa his3 $\Delta$ 1 leu2 $\Delta$ 0 met15 $\Delta$ 0 ura3 $\Delta$ 0) was purchased from Open Biosystems and stored in a -80°C refrigerator. Yeast strain atg2 $\Delta$  was generated and described previously was generated from the BY4741 parental strain by replacing Atg2 ORF with a hphNT1 cassette sequentially using homologous recombination (131).

**Plant materials and plasmids.** Wild type *N. benthamiana* plants were potted in soil and placed in grow room at 25°C under a 16-h-light/8-h-dark cycle. GenBank accession numbers of *N. benthamiana* genes analysed in this study are as follows: NbAtg2 (KU561373), NbAtg5 (KX369397). To clone Atg2 gene in plants, we used the sequence of *Arabidopsis thaliana* Atg2 (AT3G19190). RNA extraction from *N. benthamiana* and *A. thaliana* leaves was used for gene amplification. Reverse transcription was catalysed by Moloney Murine Leukemia Virus Reverse Transcriptase (M-MLV RT) (Promega) with Oligo(dT). Plasmids constructed and primers used in this study are listed in Table.

**Virus RNA replication in yeast.** To test repRNA replication, BY4741 (wild type) and atg2 $\Delta$  strains were transformed with plasmids HpGBK-Gal1-Hisp33/Gal10-DI72, LpGAD-Gal1-Hisp92 and UpYES2-NT. To test if plasmid-borne Atg2 expression can rescue virus replication, atg2 $\Delta$  strain was transformed with HpGBK-Gal1-Hisp33/Gal10-DI72, LpGAD-Gal1-Hisp92 and UpYES2-HisAtg2. To test if over-expression of Atg2 can increase tombusvirus replication in yeast, wild type BY4741 yeast was transformed with HpGBK-Gal1-Hisp33/Gal10-DI72, LpGAD-Gal1-Hisp92 and UpYES-ScAtg2. For CIRV

replication assay, BY4741 and *atg2Δ* yeast were co-transformed with plasmids HpESC-CUP1-Flagp36/Gal10-DI72 and LpESC-CUP1-Flagp95 with either UpYES2-NT or UpYES2-HisAtg2.

For TBSV replication, the transferred yeasts were grown in SC-ULH<sup>-</sup> medium supplemented with 2% galactose for 48 h at 23°C.

For CIRV replication, the transformed yeasts were pre-grown in SC-ULH<sup>-</sup> (synthetic complete medium without urea, leucine, and histidine) media supplemented with 2% galactose media and 100 μM BCS at 23 °C for 16 h. Then, the yeast cells were cultured in SC-ULH<sup>-</sup> media supplemented with 2% galactose and 50 μM CuSO<sub>4</sub> at 23 °C for 24 h.

**Virus replication in plants.** Virus induced gene silencing (VIGS) in *Nicotiana benthamiana* was performed as described in published work (234). The *NbAtg2* N-terminal fragment of 500 bp in length (#9058: CGGGATCCCCAATCGTCGAAGGATAATCTTAGA and #9059: CCGCTCGAGTCCTGTTGATCGCTGTGCATTATTCTG) was selected to insert into TRV2 vector, to generate pTRV2-NbAtg2, which was used for VIGS in *N. benthamiana*. *Agrobacterium* competent cells C58C1 were transformed with pTRV2-NbAtg2. *N. benthamiana* plants of 4-leaves stage were agroinfiltrated with pTRV1 and pTRV2-NbAtg2 or pTRV2-cGFP as a control (OD<sub>600</sub>, 0.5). On the 10th day post agroinfiltration(dpai), upper leaves were infiltrated with *agrobacterium* harboring virus infectious clone CNV<sup>20kstop</sup> or inoculated with TBSV or CIRV sap. To determine RNA accumulation of TBSV, CNV, and CIRV, the inoculated leaves were collected at 2, 2.5 and 3 dpi, respectively. Total RNA extraction and northern blot analyses were performed as

described previously (16). The transcriptional accumulation of *NbAtg2* mRNA and internal reference control *tubulin* mRNA was determined by semi-quantitative RT-PCR with primers oligo-d(T) (for RT), #8939: ACGCagatctATGTTTCCGTGGAATTTTCGCG and #8940: TTTTGCAAAGCCCTGTCCTTTTC (for PCR to detect *NbAtg2*) and #2859 and #2860 (for PCR to detect tubulin mRNA) (16).

**Real-time RT-qPCR.** Real-time quantitative RT-qPCR was also used for the detection of *N. benthamiana Atg2* expression level after TBSV and CIRV inoculation. Six-to-eight-leaf stage *N. benthamiana* plants were inoculated with TBSV sap, CIRV sap, or mock. Samples were collected 2 d post-inoculation from infected leaves for TBSV and 3 d post-inoculation from infected leaves for CIRV. Total RNA was isolated and used for RT-qPCR. Primer Pairs (#9060: GCAATTGGGCTTGGAGTGCATTTG and #9061: CCTGTCGGGCATCTCTAGGTTGAT) were designed using RT-qPCR Tool from Integrated DNA Technologies (<https://www.idtdna.com/scitools/Applications/RealTimePCR/>). The qPCR reactions were prepared using Applied Biosystem Power UP SYBR green master mix (Thermo Fisher Scientific) in a 96 well plate and the Eppendorf's Mastercycler ep realplex instrument and primers used in this assay are listed in Table S. qPCR program conditions were selected following the Power Up SYBR green master mix user manual recommendations.

**Confocal laser microscope studies in plants.** To analyze the subcellular localization of Atg2 in the presence or absence of viral components in *N. benthamiana* leaves, pGD-35S -p33-BFP, pGD-35S-C36-BFP, pGD-35S-GFP-Atg2, pGD-35S-RFP-

SKL (as a peroxisome marker) and pGD-35S-RFP-AtTim21 (as a mitochondrial marker) (92) were transformed into agrobacterium strain C58C1. Then agrobacterium suspension with different combinations were infiltrated into *N. benthamiana* leaves. At 2.5 dpai, the agroinfiltrated leaves were subjected to confocal laser microscopy.

To detect interaction of Atg2 with TBSV p33 or CIRV p36 replication proteins using bimolecular fluorescence complementation assay, pGD-35S-T33-cYFP, pGD-35S-C36-cYFP, pGD-35S-C-cYFP (as a negative control), pGD-35S-nYFP-Atg2, pGD-35S-nYFP-MBP (as a negative control), pGD-35S-RFP-SKL (as a peroxisome marker) and pGD-35S-RFP-AtTim21 (as a mitochondrial marker) were transformed into agrobacterium strain C58C1. The Agrobacterium transformants with different combinations were used to infiltrate *N. benthamiana* leaves. At 2.5 dpai, the agroinfiltrated leaves were subjected to confocal laser microscopy.

To observe the distribution of PE (phosphatidylethanolamine) in plant mesophyll protoplasts, protoplasts were isolated from *N. benthamiana* leaves 2 dpi after the agroinfiltration with pGD-p33-RFP, pGD-p19. The protoplasts were fixed with 3.7% paraformaldehyde and staining with duramycin as described previously (25).

To observe the distribution of PI(3)P (phosphatidylinositol 3-phosphate) in plants, RFP-2xFYVE was used as a PI(3)P biosensor to visualize PI(3)P distribution upon virus replication as described previously (32).

To observe the distribution of PS (phosphatidylserine) in plants, pGD-35S -p33-BFP, pGD-35S-EV (as a negative control), pGD-35S-LactC2 (as the biosensor of PS), pGD-35S-RFP-SKL (as a peroxisome marker) and p19 were transformed into agrobacterium strain C58C1. The Agrobacterium transformants with different

combinations were used to infiltrate *N. benthamiana* leaves. At 2 dpai, the agroinfiltrated leaves were subjected to confocal laser microscopy.

**Confocal laser microscope studies in yeasts.** To observe the distribution of PE in yeasts, wild type BY4741 yeast strain and *atg2Δ* were transferred with HpGBK-CUP-GFP-p33, LpGAD-CUP-Hisp92 and UpYES-DI72. After cultures were induced and harvested, the yeast cells were fixed with 3.7% formaldehyde for 40 min at room temperature in dark, washed twice with 0.1 M potassium phosphate (pH 7.5), and then re-suspended in SPP (0.1 M potassium phosphate pH 7.5, 1.2 M sorbitol) with zymolase 20T (1 mg/ml). Cells were incubated at 30 °C for 1 hour, and then incubated with SPP with 0.1 M Glycine for 15 min to quench free aldehyde groups. Spheroplasts were collected after washing twice with SPP, and then add 0.2% Triton X 100 to suspend the spheroplasts at 30°C, 10'. Use 3% BSA to block cells 1 h and incubated cells with biotin conjugated duramycin overnight at 4 °C. Fixed cells were washed and incubated with Streptavidin conjugated with Alexa Fluor® 405 (Life Technologies, Cat. #: S-32351) for 1 h before imaging.

To observe the distribution of PI(3)P in yeasts, wild type BY4741 yeast strain and *atg2Δ* were transferred with HpGBK-CUP-GFP-p33, LpGAD-CUP-Hisp92 and UpYES-2XFYVE. After cultures were induced and harvested, the yeast cells were resuspended in 1XPBS before imaging.

To observe the distribution of PS in yeasts, wild type BY4741 yeast strain and *atg2Δ* were transferred with HpGBK-CUP-GFP-p33, LpGAD-CUP-Hisp92 and UpYES-LactC2. After cultures were induced and harvested, the yeast cells were resuspended in 1XPBS before imaging.

**Protein co-purification assays.** The FLAG-tag based replicase purification from detergent-solubilized membrane fraction of *N. benthamiana* plant was employed in this study. Firstly, plasmids pGD-Flag-p33 were co-infiltrated with pGD-YFP-Atg2 or pGD-YFP (as a control) into *N. benthamiana*. 2.5 dpi, harvest infiltrated leaves, each combo need ~2g fresh leaves. The ground the fresh leaves in a cooled mortar in GEN buffer (10% [v/v] glycerol, 25 mM Tris-HCl, pH 7.5, 1 mM EDTA, 150 mM NaCl, 10 mM DTT, 0.5% [v/v] Triton X-100 and protease inhibitor cocktail). The supernatants were incubated with anti-Flag M2 affinity agarose (Sigma-Aldrich) in Bio-spin chromatography columns (Bio-rad) for 2 h at 4°C on a rotator, followed by washing with the washing buffer (10% [v/v] glycerol, 25 mM Tris-HCl, pH 7.5, 1 mM EDTA, 150 mM NaCl, 1mM DTT and 0.1% [v/v] Triton X-100). Elution of purified proteins was achieved by 1XSDS-loading dye with 85°C heating 10 min, after elution, adding  $\beta$ -ME in eluted protein and 85°C water bath another 10 min.

**Quantification and statistical analysis.** Statistical analysis was performed using GraphPad Prism 8 software. Details of the statistical tests and sample sizes are provided in the figure legends. Results with a p value of less than 0.05 were considered statistically significant, while results with a p value greater than 0.05 were considered statistically non-significant (ns).



Table 4.1: Plasmids constructed in chapter 4.

Plasmid name	insert source	insert digestion sites	primers for insert amplification	vector source	vector digestion sites
pGD-eGFP-Lact-C2	Addgene plasmid #22852	BglII and XhoI	#8751 and #8752	pGD-eGFP-NT	BamHI and Sall
pGD-eGFP-AtATG2-NT	<i>A. thaliana</i> cDNA	BamHI and EcoRI	#8878 and #8879	pGD-eGFP-NT	BamHI and EcoRI
pGD-eGFP-AtATG2	<i>A. thaliana</i> cDNA	EcoRI and Sall	#8880 and #8839	pGD-eGFP-AtATG2-NT	EcoRI and Sall
pGD-nYFP-Flag-AtATG2-NT	<i>A. thaliana</i> cDNA	BamHI and EcoRI	#8878 and #8879	pGD-nYFP-NT	BamHI and EcoRI
pGD-cYFP-Flag-AtATG2-NT	<i>A. thaliana</i> cDNA	BamHI and EcoRI	#8878 and #8879	pGD-nYFP-CT	BamHI and EcoRI
pGD-YFP-3XHA-AtATG2-NT	<i>A. thaliana</i> cDNA	BamHI and EcoRI	#8878 and #8879	pGD-YFP-3XHA-NT	BamHI and EcoRI
pGD-nYFP-Flag-AtATG2	<i>A. thaliana</i> cDNA	EcoRI and Sall	#8880 and #8839	pGD-nYFP-Flag-AtATG2-NT	EcoRI and Sall
pGD-cYFP-Flag-AtATG2	<i>A. thaliana</i> cDNA	EcoRI and Sall	#8880 and #8839	pGD-cYFP-Flag-AtATG2-NT	EcoRI and Sall
pGD-YFP-3XHA-AtATG2	<i>A. thaliana</i> cDNA	EcoRI and Sall	#8880 and #8839	pGD-YFP-3XHA-AtATG2-NT	EcoRI and Sall
TRV2-ATG2	<i>N. benthamiana</i> cDNA	BamHI and XhoI	#9058 and #9059	TRV2-EV	BamHI and XhoI
pYES2-ATG2	yeast genomic DNA	XhoI	#9080 and #9081	pYES2-NT	XhoI and SAP
pYES2-eGFP-Lact-C2	Addgene plasmid #22852	BglII and XhoI	#8751 and #8752	pYES2-eGFP	BamHI and Sall

Table 4.2: Plasmids described in previous studies of chapter 4.

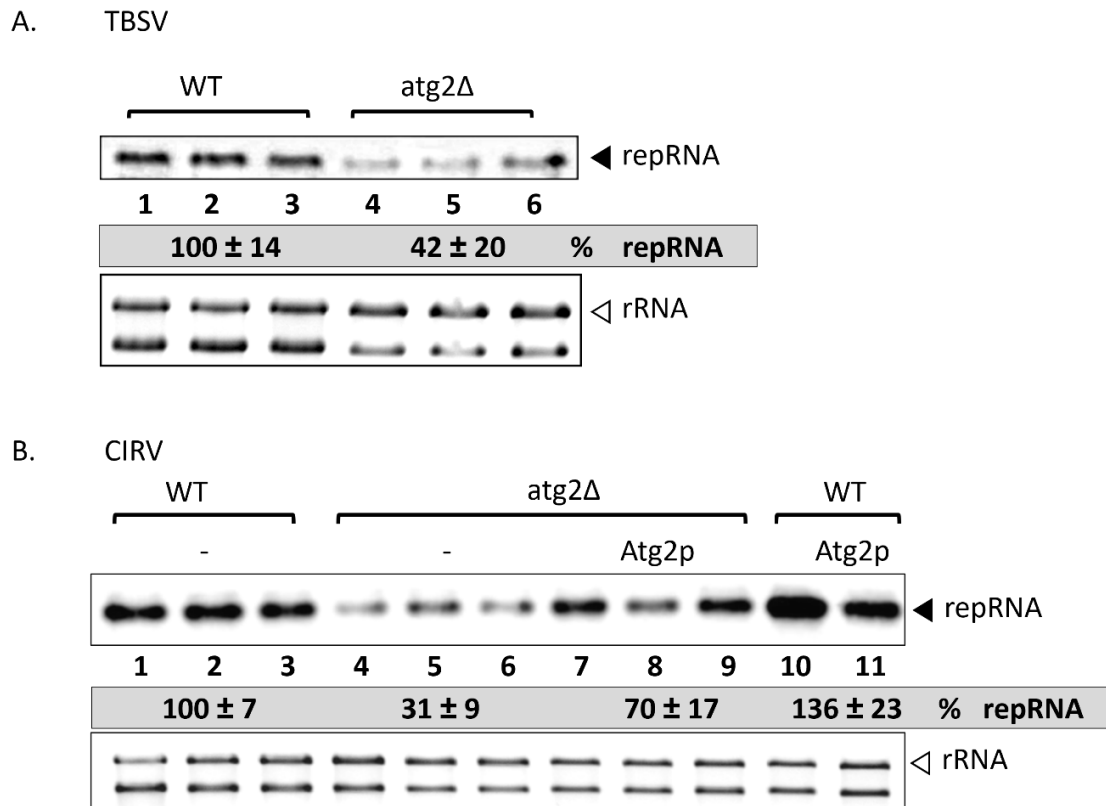
Plasmid name	Source
pGD-35S-p19	[1] Xu and Nagy, 2016
pGD-35S-T33-BFP	[1] Xu and Nagy, 2016
pGD-35S- C36-BFP	[1] Xu and Nagy, 2016
pGD-35S-T33-cYFP	[1] Xu and Nagy, 2016
pGD-35S-C36-cYFP	[1] Xu and Nagy, 2016
pGD-35S-C-cYFP	[1] Xu and Nagy, 2016
pGD-35S-nYFP-MBP	[1] Xu and Nagy, 2016
pGD-35S-RFP-SKL	[1] Xu and Nagy, 2016
pGD-35S-RFP-AtTim21	[1] Xu and Nagy, 2016
Addgene plasmid #22852	[2] Yeung et al., 2008
pGD-RFP-2XFYVE	[3] Feng et al., 2019
pYES-RFP-2XFYVE	[3] Feng et al., 2019
pGBK-His-p33-DI72	[4] Barajas et al., 2009
pGAD-His-p92	[4] Barajas et al., 2009
pGBK-Flag-p33-DI72	[4] Barajas et al., 2009
pGAD-Flag-p92	[4] Barajas et al., 2009
HpESC-CUP1-Hisp36/Gal-DI-72	[4] Barajas et al., 2009
LpESC-CUP1-Hisp95	[4] Barajas et al., 2009

Table 4.3: Reference for table 4.2.

[1]	Xu, K., and Nagy, P.D. (2016). Enrichment of phosphatidylethanolamine in viral replication compartments via co-opting the endosomal Rab5 small GTPase by a positive-strand RNA virus. <i>PLoS Biol</i> 14, e2000128.
[2]	Yeung T, Gilbert GE, Shi J, Silvius J, Kapus A, Grinstein S. (2008). Membrane phosphatidylserine regulates surface charge and protein localization. <i>Science</i> . 319(5860):210-3. 10.1126/science.1152066
[3]	Feng, Z., Xu, K., Kovalev, N., & Nagy, P. D. (2019). Recruitment of Vps34 PI3K and enrichment of PI3P phosphoinositide in the viral replication compartment is crucial for replication of a positive-strand RNA virus. <i>PLOS pathogens</i> , 15(1), e1007530.
[4]	Barajas, D., Li, Z., & Nagy, P. D. (2009). The Nedd4-type Rsp5p ubiquitin ligase inhibits tombusvirus replication by regulating degradation of the p92 replication protein and decreasing the activity of the tombusvirus replicase. <i>J. Virol</i> , 83(22), 11751-11764.

Table 4.4: Primers used in chapter 4.

Name	Sequence(5' to 3')
#8751/Lact-C2/BglIII F	GGAAGATCTATGTGCACTGAACCCCT AGG
#8752/Lact-C2/XhoI R	ACCGCTCGAGCTAACAGCCCAGCAGC TCC
#8839/AtAtg2/SalI R	ACGCGTCTGACTTATCGGTGTTGGTCCT GCTTC
#8878/AtAtg2-NT/BamHI F	ACGCGGATCCATGGTGTTCCTGGGA ACATTG
#8879/AtAtg2-NT/EcoI R	CAGAGAATTCAACCTGCCTATGAT
#8880/AtAtg2-CT/EcoI F	GGTTGAATTCTCTGCGTATAATA
#9058/TRV2-Atg2/BamHI F	CGGGATCCCCAATCGTCGAAGGATAA TCTTAGA
#9059/TRV2-Atg2/XhoI R	CCGCTCGAGTCCTGTTGATCGCTGTGC ATTATTCTG
#9080/ScAtg2/XhoI F	ACCGCTCGAGATGGCATTTCGGTTACC TCAA
#9081/ScAtg2/XhoI R	ACCGCTCGAGTTACGAATCAGTCCGA TTGGAC
#8939/NbAtg2/BglIII F	ACGCAGATCTATGTTTCCTGGGAATTT CGCG
#8940/NbAtg2/mid R	TTTTGCAAAGCCCTGTCCTTTTC
#9060/NbAtg2/qRCR F	GCAATTGGGCTTGGAGTGCATTG
#9061/NbAtg2/qRCR R	CCTGTCGGGCATCTCTAGGTTGAT

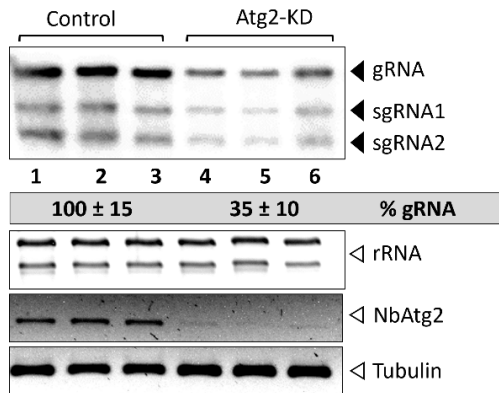


*Figure 4.1*

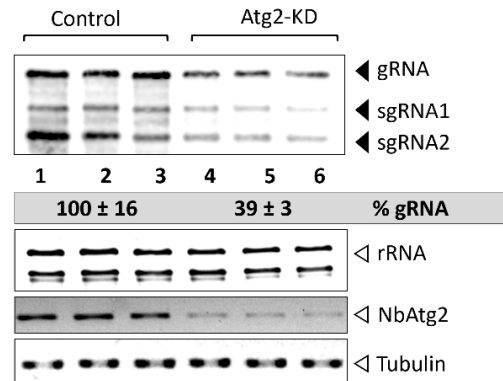
*Figure 4.1. Atg2 lipid transfer protein is a proviral host factor for tombusvirus replication in yeast.*

(A) Deletion of *ATG2* inhibits TBSV RNA replication in yeast. Top panels: northern blot analyses of repRNA using a 3' end specific probe demonstrate reduced accumulation of repRNA in *atg2Δ* yeast strain in comparison with the WT (BY4741) yeast strain. The replication proteins His<sub>6</sub>-p33 and His<sub>6</sub>-p92<sup>pol</sup> of TBSV were expressed from plasmids from the galactose-inducible *GALI* promoter. The DI-72(+) replicon (rep)RNA was expressed from the *GALI0* promoter. His<sub>6</sub>-Atg2 was expressed from the *GALI* promoter from a plasmid. Second panel: Ribosomal RNA is shown as a loading control in an ethidium-bromide-stained agarose gel. (B) Deletion of *ATG2* inhibits CIRV replication in yeast. Top panel: northern blot analyses of repRNA. The CIRV Flag-p36 and Flag-p95<sup>pol</sup> were expressed from plasmids from the *GALI* promoter. His<sub>6</sub>-Atg2 was expressed from the *GALI* promoter from a plasmid. Complementation of *atg2Δ* yeast strain and overexpression of Atg2 with plasmid-borne Atg2 enhances CIRV replication. His<sub>6</sub>-Atg2 was expressed from the *GALI* promoter from a plasmid. See further details in panel A. Each experiment was repeated three times.

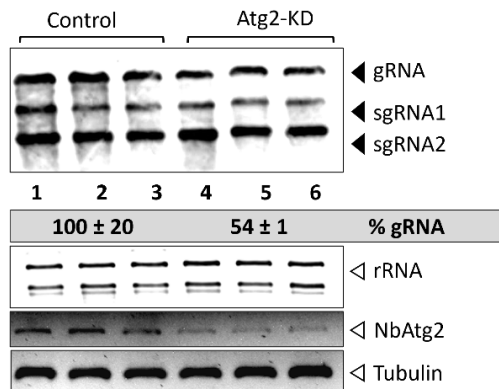
A. TBSV / *N.benthamiana*



B. CNV / *N.benthamiana*



C. CIRV / *N.benthamiana*



D. Atg2 mRNA / *N.benthamiana*

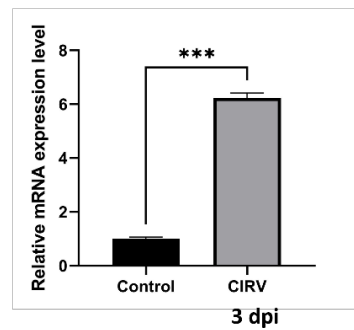
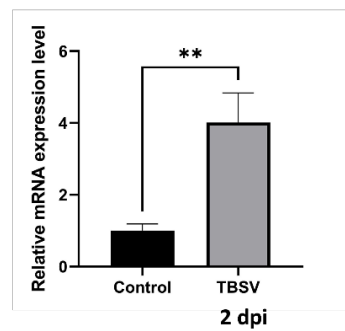


Figure 4.2

*Figure 4.2. The effect of Atg2 on tombusvirus replication in N. benthamiana plants.*

(A-C) Top panel: The accumulation of the TBSV, CNV and CIRV genomic (g)RNA in Atg2-silenced (Atg2 KD) *N. benthamiana* plants 2 dpi, 2.5 dpi and 3 dpi, respectively. (g)RNA level in the inoculated leaves was measured by northern blot analysis. Agroinfiltration of pGD-CNV<sup>20Kstop</sup> or inoculation with TBSV sap or CIRV sap was done 10 days after silencing of *Atg2* gene expression. Agroinfiltration of TRV vector carrying Nb*Atg2* or 3'-terminal GFP (as a control) sequences was used to induce VIGS. Second panel: Ribosomal RNA is shown as a loading control in an ethidium-bromide-stained agarose gel. Third panel: Semi-quantitative RT-PCR analysis of Nb*Atg2* mRNA level in the silenced and control plants. Bottom panel: Semi-quantitative RT-PCR analysis of tubulin mRNA level in the silenced and control plants. Each experiment was repeated. (D) Real time RT-qPCR analysis the induction of *Atg2* mRNA expression in the inoculated leaves (2 dpi) of *N. benthamiana* plants infected with TBSV (left) and CIRV (right). Error bars represent SD (n = 3). t-test statistically analyzed the data (\*\*P < 0.01, \*\*\*P < 0.001).

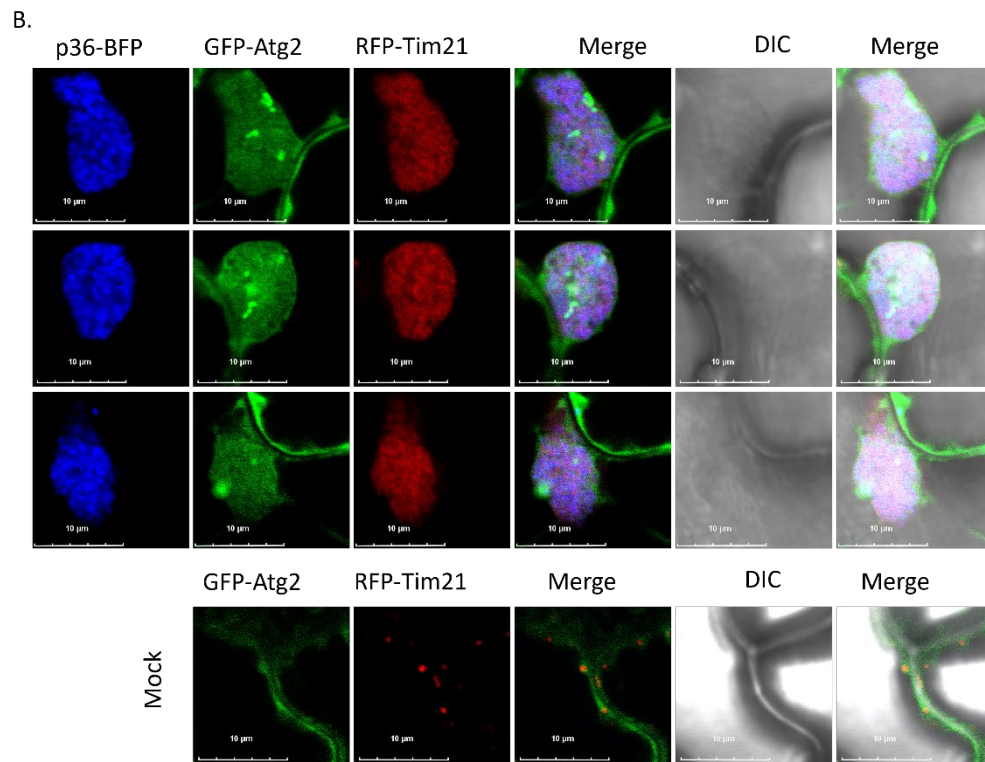
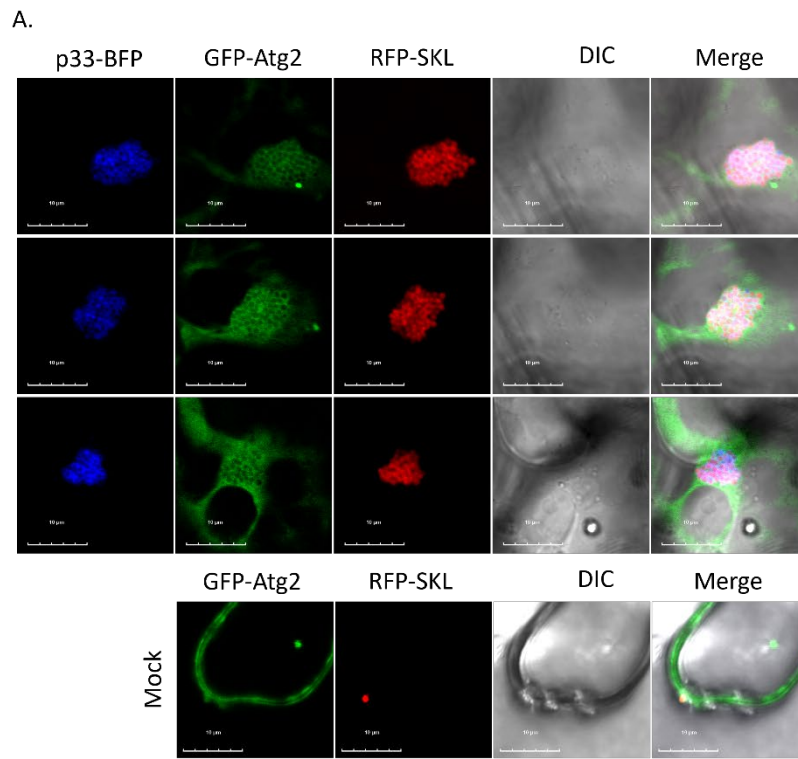


Figure 4.3



*Figure 4.3. Recruitment of Atg2 by the TBSV p33 and the CIRV p36 replication proteins into VROs in N. benthamiana.*

(A) Confocal microscopy images show efficient co-localization of TBSV p33-BFP replication protein and the GFP-Atg2 within VROs consisting of clustered peroxisomes, marked by RFP-SKL peroxisomal matrix marker in *N. benthamiana* leaves. The expression of these proteins, driven by the 35S promoter, was achieved through co-agroinfiltration into *N. benthamiana* leaves. Scale bars represent 10  $\mu\text{m}$ . (B) Confocal microscopy images show efficient co-localization of CIRV p36-BFP replication protein and the GFP-Atg2 within VROs consisting of clustered mitochondria, marked by RFP-AtTim21 mitochondrial marker in *N. benthamiana* leaves. See further details in panel A. Scale bars represent 10  $\mu\text{m}$ . Each experiment was repeated.

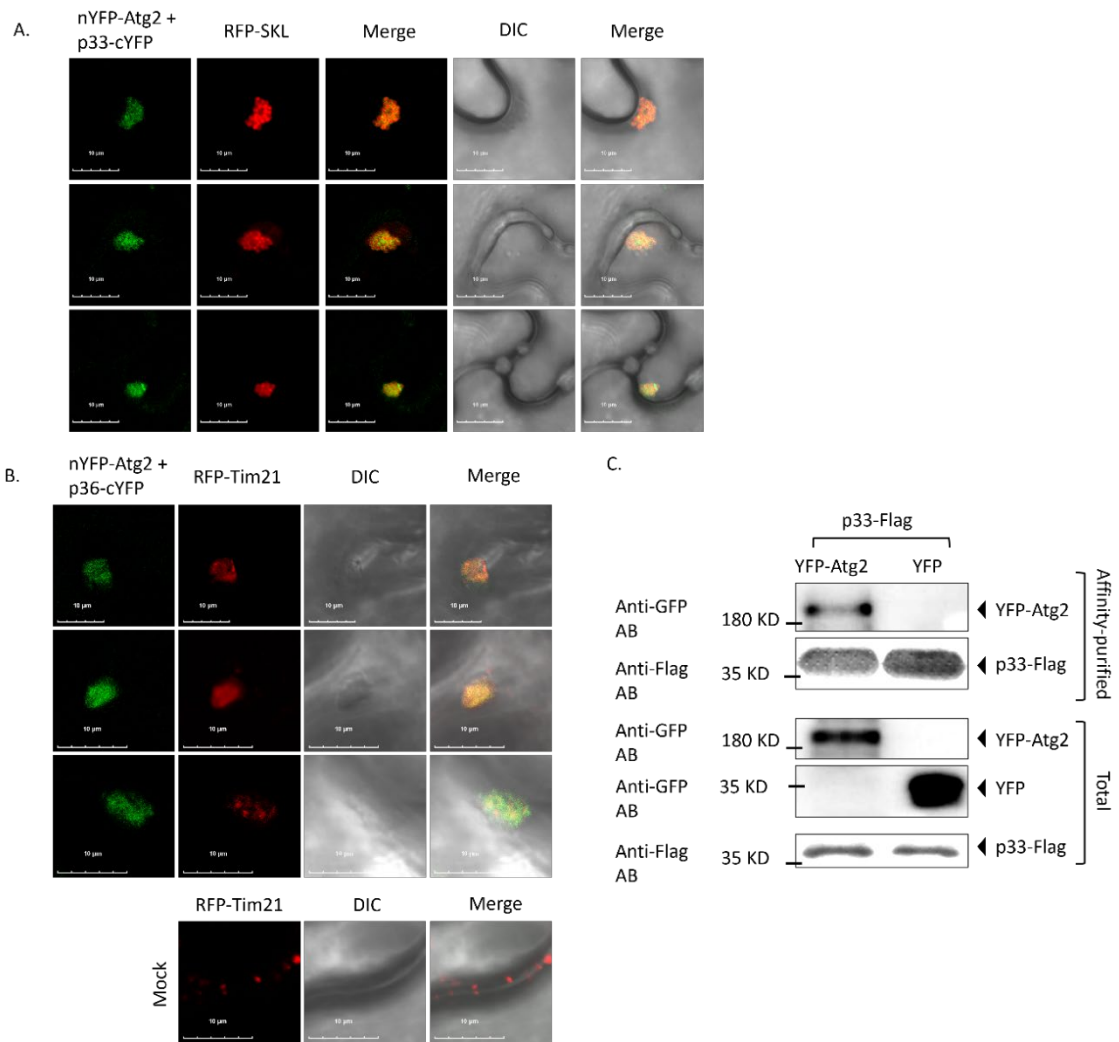


Figure 4.4

*Figure 4.4. Interaction between Atg2 and tombusvirus replication proteins in N. benthamiana.*

(A) Interaction between TBSV p33-cYFP replication protein and the nYFP-Atg2 protein was detected by BiFC. The merged images show the efficient co-localization of RFP-SKL with the BiFC signal, indicating that the interaction between p33 replication protein and Atg2 occurs in VROs in clustered peroxisomal membranes. (B) Interactions between CIRV p36-cYFP replication protein and the nYFP-Atg2 protein were detected by BiFC. The merged images show the efficient co-localization of RFP-AtTim21 with the BiFC signal, indicating that the interaction between p36 replication protein and Atg2 occurs in VROs consisting of aggregated mitochondria. See further details in panel A. Scale bars represent 10  $\mu$ m. Each experiment was repeated three times. (C) Co-IP assay of the interaction of TBSV p33 and Atg2 in plants. *N. benthamiana* plants were agroinfiltrated to express Flag-tagged p33 replication protein and YFP-Atg2. Top two panels: western blot analysis of co-purified YFP-Atg2 protein detected with anti-YFP antibody, whereas Flag-p33 was detected with anti-Flag antibody. Bottom panel: western blot of total YFP-Atg2 protein in the total protein extracts.

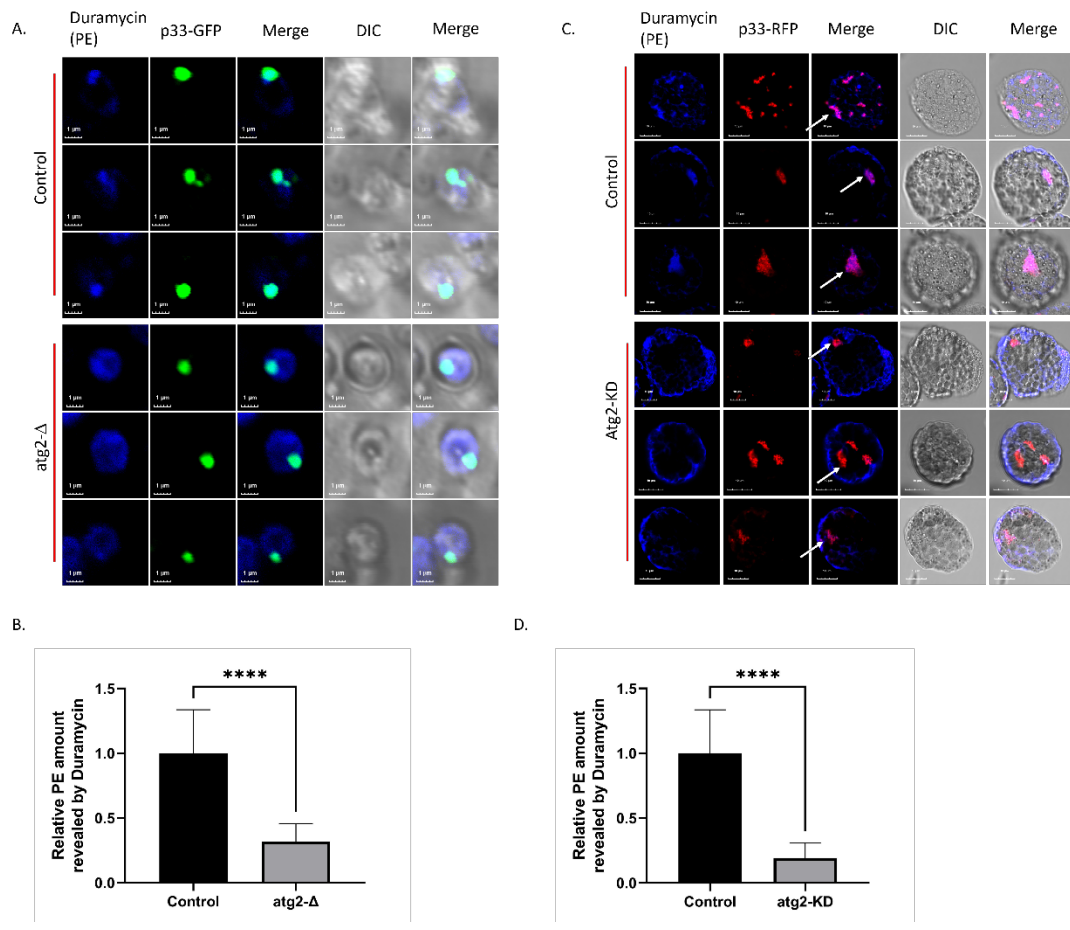


Figure 4.5

*Figure 4.5. Contributions of Atg2 to PE enrichment in the viral replication compartment in N. benthamiana protoplasts and yeast spheroplasts.*

(A) Confocal microscopy images show the PE distribution with GFP-p33 in BY4741 wild type yeast spheroplasts (top set of panels) and Atg2-knock out (*atg2Δ*) yeast spheroplasts (bottom set of panels). Spheroplasts were prepared by zymolase 20T (1 mg/ml). Scale bars represent 1  $\mu\text{m}$ . (B) The fluorescence intensity of Alexa Fluor 405 fluorescence indicating duramycin for PE in yeast VROs was quantified. Error bars represent SD (n = 15). t-test statistically analyzed the data (\*\*\*\*P < 0.0001). (C) Confocal microscopy images reveal PE enrichment and colocalization with RFP-p33 in *N. benthamiana* protoplasts (top image), whereas in Atg2-silenced (Atg2-KD) *N. benthamiana* protoplasts (bottom image), PE shows a more even cellular distribution, even in the presence of RFP-p33. Differential interference contrast (DIC) images are shown on the right. PE distribution is detected by a staining probe using biotinylated duramycin peptide and streptavidin conjugated with Alexa Fluor 405. Scale bars represent 10  $\mu\text{m}$ . Each experiment was repeated. (D) Quantitative Alexa Fluor 405 fluorescence intensity values were measured for 15 samples to calculate relative PE level in VRO. The statistical analysis was performed using a t-test, error bars represent SD (n = 15), and the results showed a significant difference between the two groups (\*\*\*\*P < 0.0001). Each experiment was repeated.

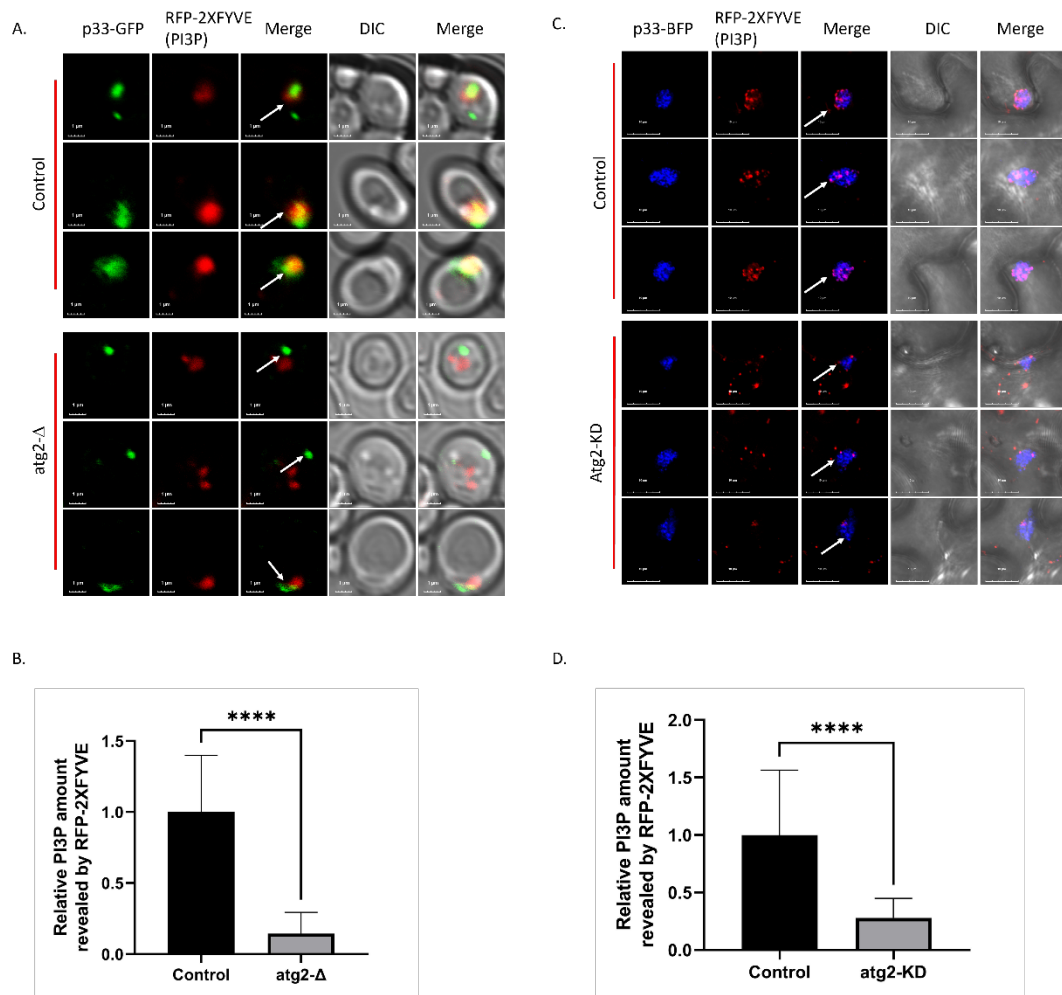


Figure 4.6

*Figure 4.6. Atg2 promotes PI(3)P enrichment within the viral replication compartment in N. benthamiana plants and yeasts.*

(A) Confocal microscopy images show PI(3)P distribution detected via RFP-2xFYVE protein with GFP-p33 in BY4741 wild type yeast (top group of images) and *atg2Δ* yeast (bottom group of images). Scale bars represent 1  $\mu\text{m}$ . (B) The fluorescence intensity of RFP-2xFYVE indicating distribution of PI(3)P in VROs was quantified. Error bars represent SD (n = 15). t-test was used to statistically analyze the data (\*\*\*\*P < 0.0001). (C) Confocal microscopy images show the distribution of PI(3)P detected via RFP-2xFYVE protein enrichment and colocalization with p33-BFP in *N. benthamiana* (top group of images), whereas in *Atg2*-silenced (*Atg2*-KD) *N. benthamiana* plants (bottom group of images), PI(3)P shows a more even cytosolic cellular distribution, even in the presence of p33-BFP. Differential interference contrast (DIC) images are shown on the right. Scale bars represent 10  $\mu\text{m}$ . (D) RFP intensity values were measured for 15 samples to calculate relative PI3P level in VRO. The statistical analysis was performed using a t-test, error bars represent SD (n = 15), and the results showed a significant difference between the two groups (\*\*\*\*P < 0.0001). Each experiment was repeated.

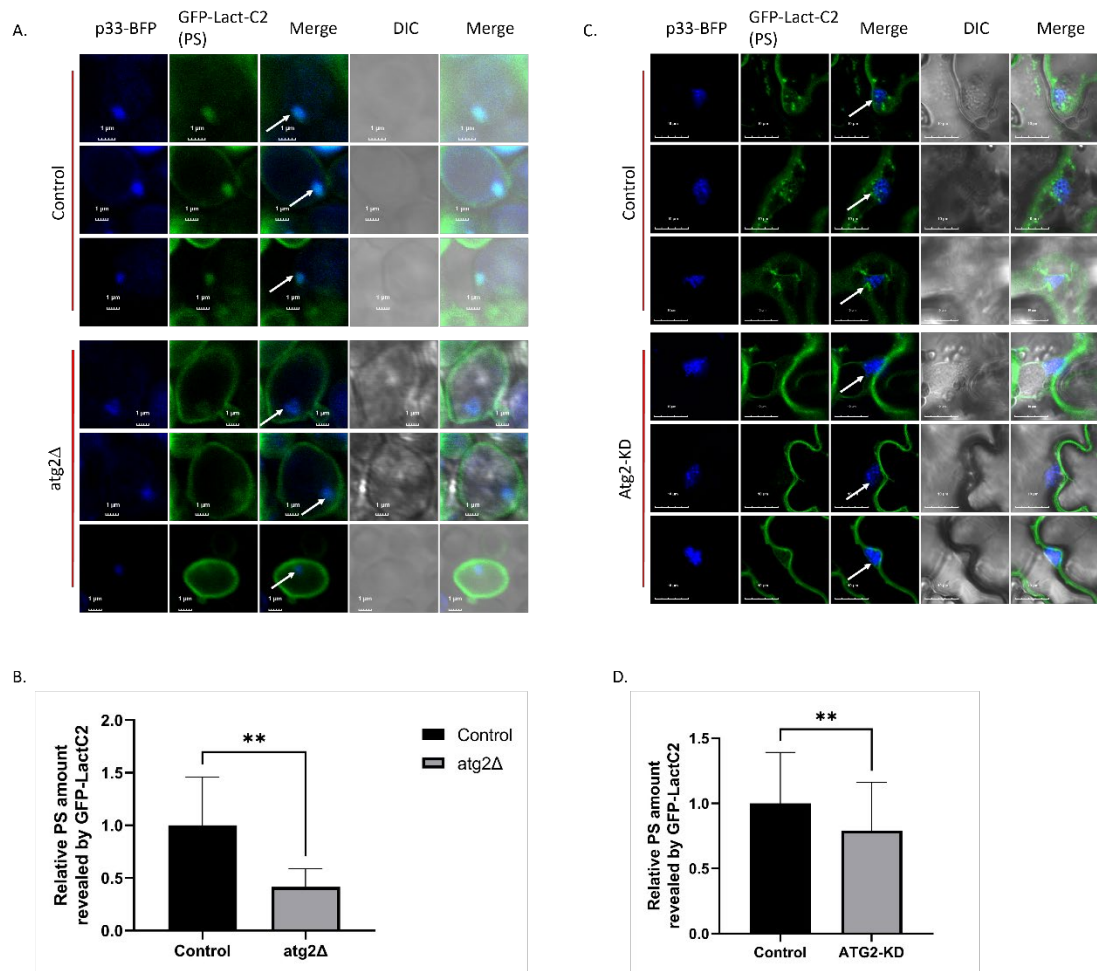


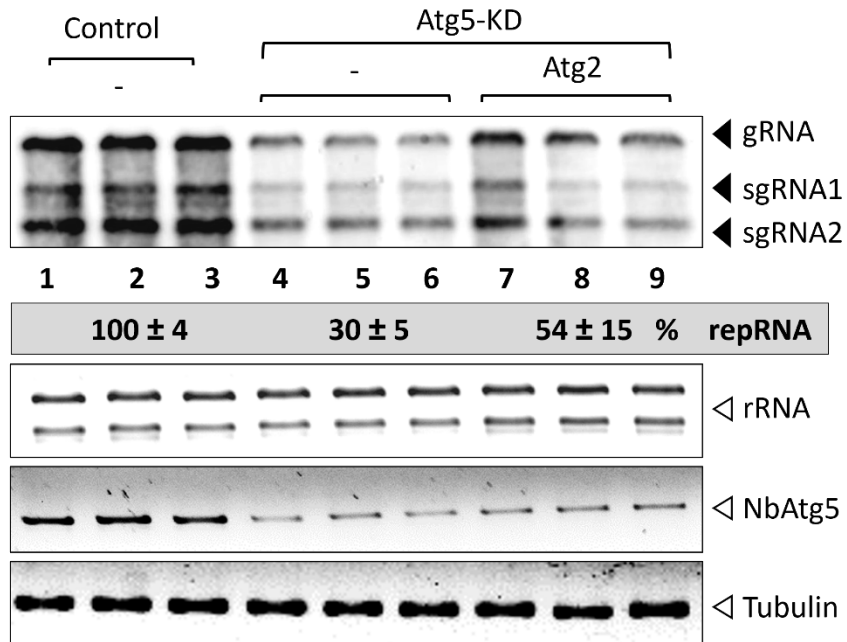
Figure 4.7



*Figure 4.7. Atg2 contributes to PS enrichment within the viral replication compartment in N. benthamiana plants and yeast.*

(A) Confocal microscopy images show the PS distribution with BFP-p33 in BY4741 wild type yeast (top group of images) and *atg2Δ* yeast (bottom group of images). Scale bars represent 1  $\mu\text{m}$ . (B) The fluorescence intensity of GFP-LactC2 indicating PS in VROs was quantified. Error bars represent SD (n=15). t-test statistically analyzed the data (\*\*P < 0.01). (C) Confocal microscopy images show co-localization of TBSV p33-BFP replication protein and the distribution of PS detected via GFP-LactC2 protein, in *Atg2*-silenced (*Atg2*-KD) (bottom group of images) or TRV2-MBP control (top group of images) *N. benthamiana* plants. (D) Quantitative GFP fluorescence intensity values were measured for 50 samples to calculate relative PS level in VRO. The statistical analysis was performed using a t-test, error bars represent SD (n=50), and the results showed a significant difference between the two groups (\*\*p < 0.01). Each experiment was repeated.

A. CNV / *N.benthamiana*



B. CNV / *N.benthamiana*

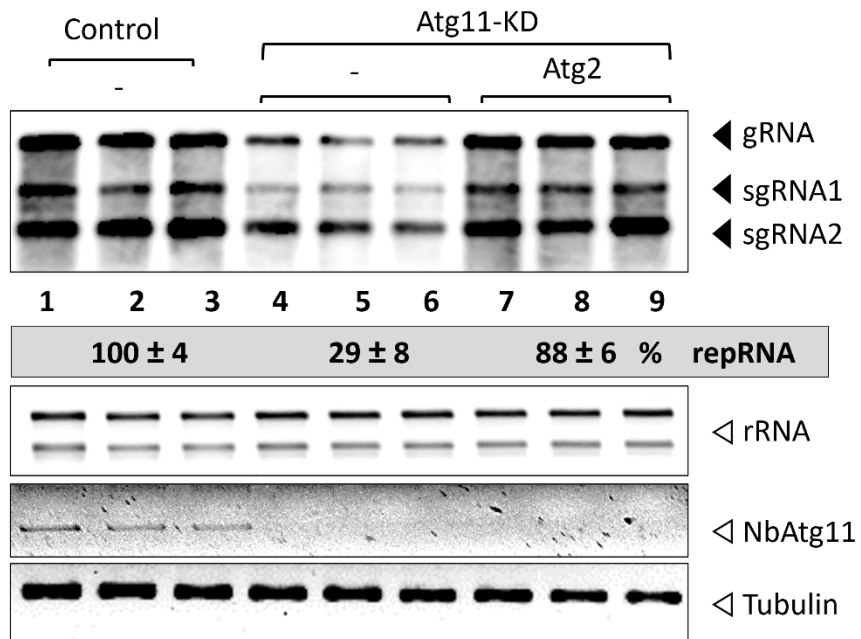


Figure 4.8

*Figure 4.8. Atg2's pro-viral role in N. benthamiana plants is autophagy-independent and unrelated to Atg11-mediated pathway.*

(A) Top panel: The accumulation of CNV genomic (g)RNA in *N. benthamiana* plants 2 dpi. (g)RNA level in the inoculated leaves was measured by northern blot analysis. Agroinfiltration of (TRV) vector carrying 3'-terminal GFP (as a control) (lane 1-3) or Nb*Atg5* (lane 4-9) sequences was used to induce VIGS. Agroinfiltration of pGD-CNV<sup>20Kstop</sup> with pGD-empty vector (lane 1-6) or pGD-*Atg2* (lane 7-9) was done 10 days after silencing *Atg5* gene expression. Second panel: Ribosomal RNA is shown as a loading control in an ethidium-bromide-stained agarose gel. Third panel: Semi-quantitative RT-PCR analysis of Nb*Atg5* mRNA level in the silenced and control plants. Bottom panel: Semi-quantitative RT-PCR analysis of tubulin mRNA level in the silenced and control plants. Each experiment was repeated. (B) Top panel: The accumulation of the CNV genomic (g)RNA in *N. benthamiana* plants 2 dpi. (g)RNA level in the inoculated leaves was measured by northern blot analysis. Agroinfiltration of (TRV) vector carrying 3'-terminal GFP (as a control) (lane 1-3) or Nb*Atg11* (lane 4-9) sequences was used to induce VIGS. Agroinfiltration of pGD-CNV<sup>20Kstop</sup> with pGD-empty vector (lane 1-6) or pGD-*Atg2* (lane 7-9) was done 10 days after silencing *Atg11* gene expression. Second panel: Ribosomal RNA is shown as a loading control in an ethidium-bromide-stained agarose gel. Third panel: Semi-quantitative RT-PCR analysis of Nb*Atg11* mRNA level in the silenced and control plants. Bottom panel: Semi-quantitative RT-PCR analysis of tubulin mRNA level in the silenced and control plants. Each experiment was repeated.

## CHAPTER 5.

### CONCLUSIONS AND PERSPECTIVES

#### 5.1 Conclusions

Autophagy is a pivotal cellular metabolic mechanism for maintaining cellular homeostasis, clearing damaged cell organelles, and preventing the invasion of pathogens (235-238). During the formation of autophagosomes, a set of intracellular lipid synthesis and membrane expansion mechanisms are involved in the development of these double-membrane structures (53, 239, 240). Considering that VRO formation requires similar membrane remodeling and lipid synthesis, these mechanisms could become potential targets for viruses. Thus, while viruses may shut down host autophagy, they can hijack proteins involved in autophagosome formation to facilitate VRO formation, turning these potentially threatening autophagy-related proteins into proviral factors for viral replication. Nonetheless, autophagy itself is a cellular defense against pathogenic invasion and remains a double-edged sword for viruses, with the potential to recognize and clear viral proteins and particles.

In the second chapter of this study, I explored the impact of the autophagy scaffold protein Atg11, which participates in selective autophagy during the initial stages of autophagy, on viral replication. In this part of the study, Atg11, as an autophagy-related protein, displayed a novel function in viral replication by stabilizing vMCS in conjunction with Fis1. This stability was evident in yeast mutant strains lacking Atg11, where the quantity of vMCS-related proteins, such as Osh proteins, and ER-resident proteins like

Sac1 PI4P phosphatase and Scs2 VAP protein, co-purified with TBSV replication proteins, significantly decreased compared to the wild type BY4741 strain, while the quantity of Fis1 on the acceptor membrane did not change significantly. This function, seemingly independent of cellular autophagy, could involve other autophagy-related proteins or represent a viral strategy to hijack Atg11 into VROs and competitively occupy Atg11 through interactions with other proteins, potentially inhibiting autophagy. However, the stabilizing role of Atg11 in vMCS seems critical, as overexpression of Atg11 in yeast or plants did not inhibit but rather enhanced TBSV replication. This suggests that viral suppression of autophagy might occur through various mechanisms beyond just one component. Despite our focus on vMCS stability and its impact on sterol enrichment within VROs, other studies have reported the specific transfer of PS by Osh proteins (241), suggesting that tombusviruses might also enrich PS within VROs through a similar vMCS, which would similarly promote TBSV replication.

The formation of autophagosomes, a hallmark event following autophagy induction, occurs in both selective autophagy and bulk autophagy (242). The conjugation of Atg8 with PE marks a critical event in membrane expansion during this process (59). In the third chapter of this study, I discussed the role of Atg8 in TBSV replication. Atg8 is an evolutionarily conserved gene that has evolved into a gene family in higher eukaryotes like plants and animals (243, 244). In the model plant *Arabidopsis thaliana*, Atg8 comprises a family of nine members, whose functional redundancy is not entirely clear. A study in *N. benthamiana* identified Atg8f's involvement in the cooperative process of TuMV replication (145). In my study, I specifically silenced three members of the Atg8 family in *N. benthamiana* – Atg8a, Atg8f, and Atg8i individually. The silencing results showed that

Atg8a and Atg8f knockdown inhibited TBSV replication to some extent, while Atg8i did not affect TBSV replication, suggesting functional differences among Atg8 family members. These differences might arise because different Atg8 gene family members take part in different cellular events or if there is temporal and spatial specificity of gene expression, which means the gene expression in different stages of plant growth and in different plant tissues. Further studies on Atg8f revealed that using a *Legionella* effector, RavZ, which permanently removes Atg8's C-terminus, preventing Atg8-PE conjugation, and inhibiting TBSV replication (175). This result showed that the active form of Atg8, Atg8-PE, is crucial for viral replication and the enrichment of PE and PI3P within VROs. Besides, the active form of Atg8-PE typically represents active autophagy within host cells. Using ratios of GFP/GFP-Atg8 and Atg8-PE/Atg8 to measure autophagy activity in host cells post-viral disturbance, we found that autophagy levels were significantly suppressed. This indicates that, while tombusviruses require a certain level of autophagic activity, primarily reflected in membrane expansion mechanisms, subsequent autophagic pathways are inhibited, ultimately preventing viral clearance. This led us to focus on the Atg8-related selective autophagy receptor NBR1.

NBR1 is a complex protein evolutionarily. In animals, p62 and NBR1 exist as separate proteins, but in plants, NBR1 has been identified, but not p62 (245). NBR1 has been extensively studied as a selective autophagy receptor, but recent studies have found that p62 in animals can exist in a condensate state within cells (246, 247). In SARS-Cov2-related research, it was discovered that ER-phagy receptors FAM134B and ATL3 interact with the dimeric viral protein ORF8 and are brought into condensates formed by ORF8 and p62, thereby preventing ER-phagy and favoring viral replication (246). In our study,

we also found that Atg8 and NBR1 BiFC signals aggregated in large spherical structures in and around VROs. Through Fluorescence Recovery After Photobleaching (FRAP) and 1,6-hexanediol treatment, we confirmed these large spherical structures as condensates formed by ATG8 and NBR1. Given that Atg8-PE is not conducive to condensate formation, this prompted our investigation into whether Atg8 within these condensates is in the PE-conjugated form. Surprisingly, silencing NBR1 enhanced cellular autophagy activity, which had been suppressed by TBSV, leading us to deduce that the condensate formed by NBR1 and ATG8 near VROs serves to hijack and trap Atg8, preventing its recycling for cellular autophagic activity. This effectively suppresses host cell autophagy while ensuring the preservation of membrane expansion mechanisms. Whether viruses use autophagic membrane synthesis and expansion mechanisms to establish their VROs, or whether they directly utilize formed phagophores or isolating membranes through fusion, remains uncertain. However, it is clear that Atg8, a core member of autophagic membrane expansion, and its active form, Atg8-PE, play a crucial role in the formation of tombusviral VROs.

During the formation of the autophagosome, a key event is the establishment of autophagosome-ER MCS (227, 248). Through these MCS, Atg2, functioning as an LTP, plays a critical role in lipid transport during the phagophore assembly site (PAS) formation (225). In Chapter 4 of this study, I investigated whether TBSV-induced VROs, which also form MCS with the ER, utilize Atg2 to acquire the necessary phospholipid components for VRO formation. My results indicate that Atg2, an autophagy-related gene, is hijacked by TBSV into the VROs and function as a pro-viral host factor. Similar to Atg11, another autophagy-related protein involved in a different type of vMCS, overexpression of Atg2 in

yeast facilitates viral replication. This suggests that both Atg11 and Atg2 are not directly affecting autophagic activity in host cells but are more involved as tools in the host cellular autophagic process. Atg2, as an LTP, contributes essential phospholipids not only for autophagosome formation in autophagy but is also involved in lysosome repair independent of autophagy (233). This discovery highlights Atg2's versatile function beyond just autophagic processes. Such flexibility also makes Atg2 useful to viruses, leading to its hijacking into VROs. Here, Atg2 assists in VRO formation by transferring phospholipids from the ER through vMCS. In chapter 2, we introduce a type of vMCS involving Atg11, this type vMCS is characterized by specific lipid exchange mediated by Osh proteins, exchanging PI4P enriched on the VROs membrane for sterols from the ER membrane. This exchange specifically alters the host membrane components used by viruses to establish VROs. In contrast, Atg2 acts as a bridge-like LTP protein in another type of vMCS. The N-terminal region of Atg2 forms a hydrophobic channel capable of non-specifically binding and transferring various phospholipids, including PE, PI, PS, and PC, all of which are crucial for viral replication (53, 227). The combined actions of these two MCS types provide viruses with a rapid and targeted source of lipids, facilitating the formation of viral VROs and enabling robust viral replication.

In study of TBSV exploitation of host cellular membranes to establish VROs, an important aspect is how the virus secures the essential lipid resources for VROs formation. This process is initiated by the viral replication protein p33, which anchored itself within ERAS subdomain. This anchoring is achieved through interactions between p33 and SNARE proteins, Ufe1 and Use1, creating a foundational platform for VRO membrane development (97). Once localized, p33 orchestrates the expansion of the membrane and



shapes it into spherical structures, employing a variety of strategies including the utilization of different sources of lipids from the host. There are three key lipid sources identified as contributing to this developmental process:

The first way for lipid acquisition involves exploiting the cellular vesicle-trafficking pathway. Notably, the TBSV replication protein p33 hijacks both Rab5-positive early endosomes and ER-derived Rab1-positive COPII vesicles into VROs as lipid sources (92, 128). These lipids enable TBSV to expand the membrane surface and create an optimal membrane microenvironment for its replication. While the direct contribution of phagophores to lipid delivery for TBSV VROs remains to be fully elucidated, it is evident in chapter 3 that Atg8, especially its active form Atg8-PE, play a crucial role in enriching PE and PI3P within the VROs. Moreover, the suppression of *ATG8* gene expression reduces the accumulation of Vps34 PI3K in VROs, suggesting that autophagic processes involving Atg8 might supply lipids to VROs in a manner similar to early endosomes, which not only provide lipids directly but also provide lipid-synthesizing enzyme Vps34 PI3K.

The second strategy employed by TBSV through establishment of vMCS at the ERAS subdomain facilitates fast and substantial lipid acquisition necessary for viral replication, leading to the rapid establishment of VROs and extensive viral replication. One form of vMCS involves ORP proteins, VAP proteins, and Sac1 PI4P phosphatase to exchange PI4P enriched on viral membranes for sterols on the ER, supported by Fis1 and the Atg11 scaffold protein along with p33 to maintain stability and long last of these MCS for continuous lipid acquisition (39, 40, 104, 167). The second form of vMCS involves ATG2, a LTP that utilizes its unique structure to form a hydrophobic channel at the N-terminus. This channel non-specifically captures essential phospholipids from the ER and

transfers them through the MCS (227). This process is not only direct and rapid, facilitating the bulk transfer of lipids over short distances without the complex involvement seen in vesicle trafficking pathways but also operates without ATP consumption, significantly benefiting virus replication under limited cellular resources (221).

The third mechanism TBSV employs is the *in situ* synthesis of phospholipids, which is facilitated by enzymes critical for lipid synthesis and modification. These enzymes include Psd2, a PS decarboxylase that converts PS to PE, is hijacked by p33 along with Rab5-positive early endosomes (92). Previous research has revealed that p33 hijacked the retromer complex, comprising Vps26, Vps29, and Vps35, to transport cargo enzymes, such as Psd2, Vps34 PI3K, and PI4K $\alpha$  into the VROs (9). These enzymes enable the *de novo* synthesis of critical lipids, including PE, PI3P, and PI4P, directly within the VROs.

In summary, the TBSV has developed sophisticated strategies to secure essential lipids for the formation of VROs, crucial for its replication. The viral replication protein p33 acts as a master regulator to interact and co-opt with numerous host factors to establish different ways to utilize host cell lipid sources for its own replication (Fig 5.1).

## 5.2 Perspectives

Based on previous research, we understand that viruses exploit a wide range of host cellular lipids to establish VROs (9, 25, 32, 97). These diverse lipid sources enable viruses to rapidly construct VROs. The newly formed VROs not only protect viral genomic RNA and proteins from host immune recognition and clearance but also concentrate viral proteins within the VRO membranes and provide catalytic surfaces for RdRp to synthesize RNA. This, in turn, facilitates extensive and robust viral replication within the VROs (39,

93). In the three chapters of this study, we explored the roles of three distinct autophagy-related genes in TBSV replication. We observed that they participate in lipid enrichment during TBSV VRO formation in three different forms. These findings provide a new major chapter in TBSV replication and further corroborate our previous conclusions that host cell lipid metabolism is critical for the establishment of VROs.

Interestingly, previous studies using GUVs have revealed that varying proportions of lipid components significantly impact TBSV replication (9). Notably, the representative lipids involved include PE, PI3P, PS, and sterols. This suggests that the specific lipid makeup of the VROs plays a crucial role in the virus's ability to replicate efficiently. The intricate balance and combination of these lipids within the VROs are therefore key determinants of the viral replication process. Understanding the precise lipid composition that favors TBSV replication could provide valuable insights into the virus-host interaction and pave new ways for potential therapeutic interventions aimed at disrupting these crucial lipids enrichment.

**Precision in host membrane remodeling by TBSV.** With TBSV encoding merely five proteins, and p33 as its master regulator for VRO formation, the virus demonstrates an extraordinary ability to precisely control host membrane components to create an optimal replication micro-environment. This phenomenon highlights a sophisticated interplay between TBSV proteins and the host cellular machinery, demonstrating the virus's ability to fine tune the host membrane constituents to proportions conducive to TBSV replication. A critical question arises from this intricate virus-host interaction: how does TBSV precisely exploit various intracellular physiological pathways to adjust the membrane

composition of VROs to a specific ratio that favors viral replication? It is challenging with current experimental methods to accurately dissect the proportional consistency of membrane components within individual viral replication complexes (VRCs). However, observations from electron microscopy reveal that, despite some extended size variations among VRCs, a regulatory mechanism should exist to ensure the balanced ratio of various lipids, thus facilitating the establishment and morphology of VROs (9). This mechanism likely involves the transport of excess lipids out of the VRC or their conversion into other lipids with a higher proportional representation. Identifying the precise nature of this regulatory mechanism needs further investigation in the future.

**Function of non-lipid related ATG proteins in VROs.** The recruitment of numerous autophagy-related (ATG) proteins to VROs may represent a strategic viral manipulation rather than an incidental occurrence. TBSV might specifically target ATG proteins involved in membrane dynamics and lipid transport to utilize the cellular autophagic machinery for viral benefits. However, it is noteworthy that many ATG protein, which do not directly participate in lipid metabolism or membrane synthesis, are also recruited to VROs. The involvement of these non-lipid related ATG proteins in TBSV replication presents a fascinating research direction. These proteins may contribute to the creation of a favorable micro-environment for viral replication, potentially by providing structural support, mediating protein-protein interactions, or modulating host defense mechanisms. Understanding their roles could uncover novel aspects of how TBSV exploits host autophagy processes for its own replication. It is still an open question if autophagic membranes contribute to VRO biogenesis. Future research should aim to elucidate the

molecular mechanisms by which TBSV utilizes host autophagy pathway, particularly its strategy for balancing the suppression of autophagy—typically a host defense mechanism—while co-opting autophagy-related processes for its replication.

**Collaboration within the Atg2 complex and other LTPs.** In the study of autophagy, Atg2 functions with Atg9 and Atg18, forming a complex integral to the nucleation of PAS and development of isolation membranes of phagophore (54, 226, 249). Interestingly, the role of Atg9 as a lipid scramblase is critical for the even distribution of a large amount of phospholipids acquired through LTP transfer across both inner and outer leaflets of membranes, a process that is critical for membrane formation and integrity during autophagy (240). However, it remains unclear whether, during TBSV replication, Atg2 is recruited individually by the virus or along with Atg9 and Atg18 as part of a complex into VROs. Furthermore, the involvement of additional ATG proteins alongside Atg2, potentially including the lipid scramblase activity of Atg9, might play a pivotal role in altering the composition of VRO membranes. Identifying these proteins and elucidating their contribution to VRO formation could uncover novel mechanisms by which TBSV, and potentially other viruses, manipulate host lipid metabolism for replication advantages.

An important question for future investigation involves determining whether the Atg2 functions as a single unit within VROs, or if additional LTPs are co-recruited with Atg2. Such investigation could reveal the elaborate strategies of TBSV for host cellular manipulation. The function of these proteins in lipid transfer and membrane remodeling is likely crucial for the rapid and efficient formation of VROs. Investigating the potential engagement of other LTPs in VRO formation, along with examining TBSV's broader

impact on host cellular physiological activities, is crucial for deepening our understanding of the complexities of host-pathogen interactions.

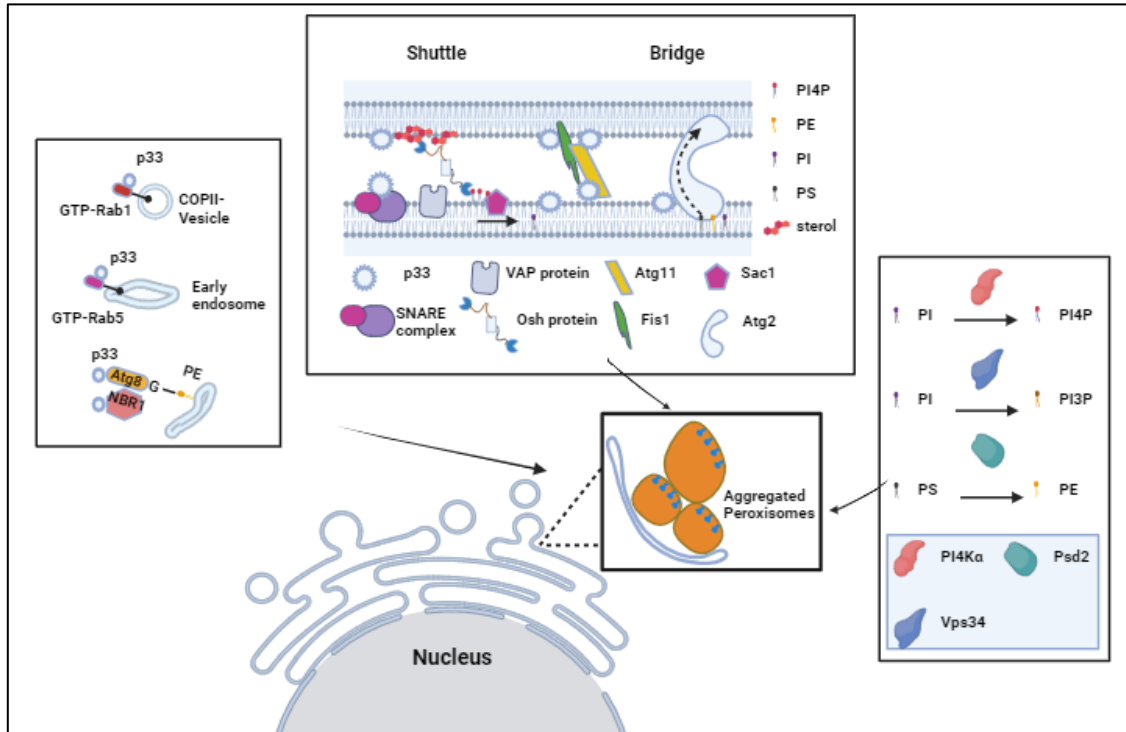


Figure. 5.1

*Figure 5.1. TBSV employed different lipid resources for VROs establishment.*

The schematic illustrates the three primary lipid resources through which TBSV acquires the lipids necessary for replication from the host cell.

(Created with BioRender.com)



## REFERENCES

1. White KA, Nagy PD. 2004. Advances in the molecular biology of tombusviruses: gene expression, genome replication, and recombination. *Prog Nucleic Acid Res Mol Biol* 78:187-226.
2. Pathak KB, Pogany J, Xu K, White KA, Nagy PD. 2012. Defining the roles of cis-acting RNA elements in tombusvirus replicase assembly in vitro. *J Virol* 86:156-71.
3. Panaviene Z, Panavas T, Nagy PD. 2005. Role of an internal and two 3'-terminal RNA elements in assembly of tombusvirus replicase. *J Virol* 79:10608-18.
4. Nagy PD, Feng Z. 2021. Tombusviruses orchestrate the host endomembrane system to create elaborate membranous replication organelles. *Curr Opin Virol* 48:30-41.
5. Scholthof KB, Scholthof HB, Jackson AO. 1995. The tomato bushy stunt virus replicase proteins are coordinately expressed and membrane associated. *Virology* 208:365-9.
6. Miller WA, Koev G. 2000. Synthesis of subgenomic RNAs by positive-strand RNA viruses. *Virology* 273:1-8.
7. Pogany J, White KA, Nagy PD. 2005. Specific binding of tombusvirus replication protein p33 to an internal replication element in the viral RNA is essential for replication. *J Virol* 79:4859-69.
8. Stork J, Kovalev N, Sasvari Z, Nagy PD. 2011. RNA chaperone activity of the tombusviral p33 replication protein facilitates initiation of RNA synthesis by the viral RdRp in vitro. *Virology* 409:338-47.
9. Feng Z, Inaba JI, Nagy PD. 2021. The retromer is co-opted to deliver lipid enzymes for the biogenesis of lipid-enriched tombusviral replication organelles. *Proc Natl Acad Sci U S A* 118.
10. Molho M, Lin W, Nagy PD. 2021. A novel viral strategy for host factor recruitment: The co-opted proteasomal Rpn11 protein interaction hub in cooperation with subverted actin filaments are targeted to deliver cytosolic host factors for viral replication. *PLoS Pathog* 17:e1009680.
11. Rajendran KS, Nagy PD. 2006. Kinetics and functional studies on interaction between the replicase proteins of Tomato Bushy Stunt Virus: requirement of p33:p92 interaction for replicase assembly. *Virology* 345:270-9.
12. Panavas T, Nagy PD. 2003. Yeast as a model host to study replication and recombination of defective interfering RNA of Tomato bushy stunt virus. *Virology* 314:315-25.
13. Ray D, White KA. 1999. Enhancer-like properties of an RNA element that modulates tombusvirus RNA accumulation. *Virology* 256:162-171.
14. Panavas T, Serviene E, Brasher J, Nagy PD. 2005. Yeast genome-wide screen reveals dissimilar sets of host genes affecting replication of RNA viruses. *Proc Natl Acad Sci U S A* 102:7326-31.
15. Pogany J, Nagy PD. 2008. Authentic replication and recombination of Tomato bushy stunt virus RNA in a cell-free extract from yeast. *J Virol* 82:5967-80.

16. Jaag HM, Nagy PD. 2009. Silencing of *Nicotiana benthamiana* Xrn4p exoribonuclease promotes tombusvirus RNA accumulation and recombination. *Virology* 386:344-52.
17. Rubino L, Burgyan J, Russo M. 1995. Molecular cloning and complete nucleotide sequence of carnation Italian ringspot tombusvirus genomic and defective interfering RNAs. *Arch Virol* 140:2027-39.
18. Di Franco A, Russo M, Martelli GP. 1984. Ultrastructure and Origin of Cytoplasmic Multivesicular Bodies Induced by Carnation Italian Ringspot Virus. *Journal of General Virology* 65:1233-1237.
19. Knoops K, Kikkert M, Worm SH, Zevenhoven-Dobbe JC, van der Meer Y, Koster AJ, Mommaas AM, Snijder EJ. 2008. SARS-coronavirus replication is supported by a reticulovesicular network of modified endoplasmic reticulum. *PLoS Biol* 6:e226.
20. Welsch S, Miller S, Romero-Brey I, Merz A, Bleck CK, Walther P, Fuller SD, Antony C, Krijnse-Locker J, Bartenschlager R. 2009. Composition and three-dimensional architecture of the dengue virus replication and assembly sites. *Cell Host Microbe* 5:365-75.
21. Joneczyk M, Pathak KB, Sharma M, Nagy PD. 2007. Exploiting alternative subcellular location for replication: tombusvirus replication switches to the endoplasmic reticulum in the absence of peroxisomes. *Virology* 362:320-30.
22. Exton JH. 1994. Phosphatidylcholine breakdown and signal transduction. *Biochim Biophys Acta* 1212:26-42.
23. Zhang J, Zhang Z, Chukkapalli V, Nchoutmboube JA, Li J, Randall G, Belov GA, Wang X. 2016. Positive-strand RNA viruses stimulate host phosphatidylcholine synthesis at viral replication sites. *Proc Natl Acad Sci U S A* 113:E1064-73.
24. Calzada E, Onguka O, Claypool SM. 2016. Phosphatidylethanolamine Metabolism in Health and Disease. *Int Rev Cell Mol Biol* 321:29-88.
25. Xu K, Nagy PD. 2015. RNA virus replication depends on enrichment of phosphatidylethanolamine at replication sites in subcellular membranes. *Proc Natl Acad Sci U S A* 112:E1782-91.
26. Pogany J, Nagy PD. 2015. Activation of Tomato Bushy Stunt Virus RNA-Dependent RNA Polymerase by Cellular Heat Shock Protein 70 Is Enhanced by Phospholipids In Vitro. *J Virol* 89:5714-23.
27. Odorizzi G, Babst M, Emr SD. 2000. Phosphoinositide signaling and the regulation of membrane trafficking in yeast. *Trends Biochem Sci* 25:229-35.
28. Gardocki ME, Jani N, Lopes JM. 2005. Phosphatidylinositol biosynthesis: biochemistry and regulation. *Biochim Biophys Acta* 1735:89-100.
29. Numata M, Voelker DR. 2022. Anti-inflammatory and anti-viral actions of anionic pulmonary surfactant phospholipids. *Biochim Biophys Acta Mol Cell Biol Lipids* 1867:159139.
30. Ishikawa-Sasaki K, Sasaki J, Taniguchi K. 2014. A complex comprising phosphatidylinositol 4-kinase IIIbeta, ACBD3, and Aichi virus proteins enhances phosphatidylinositol 4-phosphate synthesis and is critical for formation of the viral replication complex. *J Virol* 88:6586-98.
31. Berger KL, Kelly SM, Jordan TX, Tartell MA, Randall G. 2011. Hepatitis C virus stimulates the phosphatidylinositol 4-kinase III alpha-dependent

- phosphatidylinositol 4-phosphate production that is essential for its replication. *J Virol* 85:8870-83.
32. Feng Z, Xu K, Kovalev N, Nagy PD. 2019. Recruitment of Vps34 PI3K and enrichment of PI3P phosphoinositide in the viral replication compartment is crucial for replication of a positive-strand RNA virus. *PLoS Pathog* 15:e1007530.
  33. Cho NJ, Lee C, Pang PS, Pham EA, Fram B, Nguyen K, Xiong A, Sklan EH, Elazar M, Koytak ES, Kersten C, Kanazawa KK, Frank CW, Glenn JS. 2015. Phosphatidylinositol 4,5-bisphosphate is an HCV NS5A ligand and mediates replication of the viral genome. *Gastroenterology* 148:616-25.
  34. Bamunusinghe D, Seo JK, Rao AL. 2011. Subcellular localization and rearrangement of endoplasmic reticulum by Brome mosaic virus capsid protein. *J Virol* 85:2953-63.
  35. Romero-Brey I, Merz A, Chiramel A, Lee JY, Chlanda P, Haselman U, Santarella-Mellwig R, Habermann A, Hoppe S, Kallis S, Walther P, Antony C, Krijnse-Locker J, Bartenschlager R. 2012. Three-dimensional architecture and biogenesis of membrane structures associated with hepatitis C virus replication. *PLoS Pathog* 8:e1003056.
  36. Heaton NS, Perera R, Berger KL, Khadka S, Lacount DJ, Kuhn RJ, Randall G. 2010. Dengue virus nonstructural protein 3 redistributes fatty acid synthase to sites of viral replication and increases cellular fatty acid synthesis. *Proc Natl Acad Sci U S A* 107:17345-50.
  37. Borgese N, Francolini M, Snapp E. 2006. Endoplasmic reticulum architecture: structures in flux. *Curr Opin Cell Biol* 18:358-64.
  38. Roulin PS, Lotzerich M, Torta F, Tanner LB, van Kuppeveld FJ, Wenk MR, Greber UF. 2014. Rhinovirus uses a phosphatidylinositol 4-phosphate/cholesterol counter-current for the formation of replication compartments at the ER-Golgi interface. *Cell Host Microbe* 16:677-90.
  39. Barajas D, Xu K, de Castro Martin IF, Sasvari Z, Brandizzi F, Risco C, Nagy PD. 2014. Co-opted oxysterol-binding ORP and VAP proteins channel sterols to RNA virus replication sites via membrane contact sites. *PLoS Pathog* 10:e1004388.
  40. Sasvari Z, Lin W, Inaba JI, Xu K, Kovalev N, Nagy PD. 2020. Co-opted Cellular Sac1 Lipid Phosphatase and PI(4)P Phosphoinositide Are Key Host Factors during the Biogenesis of the Tombusvirus Replication Compartment. *J Virol* 94.
  41. Yang J, Chai XQ, Zhao XX, Li X. 2016. Comparative genomics revealed the origin and evolution of autophagy pathway. *Journal of Systematics and Evolution* 55:71-82.
  42. Kundu M, Thompson CB. 2008. Autophagy: basic principles and relevance to disease. *Annu Rev Pathol* 3:427-55.
  43. Mizushima N, Yamamoto A, Matsui M, Yoshimori T, Ohsumi Y. 2004. In vivo analysis of autophagy in response to nutrient starvation using transgenic mice expressing a fluorescent autophagosome marker. *Mol Biol Cell* 15:1101-11.
  44. Liu Y, Xiong Y, Bassham DC. 2009. Autophagy is required for tolerance of drought and salt stress in plants. *Autophagy* 5:954-63.
  45. Xiong Y, Contento AL, Nguyen PQ, Bassham DC. 2007. Degradation of oxidized proteins by autophagy during oxidative stress in Arabidopsis. *Plant Physiol* 143:291-9.

46. Kopitz J, Kisen GO, Gordon PB, Bohley P, Seglen PO. 1990. Nonselective autophagy of cytosolic enzymes by isolated rat hepatocytes. *J Cell Biol* 111:941-53.
47. Komatsu M, Waguri S, Koike M, Sou YS, Ueno T, Hara T, Mizushima N, Iwata J, Ezaki J, Murata S, Hamazaki J, Nishito Y, Iemura S, Natsume T, Yanagawa T, Uwayama J, Warabi E, Yoshida H, Ishii T, Kobayashi A, Yamamoto M, Yue Z, Uchiyama Y, Kominami E, Tanaka K. 2007. Homeostatic levels of p62 control cytoplasmic inclusion body formation in autophagy-deficient mice. *Cell* 131:1149-63.
48. Stolz A, Ernst A, Dikic I. 2014. Cargo recognition and trafficking in selective autophagy. *Nat Cell Biol* 16:495-501.
49. Kofinger J, Ragusa MJ, Lee IH, Hummer G, Hurley JH. 2015. Solution structure of the Atg1 complex: implications for the architecture of the phagophore assembly site. *Structure* 23:809-818.
50. Baskaran S, Carlson LA, Stjepanovic G, Young LN, Kim DJ, Grob P, Stanley RE, Nogales E, Hurley JH. 2014. Architecture and dynamics of the autophagic phosphatidylinositol 3-kinase complex. *Elife* 3:e05115.
51. Araki Y, Ku WC, Akioka M, May AI, Hayashi Y, Arisaka F, Ishihama Y, Ohsumi Y. 2013. Atg38 is required for autophagy-specific phosphatidylinositol 3-kinase complex integrity. *Journal of Cell Biology* 203:299-313.
52. Sawa-Makarska J, Baumann V, Coudeville N, von Bülow S, Nogellova V, Abert C, Schuschnig M, Graef M, Hummer G, Martens S. 2020. Reconstitution of autophagosome nucleation defines Atg9 vesicles as seeds for membrane formation. *Science* 369:1206-+.
53. Osawa T, Kotani T, Kawaoka T, Hirata E, Suzuki K, Nakatogawa H, Ohsumi Y, Noda NN. 2019. Atg2 mediates direct lipid transfer between membranes for autophagosome formation. *Nature Structural & Molecular Biology* 26:281-+.
54. Obara K, Sekito T, Niimi K, Ohsumi Y. 2008. The Atg18-Atg2 complex is recruited to autophagic membranes via phosphatidylinositol 3-phosphate and exerts an essential function. *Journal of Biological Chemistry* 283:23972-23980.
55. Geng J, Klionsky DJ. 2008. The Atg8 and Atg12 ubiquitin-like conjugation systems in macroautophagy. 'Protein modifications: beyond the usual suspects' review series. *EMBO Rep* 9:859-64.
56. Kirisako T, Ichimura Y, Okada H, Kabeya Y, Mizushima N, Yoshimori T, Ohsumi M, Takao T, Noda T, Ohsumi Y. 2000. The reversible modification regulates the membrane-binding state of Apg8/Aut7 essential for autophagy and the cytoplasm to vacuole targeting pathway. *J Cell Biol* 151:263-76.
57. Radoshevich L, Murrow L, Chen N, Fernandez E, Roy S, Fung C, Debnath J. 2010. ATG12 conjugation to ATG3 regulates mitochondrial homeostasis and cell death. *Cell* 142:590-600.
58. Matsushita M, Suzuki NN, Obara K, Fujioka Y, Ohsumi Y, Inagaki F. 2007. Structure of Atg5-Atg16, a complex essential for autophagy. *J Biol Chem* 282:6763-72.
59. Ichimura Y, Kirisako T, Takao T, Satomi Y, Shimonishi Y, Ishihara N, Mizushima N, Tanida I, Kominami E, Ohsumi M, Noda T, Ohsumi Y. 2000. A ubiquitin-like system mediates protein lipidation. *Nature* 408:488-92.

60. Zhang WX, Nishimura T, Gahlot D, Saito C, Davis C, Jefferies HB, Schreiber A, Thukral L, Tooze SA. 2023. Autophagosome membrane expansion is mediated by the N-terminus and cis-membrane association of human ATG8s. *Elife* 12:e89185.
61. Yu ZQ, Ni T, Hong B, Wang HY, Jiang FJ, Zou S, Chen Y, Zheng XL, Klionsky DJ, Liang Y, Xie Z. 2012. Dual roles of Atg8-PE deconjugation by Atg4 in autophagy. *Autophagy* 8:883-92.
62. Turco E, Savova A, Gere F, Ferrari L, Romanov J, Schuschnig M, Martens S. 2021. Reconstitution defines the roles of p62, NBR1 and TAX1BP1 in ubiquitin condensate formation and autophagy initiation. *Nat Commun* 12:5212.
63. Belov GA, van Kuppeveld FJ. 2012. (+)RNA viruses rewire cellular pathways to build replication organelles. *Curr Opin Virol* 2:740-7.
64. Nagy PD, Pogany J. 2011. The dependence of viral RNA replication on co-opted host factors. *Nat Rev Microbiol* 10:137-49.
65. Wang A. 2015. Dissecting the molecular network of virus-plant interactions: the complex roles of host factors. *Annu Rev Phytopathol* 53:45-66.
66. Fernandez de Castro I, Tenorio R, Risco C. 2016. Virus assembly factories in a lipid world. *Curr Opin Virol* 18:20-6.
67. Hyodo K, Okuno T. 2020. Hijacking of host cellular components as proviral factors by plant-infecting viruses. *Immunopathology* 107:37-86.
68. Garcia-Ruiz H. 2018. Susceptibility Genes to Plant Viruses. *Viruses* 10:484.
69. Altan-Bonnet N. 2017. Lipid Tales of Viral Replication and Transmission. *Trends Cell Biol* 27:201-213.
70. Makinen K, Lohmus A, Pollari M. 2017. Plant RNA Regulatory Network and RNA Granules in Virus Infection. *Front Plant Sci* 8:2093.
71. Schoggins JW, Randall G. 2013. Lipids in innate antiviral defense. *Cell Host Microbe* 14:379-85.
72. Paul D, Bartenschlager R. 2015. Flaviviridae Replication Organelles: Oh, What a Tangled Web We Weave. *Annu Rev Virol* 2:289-310.
73. Zhang Z, He G, Filipowicz NA, Randall G, Belov GA, Kopek BG, Wang X. 2019. Host Lipids in Positive-Strand RNA Virus Genome Replication. *Front Microbiol* 10:286.
74. Shulla A, Randall G. 2016. (+) RNA virus replication compartments: a safe home for (most) viral replication. *Curr Opin Microbiol* 32:82-88.
75. Kovalev N, Inaba JI, Li Z, Nagy PD. 2017. The role of co-opted ESCRT proteins and lipid factors in protection of tombusviral double-stranded RNA replication intermediate against reconstituted RNAi in yeast. *PLoS Pathog* 13:e1006520.
76. Jin X, Cao X, Wang X, Jiang J, Wan J, Laliberte JF, Zhang Y. 2018. Three-Dimensional Architecture and Biogenesis of Membrane Structures Associated with Plant Virus Replication. *Front Plant Sci* 9:57.
77. Hsu NY, Ilnytska O, Belov G, Santiana M, Chen YH, Takvorian PM, Pau C, van der Schaar H, Kaushik-Basu N, Balla T, Cameron CE, Ehrenfeld E, van Kuppeveld FJ, Altan-Bonnet N. 2010. Viral reorganization of the secretory pathway generates distinct organelles for RNA replication. *Cell* 141:799-811.
78. Wang X, Diaz A, Hao L, Gancarz B, den Boon JA, Ahlquist P. 2011. Intersection of the multivesicular body pathway and lipid homeostasis in RNA replication by a positive-strand RNA virus. *J Virol* 85:5494-503.

79. Nagy PD. 2020. Host protein chaperones, RNA helicases and the ubiquitin network highlight the arms race for resources between tombusviruses and their hosts. *Adv Virus Res* 107:133-158.
80. Nagy PD. 2016. Tombusvirus-Host Interactions: Co-Opted Evolutionarily Conserved Host Factors Take Center Court. *Annu Rev Virol* 3:491-515.
81. Gunawardene CD, Donaldson LW, White KA. 2017. Tombusvirus polymerase: Structure and function. *Virus Res* 234:74-86.
82. Nicholson BL, White KA. 2014. Functional long-range RNA-RNA interactions in positive-strand RNA viruses. *Nat Rev Microbiol* 12:493-504.
83. Xu K, Nagy PD. 2017. Sterol Binding by the Tombusviral Replication Proteins Is Essential for Replication in Yeast and Plants. *J Virol* 91.
84. Nagy PD, Pogany J, Lin JY. 2014. How yeast can be used as a genetic platform to explore virus-host interactions: from 'omics' to functional studies. *Trends Microbiol* 22:309-16.
85. Nagy PD. 2017. Exploitation of a surrogate host, *Saccharomyces cerevisiae*, to identify cellular targets and develop novel antiviral approaches. *Curr Opin Virol* 26:132-140.
86. Xu K, Nagy PD. 2014. Expanding use of multi-origin subcellular membranes by positive-strand RNA viruses during replication. *Curr Opin Virol* 9:119-26.
87. Kovalev N, Pogany J, Nagy PD. 2019. Interviral Recombination between Plant, Insect, and Fungal RNA Viruses: Role of the Intracellular Ca(2+)/Mn(2+) Pump. *J Virol* 94.
88. Prasanth KR, Kovalev N, de Castro Martin IF, Baker J, Nagy PD. 2016. Screening a yeast library of temperature-sensitive mutants reveals a role for actin in tombusvirus RNA recombination. *Virology* 489:233-42.
89. Chuang C, Barajas D, Qin J, Nagy PD. 2014. Inactivation of the host lipin gene accelerates RNA virus replication through viral exploitation of the expanded endoplasmic reticulum membrane. *PLoS Pathog* 10:e1003944.
90. Sharma M, Sasvari Z, Nagy PD. 2011. Inhibition of phospholipid biosynthesis decreases the activity of the tombusvirus replicase and alters the subcellular localization of replication proteins. *Virology* 415:141-52.
91. Sharma M, Sasvari Z, Nagy PD. 2010. Inhibition of sterol biosynthesis reduces tombusvirus replication in yeast and plants. *J Virol* 84:2270-81.
92. Xu K, Nagy PD. 2016. Enrichment of Phosphatidylethanolamine in Viral Replication Compartments via Co-opting the Endosomal Rab5 Small GTPase by a Positive-Strand RNA Virus. *PLoS Biol* 14:e2000128.
93. Pogany J, Nagy PD. 2012. p33-Independent activation of a truncated p92 RNA-dependent RNA polymerase of Tomato bushy stunt virus in yeast cell-free extract. *J Virol* 86:12025-38.
94. Kovalev N, Pogany J, Nagy PD. 2020. Reconstitution of an RNA Virus Replicase in Artificial Giant Unilamellar Vesicles Supports Full Replication and Provides Protection for the Double-Stranded RNA Replication Intermediate. *J Virol* 94.
95. Nagy PD, Strating JR, van Kuppeveld FJ. 2016. Building Viral Replication Organelles: Close Encounters of the Membrane Types. *PLoS Pathog* 12:e1005912.

96. Fernandez de Castro I, Fernandez JJ, Barajas D, Nagy PD, Risco C. 2017. Three-dimensional imaging of the intracellular assembly of a functional viral RNA replicase complex. *J Cell Sci* 130:260-268.
97. Sasvari Z, Kovalev N, Gonzalez PA, Xu K, Nagy PD. 2018. Assembly-hub function of ER-localized SNARE proteins in biogenesis of tombusvirus replication compartment. *PLoS Pathog* 14:e1007028.
98. Sasvari Z, Gonzalez PA, Rachubinski RA, Nagy PD. 2013. Tombusvirus replication depends on Sec39p endoplasmic reticulum-associated transport protein. *Virology* 447:21-31.
99. Jackson CL, Walch L, Verbavatz JM. 2016. Lipids and Their Trafficking: An Integral Part of Cellular Organization. *Dev Cell* 39:139-153.
100. Henne WM. 2016. Organelle remodeling at membrane contact sites. *J Struct Biol* 196:15-19.
101. Raiborg C, Wenzel EM, Pedersen NM, Stenmark H. 2016. Phosphoinositides in membrane contact sites. *Biochem Soc Trans* 44:425-30.
102. Mesmin B, Antonny B. 2016. The counterflow transport of sterols and PI4P. *Biochim Biophys Acta* 1861:940-951.
103. Olkkonen VM, Li S. 2013. Oxysterol-binding proteins: sterol and phosphoinositide sensors coordinating transport, signaling and metabolism. *Prog Lipid Res* 52:529-38.
104. Lin W, Feng Z, Prasanth KR, Liu Y, Nagy PD. 2021. Dynamic interplay between the co-opted Fis1 mitochondrial fission protein and membrane contact site proteins in supporting tombusvirus replication. *PLoS Pathog* 17:e1009423.
105. Fukuda T, Kanki T. 2018. Mechanisms and Physiological Roles of Mitophagy in Yeast. *Mol Cells* 41:35-44.
106. Yokota H, Gomi K, Shintani T. 2017. Induction of autophagy by phosphate starvation in an Atg11-dependent manner in *Saccharomyces cerevisiae*. *Biochem Biophys Res Commun* 483:522-527.
107. Oku M, Sakai Y. 2016. Pexophagy in yeasts. *Biochim Biophys Acta* 1863:992-8.
108. Delorme-Axford E, Klionsky DJ. 2015. A missing piece of the puzzle: Atg11 functions as a scaffold to activate Atg1 for selective autophagy. *Autophagy* 11:2139-41.
109. Matscheko N, Mayrhofer P, Rao Y, Beier V, Wollert T. 2019. Atg11 tethers Atg9 vesicles to initiate selective autophagy. *PLoS Biol* 17:e3000377.
110. Eickhorst C, Licheva M, Kraft C. 2020. Scaffold proteins in bulk and selective autophagy. *Prog Mol Biol Transl Sci* 172:15-35.
111. Zientara-Rytter K, Subramani S. 2020. Mechanistic Insights into the Role of Atg11 in Selective Autophagy. *J Mol Biol* 432:104-122.
112. Kang S, Shin KD, Kim JH, Chung T. 2018. Autophagy-related (ATG) 11, ATG9 and the phosphatidylinositol 3-kinase control ATG2-mediated formation of autophagosomes in *Arabidopsis*. *Plant Cell Rep* 37:653-664.
113. Li F, Vierstra RD. 2014. *Arabidopsis* ATG11, a scaffold that links the ATG1-ATG13 kinase complex to general autophagy and selective mitophagy. *Autophagy* 10:1466-7.
114. Backues SK, Klionsky DJ. 2012. Atg11: a Rab-dependent, coiled-coil membrane protein that acts as a tether for autophagy. *Autophagy* 8:1275-8.

115. Mao K, Wang K, Liu X, Klionsky DJ. 2013. The scaffold protein Atg11 recruits fission machinery to drive selective mitochondria degradation by autophagy. *Dev Cell* 26:9-18.
116. Inaba JI, Nagy PD. 2018. Tombusvirus RNA replication depends on the TOR pathway in yeast and plants. *Virology* 519:207-222.
117. Feng Z, Inaba JI, Nagy PD. 2021. Tombusviruses Target a Major Crossroad in the Endocytic and Recycling Pathways via Co-opting Rab7 Small GTPase. *J Virol* 95:e0107621.
118. Barajas D, Martin IF, Pogany J, Risco C, Nagy PD. 2014. Noncanonical role for the host Vps4 AAA+ ATPase ESCRT protein in the formation of Tomato bushy stunt virus replicase. *PLoS Pathog* 10:e1004087.
119. Fernandez-Suarez M, Chen TS, Ting AY. 2008. Protein-protein interaction detection in vitro and in cells by proximity biotinylation. *J Am Chem Soc* 130:9251-3.
120. Jan CH, Williams CC, Weissman JS. 2014. Principles of ER cotranslational translocation revealed by proximity-specific ribosome profiling. *Science* 346:1257521.
121. Li Z, Pogany J, Tupman S, Esposito AM, Kinzy TG, Nagy PD. 2010. Translation elongation factor 1A facilitates the assembly of the tombusvirus replicase and stimulates minus-strand synthesis. *PLoS Pathog* 6:e1001175.
122. Li Z, Pogany J, Panavas T, Xu K, Esposito AM, Kinzy TG, Nagy PD. 2009. Translation elongation factor 1A is a component of the tombusvirus replicase complex and affects the stability of the p33 replication co-factor. *Virology* 385:245-60.
123. Li Z, Barajas D, Panavas T, Herbst DA, Nagy PD. 2008. Cdc34p ubiquitin-conjugating enzyme is a component of the tombusvirus replicase complex and ubiquitinates p33 replication protein. *J Virol* 82:6911-26.
124. Beh CT, Cool L, Phillips J, Rine J. 2001. Overlapping functions of the yeast oxysterol-binding protein homologues. *Genetics* 157:1117-40.
125. Drinnenberg IA, Weinberg DE, Xie KT, Mower JP, Wolfe KH, Fink GR, Bartel DP. 2009. RNAi in budding yeast. *Science* 326:544-550.
126. Feng ZK, Kovalev N, Nagy PD. 2020. Key interplay between the co-opted sorting nexin-BAR proteins and PI3P phosphoinositide in the formation of the tombusvirus replicase. *Plos Pathogens* 16:e1009120.
127. Nagy PD. 2015. Viral sensing of the subcellular environment regulates the assembly of new viral replicase complexes during the course of infection. *J Virol* 89:5196-9.
128. Inaba JI, Xu K, Kovalev N, Ramanathan H, Roy CR, Lindenbach BD, Nagy PD. 2019. Screening Legionella effectors for antiviral effects reveals Rab1 GTPase as a proviral factor coopted for tombusvirus replication. *Proc Natl Acad Sci U S A* 116:21739-21747.
129. van der Schaar HM, Dorobantu CM, Albuлесcu L, Strating J, van Kuppeveld FJM. 2016. Fat(al) attraction: Picornaviruses Usurp Lipid Transfer at Membrane Contact Sites to Create Replication Organelles. *Trends Microbiol* 24:535-546.
130. Laufman O, Perrino J, Andino R. 2019. Viral Generated Inter-Organelle Contacts Redirect Lipid Flux for Genome Replication. *Cell* 178:275-289 e16.



131. Janke C, Magiera MM, Rathfelder N, Taxis C, Reber S, Maekawa H, Moreno-Borchart A, Doenges G, Schwob E, Schiebel E, Knop M. 2004. A versatile toolbox for PCR-based tagging of yeast genes: new fluorescent proteins, more markers and promoter substitution cassettes. *Yeast* 21:947-62.
132. Panaviene Z, Panavas T, Serva S, Nagy PD. 2004. Purification of the cucumber necrosis virus replicase from yeast cells: role of coexpressed viral RNA in stimulation of replicase activity. *J Virol* 78:8254-63.
133. Bachan S, Dinesh-Kumar SP. 2012. Tobacco rattle virus (TRV)-based virus-induced gene silencing. *Methods Mol Biol* 894:83-92.
134. Barajas D, Li Z, Nagy PD. 2009. The Nedd4-type Rsp5p ubiquitin ligase inhibits tombusvirus replication by regulating degradation of the p92 replication protein and decreasing the activity of the tombusvirus replicase. *J Virol* 83:11751-64.
135. Kovalev N, Barajas D, Nagy PD. 2012. Similar roles for yeast Dbp2 and Arabidopsis RH20 DEAD-box RNA helicases to Ded1 helicase in tombusvirus plus-strand synthesis. *Virology* 432:470-84.
136. Lazear HM, Diamond MS. 2015. New insights into innate immune restriction of West Nile virus infection. *Curr Opin Virol* 11:1-6.
137. Horner SM, Gale M, Jr. 2013. Regulation of hepatic innate immunity by hepatitis C virus. *Nat Med* 19:879-88.
138. Suthar MS, Diamond MS, Gale M, Jr. 2013. West Nile virus infection and immunity. *Nat Rev Microbiol* 11:115-28.
139. Schoggins JW, Rice CM. 2013. Innate immune responses to hepatitis C virus. *Curr Top Microbiol Immunol* 369:219-42.
140. Mendu V, Chiu M, Barajas D, Li Z, Nagy PD. 2010. Cpr1 cyclophilin and Ess1 parvulin prolyl isomerases interact with the tombusvirus replication protein and inhibit viral replication in yeast model host. *Virology* 406:342-51.
141. Nagy PD, Barajas D, Pogany J. 2012. Host factors with regulatory roles in tombusvirus replication. *Curr Opin Virol* 2:691-8.
142. Wu Y, Zhou T, Hu J, Liu Y, Jin S, Wu J, Guan X, Cui J. 2022. Autophagy Activation Induces p62-Dependent Autophagic Degradation of Dengue Virus Capsid Protein During Infection. *Front Microbiol* 13:889693.
143. Hou P, Wang X, Wang H, Wang T, Yu Z, Xu C, Zhao Y, Wang W, Zhao Y, Chu F, Chang H, Zhu H, Lu J, Zhang F, Liang X, Li X, Wang S, Gao Y, He H. 2023. The ORF7a protein of SARS-CoV-2 initiates autophagy and limits autophagosome-lysosome fusion via degradation of SNAP29 to promote virus replication. *Autophagy* 19:551-569.
144. Miller K, McGrath ME, Hu Z, Ariannejad S, Weston S, Frieman M, Jackson WT. 2020. Coronavirus interactions with the cellular autophagy machinery. *Autophagy* 16:2131-2139.
145. Li F, Zhang C, Tang Z, Zhang L, Dai Z, Lyu S, Li Y, Hou X, Bernardis M, Wang A. 2020. A plant RNA virus activates selective autophagy in a UPR-dependent manner to promote virus infection. *New Phytol* 228:622-639.
146. Jackson WT, Giddings TH, Jr., Taylor MP, Mulinyawe S, Rabinovitch M, Kopito RR, Kirkegaard K. 2005. Subversion of cellular autophagosomal machinery by RNA viruses. *PLoS Biol* 3:e156.

147. Jiang H, Kan X, Ding C, Sun Y. 2022. The Multi-Faceted Role of Autophagy During Animal Virus Infection. *Front Cell Infect Microbiol* 12:858953.
148. Abernathy E, Mateo R, Majzoub K, van Buuren N, Bird SW, Carette JE, Kirkegaard K. 2019. Differential and convergent utilization of autophagy components by positive-strand RNA viruses. *PLoS Biol* 17:e2006926.
149. Hafren A, Hofius D. 2017. NBR1-mediated antiviral xenophagy in plant immunity. *Autophagy* 13:2000-2001.
150. Tong X, Zhao JJ, Feng YL, Zou JZ, Ye J, Liu J, Han C, Li D, Wang XB. 2023. A selective autophagy receptor VISP1 induces symptom recovery by targeting viral silencing suppressors. *Nat Commun* 14:3852.
151. Yang M, Liu Y. 2022. Autophagy in plant viral infection. *FEBS Lett* 596:2152-2162.
152. Liu Y, Schiff M, Czymmek K, Talloczy Z, Levine B, Dinesh-Kumar SP. 2005. Autophagy regulates programmed cell death during the plant innate immune response. *Cell* 121:567-577.
153. Hafren A, Ustun S, Hochmuth A, Svenning S, Johansen T, Hofius D. 2018. Turnip Mosaic Virus Counteracts Selective Autophagy of the Viral Silencing Suppressor HCpro. *Plant Physiol* 176:649-662.
154. Haxim Y, Ismayil A, Jia Q, Wang Y, Zheng X, Chen T, Qian L, Liu N, Wang Y, Han S, Cheng J, Qi Y, Hong Y, Liu Y. 2017. Autophagy functions as an antiviral mechanism against geminiviruses in plants. *Elife* 6.
155. Jiang L, Lu Y, Zheng X, Yang X, Chen Y, Zhang T, Zhao X, Wang S, Zhao X, Song X, Zhang X, Peng J, Zheng H, Lin L, MacFarlane S, Liu Y, Chen J, Yan F. 2021. The plant protein NbP3IP directs degradation of Rice stripe virus p3 silencing suppressor protein to limit virus infection through interaction with the autophagy-related protein NbATG8. *New Phytol* 229:1036-1051.
156. Shang K, Xiao L, Zhang X, Zang L, Zhao D, Wang C, Wang X, Zhou T, Zhu C, Zhu X. 2023. Tomato chlorosis virus p22 interacts with NbBAG5 to inhibit autophagy and regulate virus infection. *Mol Plant Pathol* 24:425-435.
157. Yang M, Ismayil A, Gao T, Ye Z, Yue N, Wu J, Zheng X, Li Y, Wang Y, Hong Y, Liu Y. 2023. Cotton leaf curl Multan virus C4 protein suppresses autophagy to facilitate viral infection. *Plant Physiol* 193:708-720.
158. Yang M, Zhang Y, Xie X, Yue N, Li J, Wang XB, Han C, Yu J, Liu Y, Li D. 2018. Barley stripe mosaic virus gammab Protein Subverts Autophagy to Promote Viral Infection by Disrupting the ATG7-ATG8 Interaction. *Plant Cell* 30:1582-1595.
159. Cheng X, Wang A. 2017. The Potyvirus Silencing Suppressor Protein VPg Mediates Degradation of SGS3 via Ubiquitination and Autophagy Pathways. *J Virol* 91.
160. Kushwaha NK, Hafren A, Hofius D. 2019. Autophagy-virus interplay in plants: from antiviral recognition to proviral manipulation. *Mol Plant Pathol* 20:1211-1216.
161. Niu E, Ye C, Zhao W, Kondo H, Wu Y, Chen J, Andika IB, Sun L. 2022. Coat protein of Chinese wheat mosaic virus upregulates and interacts with cytosolic glyceraldehyde-3-phosphate dehydrogenase, a negative regulator of plant autophagy, to promote virus infection. *J Integr Plant Biol* 64:1631-1645.

162. Huang YP, Huang YW, Hsiao YJ, Li SC, Hsu YH, Tsai CH. 2019. Autophagy is involved in assisting the replication of Bamboo mosaic virus in *Nicotiana benthamiana*. *J Exp Bot* 70:4657-4670.
163. Chang C, Jensen LE, Hurley JH. 2021. Autophagosome biogenesis comes out of the black box. *Nat Cell Biol* 23:450-456.
164. Yoon SH, Chung T. 2019. Protein and RNA Quality Control by Autophagy in Plant Cells. *Mol Cells* 42:285-291.
165. Lin Y, Guo R, Ji C, Zhou J, Jiang L. 2021. New insights into AtNBR1 as a selective autophagy cargo receptor in *Arabidopsis*. *Plant Signal Behav* 16:1839226.
166. Leong JX, Langin G, Ustun S. 2022. Selective autophagy: adding precision in plant immunity. *Essays Biochem* 66:189-206.
167. Kang Y, Lin W, Liu Y, Nagy PD. 2022. Key tethering function of Atg11 autophagy scaffold protein in formation of virus-induced membrane contact sites during tombusvirus replication. *Virology* 572:1-16.
168. Wang Y, Yu B, Zhao J, Guo J, Li Y, Han S, Huang L, Du Y, Hong Y, Tang D, Liu Y. 2013. Autophagy contributes to leaf starch degradation. *Plant Cell* 25:1383-99.
169. Wu CY, Nagy PD. 2019. Blocking tombusvirus replication through the antiviral functions of DDX17-like RH30 DEAD-box helicase. *PLoS Pathog* 15:e1007771.
170. Zhuang X, Wang H, Lam SK, Gao C, Wang X, Cai Y, Jiang L. 2013. A BAR-domain protein SH3P2, which binds to phosphatidylinositol 3-phosphate and ATG8, regulates autophagosome formation in *Arabidopsis*. *Plant Cell* 25:4596-615.
171. Zhuang X, Jiang L. 2014. Autophagosome biogenesis in plants: roles of SH3P2. *Autophagy* 10:704-5.
172. Leong JX, Raffener M, Spinti D, Langin G, Franz-Wachtel M, Guzman AR, Kim JG, Pandey P, Minina AE, Macek B, Hafren A, Bozkurt TO, Mudgett MB, Bornke F, Hofius D, Ustun S. 2022. A bacterial effector counteracts host autophagy by promoting degradation of an autophagy component. *EMBO J* 41:e110352.
173. Snider J, Kittanakom S, Curak J, Stagljar I. 2010. Split-ubiquitin based membrane yeast two-hybrid (MYTH) system: a powerful tool for identifying protein-protein interactions. *J Vis Exp* doi:10.3791/1698.
174. Yang A, Pantoom S, Wu YW. 2020. Distinct Mechanisms for Processing Autophagy Protein LC3-PE by RavZ and ATG4B. *Chembiochem* 21:3377-3382.
175. Choy A, Dancourt J, Mugo B, O'Connor TJ, Isberg RR, Melia TJ, Roy CR. 2012. The *Legionella* effector RavZ inhibits host autophagy through irreversible Atg8 deconjugation. *Science* 338:1072-6.
176. Shintani T, Klionsky DJ. 2004. Cargo proteins facilitate the formation of transport vesicles in the cytoplasm to vacuole targeting pathway. *J Biol Chem* 279:29889-94.
177. Zhang Y, Chen Z. 2020. Broad and Complex Roles of NBR1-Mediated Selective Autophagy in Plant Stress Responses. *Cells* 9.

178. Laczko-Dobos H, Maddali AK, Jipa A, Bhattacharjee A, Vegh AG, Juhasz G. 2021. Lipid profiles of autophagic structures isolated from wild type and Atg2 mutant *Drosophila*. *Biochim Biophys Acta Mol Cell Biol Lipids* 1866:158868.
179. Gillooly DJ, Morrow IC, Lindsay M, Gould R, Bryant NJ, Gaullier JM, Parton RG, Stenmark H. 2000. Localization of phosphatidylinositol 3-phosphate in yeast and mammalian cells. *EMBO J* 19:4577-88.
180. Yang M, Ismayil A, Liu Y. 2020. Autophagy in Plant-Virus Interactions. *Annu Rev Virol* 7:403-419.
181. Dong P, Xiong F, Que Y, Wang K, Yu L, Li Z, Ren M. 2015. Expression profiling and functional analysis reveals that TOR is a key player in regulating photosynthesis and phytohormone signaling pathways in *Arabidopsis*. *Front Plant Sci* 6:677.
182. Sun D, Wu R, Zheng J, Li P, Yu L. 2018. Polyubiquitin chain-induced p62 phase separation drives autophagic cargo segregation. *Cell Res* 28:405-415.
183. Banani SF, Lee HO, Hyman AA, Rosen MK. 2017. Biomolecular condensates: organizers of cellular biochemistry. *Nat Rev Mol Cell Biol* 18:285-298.
184. Borchers W, Bremer A, Borgia MB, Mittag T. 2021. How do intrinsically disordered protein regions encode a driving force for liquid-liquid phase separation? *Curr Opin Struct Biol* 67:41-50.
185. Nagy PD. 2022. Co-opted membranes, lipids, and host proteins: what have we learned from tombusviruses? *Curr Opin Virol* 56:101258.
186. Kovalev N, de Castro Martin IF, Pogany J, Barajas D, Pathak K, Risco C, Nagy PD. 2016. Role of Viral RNA and Co-opted Cellular ESCRT-I and ESCRT-III Factors in Formation of Tombusvirus Spherules Harboring the Tombusvirus Replicase. *J Virol* 90:3611-26.
187. Russo M, Burgyan J, Martelli GP. 1994. Molecular biology of tombusviridae. *Adv Virus Res* 44:381-428.
188. Navarro B, Russo M, Pantaleo V, Rubino L. 2006. Cytological analysis of *Saccharomyces cerevisiae* cells supporting cymbidium ringspot virus defective interfering RNA replication. *J Gen Virol* 87:705-714.
189. Rochon D, Singh B, Reade R, Theilmann J, Ghoshal K, Alam SB, Maghodia A. 2014. The p33 auxiliary replicase protein of Cucumber necrosis virus targets peroxisomes and infection induces de novo peroxisome formation from the endoplasmic reticulum. *Virology* 452-453:133-42.
190. McCartney AW, Greenwood JS, Fabian MR, White KA, Mullen RT. 2005. Localization of the tomato bushy stunt virus replication protein p33 reveals a peroxisome-to-endoplasmic reticulum sorting pathway. *Plant Cell* 17:3513-31.
191. Richardson LG, Clendening EA, Sheen H, Gidda SK, White KA, Mullen RT. 2014. A unique N-terminal sequence in the Carnation Italian ringspot virus p36 replicase-associated protein interacts with the host cell ESCRT-I component Vps23. *J Virol* 88:6329-44.
192. Tan X, Cai K, Li J, Yuan Z, Chen R, Xiao H, Xu C, Hu B, Qin Y, Ding B. 2023. Coronavirus subverts ER-phagy by hijacking FAM134B and ATL3 into p62 condensates to facilitate viral replication. *Cell Rep* 42:112286.
193. Turco E, Witt M, Abert C, Bock-Bierbaum T, Su MY, Trapannone R, Sztacho M, Danieli A, Shi X, Zaffagnini G, Gamper A, Schuschnig M, Fracchiolla D,

- Bernklau D, Romanov J, Hartl M, Hurley JH, Daumke O, Martens S. 2019. FIP200 Claw Domain Binding to p62 Promotes Autophagosome Formation at Ubiquitin Condensates. *Mol Cell* 74:330-346 e11.
194. Zaffagnini G, Savova A, Danieli A, Romanov J, Tremel S, Ebner M, Peterbauer T, Sztacho M, Trapannone R, Tarafder AK, Sachse C, Martens S. 2018. p62 filaments capture and present ubiquitinated cargos for autophagy. *EMBO J* 37.
195. Lopez N, Camporeale G, Salgueiro M, Borkosky SS, Visentin A, Peralta-Martinez R, Loureiro ME, de Prat-Gay G. 2021. Deconstructing virus condensation. *PLoS Pathog* 17:e1009926.
196. Wu C, Holehouse AS, Leung DW, Amarasinghe GK, Dutch RE. 2022. Liquid Phase Partitioning in Virus Replication: Observations and Opportunities. *Annu Rev Virol* 9:285-306.
197. Brocca S, Grandori R, Longhi S, Uversky V. 2020. Liquid-Liquid Phase Separation by Intrinsically Disordered Protein Regions of Viruses: Roles in Viral Life Cycle and Control of Virus-Host Interactions. *Int J Mol Sci* 21.
198. Zavaliev R, Mohan R, Chen T, Dong X. 2020. Formation of NPR1 Condensates Promotes Cell Survival during the Plant Immune Response. *Cell* 182:1093-1108 e18.
199. Fang XD, Gao Q, Zang Y, Qiao JH, Gao DM, Xu WY, Wang Y, Li D, Wang XB. 2022. Host casein kinase 1-mediated phosphorylation modulates phase separation of a rhabdovirus phosphoprotein and virus infection. *Elife* 11.
200. Shen C, Li R, Negro R, Cheng J, Vora SM, Fu TM, Wang A, He K, Andreeva L, Gao P, Tian Z, Flavell RA, Zhu S, Wu H. 2021. Phase separation drives RNA virus-induced activation of the NLRP6 inflammasome. *Cell* 184:5759-5774 e20.
201. Brown SL, Garrison DJ, May JP. 2021. Phase separation of a plant virus movement protein and cellular factors support virus-host interactions. *PLoS Pathog* 17:e1009622.
202. Hafren A, Lohmus A, Makinen K. 2015. Formation of Potato Virus A-Induced RNA Granules and Viral Translation Are Interrelated Processes Required for Optimal Virus Accumulation. *PLoS Pathog* 11:e1005314.
203. Lennemann NJ, Coyne CB. 2017. Dengue and Zika viruses subvert reticulophagy by NS2B3-mediated cleavage of FAM134B. *Autophagy* 13:322-332.
204. Lan Y, van Leur SW, Fernando JA, Wong HH, Kampmann M, Siu L, Zhang J, Li M, Nicholls JM, Sanyal S. 2023. Viral subversion of selective autophagy is critical for biogenesis of virus replication organelles. *Nat Commun* 14:2698.
205. Choi Y, Bowman JW, Jung JU. 2018. Autophagy during viral infection - a double-edged sword. *Nat Rev Microbiol* 16:341-354.
206. Michaeli S, Clavel M, Lechner E, Viotti C, Wu J, Dubois M, Hacquard T, Derrien B, Izquierdo E, Lecorbeiller M, Bouteiller N, De Cilia J, Ziegler-Graff V, Vaucheret H, Galili G, Genschik P. 2019. The viral F-box protein P0 induces an ER-derived autophagy degradation pathway for the clearance of membrane-bound AGO1. *Proc Natl Acad Sci U S A* 116:22872-22883.
207. Derrien B, Baumberger N, Schepetilnikov M, Viotti C, De Cilia J, Ziegler-Graff V, Isono E, Schumacher K, Genschik P. 2012. Degradation of the antiviral component ARGONAUTE1 by the autophagy pathway. *Proc Natl Acad Sci U S A* 109:15942-6.

208. Li F, Zhao N, Li Z, Xu X, Wang Y, Yang X, Liu SS, Wang A, Zhou X. 2017. A calmodulin-like protein suppresses RNA silencing and promotes geminivirus infection by degrading SGS3 via the autophagy pathway in *Nicotiana benthamiana*. *PLoS Pathog* 13:e1006213.
209. Rajendran KS, Nagy PD. 2003. Characterization of the RNA-binding domains in the replicase proteins of tomato bushy stunt virus. *J Virol* 77:9244-58.
210. Taylor NO, Wei MT, Stone HA, Brangwynne CP. 2019. Quantifying Dynamics in Phase-Separated Condensates Using Fluorescence Recovery after Photobleaching. *Biophys J* 117:1285-1300.
211. Alberti S, Hyman AA. 2021. Biomolecular condensates at the nexus of cellular stress, protein aggregation disease and ageing. *Nat Rev Mol Cell Biol* 22:196-213.
212. Milovanovic D, Wu Y, Bian X, De Camilli P. 2018. A liquid phase of synapsin and lipid vesicles. *Science* 361:604-607.
213. Whitton JL, Cornell CT, Feuer R. 2005. Host and virus determinants of picornavirus pathogenesis and tropism. *Nat Rev Microbiol* 3:765-76.
214. Gralinski LE, Baric RS. 2015. Molecular pathology of emerging coronavirus infections. *J Pathol* 235:185-95.
215. Kaddachi I, Souiden Y, Achouri D, Chéour F. 2014. Barley yellow dwarf virus (BYDV): characteristics, hosts, vectors, disease symptoms and diagnosis. *International Journal of Phytopathology* 3:155-160.
216. Neufeldt CJ, Cortese M. 2022. Membrane architects: how positive-strand RNA viruses restructure the cell. *Journal of General Virology* 103:001773.
217. Berkhout B. 2018. RNAi-mediated antiviral immunity in mammals. *Curr Opin Virol* 32:9-14.
218. Yang Z, Li Y. 2018. Dissection of RNAi-based antiviral immunity in plants. *Curr Opin Virol* 32:88-99.
219. Wang RY, Nagy PD. 2008. Tomato bushy stunt virus co-opts the RNA-binding function of a host metabolic enzyme for viral genomic RNA synthesis. *Cell Host Microbe* 3:178-87.
220. Wu CY, Nagy PD. 2020. Role reversal of functional identity in host factors: Dissecting features affecting pro-viral versus antiviral functions of cellular DEAD-box helicases in tombusvirus replication. *PLoS Pathog* 16:e1008990.
221. Reinisch KM, Prinz WA. 2021. Mechanisms of nonvesicular lipid transport. *J Cell Biol* 220:e202012058.
222. De M, Oleskie AN, Ayyash M, Dutta S, Mancour L, Abazeed ME, Brace EJ, Skiniotis G, Fuller RS. 2017. The Vps13p-Cdc31p complex is directly required for TGN late endosome transport and TGN homotypic fusion. *Journal of Cell Biology* 216:425-439.
223. Li PQ, Lees JA, Lusk CP, Reinisch KM. 2020. Cryo-EM reconstruction of a VPS13 fragment reveals a long groove to channel lipids between membranes. *Journal of Cell Biology* 219.
224. Velikkakath AK, Nishimura T, Oita E, Ishihara N, Mizushima N. 2012. Mammalian Atg2 proteins are essential for autophagosome formation and important for regulation of size and distribution of lipid droplets. *Mol Biol Cell* 23:896-909.

225. Osawa T, Noda NN. 2019. Atg2: A novel phospholipid transfer protein that mediates autophagosome biogenesis. *Protein Science* 28:1005-1012.
226. Kotani T, Kirisako H, Koizumi M, Ohsumi Y, Nakatogawa H. 2018. The Atg2-Atg18 complex tethers pre-autophagosomal membranes to the endoplasmic reticulum for autophagosome formation. *Proc Natl Acad Sci U S A* 115:10363-10368.
227. Valverde DP, Yu S, Boggavarapu V, Kumar N, Lees JA, Walz T, Reinisch KM, Melia TJ. 2019. ATG2 transports lipids to promote autophagosome biogenesis. *J Cell Biol* 218:1787-1798.
228. Chowdhury S, Otomo C, Leitner A, Ohashi K, Aebersold R, Lander GC, Otomo T. 2018. Insights into autophagosome biogenesis from structural and biochemical analyses of the ATG2A-WIPI4 complex. *Proceedings of the National Academy of Sciences of the United States of America* 115:E9792-E9801.
229. Stenmark H, Gillooly DJ. Intracellular trafficking and turnover of phosphatidylinositol 3-phosphate, p 193-199. *In* (ed), Elsevier,
230. Del Vecchio K, Stahelin RV. 2018. Investigation of the phosphatidylserine binding properties of the lipid biosensor, Lactadherin C2 (LactC2), in different membrane environments. *J Bioenerg Biomembr* 50:1-10.
231. Darland-Ransom M, Wang X, Sun CL, Mapes J, Gengyo-Ando K, Mitani S, Xue D. 2008. Role of *C. elegans* TAT-1 protein in maintaining plasma membrane phosphatidylserine asymmetry. *Science* 320:528-31.
232. Wu G, Jia Z, Ding K, Zheng H, Lu Y, Lin L, Peng J, Rao S, Wang A, Chen J, Yan F. 2022. Turnip mosaic virus co-opts the vacuolar sorting receptor VSR4 to promote viral genome replication in plants by targeting viral replication vesicles to the endosome. *PLoS Pathog* 18:e1010257.
233. Tan JX, Finkel T. 2022. A phosphoinositide signalling pathway mediates rapid lysosomal repair. *Nature* 609:815-821.
234. Senthil-Kumar M, Mysore KS. 2014. Tobacco rattle virus-based virus-induced gene silencing in *Nicotiana benthamiana*. *Nat Protoc* 9:1549-62.
235. Liu WJ, Gan Y, Huang WF, Wu HL, Zhang XQ, Zheng HJ, Liu HF. 2019. Lysosome restoration to activate podocyte autophagy: a new therapeutic strategy for diabetic kidney disease. *Cell Death Dis* 10:806.
236. Wang K, Klionsky DJ. 2011. Mitochondria removal by autophagy. *Autophagy* 7:297-300.
237. Monastyrska I, Klionsky DJ. 2006. Autophagy in organelle homeostasis: peroxisome turnover. *Mol Aspects Med* 27:483-94.
238. Lai Z, Wang F, Zheng Z, Fan B, Chen Z. 2011. A critical role of autophagy in plant resistance to necrotrophic fungal pathogens. *Plant J* 66:953-68.
239. Nakatogawa H. 2013. Two ubiquitin-like conjugation systems that mediate membrane formation during autophagy. *Autophagy: Molecules and Mechanisms* 55:39-50.
240. Matoba K, Kotani T, Tsutsumi A, Tsuji T, Mori T, Noshiro D, Sugita Y, Nomura N, Iwata S, Ohsumi Y. 2020. Atg9 is a lipid scramblase that mediates autophagosomal membrane expansion. *Nature structural & molecular biology* 27:1185-1193.

241. Moser von Filseck J, Čopič A, Delfosse V, Vanni S, Jackson CL, Bourguet W, Drin G. 2015. Phosphatidylserine transport by ORP/Osh proteins is driven by phosphatidylinositol 4-phosphate. *Science* 349:432-436.
242. Nakatogawa H. 2020. Mechanisms governing autophagosome biogenesis. *Nat Rev Mol Cell Biol* 21:439-458.
243. Weidberg H, Shvets E, Shpilka T, Shimron F, Shinder V, Elazar Z. 2010. LC3 and GATE-16/GABARAP subfamilies are both essential yet act differently in autophagosome biogenesis. *Embo Journal* 29:1792-1802.
244. Doelling JH, Walker JM, Friedman EM, Thompson AR, Vierstra RD. 2002. The APG8/12-activating enzyme APG7 is required for proper nutrient recycling and senescence in. *Journal of Biological Chemistry* 277:33105-33114.
245. Svenning S, Lamark T, Krause K, Johansen T. 2011. Plant NBR1 is a selective autophagy substrate and a functional hybrid of the mammalian autophagic adapters NBR1 and p62/SQSTM1. *Autophagy* 7:993-1010.
246. Danieli A, Vucak G, Baccharini M, Martens S. 2023. Sequestration of translation initiation factors in p62 condensates. *Cell Rep* 42:113583.
247. Herhaus L, Dikic I. 2018. Ubiquitin-induced phase separation of p62/SQSTM1. *Cell Res* 28:389-390.
248. Graef M, Friedman JR, Graham C, Babu M, Nunnari J. 2013. ER exit sites are physical and functional core autophagosome biogenesis components. *Mol Biol Cell* 24:2918-31.
249. Gómez-Sánchez R, Rose J, Guimarães R, Mari M, Papinski D, Rieter E, Geerts WJ, Hardenberg R, Kraft C, Ungermann C. 2018. Atg9 establishes Atg2-dependent contact sites between the endoplasmic reticulum and phagophores. *Journal of Cell Biology* 217:2743-2763.



## VITA

Yuanrong Kang

### ***Education***

Master of Biochemistry and Molecular Biology

09/2014—06/2018

*College of Life Science and Technology, Huazhong Agricultural University, Wuhan, China*

Bachelor of Bioengineering

09/2010—06/2014

*College of Life Science and Technology, Huazhong Agricultural University, Wuhan, China*

### ***Publications***

**Kang Y**, Lin W, Nagy P D. Subversion of selective autophagy for the biogenesis of tombusvirus replication organelles inhibits autophagy[J]. Plos Pathogens, 2024, 20(3): e1012085.

**Kang Y\***, Lin W\*, Liu Y, et al. Key tethering function of Atg11 autophagy scaffold protein in formation of virus-induced membrane contact sites during tombusvirus replication[J]. Virology, 2022, 572: 1-16.

Liao M\*, Ma Z\*, **Kang Y**, et al. ENHANCED DISEASE SUSCEPTIBILITY 1 promotes hydrogen peroxide scavenging to enhance rice thermotolerance[J]. Plant Physiology, 2023: kiad257.

Li, N., Yang, Z., Li, J., Xie, W., Qin, X., **Kang, Y.**, et al. Two VQ proteins are substrates of the OsMPKK6-OsMPK4 cascade in rice defense against bacterial blight[J]. Rice, 2021, 14(1): 39.

Ke Y, **Kang Y**, Wu M, et al. Jasmonic acid-involved OsEDS1 signaling in rice-bacteria interactions[J]. Rice, 2019, 12: 1-12.